TECHNICKÁ UNIVERZITA V LIBERCI
Fakulta mechatroniky, informatiky
a mezioborových studií

Modification of Synthetic Polymeric Materials' Surface for Suppression of Biofilm Formation

M.Sc. Sumita Swar

The thesis submitted for the degree of Doctor of Philosophy at
The Technical University of Liberec, Czech Republic in 2018

Fakulta mechatroniky, informatiky a mezioborových studií

TECHNICKÁ UNIVERZITA V LIBERCI

Studentská 2, 461 17 Liberec 1

Teze disertační práce: **Modification of Synthetic Polymeric Materials' Surface for Suppression of Biofilm Formation**

Autor: **Sumita Swar**

Studijní program: **P3901**

Studijní obor: **3901V055 Aplikované vědy v inženýrství (AVI)**

Ústav: **NTI**

Školitel: **Prof. Ing. Ivan Stibor, CSc.**

Liberec 2018

Declaration by author

This thesis is composed of my original work, and contains no material previously published or written by another person except where due reference has been made in the text.

I have clearly stated the contribution of others to my thesis as a whole, including experiments, data analysis, significant technical procedures, professional advice and any other original research work used or reported in my thesis. The content of my thesis is the result of work I have carried out since the commencement of my research.

Signature **Date**

Acknowledgements

Firstly, I would like to express my sincerest gratitude to my supervisor Prof. Ivan Stibor for his advice, ideas, excellent guidance and enormous support during my Ph.D. study. I sincerely thank Dr. Veronika Zajícová for her special help and guidance throughout my Ph.D. study. I acknowledge all the facilities provided by Technical University of Liberec.

I am grateful to the following contributors for this thesis:

Dr. J. Horaková for the cytotoxicity and cell adhesion tests of pure and modified Nylon 6 samples;
Dr. V. Zajícová and P. Šubrtová for antibacterial tests of pure and modified Nylon 6 samples;
Dr. J. Karpíšková for N_2 sorption isotherm analysis (BET) for synthesized MSNs;
Dr. J. Müllerová for the FT-IR and Raman spectroscopy analysis;
Dr. I. Lovětinská-Šlamborová for biofilm tests for pure and modified PET samples;
Dr. M. Rysová for biocompatibility and cell adhesion assessment for PET samples;
Dr. V. Zajícová and P. Kejzlar for SEM analysis;
Dr. V. Zajícová and Dr. L. Voleský for AFM anlysis;

I would like to express my gratitude to Prof. Luisa De Cola group, Laboratoire de Chimie et des Biomatériaux Supramoléculaires, Université De Strasbourg for the assistance in XPS analyses.

My work has been supported by the following projects SGS n. 21207, 2017-2019, and SGS n. 21164, 2016. Faculty of Science, Humanities and Education, Department of Chemistry, Technical University of Liberec. I also acknowledge the assistance provided by the Research Infrastructure NanoEnviCz, supported by the Ministry of Education, Youth and Sports of the Czech Republic under Project No. LM2015073.

I would like to thank all my colleagues including Dr. M. Řezanka, Mr. J. Lukášek, Mr. V. Novotný and Mr. J. Mikšíček for their supports in laboratory.

Last but not least, I would like to express my deepest gratitude to all my family members for their cordial support and encouragement during my Ph.D. study.

CONTENTS

LIST OF SCHEMES

LIST OF FIGURES

LIST OF TABLES

1. AN OVERVIEW OF THE RESEARCH OUTPUT

Nosocomial infections (NI) have been serious problems for hospitalized patients where almost half of all the infections are device related. Various polymeric materials including polyesters and polyamides such as polyethylene terephthalate – PET and Nylon 6 are widely utilized for clinical devices. These polymers are commonly used in biomedical applications ranging from catheters to stents, vascular grafts, heart valves, wound dressings, sutures and scaffolds. Polymer surface modification is very essential factor to improve and impart desired properties for biomedical applications, making the polymers biocompatible, non-cytotoxic and antibacterial that can preferably resist biofilm formation caused by pathogenic bacteria.

At first, novel approach to anti-corrosive wet chemical surface modification of PET by insertion of alkyl and hydroxyl groups was achieved by using different Grignard reagents and confirmed by several different characterization techniques including water contact angle (WCA) measurement, free surface energy (FSE) measurement, fluorescence intensity test after fluorescence labelling with dansyl chloride, scanning electron microscopy (SEM) and atomic force microscopy (AFM). High antibacterial efficiency against four different types of biofilm active, pathogenic bacterial strains namely: *Staphylococcus aureus*, *Escherichia coli*, methicillin-resistant *Staphylococcus aureus* (MRSA) and *Pseudomonas aeruginosa* was established on the modified PET surface. Biocompatibility much higher than 70 % of the modified samples has been proved.

Our second studies were focused on an efficient reduction of amide functional groups to secondary amine on Nylon 6 film surface with borane-tetrahydrofuran (BH_3-THF) complex, followed by N-alkylation with benzyl chloride ($C_6H_5CH_2Cl$) as well as grafting on reduced Nylon 6 surface by using poly(ethylene glycol) methyl ether tosylate (H_3C-PEG-OTs). The different *N*-alkylation reactions allowed us to tune the surface properties of Nylon 6. Thus obtained modified Nylon 6 polyamide can be useful for many applications including antifouling biomaterials as the polyamide after functionalization was found to be biocompatible and resistant to pathogenic bacterial adhesion due to the presence of hydrophilic poly(ethylene glycol) methyl ether (H_3C-PEG) chains after grafting. Not only that, the grafting intensity was regulated also by the duration of preceding lithiation reaction before grafting. The grafted Nylon 6 samples were further modified by physical assemblage of copper nanoparticles (Cu NPs) on the surface. Another modification route was also examined for PEG immobilization on reduced Nylon 6 surface via *N*,*N*′-disuccinimidyl

Carbonate (DSC) conjugation. The surface modifications were confirmed by different techniques. Water contact angle (WCA), free surface energy (FSE) analyses indicated the significant change in the surface morphology that were established by scanning electron microscopy (SEM), atomic force microscopy (AFM), X-ray photoelectron spectroscopy (XPS), Fourier-transform infrared spectroscopy (FT-IR) and Raman spectroscopy. The pathogenic bacterial strains: Gram positive *Staphylococcus aureus* and Gram negative *Pseudomonas aeruginosa* were used to depict the antibacterial efficacy. The resistance to bacterial adhesion has been established for the grafted and Cu NP deposited modified Nylon 6 samples. Most of the modified samples were established to be cytocompatible.

Simultaneously, our focus was to synthesize the copper nanoparticles (Cu NPs) for the deposition on grafted Nylon 6 surface to examine the possibility of Cu NP physisorption on surface as well as to evaluate the antibacterial efficacy of prepared Cu NP deposited Nylon 6 samples. The synthesized Cu NPs were characterized by various methods including dynamic light scattering (DLS), scanning electron microscopy (SEM), UV-VIS spectroscopy and Fourier-transform infrared spectroscopy (FT-IR).

The last but not least study was concentrated on synthesis of mesoporous silica nanoparticles (MSNs) that are widely studied for drug delivery. The resulting mesoporous surfaces are now conveniently prepared making use of recently published collection of carefully verified synthetic procedures. The MSNs thus obtained were characterized by Brunauer-Emmett-Teller (BET) analysis and scanning electron microscopy (SEM). The selected MSNs with various pore diameters and morphologies were examined to evaluate the capability of L-DOPA drug loading and release that is a well-known drug for Parkinson's disease. The L-DOPA drug loading and release profiles were measured by UV-VIS spectroscopy and SBA-15 was proved to be the most effective amongst all the different types of tested mesoporous silica materials.

Keywords: pathogenic bacteria, polyethylene terephthalate, Nylon 6, mesoporous silica nanoparticles, drug delivery.

1. PŘEHLED VÝSLEDKŮ

Nosokomiální infekce (NI) představují významný problém pro hospitalizované pacienty kde téměř polovina infekcí je zprostředkována nerůznějšími lékařskými nástroji. Tyto nástroje obsahují části nebo jsou celé z polymerních materiálů typu polyamidů (např. Nylon 6) a polyesterů (např. PET). Tyto polymery se běžně používají v řadě zavedených biomedicinských aplikací, jako jsou katetry, stenty, srdeční chlopně, krycí materiály pro popáleniny a řadu dalších pomocných materiálů. Modifikace povrchu těchto a dalších polymerů je jednou z možností jak upravovat vlastnosti a s nimi spojenou aplikovatelnost těchto biomedicinských materiálů. Vhodnou funkcionalizací povrchu lze dospět k matertiálům biokompatibilním, antibakteriálním, a/nebo rezistentním k tvorbě a ulpívání biofilmu.

V první části byl rozpracován postup pro modifikaci povrchu polyesterů (konkretně PET) využívající reakci esterových funkcí s Grignardovými a organolitnými organokovovými činidly. Reakcí se do povrchové vrstvy vnáší hydroxylová skupina, ale zároveň i dva organické zbytky, odpovídající použitému organokovovém činidlu. Tím lze povrchovou vrstvu modifikovat v širokých mezích. Reakci lze monitorovat řadou technik, zde bylo využito měření kontaktního úhlu, volné povrchové energie, měření fluorescenční intenzity (po vhodném fluorescenčně aktivním označení účinkem dansyl chloridu). Vedle toho byly interpretována data SEM, AFM, i IČ analýz. Biologická aktivita modifikovaných povrchů byla testována na kmenech: *Staphylococcus aureus*, *Escherichia coli*, methicillin-resistentní *Staphylococcus aureus* (MRSA) a *Pseudomonas aeruginosa*. Biokompatibilita vyšší než 70 % byla zjištěna u některých materiálů s modifikovanou povrchovou vrstvou.

Druhá část popisuje studii, jejíž podstatou je aplikace účinné redukce amidické funkce polyamidů (zde Nylon 6) účinkem diboranu a jeho komplexů. Tato reakce byla ihned následována funkcionalizací (alkylací) vznikajícího aminu. K tomu bylo využito benzyl chloridu ($C_6H_5CH_2Cl$) a poly(ethylen glycol) methyl ether tosylátu (H_3C-PEG-OTs). Volbou alkylačních činidel bylo možné měnit povrchové vlastnosti výchozích polyamidů v širokých mezích. Takto získaný modifikovaný Nylon 6 vykazoval zajímavé vlastnosti se silně potlačenou tvorbou biofilomu. Výsledné vlastnosti polymeru byly závislé nejen na použitém činidle, ale také na využitých reakčních podmínkách. Pro další funkcionalizaci byly využity i nanočástice Cu spontánně tvořící povlak na Nylonu 6. Byl vyzkoušen i jiný postup funkcionalizace redukovaného polyamidu účinkem *N*,*N*′-disukcinimidyl karbonátu (DSC). Vlastnosti takto získaných modifikovaných povrchů byly testovány s využitím analogických

metodik a postupů, které se osvědčily u polyesterů. Většina vzorků s modifikovanými povrchy byla shledána jako cytokompatibilní.

Ve třetí části jsou popsány naše výsledky při syntéze Cu NPs, které byly využity pro funkcionalizace polyamidů. Vzniklé nanočastice byly charakterizovány s využitím běžných metod a postupů jako jsou: dynamický rozptyl světla (DLS), elektronová mikroskopie (SEM), UV-VIS a FT-IR spektroskopie.

V poslední, čtvrté části této práce jsou popsány výsledky získané aplikací testovaných syntéz mesoporézních křemičitých nanočástic (MSNs). Ty byly testovány především jako nosiče dopaminu, což je neurotransmiter, využívaný při zpomalování projevů jinak neléčitelné Parkinsonovy nemoci. Tvorba a uvolňování L-DOPA byla měřena pro různé morfologie částic i tvar pórů MSNs. Využili jsme pro to opět spektrální metody. Výsledkem tohoto výzkumu je zjištění, že komerčně dostupný MSN typu SBA-15 vykázal v tomto ohledu nejvyšší účinnost.

Klíčová slova: patogenní bakterie, polyethylentereftalát, Nylon 6, mesoporézní silika nanočástice, transport léčiv.

ABBREVIATIONS

AFM	atomic force microscopy
BET	Brunauer–Emmett–Teller
BH_3	borane
BJH	Barret-Joyner-Halenda
CH_3-PEG-OTs	poly(ethylene glycol) methyl ether tosylate
CMC	critical micelle concentration
CTAB	hexadecyltrimethylammonium bromide
Cu NPs	copper nanoparticles
DEE	diethyl ether
DFT	density functional theory
DLS	dynamic light scattering
DLVO	Derjaguin-Landau-Verwey-Overbeek
DMEM	Dulbecco's Modified Eagle's Medium
DMSO	dimethyl sulfoxide
DNSC	dansyl chloride
DSC	*N,N'*-disuccinimidyl carbonate
EPS	extracellular polymeric substance
FT-IR	Fourier transform infrared spectroscopy
FSE	free surface energy
HAI	hospital acquired infections
KIT	Korea Advanced Institute of Science and Technology type material
LCP	liquid crystal polymer
L-DOPA	3-(3,4-dihydroxyphenyl)-L-alanine
MCF	mesostructured cellular foam
MCM	mobil crystalline material
MCM-41(FS)	MCM-41 prepared be fumed silica

MCM-4 (HO)	highly ordered MCM-41
MCM-41(S)	MCM-41 with spherical morphology
MRSA	methicillin-resistant *Staphylococcus aureus*
MSNs	mesoporous silica nanoparticles
MSU	Michigan State University material
MTT	3-(4,5-dimethylthiazol-2-yl)-2,5-diphenyltetrazolium bromide
***n*-BuLi**	*n*-butyllithium
NI	nosocomial infection
NC	negative control
NPs	nanoparticles
P123	poly(ethylene glycol)-*block*-poly(propylene glycol)-*block*-poly(ethylene glycol)
PA	polyamide
PAAm	polyacrylamide
PAANa	sodium salt of poly(acrylic acid)
PC	polycarbonates (in polymer)
PC	positive control (in cytotoxicity test)
PDLA	poly(D-lactic acid)
PDMS	polydimethylsiloxane
PE	polyethylene
PEG	polyethylene glycol
PEG-CH_3	poly(ethylene glycol) methyl ether
PET	polyethylene terephthalate
PGA	polyglycolic acid
pHEMA	polyhydroxyethyl methacrylate
PHTS	plugged hexagonal templated silica
PLLA	poly(L-lactic acid)
PMMA	polymethylmethacrylate

PP	polypropylene
PTFE	polytetrafluoroethylene
PU	polyurethane
PVC	polyvinyl chloride
S1	pure Nylon 6
S2	reduced Nylon 6: Nylon 6-NH
S3	grafted Nylon 6: Nylon 6-N-PEG-CH_3 (2 h lithiation, 0.6 ml *t*-BuLi)
S4	grafted Nylon 6: Nylon 6-N-PEG-CH_3 (24 h lithiation, 0.6 ml *t*-BuLi)
S5	grafted Nylon 6: Nylon 6-N-PEG-CH_3 (2 h lithiation, 1 ml *t*-BuLi)
S6	grafted Nylon 6: Nylon 6-N-PEG-CH_3 (24 h lithiation, 1 ml *t*-BuLi)
S7	grafted Nylon 6: Nylon 6-N-PEG-CH_3 (2 h lithiation, 2 ml *t*-BuLi)
S8	grafted Nylon 6: Nylon 6-N-PEG-CH_3 (24 h lithiation, 2 ml *t*-BuLi)
S9	copper nanoparticle deposited Nylon 6: Nylon 6-N-PEG-CH_3-Cu
SBA	Santa Barbara amorphous type material
SDS	sodium dodecyl sulphate
SEM	scanning electron microscopy
***t*-BuLi**	*tert*-butyllithium
***t*-BuOK**	potassium *tert*-butoxide
TCP	tissue culture plastic
TEAOH	tetraethylammonium hydroxide
TEM	transmission electron microscopy
TEOS	tetraethyl orthosilicate
THF	tetrahydrofuran
UV-VIS	ultra violet and visible spectroscopy
WCA	water contact angle
XPS	X–ray photoelectron Spectroscopy

2. INTRODUCTION

2.1. Pathogenic Bacteria: Health Care Associated Infections

There are millions of prokaryotic microorganisms, known as bacteria, exist on our planet forming a biomass that exceeds all the plants and animals on Earth [1]. Bacteria are small and structurally simple, compared to the vast majority of eukaryotic cells. Most can be classified broadly by their shape as rods (bacilli), spheres (cocci), or spirals (spirochetes) and by their cell-surface i.e. cell wall structure (Gram positive and Gram negative). Although bacteria lack the elaborate morphological variety of eukaryotic cells, they display a surprising array of surface appendages that enable them to swim or to adhere to desirable surfaces. Their genomes are correspondingly simple [2]. Most bacteria are harmless or often beneficial, but some of them can cause infectious diseases by invading our body and are called as pathogenic bacteria, with the number of species estimated as fewer than 100 [3]. By contrast, several thousand species exist in the plant and animal body system including human.

Each species of pathogen has a characteristic spectrum of interactions with its human hosts. The skin, the mucosal surfaces (oral cavity, nasopharynx, urogenital tract) and deeper tissues (lymphoid tissue, gastric and intestinal epithelia, alveolar lining and endothelial tissue) are the primary sites of host–microbe interaction. Pathogenic bacteria infect human under conditions that favour their growth and survival. Pneumonia and diarrhoea together are the third cause of death among children under 5 years of age worldwide, accounting for 2 million deaths per year [4]. The cell walls of both Gram positive and Gram negative bacteria contain toxic components that are potent virulence factors and have central roles in the pathogenesis of bacterial septic shock, a frequently lethal condition that involves collapse of the circulatory system and may result in multiple organ system failure. Bacteria frequently implicated in septic shock include Gram negative microbes such as *Escherichia coli* (*E. coli*)*, Pseudomonas aeruginosa* (*P. aeruginosa*), and meningococci, and Gram positive bacteria such as *Staphylococcus aureus* (*S. aureus*)*, Staphylococcus epidermidis*, and streptococci. [5]. Interestingly, the mentioned group of Gram positive bacteria have emerged as the most prevalent cause of hospital acquired infections (HAI), and as such, play a significant part in nosocomial sepsis.

According to the World Health Organization a Hospital-Acquired Infection (HAI), also known as nosocomial infection (NI) is, “an infection acquired in hospital by a patient who was

admitted for a reason other than that infection. This includes infections acquired in the hospitals but appearing after discharge and also occupational infections among staff of the facility". In other words, nosocomial infections (NIs) are those infections acquired in hospital or healthcare service unit that first appear 48 hours or more after hospital admission or within 30 days after discharge following in-patient care [6]. NIs pose a constant threat to hospitalized individuals. In some studies, HAI rates have ranged from 1% in countries like Europe and North Americas to more than 40% in certain parts of Asia, Latin America and sub-Saharan Africa. However, there remains a problem with measuring the exact incidence of HAIs due to varying definitions for specific infections [7]. NIs cause prolonged hospital stay, increased antimicrobial resistance, long-term functional disability and emotional stress of the patient and in some cases, may lead to conditions that reduce the quality of life. The costs of nosocomial infections in terms of both money and human suffering are enormous [6,8]. There are various types of NIs such as central line-associated bloodstream infections due to prolonged use of catheters, catheter associated urinary tract infections, surgical site infections mainly caused by *Staphylococcus aureus* and ventilator associated pneumonia [8,9].

2.2. Biofilm and Infection on Medical Devices

In terms of biomass on the Earth, bacteria are the most successful forms of life in survival at different environments due to their phenotypic plasticity [10]. Biofilms are matrix-enclosed bacterial populations adherent to each other and/or to surfaces or interfaces and affect almost all surfaces including metals, glass, textile, polymers; causing damages to various industries, most importantly biomedical fields by contaminating medical devices [11]. In spite of the considerable success achieved with these devices, their abiotic surfaces are susceptible to bacterial colonization, particularly by pathogenic bacteria which is forming an important and challenging public health problem. More than 60 % of nosocomial infections (NIs) worldwide are accredited to pathogenic bacteria forming biofilms on medical devices as biofilm bacteria show a 10 – 1000 times higher resistance towards antibiotics than planktonic bacteria [12]. This has become a major healthcare concern as antibiotic-resistant bacterial strains like methicillin-resistant *Staphylococcus aureus* (MRSA) are increasing [13]. When a medical device is contaminated with microorganisms, several factors determine whether a biofilm develops. First, the microorganisms must adhere to the exposed surfaces of the device long enough to become irreversibly attached [14]. The bacterial attachment on device also depends on physicochemical characteristics, number as well as types of cells in the liquid and protein adsorption on the surface [11]. Biofilms usually occur on or within indwelling medical devices such as contact lenses, central venous catheters, mechanical

heart valves, peritoneal dialysis catheters, prosthetic joints, pacemakers, urinary catheters and voice prostheses. Biofilms may be composed of only a single or of different types of microbial species depending on the nature of the device [15].

Biofilm development can be divided into three distinct stages: firstly, the attachment of cells to a surface, secondly, the growth of the cells into a sessile biofilm colony, and lastly, detachment of cells from the colony into the surrounding medium. In the first stage, the initial, reversible interaction between a bacterial cell and a surface is mediated that can be explained by bacterial adhesion model using Derjaguin-Landau-Verwey-Overbeek (DLVO) theory or by thermodynamic approaches [16]. The attachment is reinforced by host- and tissue-specific adhesins that are located on the bacterial cell surface or on cellular appendages such as pili and fimbriae. This results in the irreversible attachment of the bacterial cell to the surface. The second stage of biofilm development involves the multiplication of bacteria on the surface and synthesis of an extracellular polymeric substance (EPS) [17]. The produced matrix holds the bacterial cells together in a mass and firmly attaches the bacterial mass to the underlying surface. It is worth to be mentioned that the matrix also contributes to biofilm- mediated antimicrobial resistance, either by acting as a diffusion barrier, or by binding directly to antimicrobial agents and preventing their access to the biofilm cells. In the third stage, continued growth of bacterial cells on a surface leads to the development of mature biofilm colonies containing millions of tightly packed cells gathered into pillar and mushroom-shaped masses that project outward into the surrounding medium for hundreds of microns. The matured biofilm colonies are complex due to the presence of numerous micro- environments with various metabolic activities, fluid-filled channels for the exchange of nutrients as well as waste products and heterogeneity in reproductive activity among cells. At the final stage of mature biofilm, the cells are detached from the biofilm colony and dispersed into the environment. This is an essential stage of the biofilm life cycle that contributes to biological dispersal, bacterial survival, and disease transmission [18,19]. The mechanism of biofilm formation is depicted by the **Figure 1**.

Theoretically, biofilm formation on medical devices can be prohibited by altering the device's surface using different strategies like mechanical, physical and chemical methods to prevent bacterial attachment, or by including antibacterial therapeutics in the device to prevent early stages of biofilm formation [20]. Ideally, preventing biofilm formation would be a more logical option than treating it. However, there is presently no known technique that is able to successfully prevent or control the formation of unwanted biofilms without causing adverse side effects [21].

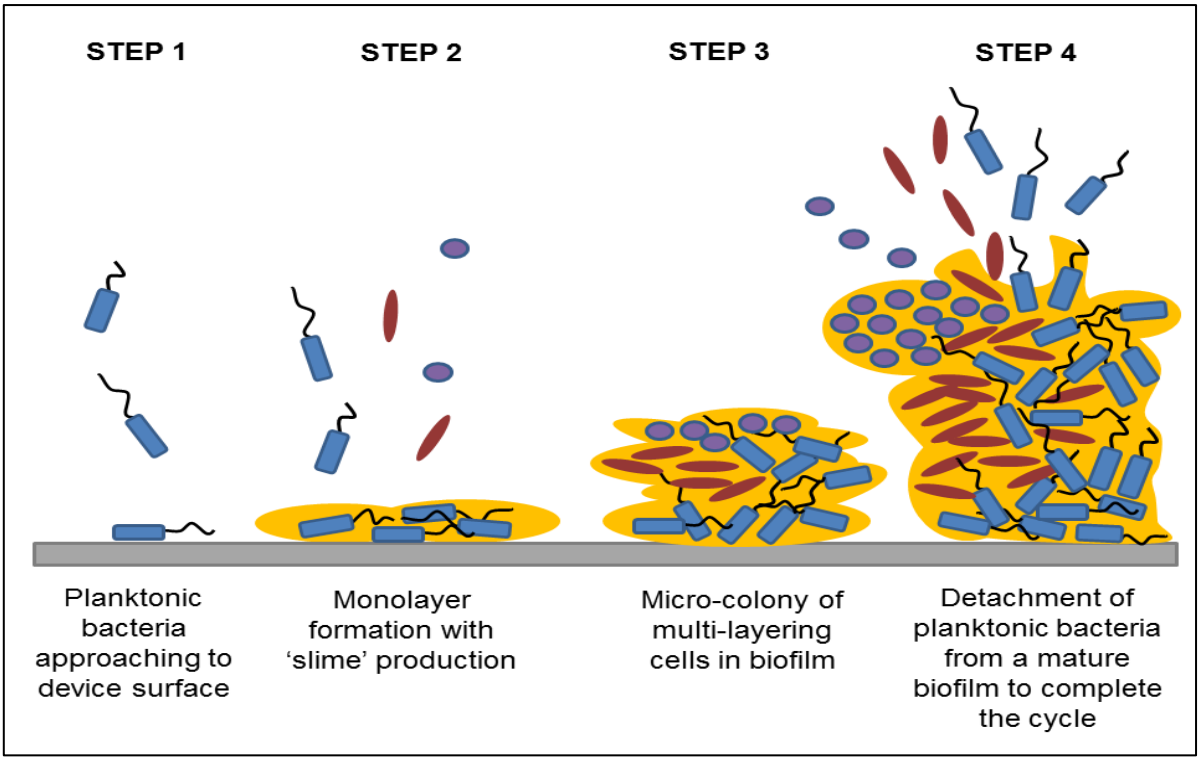

Figure 1: Formation of biofilm by adhesion of planktonic bacteria on the surface.

2.3. Importance of Biomaterial's Surface Modification for Biomedical Application: Key Strategies

The biomedical implants and devices undoubtedly enhance the quality of our lives by extending the functionality of essential body systems beyond their supposed lifespans. Across the medical industry, various implants and devices have been studied and developed for multiple applications in the human body. In the biomedical field, the high demand for medical implants and devices is expected to increase in the future. According to the U.S. Food and Drug Administration, a medical device is "an instrument, apparatus, implement, machine, contrivance, implant, *in vitro* reagent, or other similar or related article which is used in the diagnosis, cure, mitigation, treatment or prevention of a disease, or intended to affect the structure of any function of the body which does not achieve its primary intended purpose through chemical action within or on the body" [22]. Implants are objects that do not require any form of power for the device to carry out its expected functions. Devices are objects that require a form of power, which may be chemical or electrical [22]. Any substance that is used to be in contact with living tissue and biological fluids without adversely affecting the biological constituents of the entire living organism is named as biomaterial [23].

Biomaterials can be composed of metals, ceramics and polymers or their composites. Unlike 20th century, in 21st century the biomaterial are not expected to be inert as they do not elicit immunological primary or secondary foreign body reaction. Biofilms can easily develop on inert biomaterial's surface or on dead tissue. Sessile bacteria release antigens and stimulate the antibody production. But the antibodies fail to kill biofilm embedded bacteria. Depending on the type and composition of the medical device, some pathogens are more prevalent. In most of the cases, the occurrence of acute infection obligates the removal of the device. [24]. On the contrary, the use of bioactive materials helps to integrate properly with the surrounding tissue [25]. Recently, biomaterials' surface modification has gained enormous importance in the research domains to improve the device multi-functionality, topography, hydrophilicity/ hydrophobicity, free surface energy and biocompatibility/ cytocompatibility [26]. Usually, more than one approach is needed to satisfy the requirements of biomaterials [23].

It is extremely important to study and understand the fundamental aspects of the biological responses to biomaterials as a series of reactions take place between the host and biomaterial after implanting or placing them in contact of physiological fluids. Firstly, the water and protein adsorption take place, followed by provincial matrix formation, cell attachment and new tissue growth on the biomaterial. This may lead to inflammation, foreign body reaction and scar development [27].

To combat these problems, various strategies have been developed by researchers. There are predominantly four different techniques that can be employed for the change in functionality of material surface. These methods are elaborated below [23]:

1) **Physical methods**: physical adsorption, surface micro/ nano-patterning, Langmuir–Blodgett film deposition etc.
2) **Chemical methods**: ozone treatment, silanization, fluorination, wet treatments such as aminolysis and alkaline or acidic hydrolysis, incorporation of functional groups by grafting polymerization or hydrogel coating, flame treatment etc.
3) **Biological methods**: Protein–Enzyme Immobilization
4) **Radiation Methods**: Plasma Radiation, Microwave and Corona Discharge, Photoactivation by UV. Laser, Ion Beam, Gamma Irradiation etc.

The anti-infective strategies can be developed similarly by the above mentioned approaches either to prevent bacterial adsorption and adhesion, or to kill bacteria [28].

2.4. Polymers Used in Biomedical Applications

The natural fibres like horn, hair, or polymers like cellulose have been utilized by human since the beginning of human civilization, and they have found application in health care, e.g. as suture material also for long time. However, since the advent of the man-made polymers, such materials have attracted great attention and interest in various applications in the medical field for various reasons. A wide range of physical and chemical properties can be achieved based on the monomer units, polymerization reaction and formation of co-polymers consisting of different components at adjustable concentrations imparting desirable mechanical and structural properties [29]. The most common functional groups present on biomedical polymers are carboxyl (–COOH), hydroxyl (–OH), amino ($–NH_2$), and methyl ($–CH_3$) groups [30]. In the modern world, there are many polymers that have been developed and are continuously being developed by the scientists for biomedical industry. The polymeric biomaterials can be classified in various ways based on different attributes (adhesiveness, degradability, hydrophilicity etc.). Some of the commonly used biomedical polymers are listed below [22,29].

1) **Polyolefins**: Polyethylene (PE) and polypropylene (PP) are inert and hydrophobic materials which do not degrade in vivo. These polymers are mainly applied for epidural catheters, implantable cardioverter/defibrillator, pacemaker, Foley catheters, nasal implants for nose reconstruction, central venous access device and orthopaedic implants.

2) **Polytetrafluoroethylene (PTFE)**: It is commercially known as Teflon® and has an ethylene backbone with four covalently bound fluorine molecules. Left Ventricular Assist Device, epidural catheters, implantable cardioverter/defibrillator, pacemaker, neuro-stimulator in sacral nerve stimulation, synthetic blood vessels, hip implant and many ophthalmic devices are made up of PTFE.

3) **Silicone**: Silicones consist of an –Si–O– backbone with different chain lengths and crosslinks, which determine mechanical properties. The side chains may be modified, but in the most common polydimethylsiloxane (PDMS) they are methyl groups. Mechanical heart valves, artificial blood vessels, catheters, cochlear implants, stapes implants, penile implants, artificial urinary sphincter implant, breast implants and many other implants' materials are considered to be PDMS.

4) **Methacrylates**: Methyl methacrylates polymerize to very rigid polymers namely polymethylmethacrylate (PMMA) by radical polymerization and therefore find application in dentistry, ophthalmic and orthopaedics. The hydrophilic side chains in the hydroxyethyl methacrylate monomer lead to the polymerization to a hydrogel polyhydroxyethyl methacrylate (pHEMA). This has good protein repellent anti-fouling properties.

5) **Polyesters**: Bio-stable and biodegradable polyesters are used in biomedicine. Bio-stable polyesters contain aromatic groups, for examples polycarbonates (PC), polyethylene terephthalate (PET). Polyesters of small aliphatic glycolic acid or lactic acid present the most common degradable polymers such as polyglycolic acid (PGA), poly(L-lactic acid) (PLLA) and poly(D-lactic acid) (PDLA). The bio-stable polyesters are used for synthetic blood vessels, cheek, jaw and chin implants, catheter etc. The biodegradable polymers are available in different shapes from solid body for orthopaedic applications, via meshes to drug eluting coatings on vascular stents.

6) **Polyamides (PA)**: All proteins consist of units linked by amide (–$CONH_2$–) bonds. The highly repetitive proteins like collagen or silk fibroin can be classified as polyamides. The most important synthetic polyamide with clinical application is Nylon due to its high tensile strength, and is used for suture materials. Polyamide block-copolymers combine the flexibility of polyurethanes with the strength of Nylon and therefore, became the material of choice for the balloon of catheters for angioplasty.

7) Polyethers, polyurethanes (PU), polyvinyl chloride (PVC), polyhydroxyalkanoates, liquid crystal polymer (LCP) are also considered to be effective biomaterials and widely used in the clinical fields. There are many more polymers that are under extensive biomedical research.

Structures of some previously mentioned common polymers widely used in biomedicine are depicted in **Figure 2**.

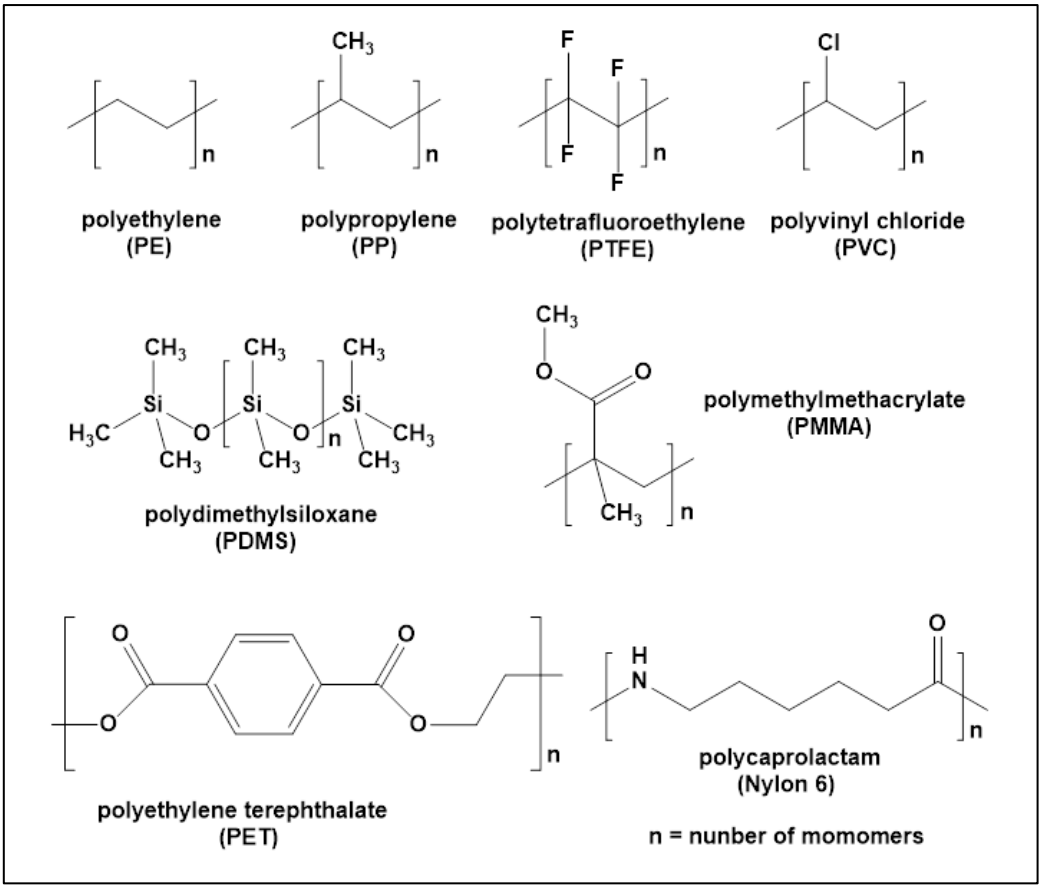

Figure 2: Structures of common biomedical polymers.

The major approaches to develop the antifouling polymer surface involve two major strategies: a) resisting protein adsorption as well as bacterial adhesion and b) incorporating bactericidal coating [31].

a) Antifouling approach by protein resistance

Protein adsorption and formation of protein layer on the surface provide a conditioning layer for colonization of microbes that subsequently leads to the biofilm formation as well as reduces the device's efficacy [32,33]. There are various key procedures for surface modifications and preparation of coatings that resist protein adsorption and thus prevent bacterial adhesion [28,34–40]. Immobilizing cytocompatible hydrophilic polymer polyethylene glycol (PEG) on the surface is one of the most commonly used trends to contribute both protein and bacterial resistance [41–46]. The polyethylene glycol (PEG) and its derivatives, in different lengths or with different functional groups [47] have been applied to maximize the antifouling effect. Unfortunately, the exact mechanisms of PEGs for repelling bacteria are still unclear. But various studies revealed that surface modification with PEG contributes to protein as well as bacteria repellence to the surfaces due to high polymer

flexibility, large excluded volume, hydrophilicity, and associated steric hindrance effects [48]. A significant decrease in bacterial adhesion and biofilm formation was confirmed in case of the PEG modified surfaces [31]. Some studies suggest interconnection between the antifouling property and molecular weight of the PEG bonded to the surface. Dong et al. designed antifouling surfaces by grafting polyethylene glycol of various molecular weights (PEG M_W 200, 400, 600, 2000, and 4600). The maximum decrease in bacterial adhesion has been observed with PEG having a M_W 2000 [49].

The other antifouling approaches are largely based on self-assembled monolayers (SAMs) containing different functional groups [50], zwitterionic surface [51,52], peptide-based surface [53], photo-activated self-cleaning films [54,55], smart materials [56].

b) Bactericidal coating

The bactericidal coatings include silver releasing coatings [57], copper/ copper alloy embedded surface [58,59], antibiotic releasing coatings [60], photo-activated antibacterial coatings [55], non-release based polycation coating [61], release-based antibacterial coating [62].

In our research work, we have used the following two biomedical polymers: PET and Nylon 6. These two polymers and their surface modifications aiming to improve the biomedical efficacy are discussed in detail.

2.4.1. Polyethylene terephthalate (PET)

Polyethylene terephthalate – PET is one of the most common polymers widely used in medicine. Biocompatible, chemically inert PET (Dacron®) biomaterials, in combination with different coatings [63,64], are used in surgical meshes, vascular grafts, heart valves, scaffolds, sutures, urinary and bloodstream catheters. The techniques applied for better performance of biomedical PET are discussed below.

PET vascular grafts are coated with either collagen or albumin protein [65] or heparin [66]. PET with polyacrylamide (PAAm; hydrophilic and neutral) and PET with sodium salt of poly(acrylic acid) (PAANa; hydrophilic and anionic) elicit an anti-inflammatory response in macrophages [67]. Very little information is available regarding the PET urinary catheter coatings. Non-thrombogenic PET biomaterials can be fabricated with PEG (polyethylene glycol) or oligo(ethylene glycol) groups, sometimes grafted with peptides [31,68,69]. Studies

revealed that silver-coated prosthetic heart valve sewing cuffs and sutures have anti-infective potential *in vitro* [70]. Various biomedical coatings (hydroxyapatite, bioactive glass, hydroxypropylcellulose, hyaluronic acid, polystyrene sodium sulfonate composite coating) are applied on PET artificial ligaments [71]. But in spite of rigorous research works in various parts of the world, the desired permanent solution is yet to be found.

PET, generally known as a thermoplastic polymer resin, belongs to the polyester family and is used in both domestic and industrial domain. Two monomers, modified ethylene glycol and purified terephthalic acid, are combined to form PET, which is usually prepared by ester exchange reaction of dimethyl terephthalate with ethylene glycol [72]. For the improvement of general and specific applications of chemically inert PET, it is necessary to find new approaches to the surface modification chemistry. Different useful techniques to introduce various functional groups on the surface of PET, without changing its bulk properties, have been explored by scientists in the PET research field including plasma treatment [73], radiation [74], hydrolysis [75,76], aminolysis [77,78], graft co-polymerization [79,80], enzymatic modification [81], PEG grafting [82] etc. PET surface modification imparts various desirable properties like dyeability, surface roughness, altered hydrophobicity, biocompatibility and many more. These new and modified surface properties are implemented in the fields of modern textile [83], filtration [84], biomaterials [85,86], and most recently in nanotechnology [87].

Straight chemical modification for PET surfaces by wet chemistry is usually very difficult due to the absence of chemically reactive groups. The effective means for PET surface modifications are hydrolysis [88] and aminolysis [77]. Hydrolysis produces mixture of hydroxyl and carboxylic functional groups, while aminolysis incorporates amine groups to the PET surfaces. The surface chain cleavage, in both types of reactions, can lead to significant sample degradation. Thus the reaction conditions are optimized with aim to maximize conversion and minimize corrosion. Based upon the mentioned reactions, the series of surface modification techniques have been developed to improve the modern PET applications. Another method, wherein the monomers can be attached onto the polymer chains via covalent bond, is grafting. It can be initiated by the chemical reaction, photo-irradiation and plasma treatment [88–92].

2.4.2. Nylon 6

Nylon 6, also known as polycaprolactam, is a commercialized polymer that is widely used in biomedical field because of its strength, flexibility, toughness and biocompatibility

[93]. During Second World War, newly developed man-made synthetic polymers like polyamides rapidly entered medical application field [29]. The biomedical applications of polyamides include suture material, coated textile for skin infection, wound dressing, catheters, bone tissue scaffolds and dialysis membranes [94–99]. But without modification of polymer surface, it may cause various problems like thrombogenesis [100]. Therefore, surface chemistry plays very important role for further modification of polymeric surface by introducing specific functional groups, which improve its performance.

Nylon 6 membranes comprise only a low concentration of terminal amino groups, thus amides conversion into amines should allow a more homogenous distribution of activated Nylon 6 surface [101]. Nylon 6 surfaces are modified by either physical or chemical methods. The first category includes particularly the treatment with UV radiation or plasma [100], [102–104], but lack of the well-designed surface formation generally leads to the limitations in the using of physical methods. Jia et al. [93] surveyed a variety of chemical reactions applicable to the amide repeating units and described that a more efficient modification approach is application of chemical methods by reaction at the amide groups through hydrolysis, *O*-alkylation and *N*-alkylation. Inman et al. [105] studied enzymes immobilization on Nylon 6 structures by their partial hydrolysis with hydrochloric acid, followed by covalent attachment of different enzymes through glutaraldehyde. *O*-alkylation related to Nylon 6 tubes was achieved by using dimethyl sulfate, diethyl sulfate or triethyloxonium tetrafluoroborate as alkylating agents to covalently attach enzymes, either directly or via cross-linking agents [106,107]. Cairns et al. [108] investigated polyamides *N*-alkylations by using formaldehyde in presence or absence of alcohols and mercaptans. Beeskow et al. [101] activated terminal Nylon 66 amino groups by *N*-alkylation for dextran immobilization. Another example regarding *N*-alkylation includes Nylon 66 yarns cross-linking, which has been achieved by reaction with diisocyanates and diacid chlorides [109]. Recently, chitosan derivatives, peptides, collagen, PEG and other biocompatible compounds have been immobilized on polyamide surfaces either by chemical treatment or physical methods, mostly plasma treatments [82,110,111]. Herrera-Alonso et al. [112] reported that Nylon 6 reduction carried out with BH_3-THF was the most efficient method for introducing secondary amine groups to the Nylon 6 surface. Surface amides conversion into amines generally provides more versatility in terms of the opportunity to introduce covalent bonding with other different functional groups for long-term use.

In the field of biomedicine, Nylon materials are physically or chemically modified according to the requirements. One of the common physical modification techniques is employing laser at various parameters to alter surface topography [113,114]. Hydroxyapatite

or calcium phosphate coatings on Nylon has been studied for bone tissue engineering [115,116]. Silver coated Nylon for wound dressing [97], chemical treated [117] and carbon nanoparticle immobilized Nylon [118] have been also explored.

2.5. Nanoparticles (NPs)

The NPs are tiny colloidal particles having size ranging from 1 to 100 nm or 1000 nm, as the definition of NPs varies [119,120]. They can be classified into different classes based on their properties, shapes or sizes. On the basis of material composition, the NPs can be classified as metal NPs and metal oxide NPs, carbon-based NPs, ceramic NPs, semiconductor NPs, polymeric NPs and liquid-based NPs [119]. They are prepared by top-down or bottom-up syntheses. Due to their size, NPs differ from their bulk material. Various physicochemical properties such as large surface area, mechanical strength, optical activity and chemical reactivity make NPs unique and suitable applicants for various fields. Presently, different metallic nanomaterials and their oxides are being produced using copper, zinc, titanium, magnesium, gold, alginate and silver. Nanoparticles can be used for diverse purposes, from the field of medicine to the development and manufacturing of solar and oxide fuel batteries for energy storage, electronics, cosmetics or clothes [121]. NPs can play very prominent role in environmental technology [122]. Presently, polymeric NPs are one of the most studied strategies for nanomedicine [123,124] and mesoporous silica nanoparticles have drawn the attention in domain of drug delivery for curing various diseases including cancer [125].

2.5.1. Nanoparticles (NPs) with antibacterial effect: Copper NPs

Numerous studies have confirmed that several NPs possess antibacterial property [126]. Apart from widely used silver (Ag) NPs, there are others such as titanium dioxide (TiO_2), gold (Au), silica (SiO_2), copper (Cu)/ copper oxide (CuO), magnesium oxide (MgO) and zinc oxide (ZnO) that have been reported to exhibit good biocidal activity [31,127]. Silver in various forms (metallic silver, silver salts and colloidal silver) has been used as an effective antibacterial agent for many centuries. In modern medicine, silver NPs are being applied widely although bacterial resistance to antibiotics has been extensively discussed in the literature. It is reported that bacteria may develop resistance to widely used silver NPs [128]. In this context, alternative NPs also started to be explored against drug-resistant pathogenic bacteria [129]. In recent times, Copper and copper based (alloy) NPs are being popular for the antibacterial efficacy [130].

The methods of synthesizing Cu NPs can be classified into five major categories namely: chemical treatment, electrochemical synthesis, photochemical method, sonochemical technique and thermal treatment. Moreover, some other sophisticated techniques (e.g. laser application) have also been reported recently [131].

Mechanism of antibacterial activity of Cu NPs to micro-organisms involves several processes, such as displacement of essential metals from their native binding sites or through ligand interactions. Toxicity towards microorganisms also results from changes in the conformational structure of nucleic acids and proteins which interferes with the oxidative phosphorylation and osmotic balance. Despite the several possible mechanisms, copper's initial site of action is thought to be at the plasma membrane as high concentrations lead to a rapid decline in membrane integrity, changing its permeability. Copper ions are the active agent able to either kill or inhibit the growth of micro-organisms by several processes. The copper free radicals can disrupt the cell membrane and release ions to enable interaction with proteins and DNA molecules inside the bacteria cell [130]. The mechanisms associated with toxicity of copper NPs as summarized in **Figure 3**.

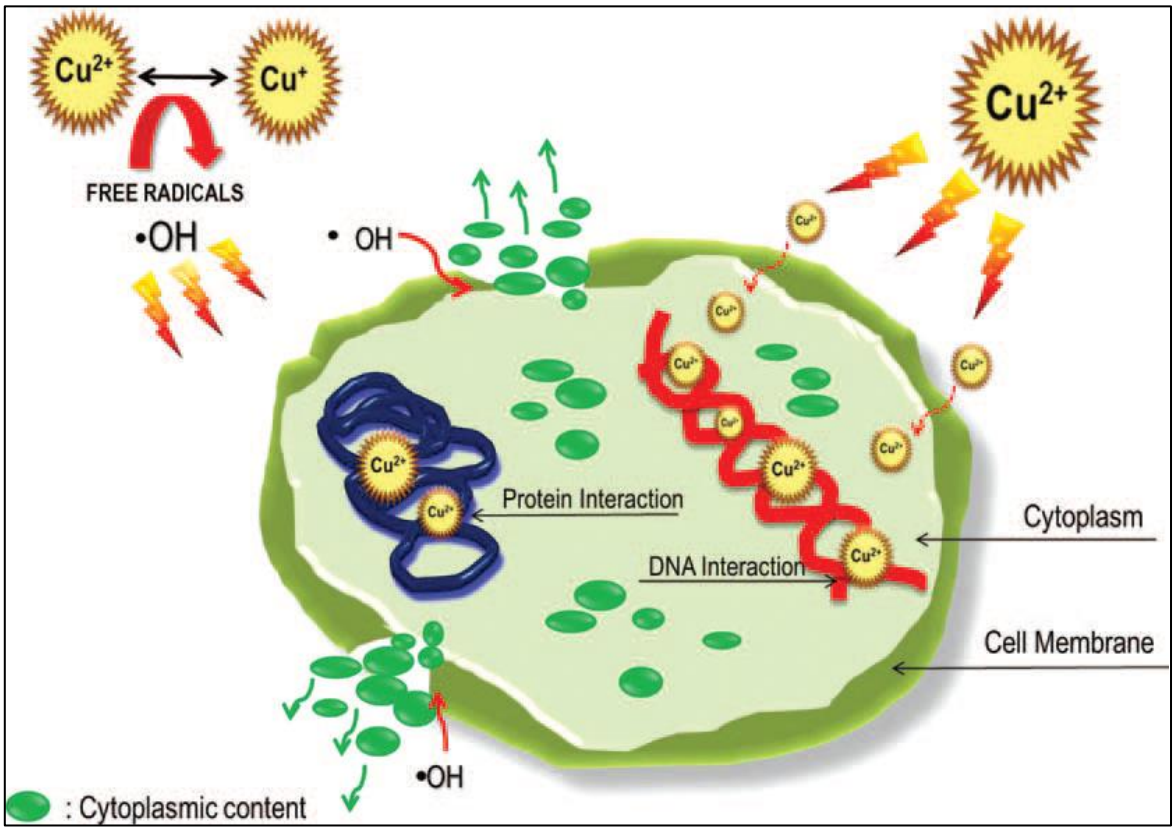

Figure 3: Different mechanisms associated with the toxicity of copper against bacterial cells [130].

Furthermore, the exposure of the human skin to the nanoparticles involves the risk of their interactions and serious consequences of deterioration in health. The investigation of toxicity on human dermal fibroblast showed that the toxicity depends on the concentration of NPs and at lower concentration, NPs appeared to be non-cytotoxic [132].

A few studies have been focused on the Cu NP coated biomaterials to investigate the antimicrobial activity. The major procedures for Cu NP coatings on materials were physical deposition [59,133,134] and radiation induced deposition [58]. Cu NPs are gaining popularity in biomedicine due to its potential as effective antibacterial agent.

2.5.2. Mesoporous silica nanoparticles (MSNs) for drug delivery systems

Mesoporous materials are defined by IUPAC as materials with pore sizes between 2 to 50 nm [135]. Mesoporous materials belong to the nanoporous material family having pore size of the materials less than 100 nm. The microporous (pore size less than 2 nm) and macroporous (pore size more than 50 nm) materials also come under the classification of nanoporous materials. Mesoporous silica nanoparticles (MSNs) are among the best known and most widely used porous materials. In 1968, Stöber et al. first discovered an effective method for the synthesis of monodispersed silica particles. The templating method has been widely applied to prepare mesoporous silicas. The innovative strategies of MSNs have made the structured materials (e.g. disordered, wormhole-like, hexagonal, cubic, and lamellar mesophases) possible with various morphologies (e.g. spheres, hollow spheres, fibers, tubules, gyroids, helical fibers, crystals and many hierarchical structures), and dimensions (nanometer to centimeter) by controlling the reaction conditions (such as reaction temperature, pH value, surfactants concentration, silica sources etc.) [136]. These new architectures with high surface area, tunable pore sizes, large pore volumes enable mesoporous silica for diverse applications in catalysis, sorption, separations, sensing, optics, drug delivery etc. [135]. The surfactant micelle-templated mesoporous silica materials are mainly classified as: mobil crystalline materials - MCM-41/ 48/ 50, Santa Barbara amorphous type materials - SBA-15/ 16, Michigan State University materials - MSU, Korean Advanced Institute of Science and Technology material – KIT-1/ 6, plugged hexagonal templated silica - PHTS, mesostructured cellular foam - MCF and FSM-16 [135,137].

The mesoporous material MCM-41 was first proposed for a drug delivery system by Vallet-Regi *et al*. in 2007. Biocompatible MSN-based controlled release systems have been demonstrated to be able to deliver different guest molecules (drugs) [137]. With the rapid development of silica-based drug delivery systems over the past decades, the use of pure

mesoporous silica suffers from limitations such as targeted drug delivery mechanisms' study, drug kinetics marker in pharmacological research, and track/evaluate the efficiency of the drug release in disease diagnosis and therapy. Therefore, functionalized mesoporous silica materials with luminescence or magnetism have been emerged with time [138]. The smart combination of different functional groups with MSNs has been investigated for the development of multifunctional medical platforms aiming simultaneous targeted delivery, fast diagnosis, and efficient therapy [125,138,139]. Very recently, the redox responsive mesoporous organosilica nanoparticles containing disulfide (S–S) bridges have been developed with higher efficacy for drug delivery system [140]. Therefore, more researches are being attracted for exploring new possibilities for MSN application in drug delivery.

2.6. Aim and Objective of the Thesis

Surface modification of polymers has been made possible by various approaches as have been discussed earlier. In case of PET chemical surface functionalization, mostly aminolysis and hydrolysis have been used as ester bonds are available on PET surface. For both the methods corrosion rate is high and therefore, the material may lose its mechanical strength which plays very crucial role in biomaterials. Although the cleavage of ester by Grignard reagent is very common in general organic chemistry, PET modification has not been explored using Grignard reagent as a major chemical. In the first section, we have explored the new possibility of surface functionalization on PET using Grignard reagents. The non-corrosive modification of PET has been desirable that can exhibit bacterial adhesion and biofilm resistance with biocompatibility.

Being a common choice for biomaterial, different techniques of Nylon surface modification have been investigated. As already discussed, PEG immobilization on biomaterials' surface is a popular concept to impart antifouling property to the surface that can efficiently resist bacterial adhesion. Tethering PEG on Nylon or polyamide surface needs either complex multi-step chemical treatments or expensive physical treatment like plasma treatment. The second section of the thesis has been dedicated to the easy, but efficient surface reduction of Nylon 6, followed by grafting PEG covalently via lithiation. The antibacterial efficacy as well as bacterial adhesion resistance has been thoroughly investigated. The cytocompatibility has been measured to confirm the efficiency of the modified Nylon 6 as a biomaterial. The *N*-alkylation of reduced Nylon 6 has also been explored as a model reaction for further possibilities of tuning surface by different other desired molecules/ functional groups.

The preparation of Cu NPs is not always an easy task because of their high reactivity towards oxidation and the tendency to agglomerate. There are many procedures for Cu NP synthesis, whereas the easy and reproducible reduction method has been applied here to obtain Cu NPs. The characteristics (including shape and size) of the NPs have been investigated. The main aim for Cu NP synthesis was to explore the possibility of Cu NP physisorption on grafted Nylon 6 surface for better antibacterial efficacy compared to PEG grafted Nylon 6.

The last section of the thesis has described the MSN syntheses done with the aid of carefully tested procedures recently published. Five well characterized MSNs (MCM-41, MCM-48, SBA-15, PHTS and MCF) have been obtained and their application in drug (dopamine) delivery profile examined. The goal of this section was to compare the efficiency of various MSNs depending on their surface morphologies and mesopore sizes.

3. EXPERIMENTAL

3.1. Materials

PET fabric, with the thickness of 100 µm, was supplied by Silk and Progress, CZ. PET foil, having 150 µm of thickness, was supplied by TENOLANVR (IA 0001), Fatra, a.s., CZ. Nylon 6 film (thickness of 15 µm), was supplied by Goodfellow Cambridge Ltd., (Huntingdon, UK). The Grignard reagents — methylmagnesium bromide (3.0 M CH_3MgBr), butylmagnesium chloride (2.0 M C_4H_9MgCl), hexylmagnesium bromide (2.0 M $C_6H_{13}MgBr$), octylmagnesium bromide (2.0 M $C_8H_{17}MgBr$), dodecylmagnesium bromide (1.0 M $C_{12}H_{25}MgBr$) all in diethyl ether and octadecylmagnesium chloride (0.5 M $C_{18}H_{37}MgCl$) in tetrahydrofuran (THF) were obtained from Sigma-Aldrich Co., CZ. Diethyl ether (99.7%), methanol (99.8%) and hexane (99.9%) were supplied by PENTA Ltd., CZ. Borane-Tetrahydrofuran complex (1 M, BH_3-THF), potassium *tert*-butoxide (≥98%, *t*-BuOK), benzyl chloride (99%, $C_6H_5CH_2Cl$), benzophenone (≥99%, $C_{13}H_{10}O$), *N,N'*-disuccinimidyl carbonate (≥95%, DSC), 5-(dimethylamino)naphthalene-1-sulfonyl chloride/ dansyl chloride (≥99%, DNSC/ $C_{12}H_{12}ClNO_2S$), poly(ethylene glycol) methyl ether tosylate (M_W = 2000 g/mol, H_3C-PEG-OTs), polyethylene glycol (M_W = 1450 g/mol, PEG), *n*-butyllithium (2.5 M in hexane, *n*-BuLi), *tert*-butyllithium (1.7 M in hexane, *t*-BuLi), *N,N*-diisopropylethylamine (≥99%), 4-(dimethylamino) pyridine (≥98%) and sodium (cubes, contains mineral oil, 99.9% trace metal basis; Na) were obtained from Sigma-Aldrich Co., CZ. Solvents tetrahydrofuran (99.95% THF), dimethyl sulfoxide (99% DMSO), acetone (99.5%), ethanol (96%), ethanol (absolute), 2-propanol (99.8%), concentrated hydrochloric acid (35% HCl) and ammonia (22.7%) were purchased from Lach:Ner, s.r.o., CZ. Sodium hydroxide (NaOH), calcium hydride (CaH_2) and calcium chloride ($CaCl_2$) were supplied by PENTA Ltd. CZ. Dry DMSO (anhydrous, ≥99.9%) were supplied by Sigma-Aldrich Co., CZ. All unmodified and modified sample washings were performed by deionized water. All the chemicals and reagents were used directly without any further purification, except diethyl ether and THF. 4 Å molecular sieves (pellets, 3.2 mm diameter, Sigma-Aldrich, CZ) were used as drying agent for collection of dry diethyl ether after distillation.

Copper(II) chloride dihydrate (99.999%, $CuCl_2.2H_2O$), Sodium borohydride (99%, $NaBH_4$), sodium dodecyl sulphate (≥99%, SDS), hexadecyltrimethylammonium bromide ((≥99%, CTAB), tetraethyl orthosilicate (98%, TEOS), Fumed silica (powder, 0.2 – 0.3 µm average particle size, SiO_2), poly(ethylene glycol)-*block*-poly(propylene glycol)-*block*-poly(ethylene glycol) – known as P123 (M_w = 5800 g/ mol), 1,12-dibromododecane (≥96%),

N,N-dimethyl hexadecylamine (≥95%, GC) and mesitylene (98%) were supplied by Sigma Aldrich Co., CZ. Tetraethylammonium hydroxide (25% in water, TEAOH) and pyridine (99.5%, extra dry, over molecular sieves) were purchased form ACROS organics, Belgium. Ammonium fluoride (p.a., NH_4F) was supplied by Lach:Ner, s.r.o., CZ (99.2%). Milli-Q water was used for nanoparticle synthesis and washings. 3-(3,4-dihydroxyphenyl)-L-alanine (>98%, L-DOPA) was purchased from TCI EUROPA N.V., Belgium. Liquid nitrogen (N_2) was obtained from Linde (99.999% purity).

For biofilm test on PET surfaces, brain Heart Infusion (BHI) Agar supplied by Fluka CZ, D-glucose monohydrate G.R., Lach:ner CZ. Ethanol (96%) by PENTA Ltd., crystal violet dye $C_{25}N_3H_{30}Cl$, Lach:ner CZ. *Staphylococcus aureus* CCM - 2260; *Escherichia coli* CCM - 2024; methicillin-resistant *Staphylococcus aureus* (MRSA) CCM - 4223; *Pseudomonas aeruginosa* - CCM 1959 (according to ALE-G18, CSNI, collection of microorganisms from Masaryk University Brno, CZ) were used for the biofilm tests. The following bacterial strains were used to test antibacterial activity and adhesion behaviours of bacteria on the pure and functionalized Nylon 6 sample surfaces; Gram positive bacterial strain *Staphylococcus aureus*, CCM 3953 and Gram negative bacterial strain *Pseudomonas aeruginosa*, CCM 3955. Soyabean Casein Didest Medium: HIMEDIA®REF, Plate Count Agar without Dextrose (BIORAD a.s., CZ) and sterile physiological solution (6 % NaCl) were used for bacterial inoculums preparation. Globular protein Bovine Serum Albumin (BSA, Sigma-Aldrich, CZ) was used as support for *Staphylococcus aureus* better proliferation (0.15 g BSA into 100 ml 6 % NaCl solution).

Cell experiments were performed using 3T3 clone A31 mouse fibroblast cell line. Dulbecco's Modified Eagle's Medium (DMEM), penicillin/streptomycin antibiotic mixture and 3-(4,5-dimethylthiazol-2-yl)-2,5-diphenyltetrazolium bromide (MTT) were supplied by Sigma-Aldrich Co., CZ. Fetal bovine serum (Biosera, France) and new born calf serum (GibcoVR, Thermo Fisher Scientific, CZ) were used as protein supplements. Positive (PM-A) and negative (RM-C) cytotoxicity controls were supplied by Hatano Research Institute, FDSC, Japan. Staining of cell nuclei and cytoplasm was performed using 3,3' dihexyloxacarbocyanine iodide (DiOC6(3)), Triton X-100 and propidium iodide (PI) supplied by Sigma Aldrich Co., CZ.

3.2. Methods

3.2.1. Surface modification techniques

3.2.1.1. Preparation of the samples and solvents

Both fabric (density = 65.4 g/m^2; thickness = 100 µm) and PET foil (density = 211.4 g/m^2; thickness = 150 µm) were cut into pieces (size 5 × 5 cm^2). These samples were washed three times with acetone and then three times with hexane using sonicating bath 5 mins each time to remove all impurities. Finally, the samples were dried in desiccator using vacuum pump for 5 h.

Nylon 6 films (size 6 cm × 6 cm), were thoroughly rinsed with water, ethanol, 2-propanol, acetone, THF and hexane in sonicating bath for 3 mins per solvent. The washed samples were dried at 50 °C/ 3 h in vacuum and stored in desiccator over silica gel until used.

Diethyl ether (500 ml) was distilled for 3 h in presence of 12 g metallic sodium, under the argon atmosphere. The dry diethyl ether was stored with molecular sieves under inert atmosphere.

Tetrahydrofuran (THF; 1.5 l) was first stirred for 2 days with 5 g calcium hydride powder (CaH_2) at room temperature (r.t.); 500 rpm, sealing the neck of flask with anhydrous (anhy.) calcium chloride ($CaCl_2$) cap. THF was distilled under the argon atmosphere and collected over argon. In the second step, 24 g benzophenone ($C_{13}H_{10}O$) and 10 g sodium (Na) were added to the distilled THF and stirred overnight at r.t.; 500 rpm under inert condition, until the solvent turned violet in colour. Anhy. THF was prepared by distillation of it again and freshly prepared anhy. THF was used for all the required reactions.

3.2.1.2. Chemical modification of PET surface

A series of Grignard reagents such as CH_3MgBr, C_4H_9MgCl, $C_6H_{13}MgBr$, $C_8H_{17}MgBr$, $C_{12}H_{25}MgBr$ and $C_{18}H_{37}MgCl$ (with various numbers of carbons in alkyl groups) were used for modification of PET fabric and foil. 60 ml of 0.1 M Grignard reagent in anhydrous diethyl ether was added to 250 ml 3-necked round bottom flask containing PET foil sample and a magnetic stir bar. The flask was attached to Schlenk line to provide argon to the system. The reaction mixture was stirred under inert condition at r.t. (20°C); 200 rpm for 1, 2, 3, 4, and 5

h respectively. After each reaction, the modified PET sample was washed thoroughly with diethyl ether, methanol, 0.01 M hydrochloric acid, and finally three times with distilled water, taking 80 ml of each washing solution. The sonicating water bath (K230HTDP 3L variable power ultrasonic bath ultrasonic cleaner) was employed for cleaning the surface efficiently. Washed samples were dried under the vacuum in the desiccator. The modified samples were named after the alkyl groups introduced to the surface: PET–CH_3, PET–C_4H_9, PET–C_6H_{13}, PET–C_8H_{17}, PET–$C_{12}H_{25}$ and PET–$C_{18}H_{37}$ respectively.

PET samples were allowed to react with $C_{18}H_{37}MgCl$ in dry diethyl ether at various concentrations (0.1 M, 0.5 M and 1.0 M) for 1 h and 140 h respectively under argon environment controlled by Schlenk line. It was useful to study the effect of Grignard reagent reaction time and concentration on PET surface modification.

All the modified samples (size 5 cm × 5 cm) were cut into 4 pieces (each size 2.5 cm × 2.5 cm) for the further tests.

3.2.1.3. Fluorescence labelling of PET surface

A standard procedure was followed for the fluorescence labelling [141]. Virgin PET and all Grignard reagent (3 h) modified foils (size 2.5 cm × 2.5 cm; PET–CH_3, PET–C_4H_9, PET–C_6H_{13}, PET–C_8H_{17}, PET–$C_{12}H_{25}$ and PET–$C1_8H_{37}$) were stirred at r.t./ 150 rpm in a solution of 10 mg dansyl chloride ($C_{12}H_{12}ClNO_2S$) in 5 ml dry pyridine. After 3 h, the samples were removed and washed with 10 ml ethanol for 4 h, using a mechanical shaker. Again the samples were washed overnight with acetone. The reaction and washing processes were carried out under dark condition. For calibration, the above mentioned procedure was followed by using pure PET foils. All samples were air-dried before the fluorescence intensity measurement.

3.2.1.4. Reduction of Nylon 6 with BH_3-THF

The amide functional groups present in Nylon 6 were reduced to secondary amine according to procedure described by Herrera-Alonso *et al.* [112]. Dry THF (50 ml) was introduced into the Schlenk flask (250 ml) kept under argon atmosphere, containing 1 weighed dry sample (~ 90 mg). BH_3-THF solution [8 ml, 1 M (8 mmol)] was added at 0°C with stirring (150 rpm). Reaction mixture was stirred for 1 hour at r.t. and overnight at 50 °C. After cooling down to r.t., the reduced samples were washed with THF, 1 M HCl, deionized water, 1 M NaOH, deionized water, THF, ethanol, acetone and hexane, each by sonication

for 3 minutes. The samples were dried at 50 °C/ 3 h in vacuum and stored in the desiccator until further modification. For long-time storage, 1 M NaOH solution was skipped and modified Nylon 6 was stored as ammonium chloride salt prepared by HCl washing. Reduced samples have been referred as Nylon 6-NH.

All the modified Nylon 6 samples (size 6 cm × 6 cm) were cut into 2 cm × 2 cm size pieces for the further tests.

3.2.1.5. N-alkylation with benzyl chloride ($C_6H_5CH_2Cl$)

t-BuOK (0.056 g, 0.5 mmol) was introduced into the round bottom flask (100 ml), kept under dry argon, containing 5 weighed Nylon 6-NH samples (~ 50 mg). Dry DMSO (20 ml) was added into the flask and stirred at 150 rpm/ r.t./ 1 h. Subsequently, the second solution containing dry DMSO (10 ml) and benzyl chloride (0.115 ml, 1 mmol), premixed and equilibrated at r.t./ 1 h, was dropped into the reaction mixture. The reaction was allowed to proceed for 1 h and 3 h respectively. The modified samples were rinsed thoroughly in the sonicating bath with DMSO, deionized water, ethanol, THF, acetone and hexane; then dried at 50 °C/ 3 h in vacuum and stored in the desiccator. Modified samples have been referred as Nylon 6-NCH_2Ph.

3.2.1.6. Grafting of Nylon 6-NH with H_3C-PEG-OTs

Dry THF (50 ml) was added into the Schlenk flask (250 ml) containing 10 Nylon 6-NH (~ 100 mg) samples. Then *t*-BuLi [1.7 M; 0.6 ml (~ 1 equiv.), 1 ml (~ 1.7 equiv.), 2 ml (~ 3.3 equiv.)] was introduced into the flask. *n*-BuLi [2.5 M; 0.4 ml (~ 1 equiv.), 7ml (~ 1.7 equiv.), 1.3 ml (~ 3.3 equiv.)] can also be used instead of *t*-BuLi (1.7 M) for the same reaction. The lithiation was allowed to occur at r.t./ 250 rpm in different time intervals (2 h, 4 h, 6 h and 24 h). Into the second Schlenk flask, containing H_3C-PEG-OTs (2 g, 1 mmol) was added dry THF (50 ml) and the mixture was stirred at r.t./ 700 rpm/ 1 h. After lithiation, the solution of remaining *t*-BuLi was carefully removed from the first flask via syringe and washed twice with dry THF under argon flow. Subsequently, H_3C-PEG-OTs solution was added into the first flask containing lithiated Nylon 6-NH samples and was allowed to react at r.t./ 250 rpm in different time intervals (2 h, 4 h, 6 h, 15 h). The grafted samples were washed thoroughly with THF, ethanol, acetone and hexane; then dried at r.t./ 5 h in the vacuum and stored in the desiccator. Modified samples have been referred as Nylon 6-N-PEG-CH_3.

3.2.1.7. Tethering of PEG on Nylon 6-NH surface by conjugating DSC

A verified procedure was followed for the following conjugation reaction [142]. 5 ml *N,N*-diisopropylethylamine and 0.3843 g DSC (1.5 mmol) were stirred in 60 ml dry acetone at r.t./ 500 rpm/ 1 h. This suspension was added into the Schlenk flask (250 ml) containing 5 Nylon 6-NH samples and stir bar under argon and stirred at r.t./ 200 rpm/ 3 h. The reaction media was removed carefully via syringe and washed twice with dry acetone in the closed system. Meanwhile, Polyethylene glycol (2.9 g, 2 mmol PEG) was dried at r.t. for 2 h in cold trap using liquid nitrogen (N_2). 35 ml of dry acetone was added to 100 ml round bottom flask containing dry PEG and a sir bar, under inert atmosphere and stirred at r.t./ 400 rpm for 2 h. In another flask, 1.466 g of 4-(dimethylamino) pyridine (12 mmol) was dissolved in 20 ml dry acetone and stirred at r.t./ 200 rpm for 1 h. First, the PEG solution was added to the washed Nylon 6-NH samples after reaction with DSC. Then, 4-(dimethylamino) pyridine solution was introduced, stirred at r.t./ 200 rpm and allowed to react overnight. Finally, the samples were removed and rinsed with acetone, ethanol and hexane by sonication; then dried at r.t./ 5 h in the vacuum and stored in the desiccator. Modified samples have been referred as Nylon 6-N-PEG.

3.2.1.8. Deposition of Cu NPs on grafted Nylon 6 (Nylon 6-N-PEG-CH_3) surface

4 mg of Copper nanoparticles (Cu NPs, 500 – 900 nm particle size) were dissolved in 40 ml deionized water under inert atmosphere and introduced to 100 ml Schlenk flask under argon containing 4 Nylon 6-N-PEG-CH_3 (2 h lithiation, 1 ml *t*-BuLi) samples and kept the samples immersed into the solution overnight at r.t; washed twice with water and twice with ethanol using sonicating bath each time for 1 min to remove excess Cu NPs on surface. The samples were dried at 45°C/ 4 h in the vacuum and stored in the desiccator. Cu NP deposited samples have been referred as Nylon 6-N-PEG-CH_3-Cu.

3.2.2. Surface characterization

3.2.2.1. Water contact angle (WCA) and free surface energy (FSE) analyses

The WCAs and FSEs (Kwok-Neumann model) were measured using a portable computer-based instrument with special purpose software following ISO 27448:2009 test method (See System E, Advex Instruments, CZ). WCA measurement is one of the rapid, easy and useful surface analytical techniques. The θ/2 method was used to analyse the

profile of sessile drop, assuming the liquid drop to be part of a sphere. WCA values were calculated by the following equation (1),

$$tan\,(\theta/2) = h/x \quad (1)$$

where, θ = static contact angle, h = droplet height and x = half of the droplet width [143]. Contact angle measurements were performed by vertically dispensing 20 droplets (3.5µl/ droplet) of deionized water on each sample. The droplets were allowed to equilibrate for 10 seconds before the measurement. The mean values were taken for plotting the WCA histograms including standard deviations (± SD); all the values for each sample were in a range of ±5°. The FSEs related to the mean values of WCAs were directly measured by the software using Kwok-Neumann model. Neumann and Kwok proposed the following equation (2) for the FSE determination of solids by using one liquid [144].

$$\gamma_L(1 + \cos\theta) = 2\sqrt{\gamma_L.\gamma_S}\,[1 - 0.0001057(\gamma_L - \gamma_S)^2] \quad (2)$$

Where γ_L and γ_S are the FSE of the liquid and solid respectively, θ is the contact angle. Both, γ_L (experimental surface tension) and θ can be easily determined. The water surface tension (γ_L) is a known value at a definite temperature.

3.2.2.2. Fluorescence intensity assessments

Synergy™ HTX Multi-Mode Microplate Reader (BioTek, Germany) with UV-VIS absorbance and filter-based fluorescence was used to measure the fluorescence intensity of dansylated PET foils. The samples were cut into 1 cm x 1 cm size to fit in the 24 welled cell culture plates. The chemically bonded dansyl groups on the surface were determined by excitation at 360 nm and emission maximum at 528 nm at the gain of 200.

3.2.2.3. Scanning electron microscopy (SEM) and atomic force microscopy (AFM) analyses

The surface morphology changes were examined by the SEM (ZEISS, Sigma Family, Germany). PET fabrics were sputtered with platinum and PET foils were sputtered with gold. Subsequently they were viewed as secondary electron images (2 kV). Modified and unmodified Nylon 6 samples were sputtered with 2 nm platinum layer, subsequently were viewed as secondary electron images (1 kV).

The topography of the pure and modified PET as Well as Nylon 6 films was studied in the air at atmospheric pressure with NanoWizard® 3 NanoScience AFM (JPK Instruments, Germany). For more accurate scanning, a contact mode with Cantilever NANOSENSORS^{TM} PPP-CONTSCR (resonance frequency = 23 kHz; contact force = 0.2 Nm^{-1}; tip radius <10 nm; tip height 10–15 µm) was used. Sample scans and subsequent surface roughness (Ra) evaluation were performed on areas 10 µm x 10 µm and 1 µm x 1 µm. Obtained data were processed by using the freeware software Gwyddion and JPK Data Processing.

3.2.2.4. X-ray photoelectron spectroscopy (XPS) analyses

X–ray photoelectron Spectroscopic (XPS) measurements investigating C_{1s} and N_{1s} binding energies (eV) before and after Nylon 6 modification were done by a Thermo Scientific K-Alpha X-ray Photoelectron Spectrometer (Thermo Fisher Scientific) using a monochromatic Al K_{α} radiation (hγ= 1486.6 eV).

3.2.2.5. Fourier transform infrared (FT-IR) and Raman spectroscopy analyses

The Nicolet™ iS™10 FT-IR Spectrometer (Thermo Scientific™, USA) was employed for the investigation of modified PET foils and Nylon 6 samples compared to the pure ones. The DXR™ Raman Spectrometer (Thermo Scientific™, USA) were used to examine the changes in surface composition after the conversion of Nylon 6-NH to Nylon 6-NCH_2Ph, due to the FT-IR limitations.

3.2.3. Antibacterial and cell experiments

3.2.3.1. Biofilm tests of PET

A standard procedure was followed to perform biofilm experiments with pure PET, PET–CH_3 and PET–$C_{12}H_{25}$ foil samples [145]. Four different pathogenic bacterial strains namely; *E. coli, S. aureus,* methicillin-resistant *S. aureus* (MRSA)*,* and *P. aeruginosa* were enlivened, inoculated, and cultivated to obtain individual bacterial colonies on the agar. Brain heart infusion (BHI) agar was used to prepare solution for bacterial growth (BHI 5.2 g/ 1000 ml). BHI was dissolved in distilled water and was sterilized in an autoclave for 15 min at 121°C. After cooling down to 37°C, 10 ml of the solution was added into the sterile container and subsequently one colony of chosen bacterial strain was added through inoculating loop. The container was vortexed and kept in the thermostat for 24 h at 37°C. After incubation for

24 h, samples were immersed into the cultivated solution and whole system was cultivated in the thermostat for 72 h. Glucose (1 g/ 50 ml BHI) was added into the solution to prepare better nourishing conditions. Samples were removed from the solution and washed twice with distilled water, twice with physiological solution and finally kept for 20 min in the container with ethanol. Subsequently, samples were washed with distilled water and immersed into the containers containing dye solution (crystalline violet 2.5 g/100 ml of ethanol mixed with diammonium oxalate 4 g/ 400 ml of distilled water) for 45 min. Marked samples were washed with distilled water, dried at room temperature and observed through optical microscope Leica DM750. Magnifications 40X (HI Plan 4X/ 0.10 NA, 18.0 mm W.D.) and 100X (HI Plan 10X/ 0.25 NA, 12.0 mm W.D) were used.

3.2.3.2. Antibacterial tests of Nylon 6

Antibacterial action assessments were performed in a compliance with commonly used standard method CSN EN ISO 6222. Cultivation was done from lyophilized bacterial strains that were added into the Soyabean Casein Didest Medium. After cultivation in the medium for 48 h/ 37°C, both bacterial strains were re-inoculated on the Plate Count Agar without Dextrose. *S. aureus* culture was cultivated for 48 h and *P. aeruginosa* for 24 h. Both, thus obtained, cultures were used to prepare the bacterial inoculums with initial concentration 3.0 x 10^7 CFU/ ml for the following antibacterial tests. In detail, fresh cultured bacteria were added by sterilized loop into 10 ml of sterile physiological solution (6 % NaCl) until it reached the required McFarland standard concentration (0.1 McFarland standard concentration = 3.0 x 10^7 CFU/ ml). This concentration is referred further as 10^0.

For convenience, all the Nylon 6 samples were named as follows: sample 1 (**S1**) - pure Nylon 6, sample 2 (**S2**) - Nylon 6-NH, sample 3 (**S3**) - Nylon 6-N-PEG-CH_3 (2 h lithiation, 0.6 ml *t*-BuLi), sample 4 (**S4**) - Nylon 6-N-PEG-CH_3 (24 h lithiation, 0.6 ml *t*-BuLi), sample 5 (**S5**) - Nylon 6-N-PEG-CH_3 (2 h lithiation, 1 ml *t*-BuLi), sample 6 (**S6**) - Nylon 6-N-PEG-CH_3 (24 h lithiation, 1 ml *t*-BuLi), sample 7 (**S7**) - Nylon 6-N-PEG-CH_3 (2 h lithiation, 2 ml *t*-BuLi) and sample 8 (**S8**) - Nylon 6-N-PEG-CH_3 (24 h lithiation, 2 ml *t*-BuLi). All the samples (2 cm x 2 cm size) were sterilized for 20 minutes by UV A for each bacterial test. Subsequently, 50 ml of bacterial inoculum homogenous solution (3.0 x 10^7 CFU/ ml) was added to each sample kept in a 100 ml Fisher bottle. Total 16 sets were prepared, 8 sets (samples 1 - 8) with *S. aureus* and other 8 sets with *P. aeruginosa*. The bacterial solutions were incubated 24 h/ 37 °C.

The control tests related to the both bacterial strains were performed directly by adding 1 ml of initial and diluted control solution into a Petri dish at required concentration (10^0, 10^{-1}, 10^{-2}, 10^{-3}, 10^{-4}, 10^{-5}, 10^{-6} and 10^{-7}) to the agar medium. The Petri dishes were incubated 48 h/ 37 °C. The grown bacteria were counted after 48 h incubation. Samples 1 - 8 were tested with the following procedure; 1 ml each of the solution at different concentrations (10^0, 10^{-1}, 10^{-2}, 10^{-3}, 10^{-4}, 10^{-5}, 10^{-6} and 10^{-7}) was directly used for bacterial proliferation in agar medium. In each Petri dish, 1 ml of bacterial solution (with specific required concentration already mentioned above) was added and the liquid agar media was poured at 37 °C, shaking gently to spread the bacterial solution homogenously in agar. After cooling the agar medium to set, all the covered Petri dishes were kept into the incubator 48 h/ 37 °C. Finally, the grown bacteria were counted. All the tests were repeated twice.

To examine the bacterial adhesion on the surface of each sample (samples 1 - 8), the following procedure was used: each sample incubated in bacterial inoculum (3.0×10^7 CFU/ ml) for 24 h/ 37 °C was taken out from the inoculum and transferred to 100 ml Fisher bottle containing 20 ml sterile physiological solution (6% NaCl). The bottles were shook vigorously for 1 h to remove surface adhered bacteria in solution. 1 ml of each solution at different concentrations (10^0, 10^{-1}, 10^{-2}, 10^{-3}, 10^{-4}, 10^{-5}, 10^{-6} and 10^{-7}) was directly used for bacterial proliferation in agar medium into the incubator for 48 h/ 37 °C as mentioned in the previous paragraph.

3.2.3.3. Antibacterial tests of Nylon 6-N-PEG-CH_3-Cu

The Zone of Inhibition Test (Kirby-Bauer test), a qualitative method was used to measure the ability of Nylon 6-N-PEG-CH_3-Cu sample (named as sample 9 or **S9**) to inhibit microbial growth (*S. aureus* and *P. aeruginosa*). 1 ml of both the bacterial inoculums (prepared as mentioned previously) with initial concentration 1×10^7 CFU/ ml, were spread over two agar plates separately using sterile swabs, then 2 cm x 2 cm size Nylon 6-N-PEG-CH_3-Cu sample is placed to the centre of the agar plate and incubated at 37°C for 48 h and 96 h. The bacterial growth-inhibiting effect was determined by the size of inhibition zone (clear zone) appeared around the sample.

The quantitative antibacterial test procedure was same as the antibacterial test of pure and functionalized Nylon 6.

3.2.3.4. Cytotoxicity and cell adhesion of pure and modified PET

Cytotoxicity test

Potential cytotoxic effect of the surface modification was evaluated *in vitro* by test in direct contact. The test was performed in compliance with standard ISO 10993–5:2009 Biological evaluation of medical devices—tests for *in vitro* cytotoxicity. Before exposure to the tested samples (pure PET, PET–CH_3 and PET–$C_{12}H_{25}$ foil), 3T3 fibroblast cells were pre-cultured under standard conditions up to ~90% confluence. Tested samples and positive and negative control were applied to each culture vessel covering exactly one eighth of the cell layer surface. Testing of each sample was performed in triplicate. Cell viability was evaluated after 24 h of exposure in complete culture media (DMEM, 5% FBS, 5% NBCS, ATB) via standard mitochondrial oxidoreductases metabolic activity test. Degree of reduction of MTT was determined spectrophotometrically by reading at 570 nm (background subtracted at 650 nm). Percentage of viable cells in each vessel was compared to viability of blank. In order to reveal potential cytotoxic effect of the surface treatment and distinguish possible distorting effect of mechanical damage caused to the cell layer and the effect of the original unmodified foil, the metabolic activity was compared to three types of blank. The blanks used in this study were unaffected cell control (CC), negative control (NC), and untreated PET foil.

Cell adhesion and proliferation

The influence of surface treatment on cell adhesion and proliferation were evaluated using the same fibroblastic cell line. Samples (pure PET, PET–CH_3 and PET–$C_{12}H_{25}$ foil) of 1 × 1 cm^2 sizes were fixed to a culture vessel bottom and exposed to cell suspension of 40 × 10^3 cells/ml for 24 h. Both, the density of adhered cells and their morphology were determined microscopically. After the 24 h of exposure, samples were fixed in methanol and stained with propidium iodide (PI) for cell nuclei imaging (red, Ex/ Em = 540/ 608 nm) and DiOC6(3) for membrane structures in cytoplasm imaging (green, Ex/ Em = 482/ 501 nm). The imaging was carried out on Axio Imager M2 microscope using EC Plan-Neofluor objectives 10X, 20X, 40X (Carl Zeiss Tld.). Density of the adhered cells was evaluated through cell nuclei count performed on 10 images (magnification 100X) of each sample using ImageJ software. For cell morphology evaluation imaging under magnifications 100X, 200X, and 400X was used.

3.2.3.5. Cytotoxicity and cell adhesion of pure and modified Nylon 6

Cytotoxicity of extracts

Extracts of all types of foils materials were tested according to ISO 10993-5. Prior to *in vitro* experiment, materials (samples 1 - 9) were sterilized by immersion in 70% ethanol for 30 minutes followed by double washing in phosphate buffer saline (PBS). Mouse 3T3-SA fibroblasts (passage 7) were used for cytotoxicity assessment of foils according to ISO 10993-5. Extracts of the three types of materials in concentrations of 10 mg/ ml and 5 mg/ ml were prepared. Materials were put in sterile test tube and soaked in complete media (DMEM, 10% FBS, 1% ATB, 1% glutamine). After 24 h of shaking in 37°C (100 rpm), the extracts were added to subconfluent layer of fibroblasts seeded in 96 well plates. Two concentrations of extracts were tested: 10 mg/ml and 5 mg/ml. Cells in complete media served as negative control (NC). Complete media with addition of cytotoxic agent Triton X-100 was used as positive control (PC). After 24 h of incubation, cell metabolic activity was determined by colorimetric MTT assay (n = 12 per each group). Measured absorbance of negative control was considered as 100% viability. Recalculated values of cell viability were plotted in the graph showing the cytotoxic effect of materials that is determined by viability decrease under 70% of control cells. Before performing metabolic MTT tests for the samples, cells were also captured by optical microscopy (KRD, NIB-100, CZ) with magnification 100X.

Direct contact cytotoxicity

Fibroblasts were seeded in 12 well plates. After reaching subconfluency, tested materials (samples 1 – 9) in size of approximately 5 mm x 5 mm were added into the wells (n = 4 per each material). After 37°C/ 24 h of incubation, cells were observed by optical microscopy and cell metabolic activity was determined as previously by MTT test. The same control was used for calculation of cell viability (NC – cells in complete media, PC – cells in media + Triton X-100). Before MTT assay, cells were examined microscopically with magnification 100X.

Cell adhesion and proliferation

Sterile samples (samples 1 – 8) in size of approximately 2 cm x 2 cm were placed in the bottom of 6 well plates and seeded with fibroblasts. After 1 and 7 days of incubation at 37°C, foils with adhered cells were washed twice in PBS and fixed in 2.5% glutaraldehyde.

Then, cells were stained by phalloidin-FITC that binds to actin filaments in the cytoplasm and DAPI that visualize cell nuclei in blue. Fluorescence microscope (Nikon ECLIPSE Ti-E/B) was used to capture cell spreading (objective 20X). Optical microscope (KRD, NIB-100, Cz) with magnification 100X, was also used to observe the cell proliferation on sample surface. Cell proliferation was also assessed by SEM (VEGA3, TESCAN, Cz). Samples (1 – 8) were fixed and dehydrated by gradually increased ethanol. Then, they were placed on holder, coated with gold and analysed using VEGA 3SB Easy probe.

Cell viability was measured by metabolic MTT test in the same time periods of 1 and 7 days after seeding. Tested samples (1 – 8) were transferred into new well plate and incubated at 37°C for 3 h with MTT solution. Similarly, control tissue culture plastic (TCP) was also analysed. The formed violet crystals were dissolved in acidic isopropanol and resulting absorbance (570 - 650 nm) was measured.

3.2.4. Nanoparticles preparation, characterization and application

3.2.4.1. Synthesis of copper nanoparticles (Cu NPs)

The synthesis was carried out in aqueous phase and inert condition using a reducing agent [146]. 100 ml 0.03 M copper (II) chloride dihydrate ($CuCl_2$. $2H_2O$) solution was added to 100 ml 0.1 M sodium dodecyl sulphate (SDS) solution (pH = 7) under inert condition in a 250 ml round bottom flask containing stir bar. 43 ml 0.12 M sodium borohydride ($NaBH_4$) solution was added to the flask under a continuous flow of argon. The solution was turned to dark brown immediately after $NaBH_4$ addition and stirred at r.t./ 800 rpm until the characteristic brick red colour of Cu NPs appeared. CuNPs were separated from the aqueous solution by centrifugation at 12,000 rpm for 45 mins and washed twice with ethanol. Then dried at r.t./ 4 h in the vacuum and stored under argon. The synthesized Cu NPs were used in section **3.2.1.7.** for making Nylon 6-N-PEG-CH_3-Cu sample.

Yield = ~170 mg

3.2.4.2. Characterization techniques for Cu NPs

Dynamic light scattering (DLS) is a well-established technique for measuring the size of nanoparticles. Malvern Zetasizer Nano Series (Malvern Instrument Ltd., UK), particle size range 0.3nm - 10µm, was used to determine the Cu NPs size immediately after the reduction of $CuCl_2$ to zero-valent Cu and at other various intervals (1 h, 3 h and 24 h, 1

month). 2 µl reaction solution was transferred to cuvette (capacity = 2.5 µl) and the particle size was measured.

FT-IR spectra (Nicolet™ iS™10; Thermo Scientific™, USA) of pure SDS and SDS-capped Cu NPs were recorded to determine the binding interactions of SDS with zero-valent Cu NPs.

Size distribution and shape homogeneity of Cu NPs were examined by SEM (ZEISS, Sigma Family, Germany) images. Samples were prepared by taking small quantities of Cu NPs dispersed in deionised water. Then the solution was dropped on carbon-coated copper grid and kept in the freezer at -80° for 15 mins. The grid was immediately transferred to lyophilizer (FreeZone 2.5 Liter Benchtop Freeze Dry System, Labconco, Canada) and dried under vacuum (3 mbar at -52°C) to ensure complete removal of water. Image J software was used to measure the nanoparticle size.

UV-VIS spectroscopy (HACH® DR 6000, wavelength range: 190 – 1100 nm, scanning speed: 900 nm/ min) was used for preliminary estimation of Cu NPs synthesis immediately after the reaction and at other time intervals (15 mins, 30 mins, 1 h and 2 h).

3.2.4.3. Synthesis of mesoporous silica (SiO_2) nanoparticles (MSNs)

The following MSNs (mobil crystalline material – MCM, Santa Barbara amorphous – SBA, Plugged hexagonal templated silica – PHTS and mesostructured cellular foam – MCF) were prepared by the selected procedures described in various verified literatures [135,147].

MCM-41 (from fumed silica)

6.2 g CTAB was added to 40.4 g Milli-Q water in a 250 ml round bottom flask containing stir bar and stirred vigorously at 45 °C until dissolved completely. The solution was cooled down to room temperature. Then, 10 g of TEAOH (20%) solution was added to it and stirred for 5 mins at 500 rpm. After that, 4.1 g fumed silica was added and stirred at 70°C for 2 h, followed by further 24 h of vigorous stirring at r.t. The viscous solution was heated to 130°C for 48 h, sealing the flask tightly. After the heat treatment, the solution was filtered. The solid was washed with 150ml deionized water and transferred into an autoclave and some fresh water was added until the solid was just covered. It was heated a second time to130°C for 72 h. After hydrothermal treatment, the solid was filtered using vacuum pump, washed 3 times with 25 ml water and dried. The product was crushed into fine

powders for calcination at 550°C during 6 h with a heating rate of 1° C/min in ambient atmosphere. The final white product was cooled down slowly and stored. The obtained product has been referred as MCM-41(FS).

Yield = 3.2 g

MCM-41 (spherical)

3.75 g CTAB was added to 70.71 g Milli-Q water in a 250 ml round bottom flask containing stir bar and stirred at 45°C until complete dissolution. The solution was cooled down to room temperature. 25.74 g NH_3 (25%) and 90 g ethanol were added to it and stirred at 500 rpm for 30 mins. 7.05 g TEOS was introduced dropwise stirring the solution for 3 h at 500 rpm and then for 12 h at 300 rpm /25°C. The solution was filtrated under vacuum and the solid was subsequently washed with 150 ml distilled water and thereafter with 150 ml methanol. The solid was heated at 90°C for 20 h. The post-synthesis treatment was achieved by calcination of the product at 550°C during 5 h with a heating rate of 1°C/ min in ambient atmosphere. The product was cooled down slowly and stored. The obtained product has been named as MCM-41(S).

Yield = 2 g

MCM-41 (Highly ordered MSNs)

121 ml of $NH_3.H_2O$ (22.7%) was mixed with 116.5 ml of Milli-Q water to form a homogeneous solution in a round bottom flask (250 ml) containing stir bar. 1.0 g of CTAB was added into this solution and stirred vigorously at 500 rpm/ 45 °C until a homogeneous solution is obtained. When CTAB was completely dissolved, the solution was cooled down to room temperature. Then, 5 ml of TEOS was added to the surfactant solution in one injection and stirred at r.t./ 500 rpm for 2 h. Precipitation occurred very quickly, and that indicated the hydrolysis of TEOS. After 2 h of stirring, the resulting precipitate was collected using vacuum filtration. The solid was washed with copious amounts of distilled water until neutralized and dried at 90 °C overnight. The dried solid was crushed into fine powders and transferred into a crucible for calcination at 550 °C in 6 h with a heating rate of 1°C/ min in ambient atmosphere. The final product was cooled down slowly, stored and named as MCM-41(HO).

Yield = 0.94 g

MCM-48

(A) Synthesis of gemini 16-12-16 surfactant:

12 g of 1.12-dibromododecane and 25.5 ml of *N,N*-dimethylhexadecylamine were added to 50 ml acetone in round bottom flask (250 ml) containing stir bar and attached to an air cooler. The temperature was increased to 65°C until refluxing started. Refluxing was continued at 500 rpm for 24 h. The gemini surfactant started to crystallize after 12 h. The system was cooled down. Then, the surfactant crystals were filtered and washed with acetone. The gemini was recrystallized in a beaker with acetone. The final product was collected by vacuum filtration and washed twice with acetone. The gemini surfactant is dried at room temperature in ambient conditions.

Yield of gemini 16-12-16 surfactant = ~20 g

(B) Synthesis of MCM-48

120 ml of Milli-Q water and 0.6922 g NaOH were added to 5.7734 g gemini 16-12-16 surfactant in a round bottom flask (250 ml) containing stir bar. The solution was stirred at r.t./ 700 rpm until gemini is dissolved. 4 g fumed silica was added and stirred for 2 h. The sealed flask was aged in an oven at 130°C during 3 days. After heat treatment, the flask was brought to r.t. and the product was filtered and washed with 100 ml water. The solid was crushed further washed 4 times with deionized water using centrifuge for 5 mins each time at 10,000 rpm. The residue was transferred to an autoclave and 60 ml of deionized water was added. The autoclave was heated in an oven at 130°C for 1 day. After heat treatment, the product was recovered by vacuum filtration and further washed thrice with 150 ml distilled water; then dried at ambient condition. The final product was obtained after the solid was calcined at 550°C during 6 h with a heating rate of 1°C/ min in ambient atmosphere. The product was cooled down slowly and stored.

Yield = 3 g

SBA-15

4 g of P123 was added to 130 ml of Milli-Q water and 21 ml of HCl (35%) in round bottom flask (250 ml) containing stir bar. The solution was stirred at r.t./ 800 rpm/ 3 h until complete dissolution. 9.14 ml of TEOS was introduced and continued stirring overnight at

45°C. Ageing of the white precipitate was carried out for 24 h at 80°C, in the sealed flask without stirring. The system was cooled down and the product was recovered by vacuum filtration, washed thrice with 50 ml of distilled water and then dried overnight at 80°C. The final product was calcined at 550°C during 6 h with a heating rate of 1°C/ min in ambient atmosphere. Cooling down was occurred slowly and collected.

Yield = 2.8 g

PHTS (Plugged hexagonal templated silica)

4 g of P123 was added to 130 ml of Milli-Q water and 21 ml of HCl (35%) in round bottom flask (250 ml) containing stir bar. The solution was stirred at r.t./ 800 rpm/ 3 h until complete dissolution. 16 ml of TEOS was introduced and continued stirring during overnight at 60°C. Ageing of the white precipitate was carried out for 24 h at 80°C, in the flask sealed. The system was cooled down to r.t. and the product was collected by vacuum filtration. Then it was washed thrice with 50 ml of distilled water and then dried overnight at 80°C under ambient atmosphere. The final product was calcined at 550°C during 6 h with a heating rate of 1°C/ min in ambient atmosphere. The product was cooled down and collected.

Yield = 4.2 g

MCF (mesostructured cellular foam)

4 g of P123 and 21 ml of HCl (35%) were added to 130 ml of Milli-Q water; stirred at r.t./ 700 rpm, in a 250 ml round bottom flask with stir bar, until the surfactant was dissolved. 0.0467 g of NH4F and 4.6 ml of mesitylene were introduced into the flask. The temperature was raised to 40°C and stirring was continued at 800 rpm for 1 h. Then, 9.14 ml of TEOS was added and stirred for another 20 h at 40°C. The mixture was transferred to an autoclave and kept at 100°C for 24 h. After the heat treatment, the autoclave was quenched to r.t.. Product recovery was accomplished by vacuum filtration, followed by washing the solid thrice with 50 ml of water and dried at ambient atmosphere. The final product was collected after calcination at 550°C during 6 h in ambient atmosphere with a heating rate of 1°C/ min. The product was cooled down slowly.

Yield = 2.3 g

3.2.4.4. Characterization techniques: BET and SEM

The gas sorption analyser (Autosorb® iQ, Quantachrome Instruments) was employed to examine the surface areas and pore size distributions for MSNs. The surface areas and pore size distributions were calculated using ASiQwin software based on adsorption-desorption isotherms. The pristine samples were degassed at 300°C for 3 h. Then N_2 adsorption and desorption isotherms were measured at the temperature of -196 °C. Multipoint BET (Brunauer–Emmett–Teller) analysis was applied for the total surface area calculation. Models of DFT (Density Functional Theory) were used to determine pore size distribution and also compared to relatively old BJH (Barret-Joyner-Halenda) model.

Size distribution and shape homogeneity of Cu NPs were examined by SEM (ZEISS, Sigma Family, Germany) images. Samples were prepared by taking small quantities of MSNs dispersed in distilled water. Then the solution was dropped on carbon-coated copper grid and dried under vacuum to ensure the complete removal of the solvent. MSNs were sputtered with 2 nm platinum layer, subsequently were viewed as secondary electron images (2 kV).

3.2.4.5. Drug loading on and releasing from MSNs

Preparation of L-DOPA solution

50 ml Milli-Q water was added to 50 mg L-DOPA in an Erlenmeyer flask (100 ml) covered with aluminium foil and sonicated during 1 h at r.t. for complete dissolution. This solution was used for drug loading as well as for calibration.

Drug loading

The drug L-DOPA was loaded by soaking 10 mg of silica in 1 mg/ ml of L-DOPA solution (in Milli-Q water) for 2 h, 4 h, 6 h, 15 h and 24 h. The drug-loaded MSNs were stored into the refrigerator (4°C) covered with aluminium foil as L-DOPA solution is very sensitive towards heat and light. The drug-loaded samples were centrifuged at 10,000 rpm for 10 mins and the clear solution above the precipitate was collected for examining the loading profiles for each of the samples. The L-DOPA loaded solid samples were collected after filtration and dried at dark in the desiccator.

Drug release

100 mg of the L-DOPA loaded samples were dispersed in 10 ml of phosphate buffer solution with pH 7.2 (PBS, K_2HPO_4 and KH_2PO_4) and kept at 37°C using an incubator in order to simulate the body temperature during 15 mins, 30 mins, 1 h, 2h and 3 h. A higher amount of drug was expected to be released into the intestine at pH range 7–8 [148].

3.2.4.6. Monitoring of drug loading and releasing by UV method

Both the drug loading and releasing profiles for each of the samples were determined by monitoring the absorbance change using the UV-VIS spectrophotometer (HACH® DR 6000, wavelength range: 190 – 1100 nm, scanning speed: 900 nm/ min). The calibration curve (for drug loading profile) was prepared by measuring the absorbance at various suitable concentrations of L-DOPA solution in water and absorption peaks were recorded at 290 nm for L-DOPA. Similarly, for drug releasing profile, the calibration curve was also obtained for L-DOPA solution in PBS.

4. RESULTS AND DISCUSSION

4.1. PET

4.1.1. PET surface modification

4.1.1.1. General mechanism of Grignard reagent reaction with esters

Esters react with Grignard reagents (R–Mg–X; R = alkyl group, X = halogen such as Cl, Br or I) to yield tertiary alcohols in which two of the substituents (–R) bonded to the hydroxyl-bearing carbon always come from the Grignard reagent. Grignard reaction involves addition of a carbanion nucleophile ($R:^{-}\ ^{+}MgX$) [149]. The general mechanism of Grignard reagent reactions are depicted below in **Figure 4** using ethyl acetate (CH_3COOEt where Et represents ethyl group) as a model ester. The given mechanism is also applicable for polyesters such as PET.

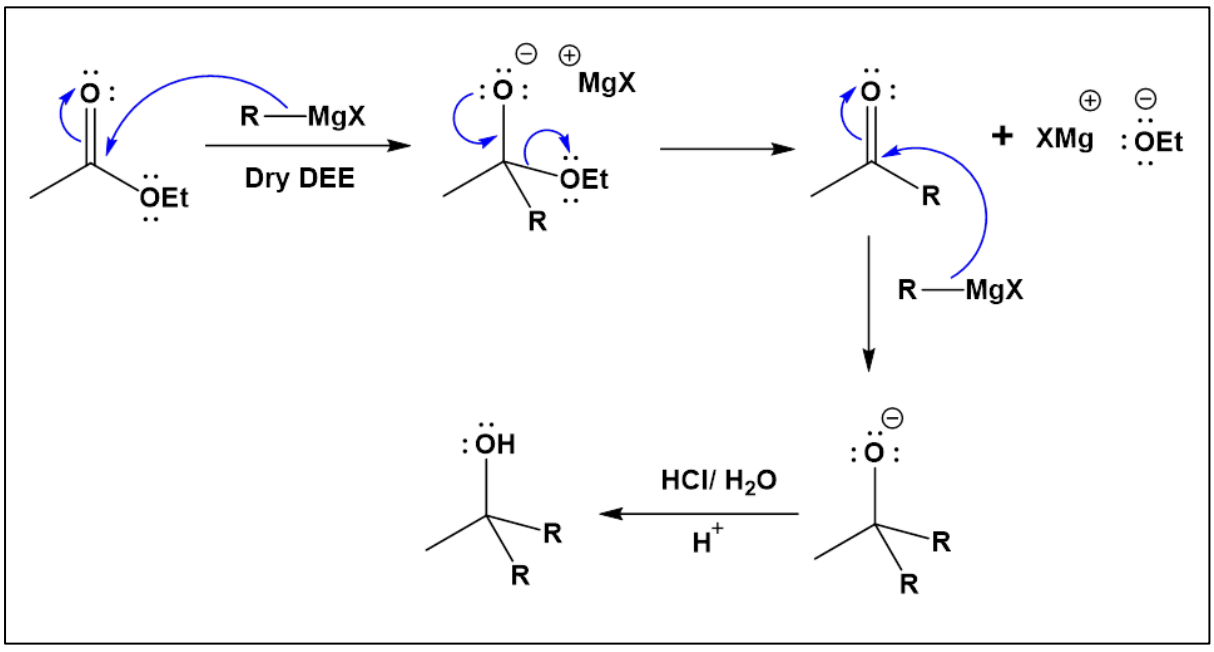

Figure 4: Mechanism of Grignard reagent reaction with ester (ethyl acetate).

4.1.1.2. Ester bond cleavage of PET

The PET fabric and foil surface functionalization with hydroxyl and alkyl groups was achieved by chemical reaction under inert condition that involved the cleavage of ester bond on the surface with Grignard reagents. The modification by Grignard reagents with various

alkyl groups having different C chain lengths (–CH_3, –C_4H_9, –C_6H_{13}, –C_8H_{17}, –$C_{12}H_{25}$ and –$C_{18}H_{37}$), represented by **R,** is shown in **Scheme 1**. The C atoms of carboxylate groups on the PET surface were attacked by the Grignard reagents, resulting in the elimination of ethylene glycol [150].

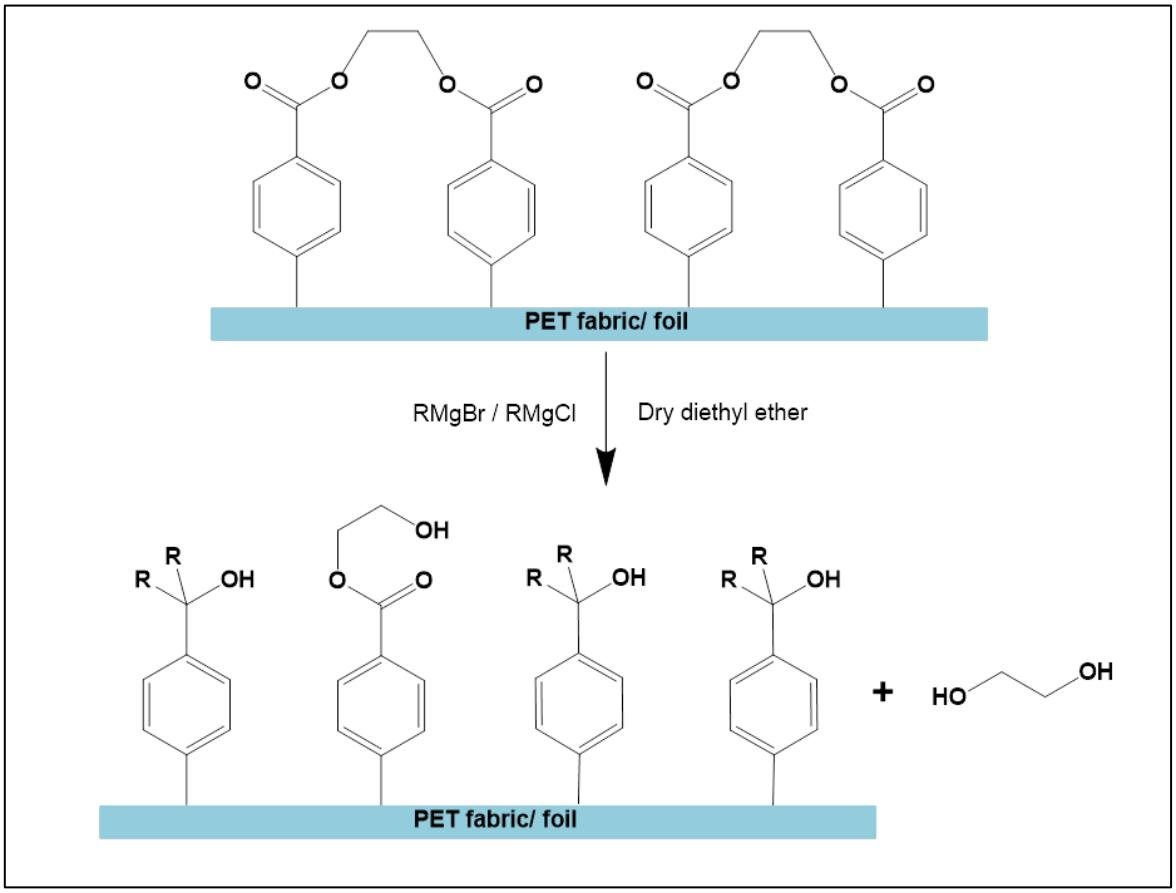

Scheme 1: PET surface functionalization by Grignard reagents in dry diethyl ether (**R** = –CH_3, –C_4H_9, –C_6H_{13}, –C_8H_{17}, –$C_{12}H_{25}$ and –$C_{18}H_{37}$).

4.1.1.3. Dansyl chloride (DNSC) coupling

Dansyl chloride (DNSC) is used in analytical chemistry for fluorescence labelling of certain functional groups, such as hydroxyl group (–OH), carboxylic acid group (–COOH) and extensively for primary and secondary amines. The dansylation of hydroxyl group (–OH) by coupling creates a fluorescent derivative that can be detected by UV-VIS spectroscopy with great sensitivity [151]. The DNSC coupling was applied to confirm the presence of –OH groups on the PET foil surfaces treated with different Grignard reagents. **Scheme 2** shows the reaction involved.

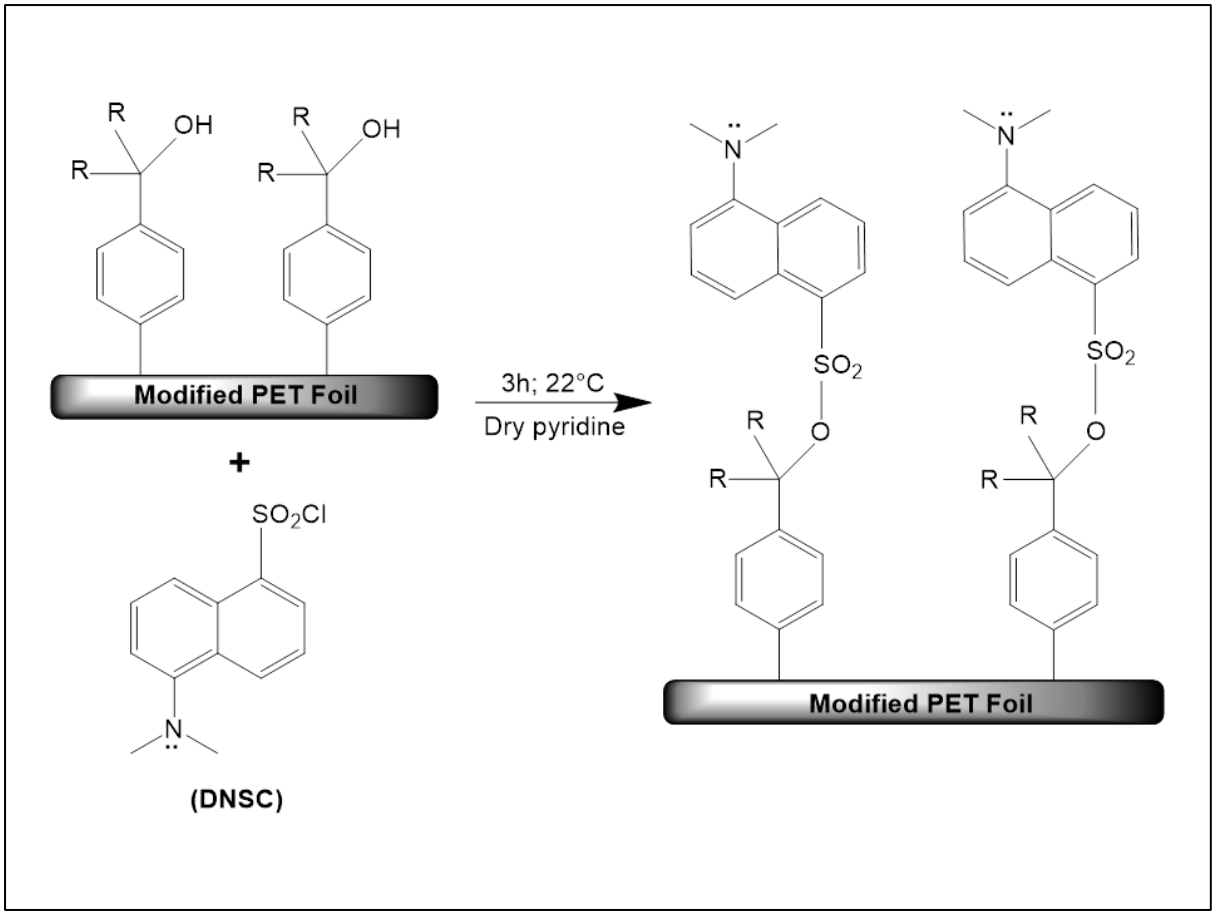

Scheme 2: Dansyl chloride coupling with hydroxyl groups (–OH) on modified PET foils (**R** = $–CH_3$, $–C_4H_9$, $–C_6H_{13}$, $–C_8H_{17}$, $–C_{12}H_{25}$ and $–C_{18}H_{37}$).

4.1.2. Characterization

4.1.2.1. WCA and FSE analyses of pure and modified PET samples

The mean WCAs for Grignard reagent modified PET samples (both fabric and foil) were decreased after the reaction with CH_3MgBr compared to the pure PET. The WCAs increased gradually in case of binding longer alkyl groups ($–C_4H_9$, $–C_6H_{13}$, $–C_8H_{17}$, $–C_{12}H_{25}$ and $–C_{18}H_{37}$). The measured WCAs of PET–C_6H_{13} were almost equal to the virgin PET. PET–$C_{12}H_{25}$ and PET–$C_{18}H_{37}$ fabric and foil samples exhibited similar increase in WCAs. In case of all modified PET fabrics, the samples prepared after 3 – 4 h reactions showed maximum modifications in terms of WCAs compared to 1 h, 2 h and 5 h reactions (**Figure 5 a**). On the other hand, for modified PET foils, the WCAs were almost same within 1 to 5 h of reaction times. The time of the treatment with Grignard reagent was not correlated to WCAs (**Figure 5 b**). PET–$C_{18}H_{37}$ foils with various concentrations (0.1 M, 0.5 M and 1.0 M) and reaction times (1 h and 140 h) did not show significant alteration of WCAs (**Figure 5 c**). The

variations of WCAs for PET fabric as well as foil with different Grignard reagents and reaction times are compared in **Figure 5 (a, b, c)**. By the observation of WCAs before and after modification of PET, it can be inferred that 0.1 M Grignard reagent under 3 h reaction time was sufficient for maximum surface modification at room temperature. The alkyl groups were responsible for the hydrophobicity enhancement on the modified PET surface with the increase in number of carbon atoms in alkyl groups present in the Grignard reagents. On the other hand, the presence of hydroxyl groups responsible for enhancing hydrophilicity. PET surface treated with CH_3MgBr (1C) had the lowest value of WCAs compared to pure PET and the other modified PET samples since the polar hydroxyl groups (–OH) on the surface dominated and finally increased the net hydrophilicity of PET fabric and foil. The PET samples treated with C_4H_9MgCl (4C), $C_6H_{13}MgBr$ (6C), $C_8H_{17}MgBr$ (8C), $C_{12}H_{25}MgBr$ (12C) and $C_{18}H_{37}MgCl$ (18C) increased the hydrophobicity on the surface gradually as the longer alkyl chains caused the hindrance to polar hydroxyl groups (-OH). Therefore, hydrophobicity of PET–C_6H_{13} was almost equal to the virgin PET. PET–$C_{12}H_{25}$ and PET–$C_{18}H_{37}$ exhibited maximum hydrophobicity as both of them had long alkyl chains (12C and 18C respectively) on the surfaces that caused maximum hindrance to the hydroxyl groups (–OH).

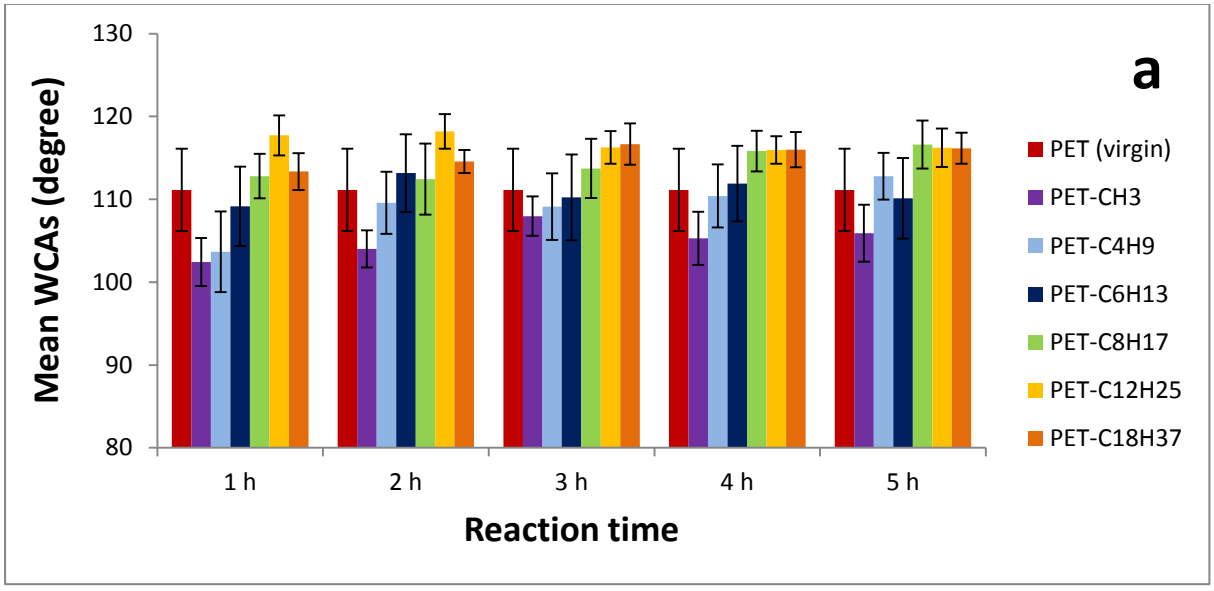

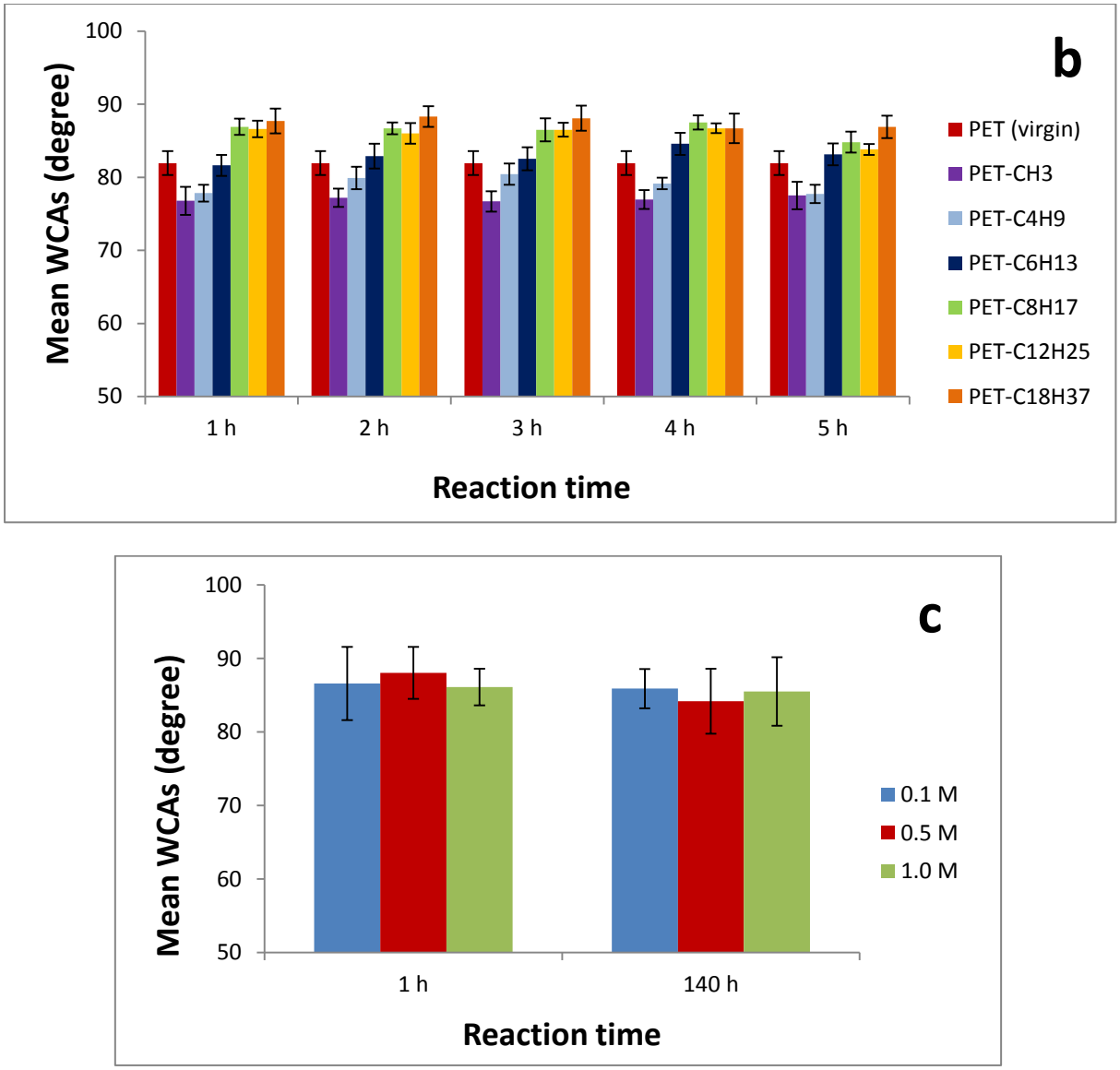

Figure 5: The mean WCA measurements comparing virgin and modified PET fabrics **a**); virgin and modified PET foils **b**) and PET–$C_{18}H_{37}$ foils prepared by different $C_{18}H_{37}MgCl$ (G. R.) concentrations with various reaction time.

The FSE plays an important role on bacterial adhesion and therefore the parameter is considered to be very important in surface characterization [26]. The FSEs of samples modified with CH_3MgBr and C_4H_9MgCl increased compared to the virgin PET. PET-C_6H_{13} showed nearly equal FSE values as pure PET. Moreover, FSEs values gradually decreased after treating with $C_8H_{17}MgBr$. $C_{12}H_{25}MgBr$ and $C_{18}H_{37}MgCl$. The variations of FSEs with different Grignard reagents and reaction times are shown in **Figure 6** (**a, b**) compare to pure PET foil and fabric. The effect of reaction time and Grignard reagent ($C_{18}H_{37}MgCl$) concentrations on FSEs are presented in **Figure 6 c**. The significant differences in the FSE

changes with reaction time were not observed for PET foil or fabric with the same Grignard reagent.

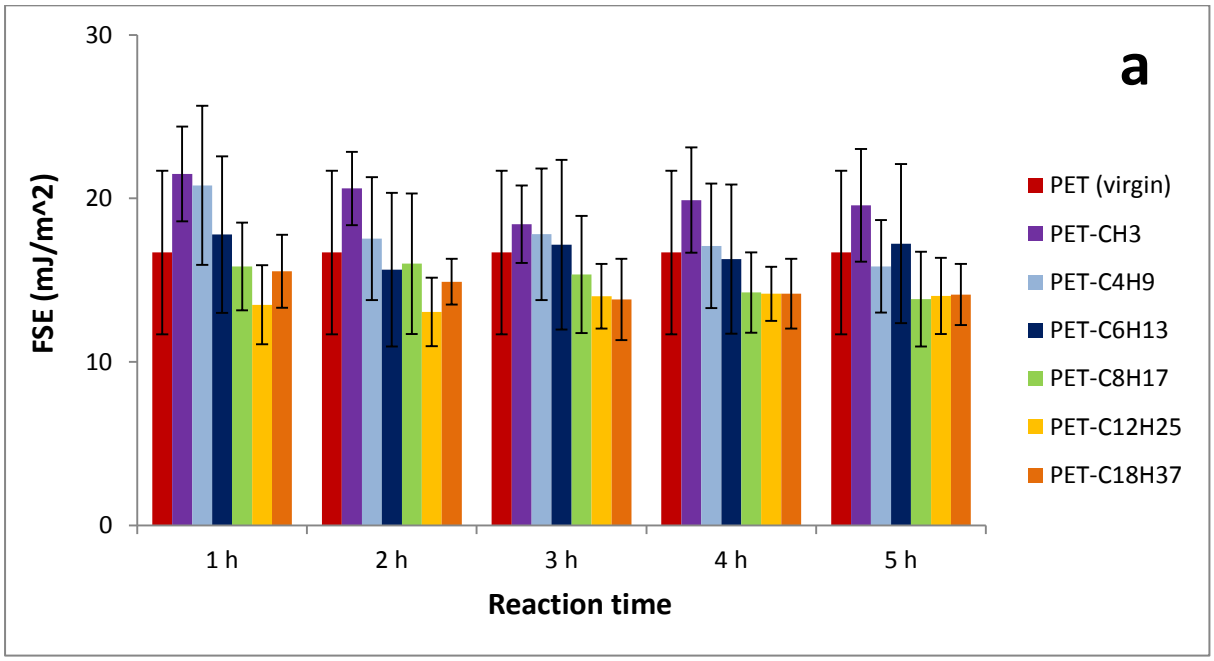

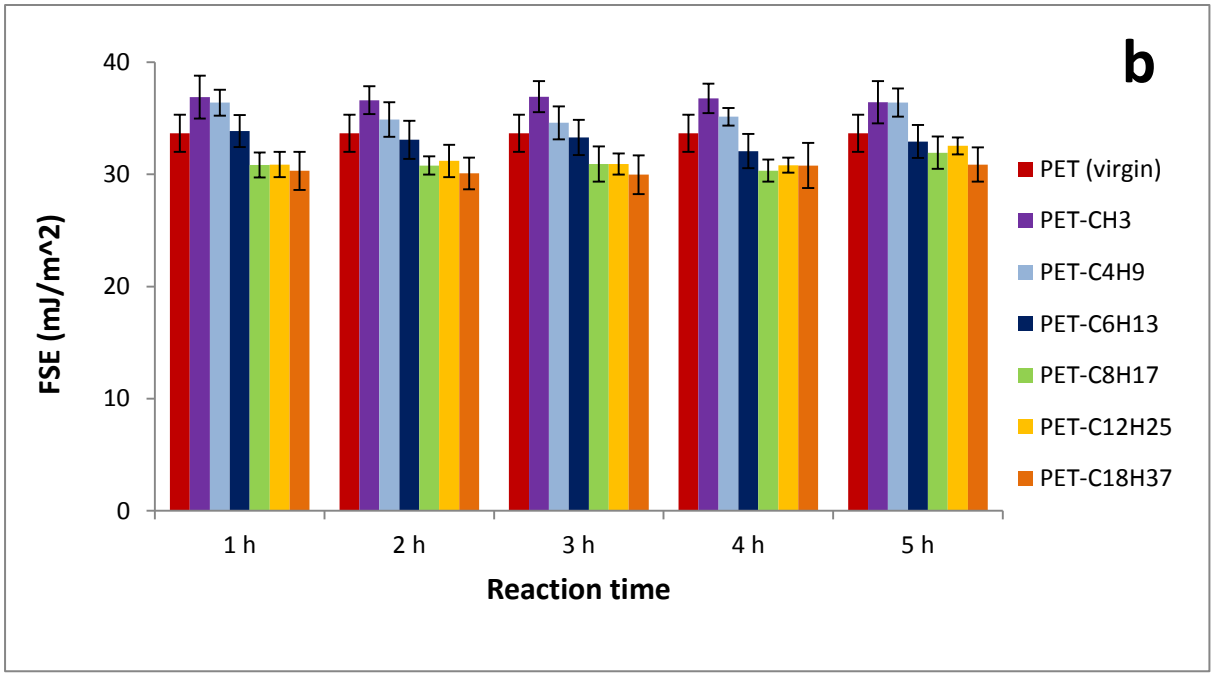

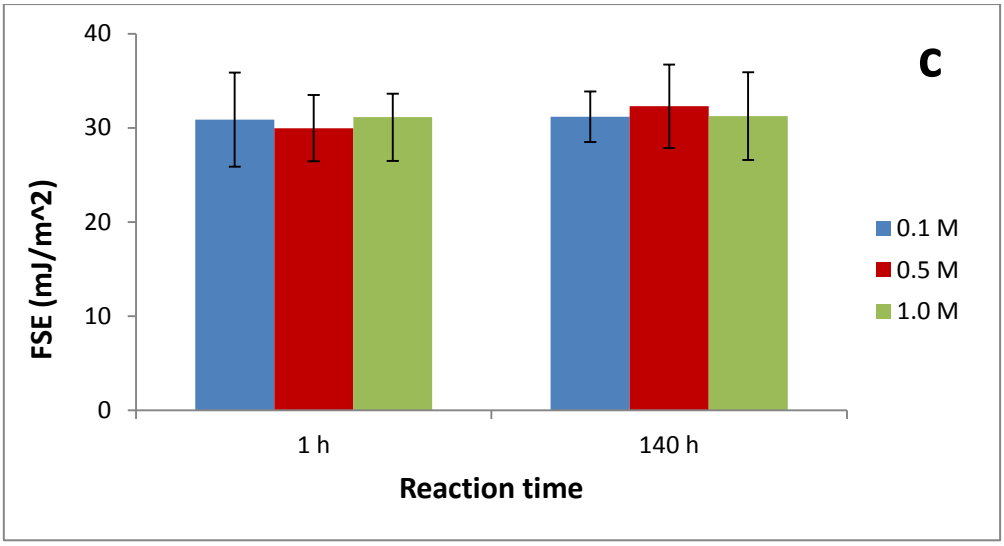

Figure 6: The FSE measurements of virgin and modified PET fabrics **a**); virgin and modified PET foils **b**) and PET–$C_{18}H_{37}$ foils prepared by different $C_{18}H_{37}MgCl$ (G. R.) concentrations with various reaction time.

4.1.2.2. Fluorescence intensity assessments of functionalized PET foils

The analysis of a thin layer chemical composition on the polymer surface is hardly possible by the conventional tools for chemical structural analysis, such as NMR and FT-IR spectroscopy. In that case, fluorescence spectrometry has been reported to be a powerful complementary tool for the surface chemical analysis by coupling dye [141]. Virgin PET, calibrated PET (DNSC treated) and Grignard reagent modified (3 h) PET foils, examined by fluorescence intensity test, revealed that the virgin PET had no reaction with DNSC as the pure PET and DNSC treated PET showed almost same fluorescence intensity, whereas all the functionalized PET foils exhibited much higher fluorescence intensity compared to pure PET. It was interesting to notice that PET–CH_3 showed maximum fluorescence intensity as expected due to the presence of –OH groups with shortest alkyl chain (–CH_3). On the other hand, the fluorescence intensity consistently decreased most probably due to the steric hindrance caused by other bulky alkyl chains. PET–$C_{18}H_{37}$ displayed minimum fluorescence intensity due to the presence of octadecyl (–$C_{18}H_{37}$) group that caused maximum hindrance over –OH groups on modified PET surface and much less activation with DNSC. **Figure 7** shows the fluorescence intensity variations of the PET foils.

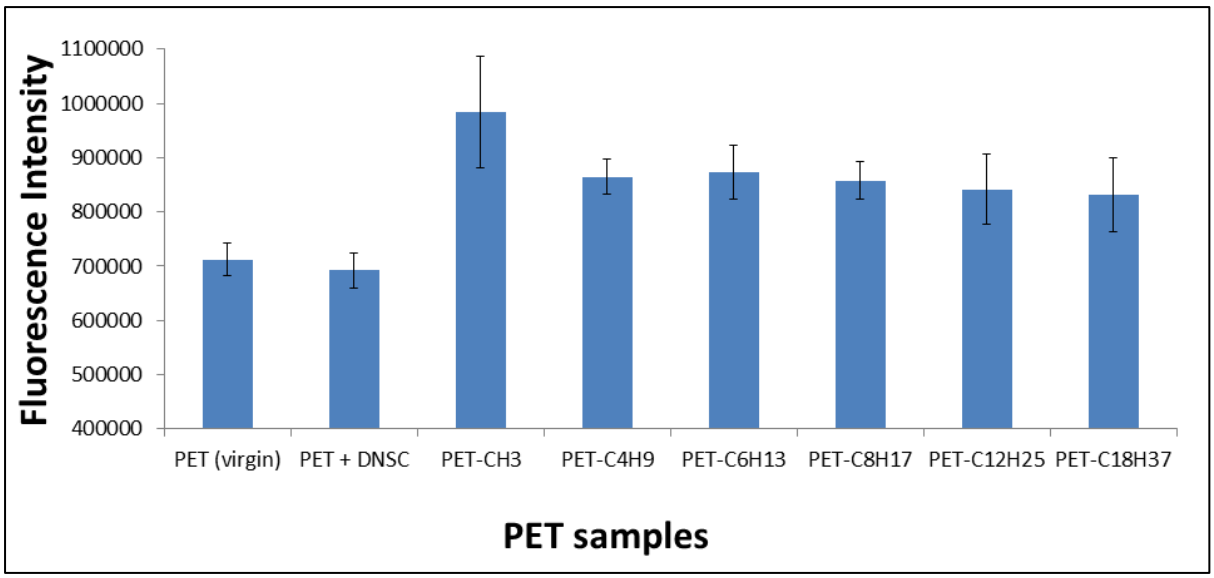

Figure 7: The fluorescence intensity measurements for pure and different Grignard reagent modified PET foils.

4.1.2.3. SEM analyses

Changes in the surface morphology of all prepared samples were observed by SEM **(Figure 8 and 9)** and subsequently by AFM (**Figure 7 and 8**).

The surface modifications of both PET fabric (**Figure 8**) and foil (**Figure 9**) were successfully analysed by SEM. The better results were obtained through the reaction with Grignard reagents having higher number of carbon chains starting from $C_6H_{13}MgBr$. The best modification was achieved by $C_{12}H_{25}MgBr$/ 3 h for both types of samples. Coating was rarely visible on PET–CH_3/ 3 h surface (**Figure 8 b** and **9 b**) whereas PET–C_6H_{13}/ 3 h and PET–$C_{12}H_{25}$/ 3 h samples apparently showed the coating on the surface of both fabric and foil (**Figure 8 c, d** and **9 c, d**)**.** Moreover, a very little corrosion and several pores were identified in the coatings (**Figure 8 c, d** and **9 b, c, d**). Most probably the porosity occurred due to the thickness of the coating, and/ or due to the worse adhesion of the coating to the PET surface. We suggest that all prepared coatings had different thickness in the different parts of the samples. In SEM images analyses, similar results were observed for both fabric and foil modified PET samples. Moreover, AFM was used as another method confirming the changes in surface morphology in detail (**Figure 10** and **11**).

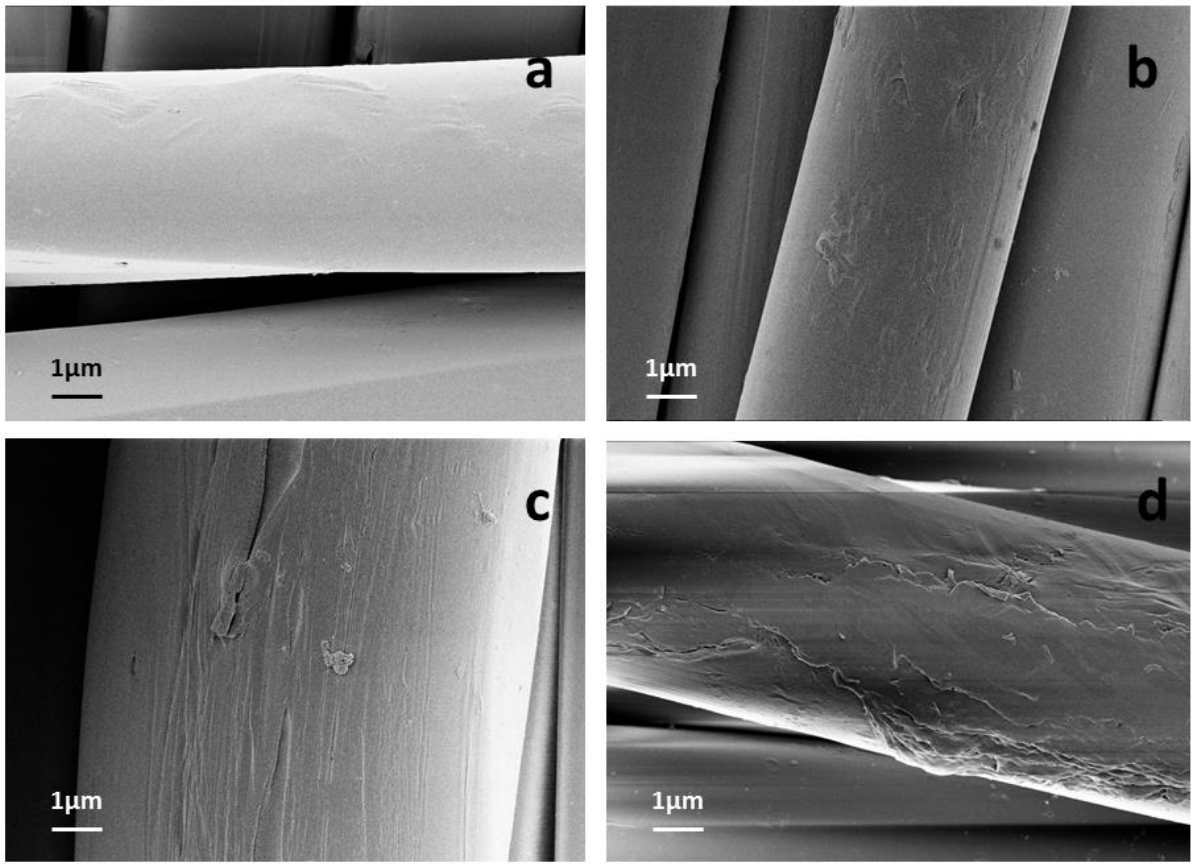

Figure 8: The SEM images of the virgin PET fibres **a**); PET fibres modified with CH_3MgB_r/ 3 h **b**); PET fibres modified with $C_6H_{13}MgBr$/ 3 h **c**) and PET fibres modified with $C_{12}H_{25}MgBr$/ 3 h **d**) in the fabric.

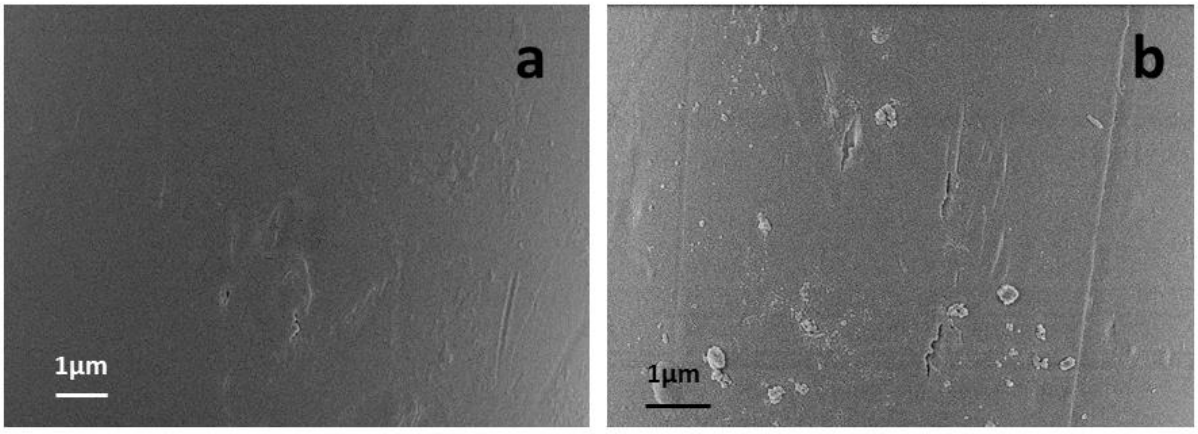

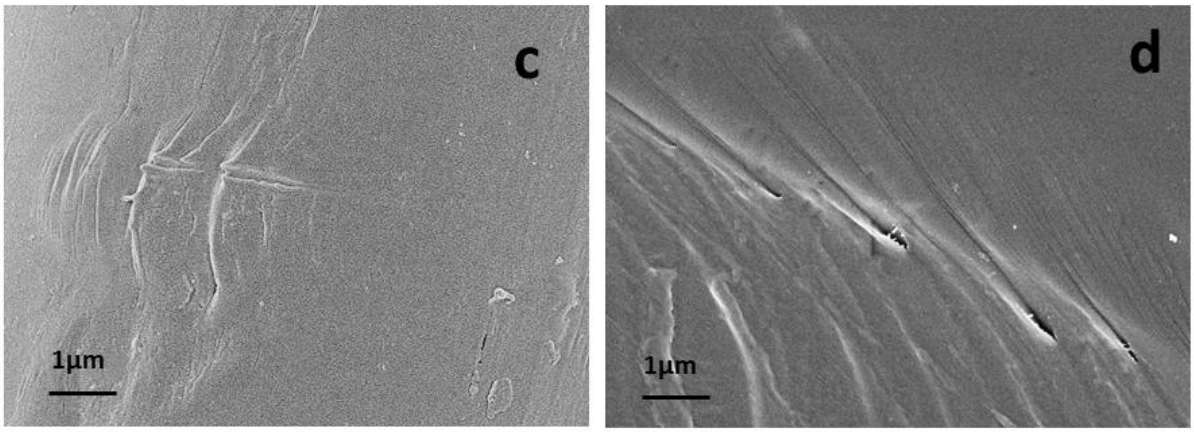

Figure 9: The SEM images of the virgin PET foil **a**); PET foil modified with CH_3MgB_r/ 3 h **b**); PET foil modified with $C_6H_{13}MgBr$/ 3 h **c**) and PET foil modified with $C_{12}H_{25}MgBr$/ 3 h **d**).

4.1.2.4. AFM analyses

The modification of the PET foils was analysed through the changes in the surface roughness (Ra) compared to the unmodified one. The increase in the surface roughness of the modified PET foil was significantly proved by AFM analysis (**Table 1**) with obtained Ra values. **Figure 10** (**a, b, c**) and **11** (**a, b**) showed the changes in the surface topography before and after the modifications. At first, surface topography of an unmodified PET samples (size 9 mm x 6 mm) were studied. The same samples were subsequently kept in 15 ml of diethyl ether for 3 h under argon atmosphere and measured again, in the same area, to examine the swelling effect. Finally, these samples were allowed to react with 15 ml of previously mentioned Grignard reagents (0.1M) with different alkyl groups in diethyl ether in argon atmosphere for 3 h. The changes in the surface topography of PET foil treated with the Grignard reagents were analysed through AFM micrographs again in the same area as in the previous two experiments. It was proved that, surface roughness (Ra) was increased significantly for the Grignard reagent with long alkyl chain (8C, 12C and 18C) treated PET foils compared to the swelled (in diethyl ether) and unmodified samples whereas, short alkyl chain (1C, 4C and 6C) modified PET foils did not demonstrate any noticeable difference in Ra values. The comparative study of Ra values to the virgin, swelled and chemically modified PET foils (PET–C_8H_{17}, PET–$C_{12}H_{25}$ and PET–C18H37) are introduced in the **Table 1**, where two different areas (10 µm x 10 µm and 1 µm x 1 µm) were compared. **Figure 10 (a, b, c)** shows the AFM micrographs obtained from 1 µm x 1 µm area comparing virgin, solvated and modified PET–$C_{12}H_{25}$. **Figure 11 (a, b)** shows the significant differences in surface topography between PET–CH_3 (1 C) and PET–$C_{18}H_{37}$ (18 C) within 10 µm x 10 µm surface area.

Table 1: The surface roughness (Ra) values before and after modification of PET foils.

Samples / Surface Area	Surface roughness (Ra) values				
	PET foil (virgin)	**PET foil (in diethyl ether)**	**PET–C_8H_{17} (modified)**	**PET–$C_{12}H_{25}$ (modified)**	**PET–$C_{18}H_{37}$ (modified)**
(10 × 10) µm^2	6.69 nm	10.09 nm	10.65 nm	18.05 nm	24.30 nm
(1 × 1) µm^2	1.17 nm	1.53 nm	2.11 nm	2.72 nm	10.29 nm

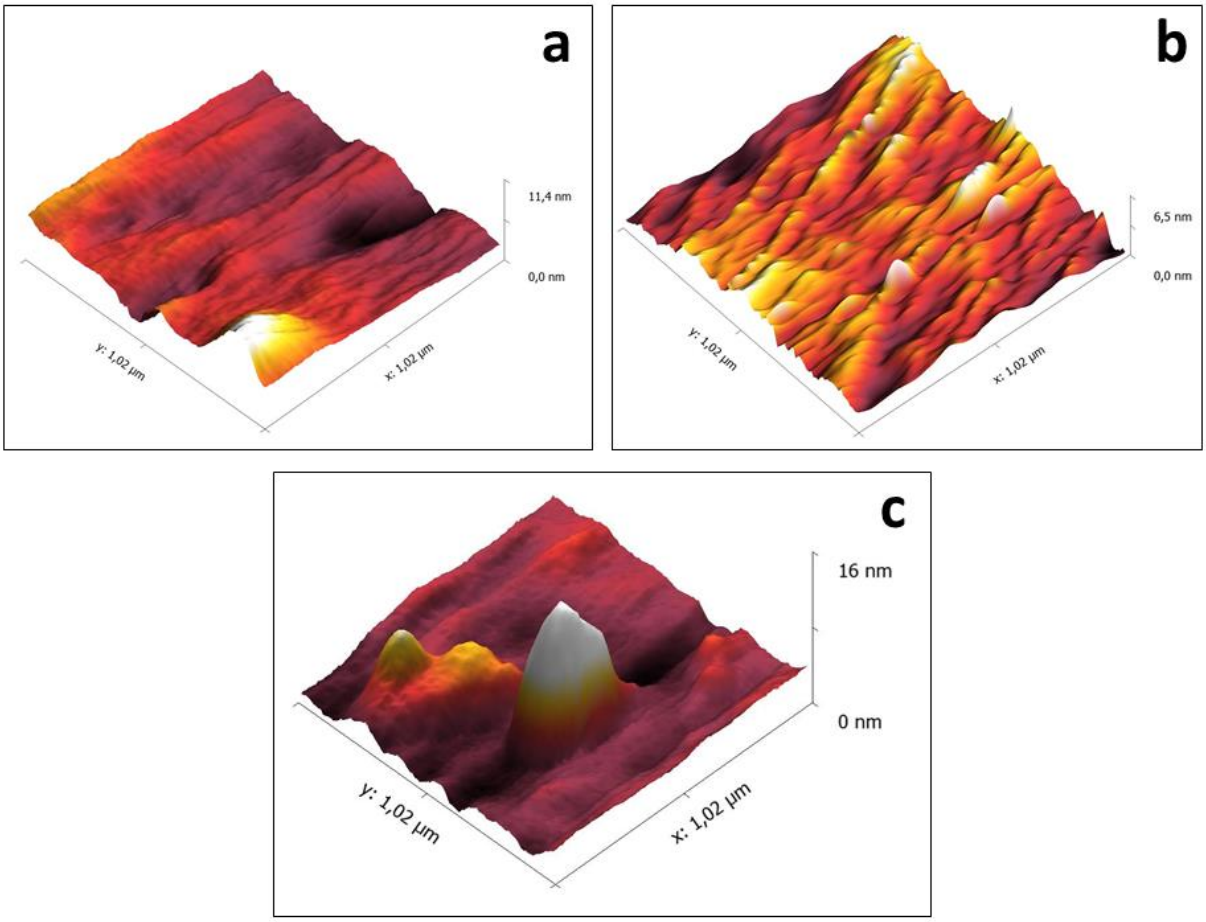

Figure 10: The AFM images (1 x 1) µm^2 of unmodified PET foil **a**); PET foil swelled in diethyl ether for 3 h **b**) and PET foil modified with $C_{12}H_{25}MgBr$ for 3 h **c**).

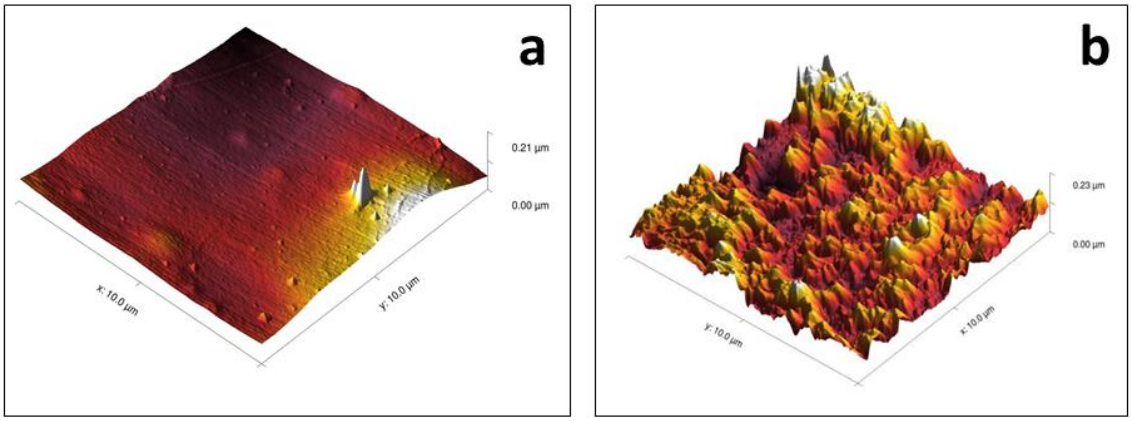

Figure 11: The AFM images (10 X 10) μm^2 of PET foil modified with CH_3MgBr for 3 h **a**) and PET foil modified with $C_{18}H_{37}MgCl$ for 3 h **b**).

4.1.2.5. FT-IR analyses

All pure and functionalized PET foils were characterized by FTIR and the measurement was performed in two different spots. In **Figure 12,** the difference in stretching vibrations of PET–CH_3 and PET–$C_{12}H_{25}$ samples can be clearly seen when compared to the unmodified PET (i.e. 2848 cm^{-1}, 2862 cm^{-1}, 2918 cm^{-1} and 2952 cm^{-1}). The asymmetric and symmetric stretching vibrations of C–H bonds for immobilized alkyl chains (–CH_3 and –$C_{12}H_{25}$) were visible on Grignard reagent modified samples. Interestingly, the PET–$C_{12}H_{25}$ sample showed stronger absorption band than PET–CH_3 sample. Pure PET demonstrated its characteristic stretching vibrations at 2906 cm^{-1} and 2970 cm^{-1} along with the modified ones.

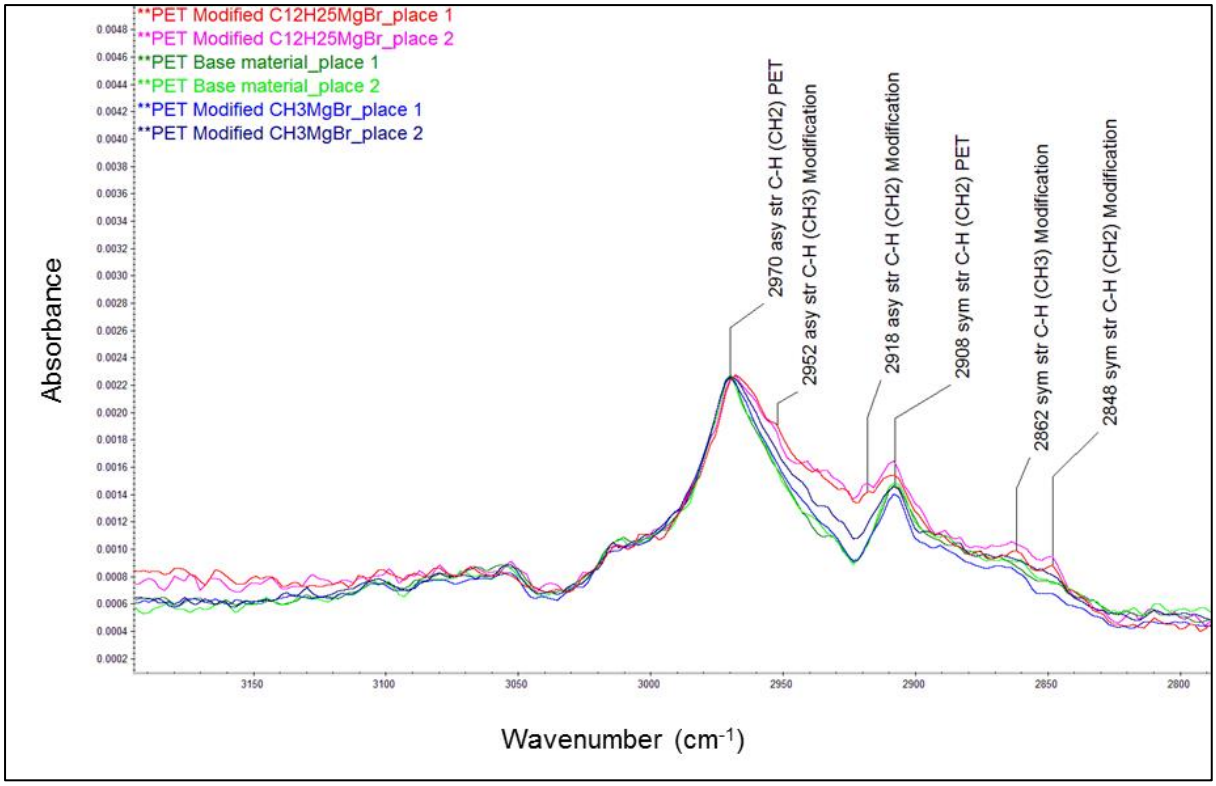

Figure 12: FTIR spectra showing the characteristic peaks of the stretching vibrations of pure PET and alkyl chains (–CH_3 and –$C_{12}H_{25}$) covalently linked to the surface after modifications.

4.1.3. Analyses of antibacterial activity and cell experiments

4.1.3.1. Biofilm assessment of pure and functionalized PET

Biofilm experiments were performed with four pathogenic bacterial strains on the pure PET, PET-CH_3 and PET–$C_{12}H_{25}$ foils. Due to the smooth surface of foils, compare to the rough PET fabrics, the foils only were used for biofilm experiments. Firstly, Gram negative bacteria *Escherichia coli* (*E. coli*) and *Pseudomonas aeruginosa* (*P. aeruginosa*) were tested, followed by Gram positive cocci bacteria and biofilm positive bacterial strains *Staphylococcus aureus* (*S. aureus*) *and* methicillin-resistant *Staphylococcus aureus* (MRSA).

PET–CH_3 and PET–$C_{12}H_{25}$ foils were effective against growth of the *S. aureus,* MRSA *and E. coli* biofilms. Gram negative *E. coli* is rod shaped bacterium proved to be biofilm negative bacterial strain for both the modified PET foils (**Figures 13 b_1 and c_1**). Surprisingly, unmodified PET sample also didn´t indicate biofilm growth (**Figure 13 a_1**). This effect can be attributed to the surface morphology of the tested PET foils. *E. coli* is well known as a bacterial strain, which usually doesn´t have tendency to adhere to the smooth surfaces and form the uniform biofilm there, therefore only individual colonies can be formed

on such a surface. The same effect was observed in all three tested samples (PET, PET–CH_3 and PET–$C_{12}H_{25}$). *P. aeruginosa* was another tested pathogenic bacterial strain. *P. aeruginosa* is a common Gram negative, rod-shaped bacterium and biofilm positive bacterial strain. Thin biofilm layer formed with *P. aeruginosa* was observed in the several parts of the both modified PET samples (**Figures 13 b_2 and c_2**), although the pure PET foil was more vulnerable towards biofilm growth (**Figures 13 a_2**). In this case we suppose, that modification through -CH_3 and -$C_{12}H_{25}$ functional groups was not efficient enough to resist biofilm formation.

Figures 14 b_1 (sample modified with –CH_3) and **14 c_1** (sample modified with –$C_{12}H_{25}$) demonstrated very significant elimination of the *S. aureus* biofilm, compare to the unmodified sample in **Figure 14 a_1**, where the formation of polysaccharide matrix caused by *S. aureus* was clearly visible. It is worth to mention that, the similar results were obtained for MRSA, which belongs to the same bacterial class as *S. aureus* is. Moreover, modified PET samples (**Figures 14 b_2** and **c_2**) tested against *S. aureus* contained only a few individual bacterial colonies on their surface compared to the intensely covered unmodified PET sample (**Figure 14 a_2**).

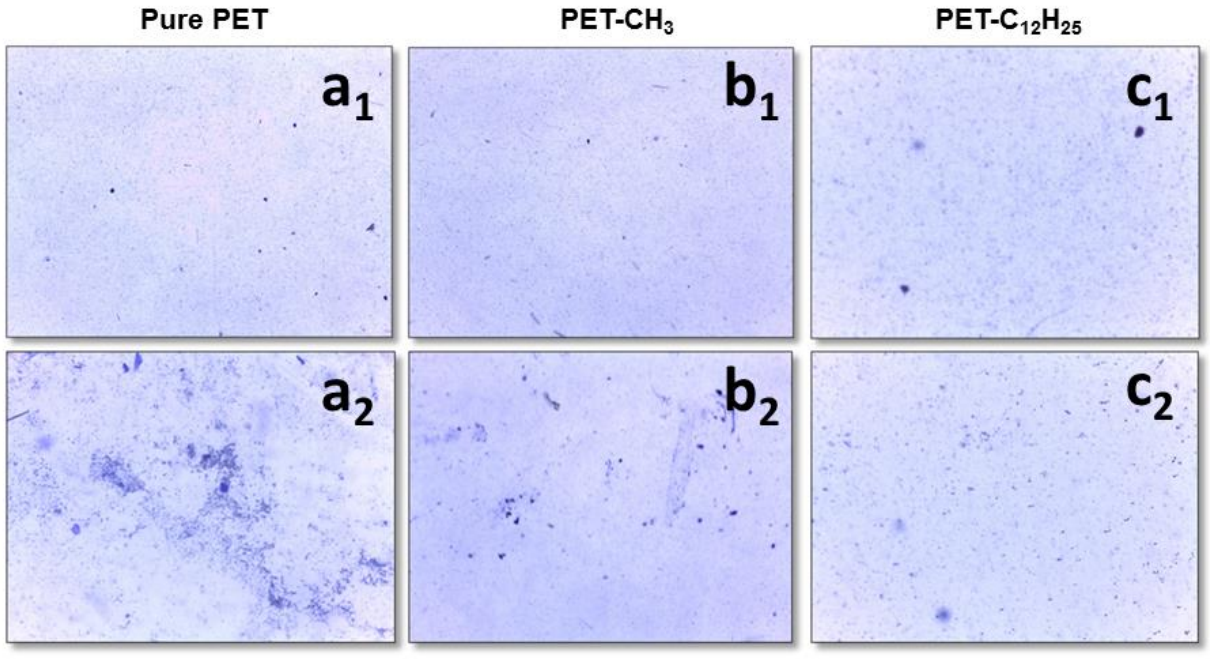

Figure 13: Biofilm tests with *E. coli* for pure PET **a_1**); PET–CH_3 **b_1**); PET–$C1_2H_{25}$ **c_1**) and *P. aeruginosa* for pure PET **a_2**); PET–CH_3 **b_2**); PET–$C1_2H_{25}$ **c_2**) [Magnification 40X].

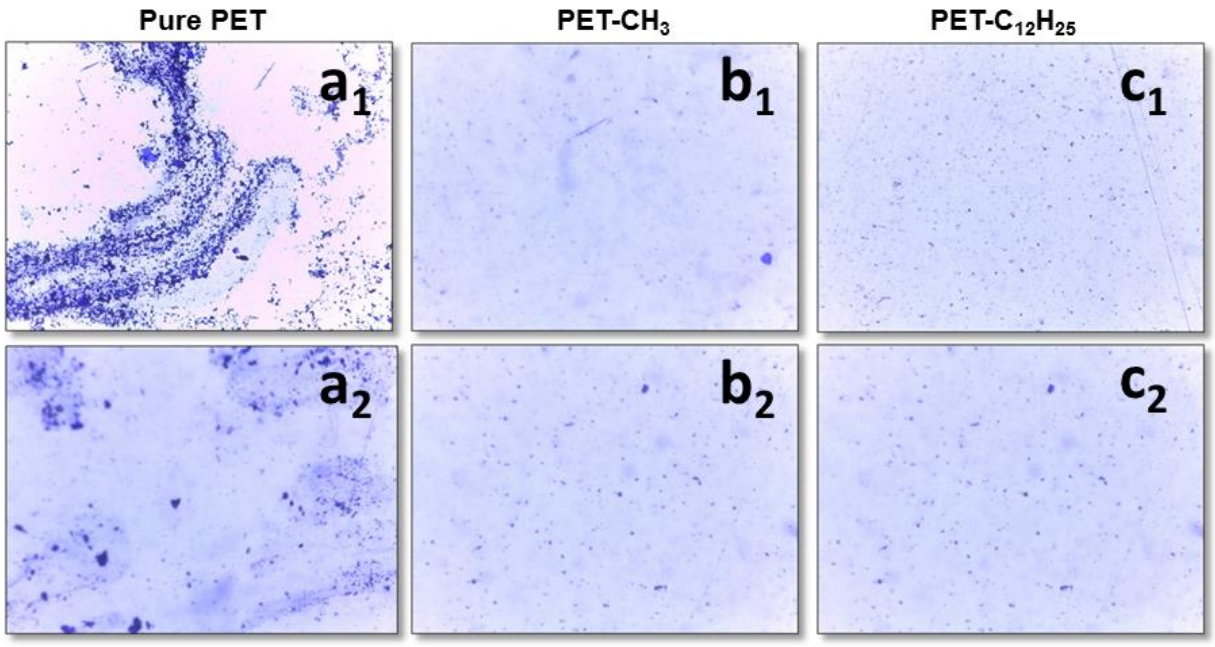

Figure 14: Biofilm tests with *S. aureus* for pure PET **a_1**); PET–CH_3 **b_1**); PET–$C1_2H_{25}$ **c_1**) and MRSA for pure PET **a_2**); PET–CH_3 **b_2**); PET–$C1_2H_{25}$ **c_2**) [Magnification 40X].

The overall experimental results showed that the biofilm inhibition was higher than 90% for both modified PET foils, implemented through Grignard reagents, against *S. aureus,* MRSA and *E. coli*, compared to the 40% inhibition of *P. aeruginosa*. Samples modified with –CH_3 functional groups (PET–CH_3) show in all experiments slightly better results. These samples contained less bacterial colonies compared to the –$C_{12}H_{25}$ modified samples (PET–$C_{12}H_{25}$). However, the difference was only in the units of bacterial colonies, but was observed in all tested and compared samples.

Bacterial adhesion on a surface is very complex and dynamic process. Functional groups on the material surface play important roles in hydrophilicity as well as bacterial adhesion on the surface. Hydroxyl (–OH) and methyl (–CH_3) groups are very common functional groups in biomaterials as these groups are also present in protein structures [26]. The materials' FSEs that were calculated by using the WCAs, significantly influenced the bacterial attachment to the material surface and thus are considered to be one of the major parameters [152]. Wide scientific studies reported that FSE between 23 and 30 mJ/ m^2 was related to the lowest bacterial adhesion [153]. Both modified PET foils had FSE between 31 and 37 mJ/ m^2 (**Figure 6 b**), yet the modified PET had effective functional groups to reduce bacterial attachment to the PET surface.

4.1.3.2. Cytocompatibility assessment of pure and functionalized PET

Polymeric materials that come in contact with the human body are expected to perform their intended functions without resulting in any adverse effect to a patient. Potential adverse effects can range from short-term (acute) to long-term (chronic) adverse effects to the body. From this point of view, polymeric medical devices are typically subject to biocompatibility testing to assess the interaction between a device and tissue, cells or body fluids of the patient. Tests performed within this study are related primarily to the acute toxicity evaluation.

Table 2: The results of cytotoxicity test (cell viability calculated as percentage of metabolic activity of the cell population) in direct contact performed on 3T3 fibroblasts *in vitro*

SAMPLES	ABBREVIATIONS	NC as blank		PET foil as blank	
		MEAN (%)	S.D. (%)	MEAN (%)	S.D. (%)
Cell control	**CC**	110.80	7.97	113.25	8.15
Positive control	**PC**	8.15	1.59	8.33	1.63
Negative control	**NC**	100.00	9.33	102.21	9.54
Unmodified foil	**PET foil**	97.84	8.83	100.00	9.03
Methyl-treated foil	**PET-CH_3 (3h)**	96.82	10.36	98.96	10.59
Dodecyl-treated foil	**PET-$C_{12}H_{25}$ (3h)**	93.19	6.92	95.24	7.07

The results showed that both types of the modified samples reached viability of the exposed cells higher than 70% compared to the cell control (CC) as a blank (**Figure 15**). Methyl-treated foil PET–CH_3 (3 h) reached viability (87.38%) of CC and the dodecyl-treated foil PET–$C_{12}H_{25}$ (3 h) reached viability (84.10%) of CC. According to these results, both the samples were proved to be cytocompatible. The possible influence of mechanical damage was evaluated using certain PET foil. Using negative control (NC) as a blank for viability calculation the effect of mechanical damage of the cell layer was proven resulting in about 10% decrease of cell viability per sample. Using the unmodified PET foil as a blank for the viability calculation it was shown that both the surface treatments performed have a minimal impact on the 3T3 cells viability. The PET–CH_3 (3 h) reached viability (98.96%) of pure PET foil and the PET–$C_{12}H_{25}$ (3 h) reached viability (95.24%) of unmodified PET foil. Complete results of cell viability are mentioned in **Table 2**.

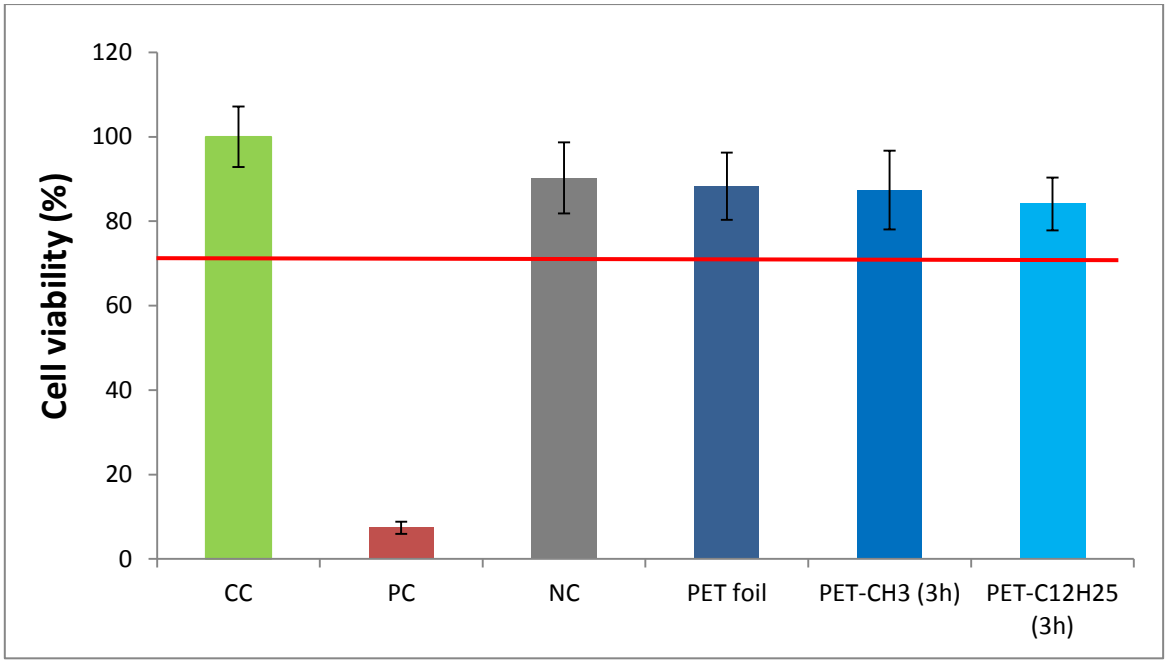

Figure 15: The results of the cytotoxicity test compared to cell control (CC) as a blank. Line (-) on 70% of cell viability represents limit established as the minimal value for biocompatibility assessment.

4.1.3.3. Cell adhesion of pure and functionalized PET

Both tested samples exhibited decreased cell adhesion in comparison to pure PET foil (**Figure 16**). Better adhesion by the 3T3 cells/ cm^2 of PET–CH_3 (mean value = 12254) in comparison to the PET–$C_{12}H_{25}$ surface (mean value = 10593) can be attributed to the different surface energy and morphology. Application of the dodecyl group modification led to decrease of the adhered cells/ cm^2 of the surface. In the both cases, modified surfaces contain hydrophilic –OH groups together with hydrophobic –CH_3 or –$C_{12}H_{25}$ groups. Therefore, the accessibility of the -OH groups the most probably played an important role in the adhesion of the cells together with the resulted biocompatibility of both the functionalized surfaces (PET–CH_3 and PET–$C_{12}H_{25}$). For PET–CH_3 hydroxyl (–OH) groups were accessible easily, whereas long dodecyl groups on the surface of PET-$C_{12}H_{25}$ samples could cover the hydrophilic hydroxyl groups and led to reduced protein adsorption and cell adhesion. Mentioned conclusions are supported by the morphology of adhered cells analysed by fluorescence microscopic images (**Figure 17**). It was evident that the surface modification not only exhibited reduction of the cell adhesion but also affected morphology of the 3T3 cells in terms of shape and size. In the case of the pure PET foil, well spread cells were observed (**Figure 17 a_1 – a_3**). In both cases of modifications, the surface treatment led to reduction of the cell size as smaller and less spread cells were observed. This effect was

most apparent on the PET–$C_{12}H_{25}$ surface (**Figure 17 c_1 – c_3**) and can be attributed to the previously mentioned changed in surface chemistry and morphology.

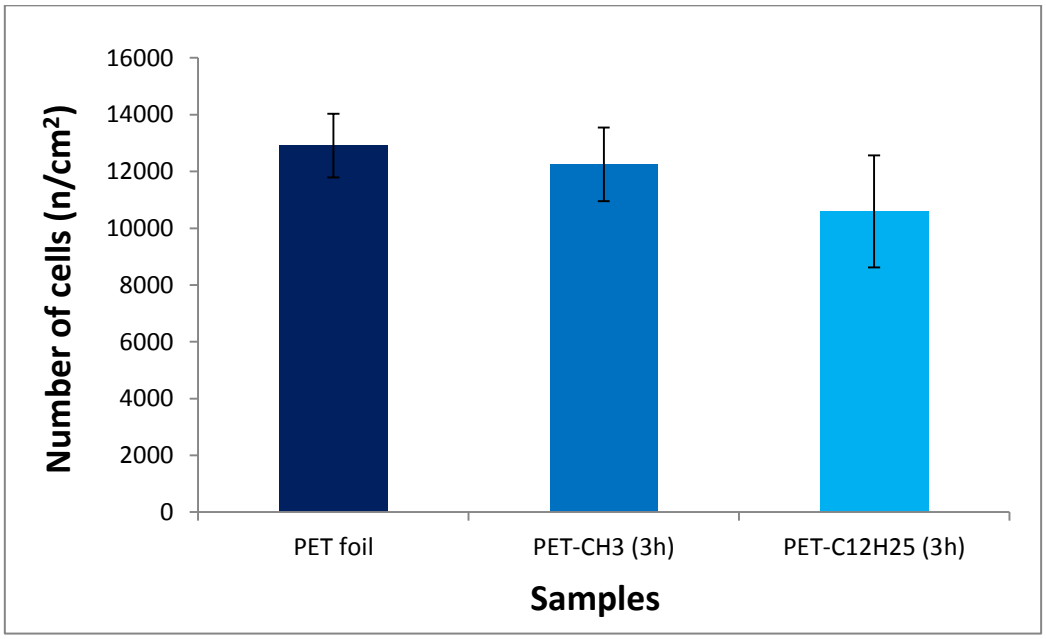

Figure 16: Results of cell adhesion test showing number of cells adhered to the surface of tested samples in 24 h. Results (MEAN ± S.D.) are given in number of 3T3 cells/ cm^2 of the sample.

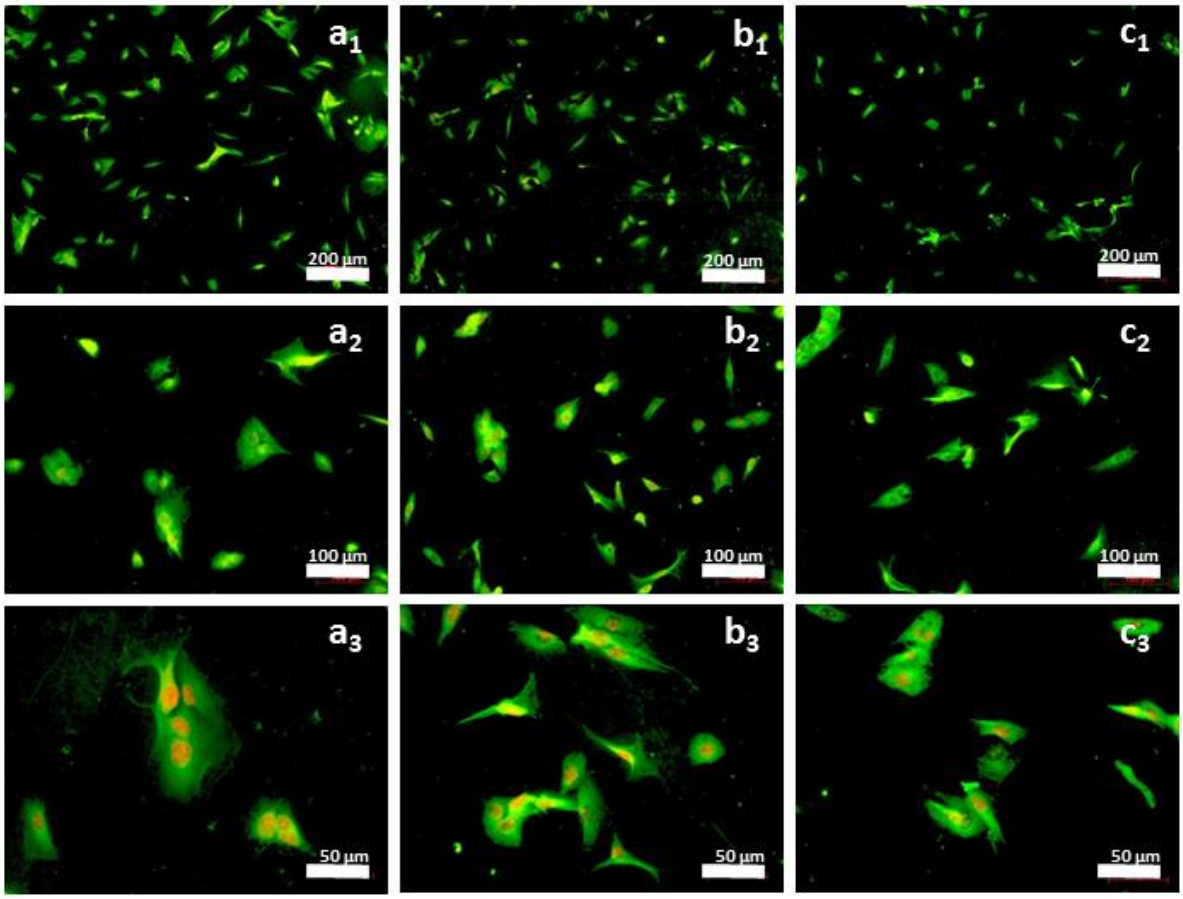

Figure 17: Results of fluorescent microscopic analysis showing morphology of 3T3 cells after 24 hours of adhesion to the pure PET foil **a_1 - a_3**); PET–CH_3 (3 h) foil **b_1 – b_3**) and PET–$C_{12}H_{25}$ (3 h) foil **c_1 – c_3**) [Magnifications 100X, 200X and 400X].

A number of polymer surface parameters; such as morphology, roughness, WCAs or hydrophilicity/ hydrophobicity, FSEs, along with surface chemical composition; are responsible for biocompatibility and cell adhesion [154,155]. Moreover, no significant correlation has been found between the WCAs as well as wettability parameters or the FSE parameters and cell proliferation characteristics in spite of various investigations by many researchers [154]. No clear correlation between FSEs/ WCAs results and cell adhesion were found by this study.

4.2. Nylon 6

4.2.1. Nylon 6 surface modification

4.2.1.1. General mechanisms for amides: reduction followed by N-alkylation and grafting

The mechanisms for reduction of amide to amine, *N*-alkylation of amine using *t*-BuOK for amine group ($–NH_2$ or >NH) activation and grafting of $PEG–CH_3$ via lithiation are shown in **Figure 18** (**a**, **b**, **c**). In case of amide reduction to amine (**Figure 18 a**), the Lewis basic carbonyl groups in amides form complex with the empty p orbital of the Lewis acidic borane (BH_3). Hydride transfer is then occurred from anionic boron to electrophilic carbon. The resulting tetrahedral intermediates collapse to an iminium ion that is reduced again by the borane [156]. Here, a model amide ($R–CO–NH_2$) has been used to explain the reduction mechanism. **Figures 18 b** and **c** depict the common nucleophilic substitution reactions that take place with amines for *N*-alkylation and grafting respectively. Moreover, *t*-BuOK and *t*-BuLi activate the amine group for *N*-alkylation and grafting respectively. For both the mechanisms, a model primary amine ($R–CH_2–NH_2$) has been used.

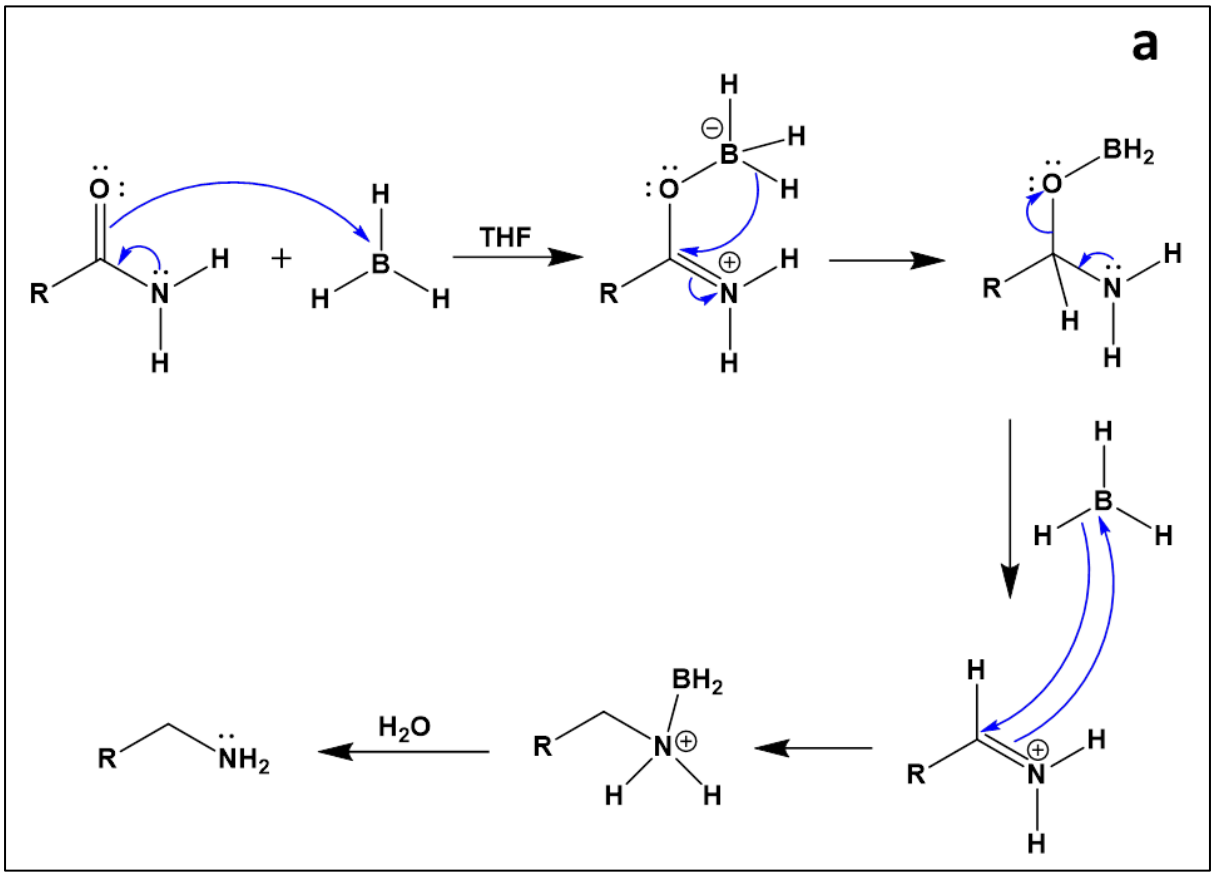

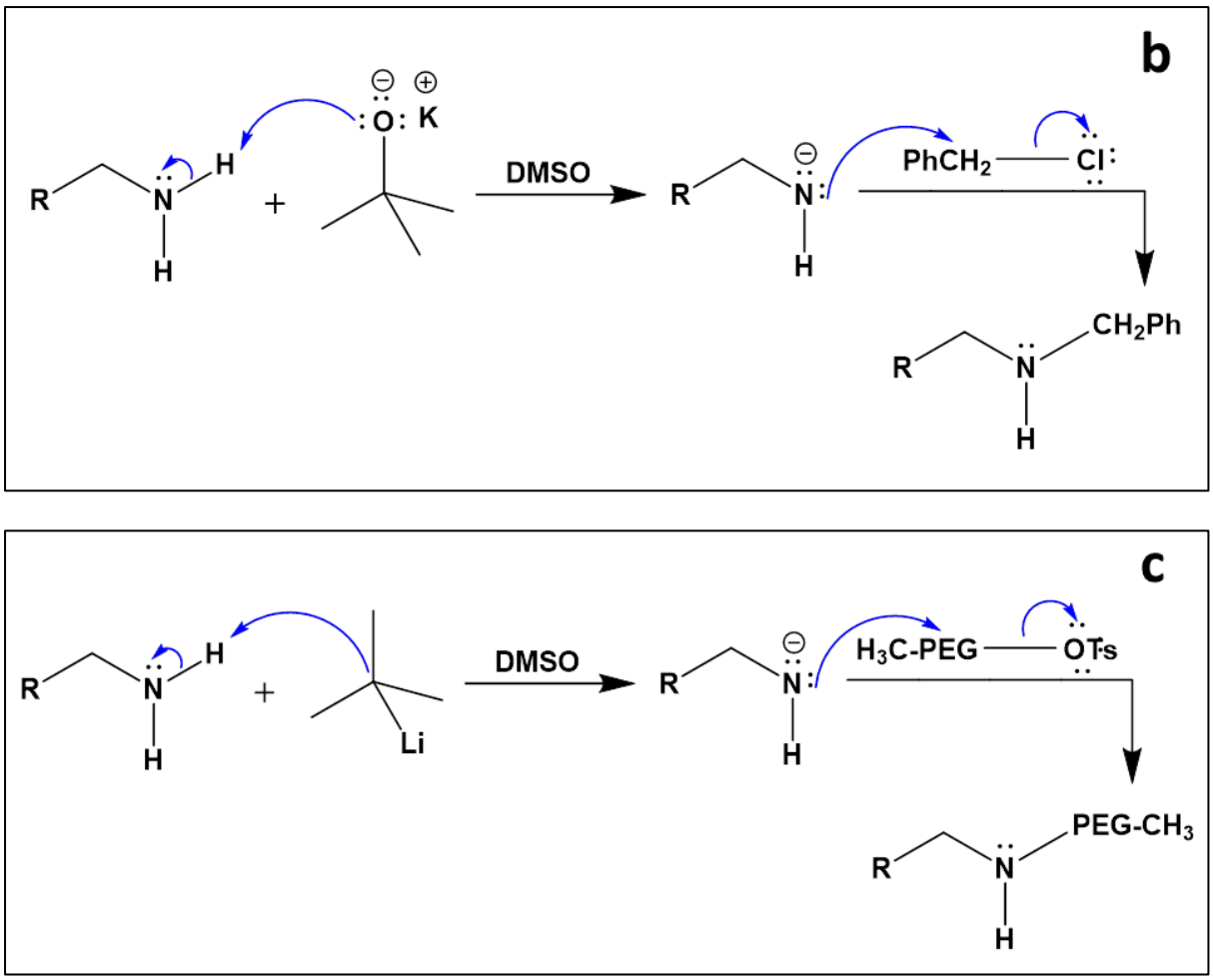

Figure 18: The general mechanisms for reduction of amide to amine **a**); *N*-alkylation of amine using *t*-BuOK **b**) and grafting of PEG–CH_3 via lithiation **c**).

4.2.1.2. Reduction, N-alkylation and grafting of Nylon 6

The reduction of amide (–CONH–) functional groups on Nylon 6 surface to secondary amine (–CH_2NH–) on Nylon 6-NH using borane-tetrahydrofuran (BH_3-THF) complex, followed by *N*-alkylation reaction of Nylon 6-NH with benzyl chloride ($C_6H_5CH_2Cl$) in presence of potassium *t*-BuOK forming Nylon 6-NCH_2Ph are shown in **Scheme 3 a**. The Nylon 6-NH surface grafted with H_3C-PEG-OTs via lithiation is proposed on the right hand side of the **Scheme 3 a**. The *N*-alkylation can be considered as the conversion confirmation of Nylon 6 to Nylon 6-NH. Nylon 6-NH, washed with 1 M HCl, prohibits any side reaction during modified samples storage. **Scheme 3 b** shows the pictorial representation of Nylon 6 surface modification.

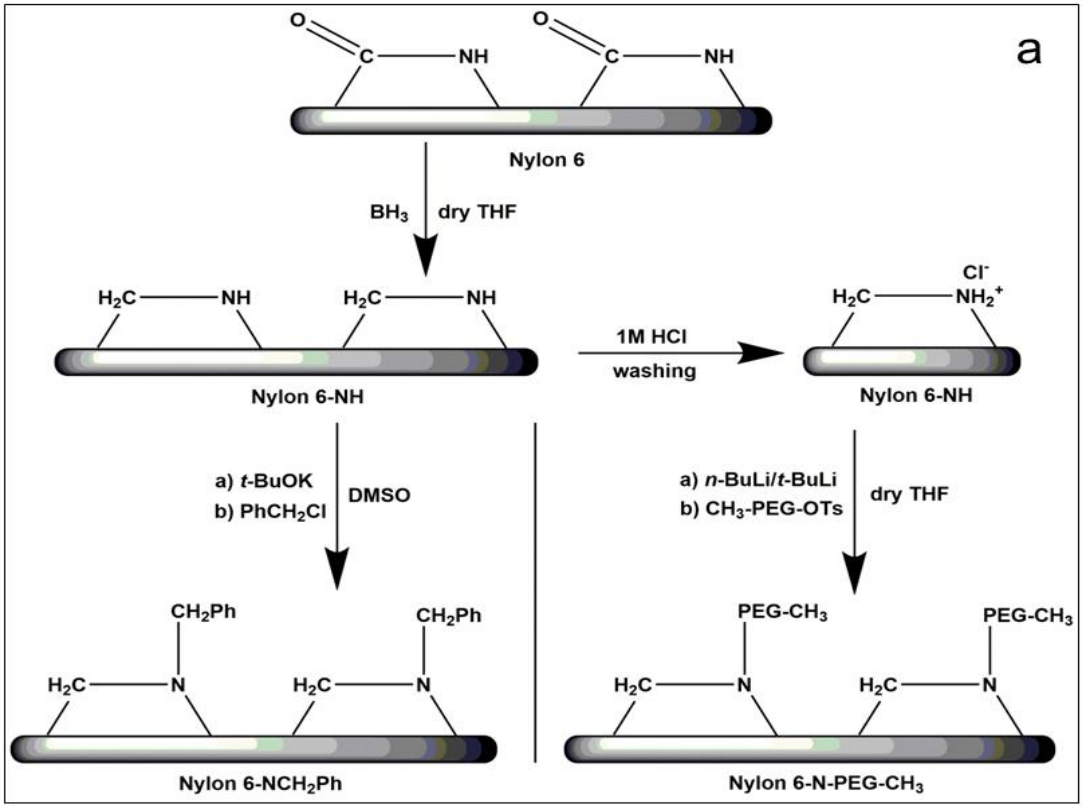

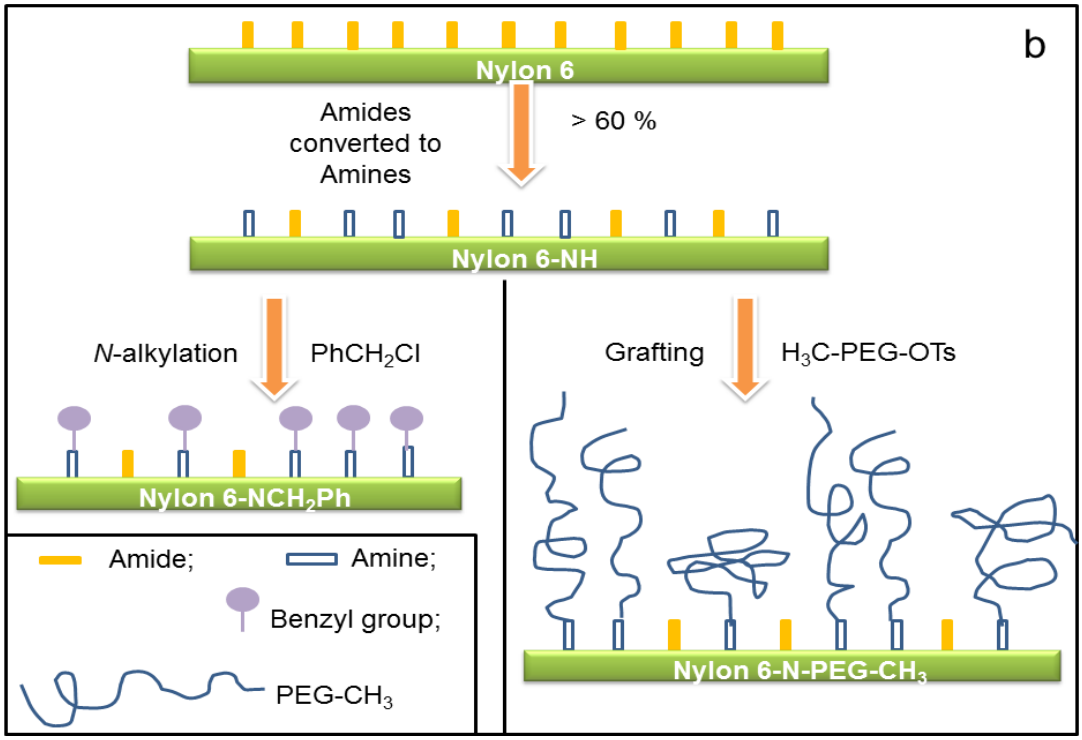

Scheme 3: Conversion of Nylon 6 into Nylon 6-NH, followed by *N*-alkylation to form Nylon 6-NCH_2Ph and grafting on Nylon 6-NH by H_3C-PEG-OTs to form Nylon 6-N-PEG-CH_3 **a**); Pictorial representation of Nylon 6 surface modification **b**).

4.2.1.3. Tethering of PEG on Nylon 6-NH surface by conjugating DSC

N,*N*′-disuccinimidyl carbonate (DSC) is the smallest homo-bifunctional *N*-Hydroxysuccinimide (NHS) ester crosslinking reagent that is highly reactive toward nucleophiles [142]. DSC can activate both hydroxyl (–OH) and amine ($–NH_2$ and >NH) groups. DSC undergoes rapid hydrolysis in aqueous solution and therefore anhydrous organic solvents are needed to be used during the treatments. **Scheme 4** shows the two-step preparation protocol for immobilizing PEG on the Nylon 6-NH surface by activating the secondary amine groups on the surface first via DSC. The amine activated surface is named as Nylon 6-N-SC and the PEG tethered final surface is Nylon 6-N-PEG.

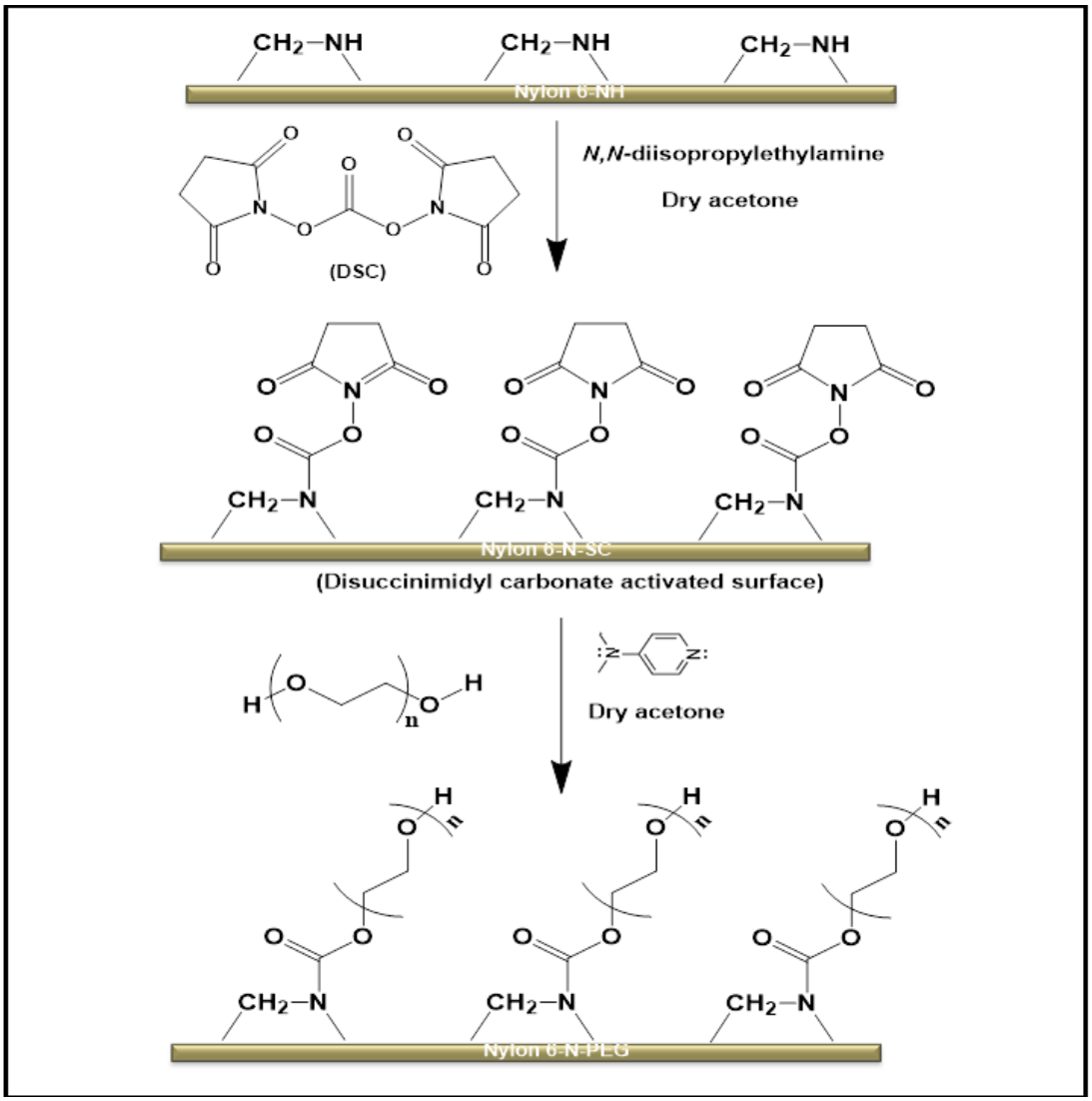

Scheme 4: Preparation of PEG tethered Nylon 6-NH surface (Nylon 6-N-PEG) via DSC.

4.2.1.4. Deposition of Cu NPs on grafted Nylon 6 (Nylon 6-N-PEG-CH_3) surface

The Cu NPs stabilized with SDS were physically adsorbed on the Nylon 6-N-PEG-CH_3 (2 h lithiation, 1 ml *t*-BuLi) surface (**Scheme 5**). SDS could be highly solvated in pure water and therefore, it provided steric hindrance between SDS capped Cu NPs dispersed in an aqueous phase [157]. This quality allowed for the production of stable Cu NP dispersions with a strong affinity to a broad range of surface immobilized with polar poly(ethylene glycol) methyl ether (PEG-CH_3) that allowed the nanoparticles to physisorb onto a range of interfaces .

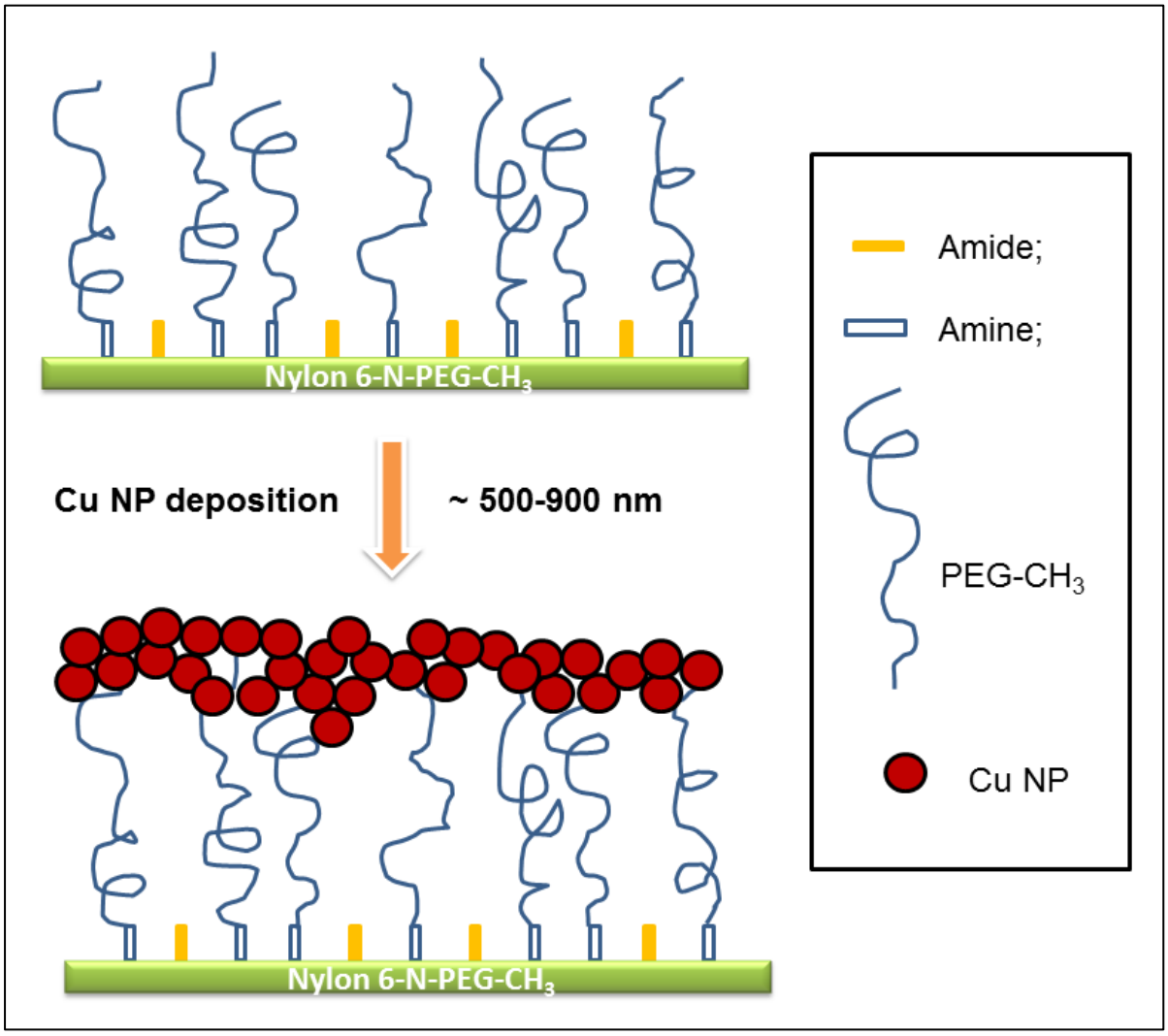

Scheme 5: Schematic diagram of physical adsorption with SDS stabilized Cu NPs on Nylon 6-N-PEG-CH_3 surface.

4.2.2. Characterization

4.2.2.1. WCA and FSE analyses of pure and modified Nylon 6 samples

The WCAs measurements related to the unmodified and modified films are presented in **Figure 19 (a, b)**. The significant increase in WCAs mean by 11° after Nylon 6 films modification into Nylon 6-NH indicated the surface alteration [158]. Further Nylon 6-NH conversion into Nylon 6-NCH_2Ph increased the mean WCAs by 11° and 12° for 1 h and 3 h reactions respectively due to the benzyl group insertion to the Nylon 6-NH surface. DSC activated Nylon 6-N-PEG surface (mean WCA ~ 52°) made the Nylon 6-NH films more hydrophilic by tethering PEG chains [57]. The deposition of Cu NPs made Nylon 6-N-PEG-CH_3-Cu surface significantly hydrophobic and the WCA was increased to 124° (**Figure 19 a**). The mean WCAs decreased significantly after grafting with H_3C-PEG-OTs. The WCA differences between Nylon 6-NH and grafted Nylon 6-N-PEG-CH_3 films, after 2 h lithiation using 0.6 ml, 1 ml and 2 ml *t*-BuLi, were 37°, 36° and 22° respectively. This observation claimed that the modified Nylon 6 films become more hydrophilic, a property due to the ability of PEG chains to engage in hydrogen bond interaction with surrounding water molecules [159]. An interesting point was that, the H_3C-PEG-OTs grafted Nylon 6-NH films via 4 h, 6 h and 24 h lithiation become less hydrophilic than H_3C-PEG-OTs grafted Nylon 6-NH via 2 h lithiation with a particular *t*-BuLi concentration. Nylon 6-N-PEG-CH_3 films, which were obtained by different reaction times, using 0.6 ml and 2 ml *t*-BuLi, were correlated significantly with respect to *t*-BuLi concentration and lithiation reaction time. Although Nylon 6-N-PEG-CH_3 films procured by using 1 ml *t*-BuLi showed more hydrophilicity than expected with the lithiation time increase (**Figure 19 b**). The hydrophilicity decrease together with the reaction time and *t*-BuLi concentration increase may be explained by the grafting intensity (due to the higher surface activation) that was provided by SEM analyses (**Figure 21 e, f, g**). The WCAs did not depend on grafting reaction time (2 h, 4 h, 6 h and 15 h) with H_3C-PEG-OTs. In a compliance with several analyses we concluded that, 2 h reaction time was sufficient for the grafting. It is worth to be mentioned that, Nylon 6 polymer swelling may have played a role for surface activation together with the lithiation reaction time.

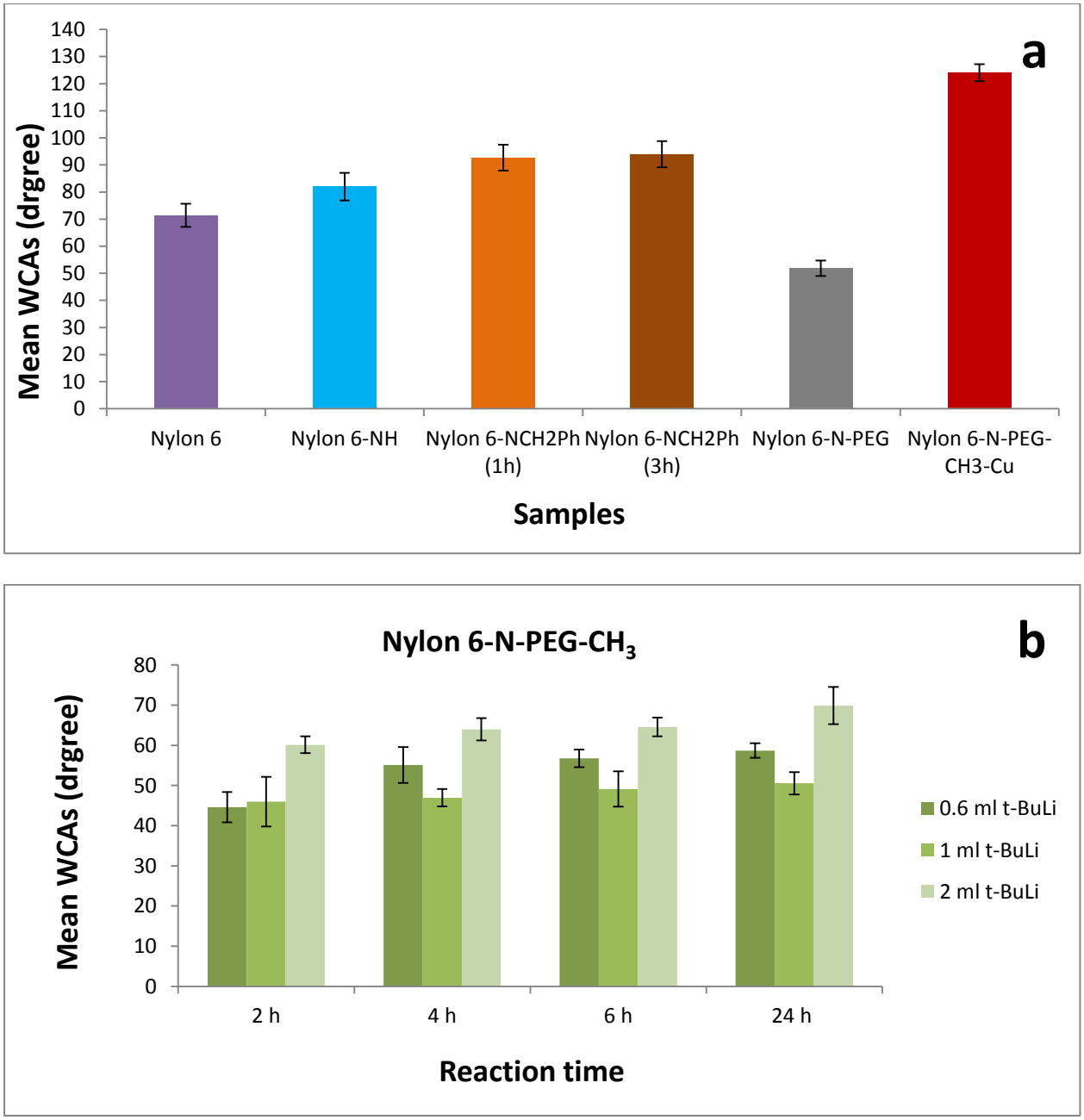

Figure 19: The mean WCA data for pure and modified Nylon 6 films **a**) and Nylon 6-N-PEG-CH_3 after grafting at various conditions **b**).

The FSEs decreased consecutively after Nylon 6 reduction to Nylon 6-NH and further modification to Nylon 6-NCH_2Ph (1 h, 3 h) as the mean WCAs increased after modification of Nylon 6. There was a significant change in FSE value after tethering PEG on Nylon 6-NH surface via DSC to form Nylon 6-N-PEG (**Figure 20 a)**. As the PEG immobilization made the surface more hydrophilic, the FSE was enhanced significantly (33.36 mJ/ m^2 to 52.26 mJ/ m^2). Again, the FSE was reduced (10.26 mJ/ m^2) in case of hydrophobic Nylon 6-N-PEG-CH_3-Cu due to the presence of Cu NPs on the surface. The grafted Nylon 6-N-PEG-CH_3 showed expected hydrophilicity due to the presence of PEG-CH_3 chains. Moreover, the

hydrophilicity of the grafted surface depends on the fact how densely the surface is packed with PEG-CH_3 chains. Terminal -CH_3 groups increase seems to be the reason for decreasing the hydrophilicity. As a consequence, the FSEs increased significantly in case of Nylon 6-N-PEG-CH_3 compared to Nylon 6-NH; but vary with the alteration of *t*-BuLi concentration and reaction time. The FSE values of grafted Nylon 6-N-PEG-CH_3 are shown in **Figure 20 b**.

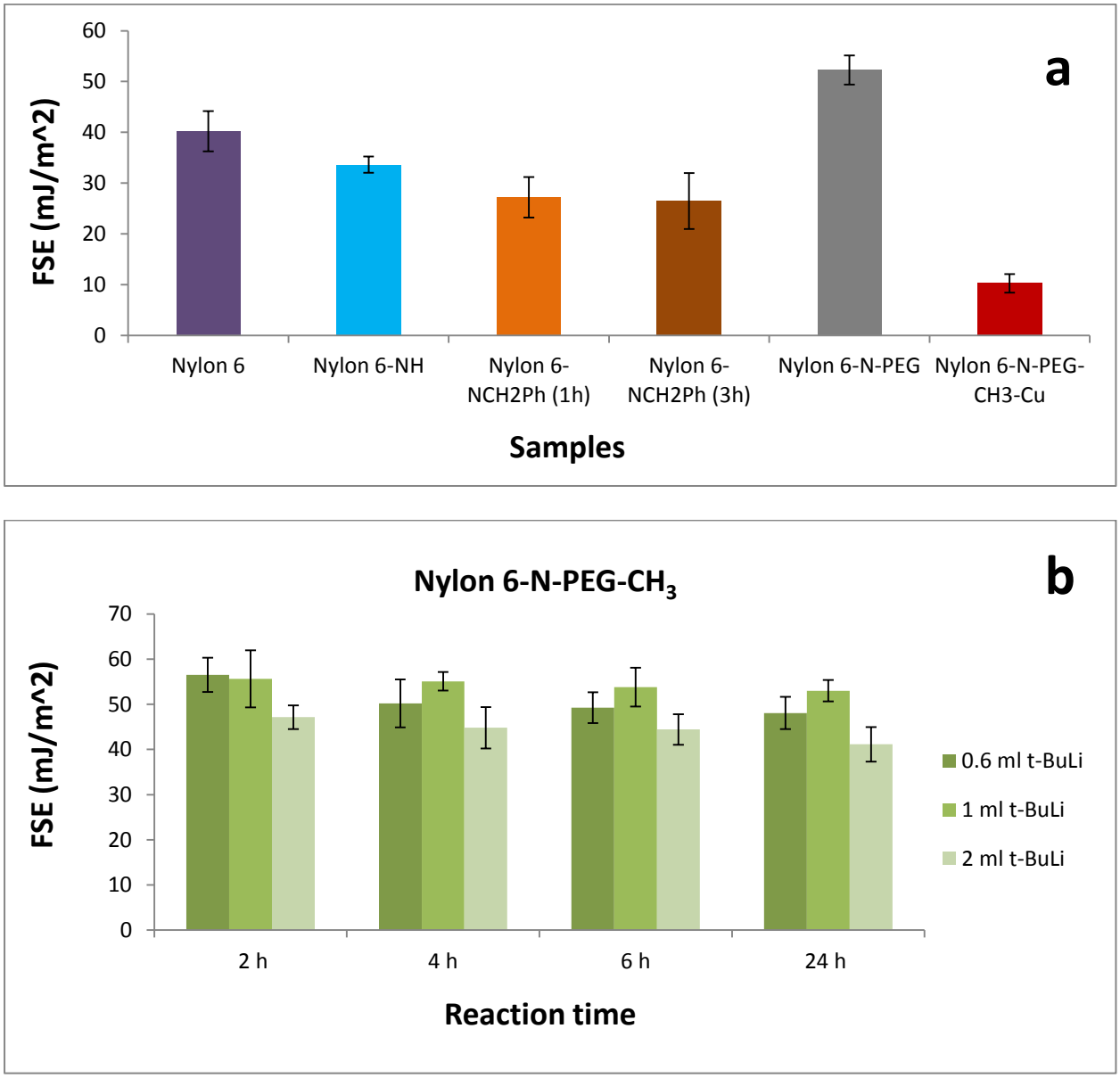

Figure 20: The FSE values for pure and modified Nylon 6 films **a**) and Nylon 6-N-PEG-CH_3 after grafting at various conditions **b**).

4.2.2.2. SEM analyses

Surface morphologies observed by SEM images for unmodified and modified samples, revealed that the surfaces of Nylon 6 and Nylon 6-NCH_2Ph samples are uneven compared to Nylon 6-NH (**Figure 21 a, b, c**), which were further confirmed by AFM analyses (**Table 3**). SEM analysis clearly demonstrated that Nylon 6-NCH_2Ph surface has formed a layer on the Nylon 6-NH surface (**Figure 21 c**). The uniform layer was seen for the PEG tethered Nylon 6-N-PEG (**Figure 21 d**). The image of Nylon 6-N-PEG-CH_3-Cu surface confirmed the presence of Cu NPs. The nanoparticles, prepared by our standard protocol, were distributed on the surface and the sizes were ranged from 500 – 900 nm. In case of H_3C-PEG-OTs grafting on Nylon 6-NH, the SEM images supported successful grafting as the formed layers can be identified on the Nylon 6-NH surfaces (**Figure 21 e, f, g**). The Nylon 6-NH films, modified with 2 lithiation reaction by the different *t*-BuLi concentrations (0.6 ml, 1 ml and 2 ml) were compared with aim to show significant changes occurring on the surface. Moreover, Nylon 6-N-PEG-CH_3 (2 h lithiation, 2 ml *t*-BuLi) showed denser grafting layer on the surface than Nylon 6-N-PEG-CH_3 (2 h lithiation, 0.6 ml *t*-BuLi) and Nylon 6-N-PEG-CH_3 (2 h lithiation, 1 ml *t*-BuLi). No significant differences were noticed in the SEM images of Nylon 6-N-PEG-CH_3 samples produced by various lithiation time keeping the *t*-BuLi concentration constant.

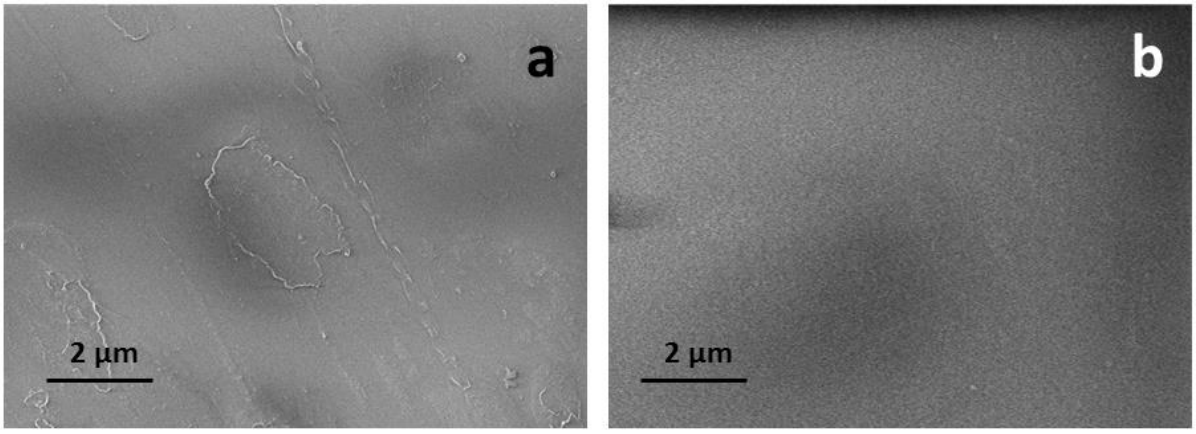

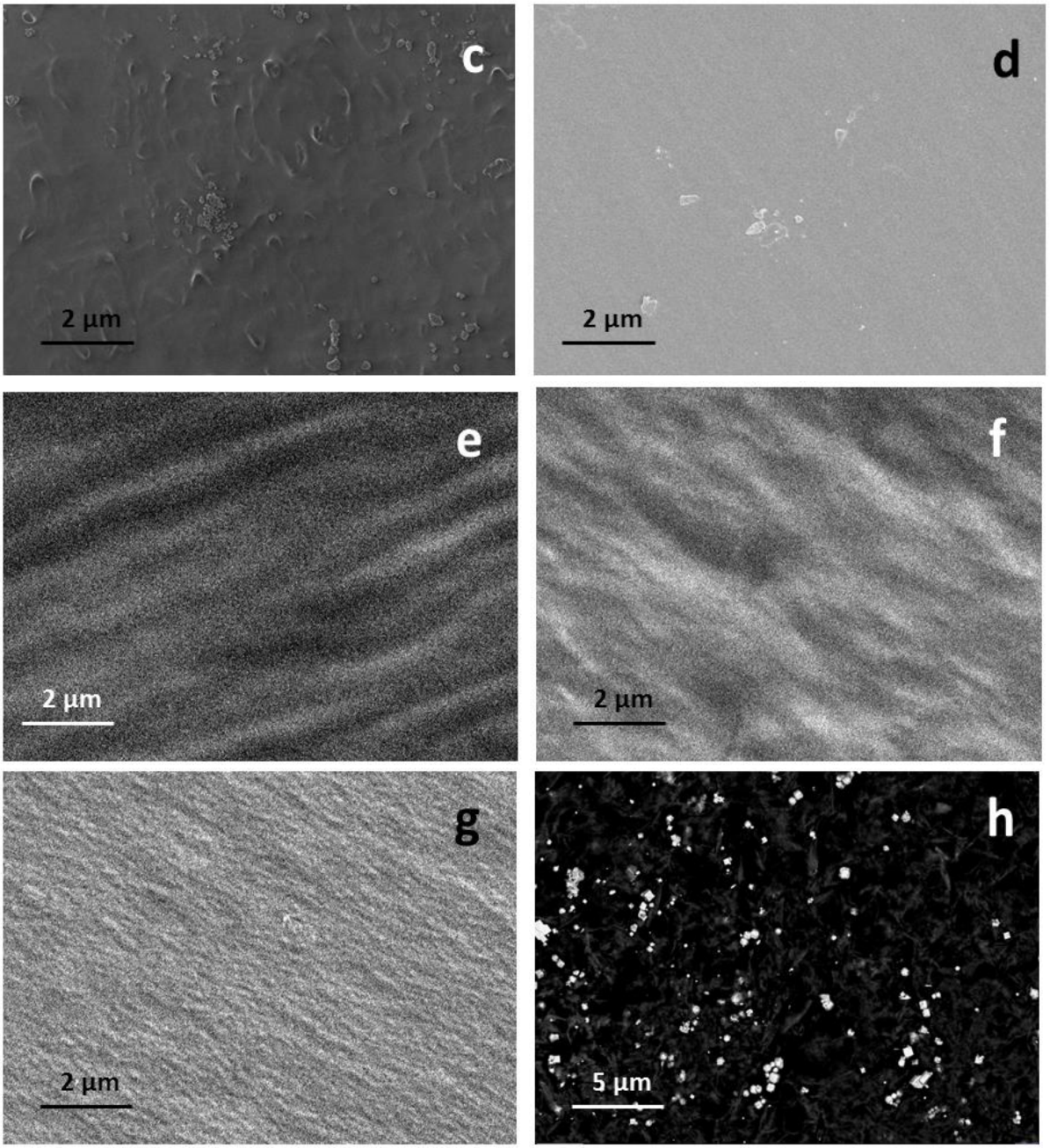

Figure 21: Nylon 6 **a**); Nylon 6-NH **b**); Nylon 6-NCH_2Ph (3 h) **c**); Nylon 6-N-PEG **d**); Nylon 6-N-PEG-CH_3/ 2 h lithiation, 0.6 ml *t*-BuLi **e**); Nylon 6-N-PEG-CH_3/ 2 h lithiation, 1 ml *t*-BuLi **f**); Nylon 6-N-PEG-CH_3/ 2 h lithiation, 2 ml *t*-BuLi **g**) and Nylon 6-N-PEG-CH_3-Cu **h**).

4.2.2.3. AFM analyses

The surface roughness (Ra) values of two different areas (1 µm x 1 µm and 10 µm x 10 µm) obtained for unmodified Nylon 6 and modified Nylon 6-NH, Nylon 6-NCH_2Ph (1 h, 3 h), Nylon 6-N-PEG-CH_3 (2 h lithiation, 0.6 ml *t*-BuLi and 24 h lithiation, 2 ml *t*-BuLi), Nylon 6-N-PEG, Nylon 6-N-PEG-CH_3-Cu indicated significant changes after chemical modifications

and deposition of Cu NPs. We suggest that the notably high Ra values for Nylon 6-NCH_2Ph are the results related to the corrosion which occurred on the surface due to the reaction with strong base *t*-BuOK before *N*-alkylation. The obtained Ra values are presented in the **Table 3**. The Ra value decreased noticeably after Nylon 6 reduction. On the contrary, *N*-alkylation and H_3C-PEG-OTs grafting on Nylon 6-NH surface have increased the surface roughness. The Cu NP deposition on Nylon 6-N-PEG-CH_3 significantly increased the surface roughness of Nylon 6-N-PEG-CH_3-Cu as expected. Nylon 6-N-PEG film demonstrated more surface roughness than Nylon 6-N-PEG-CH_3 films. Measured Ra values also supported the obtained SEM images (**Figure 21, a - h**) and confirmed the Nylon 6 films modifications.

Table 3: Changes in the surface roughness (Ra) observed before and after the Nylon 6 surface modification

Samples	**Surface area**	
	(1 × 1) μm^2	**(10 × 10) μm^2**
Nylon 6	5.1 nm	34.8 nm
Nylon 6-NH	1.3 nm	7.2 nm
Nylon 6-NCH_2Ph (1 h)	22.3 nm	138 nm
Nylon 6-NCH_2Ph (3 h)	21.1 nm	187.6 nm
Nylon 6-N-PEG-CH_3 (2 h lithiation, 0.6 ml *t*-BuLi)	1.3 nm	12.8 nm
Nylon 6-N-PEG-CH_3 (24 h lithiation, 2 ml *t*-BuLi)	1.1 nm	12.7 nm
Nylon 6-N-PEG	3.79 nm	18.42 nm
Nylon 6-N-PEG-CH_3-Cu	11.83 nm	30.37 nm

AFM micrographs (3D) of pure Nylon 6 and modified ones are displayed for the visual understanding related to surface topography changes in (10 x 10) μm^2 surface area after various modifications (**Figure 22 a – d**).

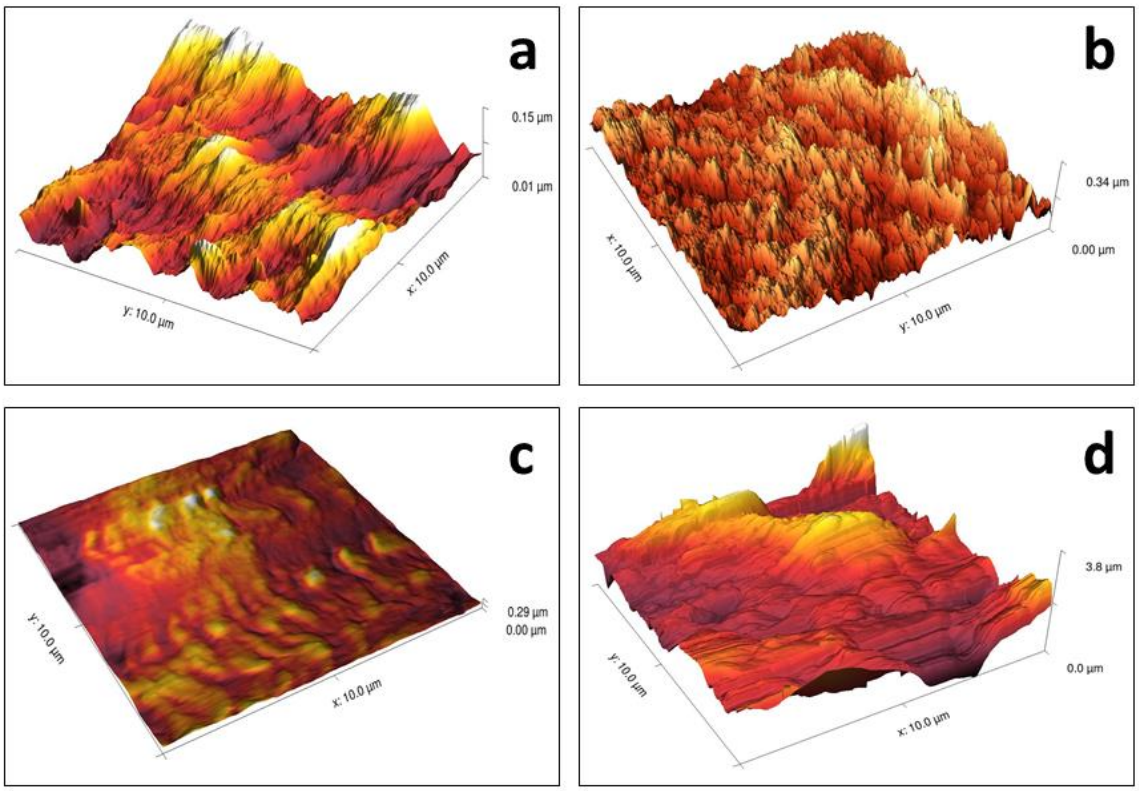

Figure 22: AFM analyses of 3D images related to Nylon 6 **a**); Nylon 6-NCH_2Ph/ 3 h **b**); Nylon 6-N-PEG **c**) and Nylon 6-N-PEG-CH_3-Cu **d**).

AFM images related to Nylon 6-NH and Nylon 6-N-PEG-CH_3 grafted samples 2D (**Figures 23 a, b. c)** and 3D (**Figures 24 a, b, c**) (10 x 10) μm^2 size were investigated to compare Nylon 6-NH with other two grafted samples. Obtained images showed significant changes in the surface roughness between Nylon 6-NH and Nylon 6-N-PEG-CH_3 [111]. Apparently, the differences in surface morphologies of the Nylon 6-N-PEG-CH_3 films have not been seen for two different lithiation times with two different concentrations (2 h lithiation, 0.6 ml *t*-BuLi and 24 h lithiation, 2 ml *t*-BuLi), but the SEM micrographs and WCA differences support the denser grafting via 4 h lithiation reaction than 2 h lithiation.

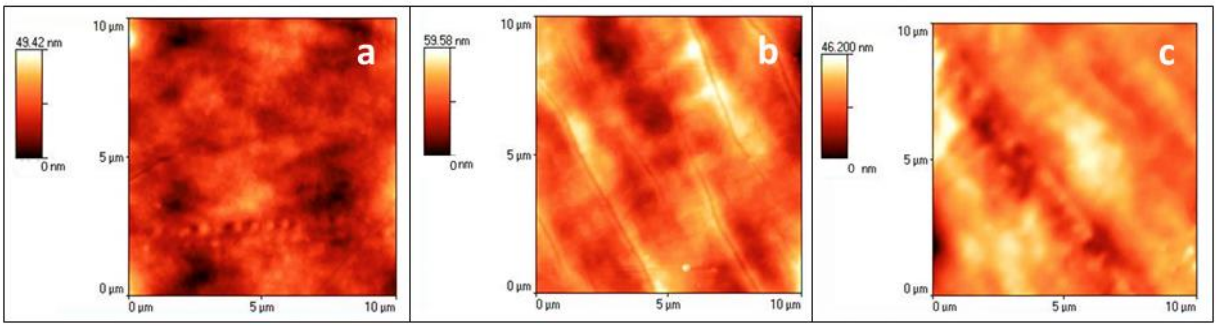

Figure 23: 2D (10×10) μm^2 AFM images showing Nylon 6-NH **a**); Nylon 6-N-PEG-CH_3/ 2 h lithiation, 0.6 ml *t*-BuLi **b**) and Nylon 6-N-PEG-CH_3/ 24 h lithiation, 2 ml *t*-BuLi **c**).

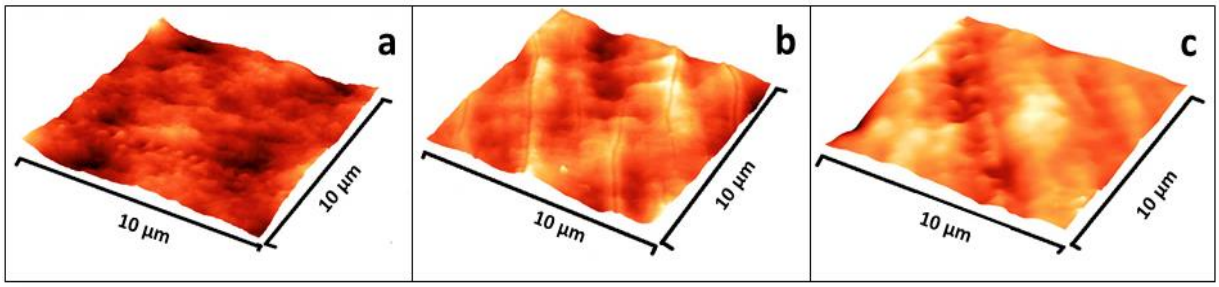

Figure 24: 3D (10×10) µm^2 AFM images of Nylon 6-NH **a**); Nylon 6-N-PEG-CH_3/ 2 h lithiation, 0.6 ml *t*-BuLi **b**) and Nylon 6-N-PEG-CH_3/ 24 h lithiation, 2 ml *t*-BuLi **c**).

4.2.2.4. XPS analyses of pure and modified Nylon 6

The shifts in the binding energy of high resolution C_{1s} and N_{1s} spectra, comparing Nylon 6 and Nylon 6-NH (**Figure 25 a, b**), clearly indicated the amide functional groups reduction on Nylon 6 surface to secondary amines after modification with BH_3-THF. The C_{1s} peak had binding energy at 288.5 eV for Nylon 6 due to the carbonyl group (C=O) presence in amide and C-C peak was observed at 285 eV. After reduction, only C-C peak coming from C_{1s} (285 eV) was observed (**Figure 25 a**), these results indicated the amine groups formation on the reduced Nylon 6 surface [111]. The slight shift observed in N_{1s} peak from 399 eV to lower binding energy occurred due to the BH_3-THF reduction and may be the result related to the imine (C=N) groups formation on the Nylon 6-NH surface (**Figure 25 b**). Noticeably, the strong satellite peaks belonging to the N_{1s} spectra indicate occurring reduction on the Nylon 6 surface. The benzyl group (-CH_2Ph) introduction to Nylon 6-NH via *N*-alkylation for 1 and 3 h was successfully confirmed by N_{1s} spectra showing very weak satellite peaks which are significantly different from Nylon 6-NH (**Figure 25 d**). The small C_{1s} peak visible at 288.5 eV in case of Nylon 6-NCH_2Ph samples may indicate the presence of some amide groups on the surface (**Figure 25 c**).

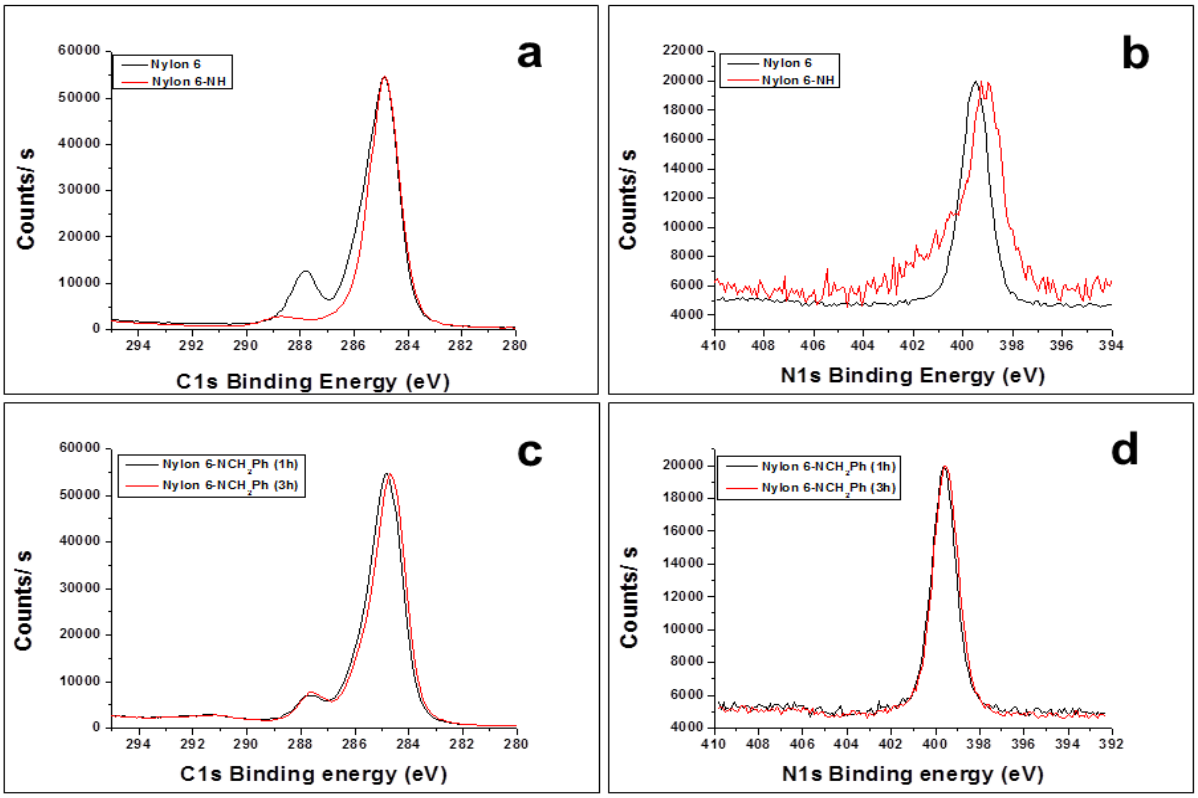

Figure 25: Nylon 6 surface modification to Nylon 6-NH: C_{1s} spectra **a**); N_{1s} spectra **b**); benzyl groups immobilization via 1 and 3 h reactions forming Nylon 6-NCH_2Ph: C_{1s} spectra **c**), N_{1s} spectra **d**).

The surface atomic compositions before and after functionalization of Nylon 6 investigated by XPS analyses are given in **Table 4**. The oxygen (O) decreased percentage [112], which occurred after Nylon 6-NH formation, indicates successful reduction that is also supported by FT-IR spectra in **Figure 26**. The presence of chlorine on Nylon 6-NH surface confirms ammonium salt formation as a result of washing with 1 M HCl. The chlorine (Cl) percentage decrease after *N*-alkylation and grafting reactions can be considered as a signal for the reaction on the Nylon 6-NH surface with secondary amine groups. The achievement of *N*-alkylation on Nylon 6-NH samples leading to the Nylon 6-NCH_2Ph formation has been reinforced by Raman spectroscopy (**Figure 29**). The conversion of Nylon 6-NH to Nylon 6-N-PEG-CH_3 (2 h lithiation, 0.6 ml *t*-BuLi) was indicated by the decrease percentage of chlorine on the surface after grafting that explains the *N*-alkylation reaction with H_3C-PEG-OTs on the sites of ammonium ion on the nylon 6-NH surface. Nylon 6-N-PEG-CH_3 (24 h lithiation, 2 ml *t*-BuLi) indicated more intensity of grafting as chlorine was completely absent in the composition of material. Moreover, the oxygen (O) percentage was increased after grafting due to immobilization of PEG-CH_3 chains. This was further employed by Nylon 6-N-PEG-CH_3 samples' FT-IR spectra **Figure 26**.

Table 4: XPS data for the modified and unmodified Nylon 6 films

Sample	Elemental composition (%) of sample surface			
	C	N	O	Cl
Nylon 6	75.89	11.05	13.06	--
Nylon 6-NH	78.91	10.31	6.27	4.51
Nylon 6-NCH_2Ph (3 h)	83.62	7.46	8.83	--
Nylon 6-N-PEG-CH_3 (2 h lithiation, 0.6 ml *t*-BuLi)	75.88	7.92	11.42	1.98
Nylon 6-N-PEG-CH_3 (24 h lithiation, 2 ml *t*-BuLi)	76.87	12.41	8.07	0

4.2.2.5. FT-IR and Raman analyses

Figure 26 shows the comparison between the FT-IR spectra of Nylon 6 and modified Nylon 6-NH films. The characteristic stretching vibrations were seen for amide I and amide II groups (1660 cm^{-1} and 1541 cm^{-1}), the aliphatic groups (2858 cm^{-1} and 2931 cm^{-1}) and the secondary amine groups (3293 cm^{-1}) present on Nylon 6 were visible for both samples before and after the reduction with BH_3-THF. This was because of the FT-IR penetration depth, which was approximately 1 µm and formed layer was significantly thinner than 1 µm [111]. There was a new band appearing at 2420-2250 cm^{-1} and spectra band (2382 cm^{-1}) which corresponded to imine groups introduced via chemical treatment, indicating the step towards reduction of amide to amine. Moreover, the increase in intensity of aliphatic band stretching vibration confirmed the amide conversion into amine due to the Nylon 6 film reduction. The FT-IR spectra of the Nylon 6-N-PEG-CH_3 (2 h/ 0.6 ml *t*-BuLi), Nylon 6-N-PEG-CH_3 (2 h/ 1 ml *t*-BuLi) and Nylon 6-N-PEG-CH_3 (2 h/ 2 ml *t*-BuLi) samples showed that the imine stretching band (2420 - 2250 cm^{-1}) disappeared completely. This fact was significant and indicated the Nylon 6-NH surface modification which occurred via lithiation. The characteristic PEG stretching band (1087 cm^{-1}) was also very prominent for all the grafted samples. Again the stretching vibration intensities at 1087 cm^{-1} for the grafted samples were proportional to the *t*-BuLi concentration during lithiation. The WCA measurement (**Figure 19**), SEM analysis (**Figure 21 e, f, g**), AFM analysis (**Figure 23, 24**) and XPS atomic composition data (**Table 4**) supported PEG-CH_3 grafting on Nylon 6-NH via lithiation.

Figure 27 shows the spectra for Nylon 6-N-PEG-CH_3-Cu, where some additional peaks appeared at 1726 cm^{-1}, 1250 cm^{-1} and 952 cm^{-1}. The absorption bands at 1726 $cm^{-1,}$ 1250 cm^{-1} and 952 cm^{-1} attributed to the aliphatic ketone, asymmetric stretching vibration of S=O of sulfate (head group) in SDS molecules and C-O-S bond in SDS respectively. These additional stretching vibrations compared to Nylon 6-N-PEG-CH_3 spectra confirmed the adsorption of SDS capped Cu NPs [146,160]. The characteristic PEG stretching band (1087 cm^{-1}) on Nylon 6-N-PEG-CH_3 was red shifted to 1078 cm^{-1} as a result of the presence of SDS capped Cu NP on Nylon 6-N-PEG-CH_3 surface.

Figure 28 compares the FT-IR spectra of Nylon 6-NH and Nylon 6-N-PEG. The characteristic stretching vibration at 1078 cm^{-1} was attributed to PEG chains tethered by conjugation with DSC [158]. The additional peaks appeared at 1207 cm^{-1} and 1726 cm^{-1} represented the ester bond formation during conjugation of PEG with DSC and aliphatic ketone on the surface. Nylon 6-N-PEG sample also showed that the imine stretching band present in Nylon 6-NH (2420 - 2250 cm^{-1}) disappeared completely. Therefore, it was an indication for successful immobilization of PEG via DSC conjugation.

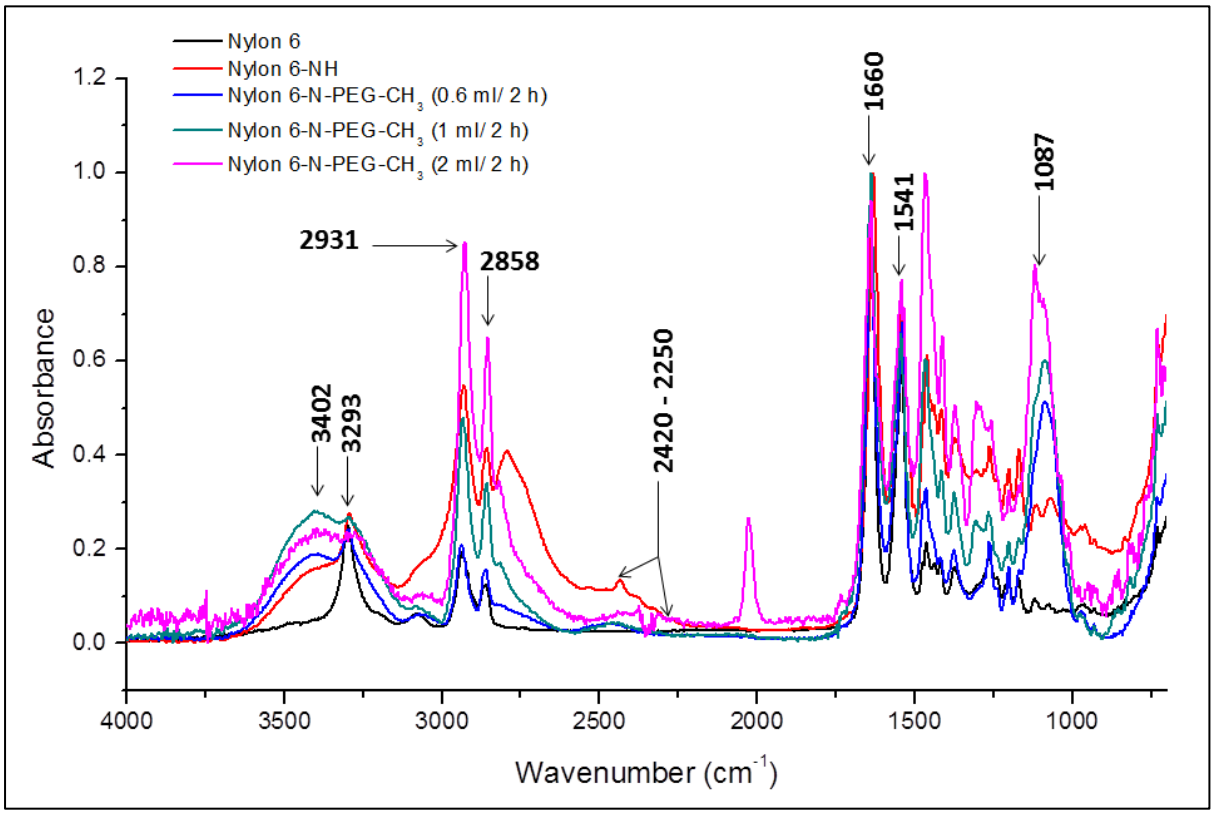

Figure 26: FT-IR spectra showing Nylon 6, Nylon 6-NH and Nylon 6-N-PEG-CH_3 samples.

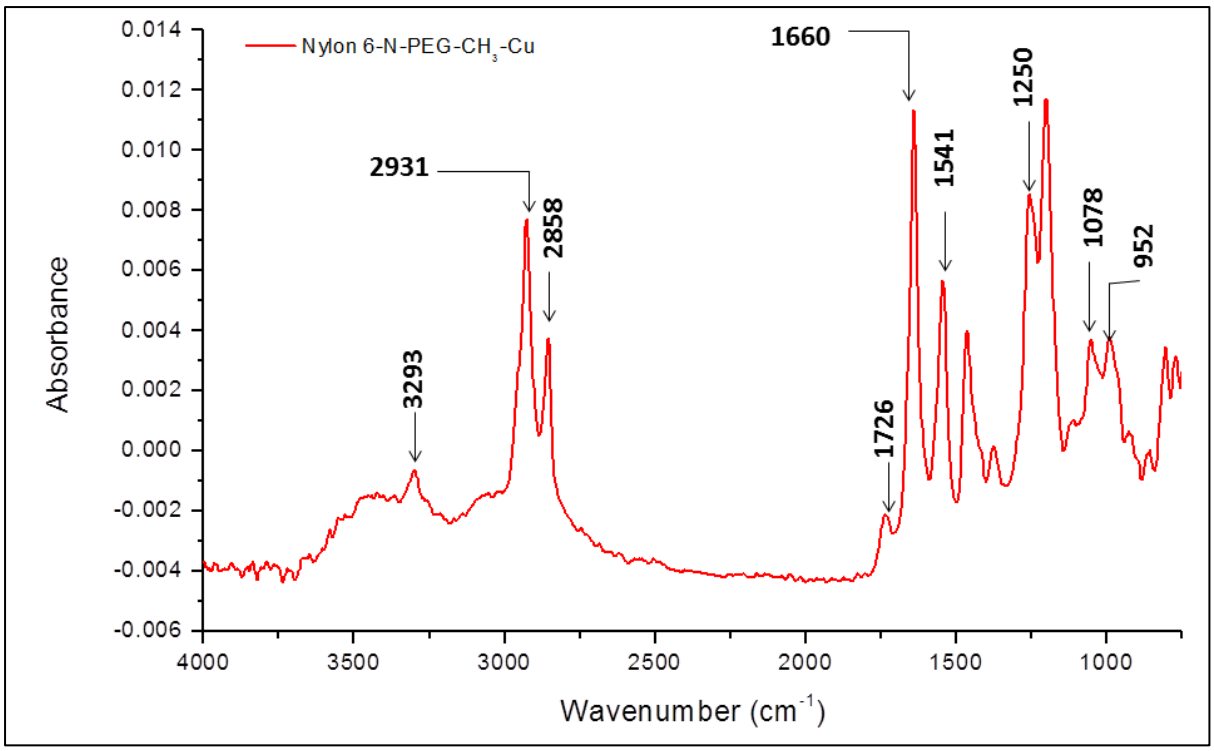

Figure 27: FT-IR spectra showing Cu NP deposited Nylon 6-N-PEG-CH_3 sample.

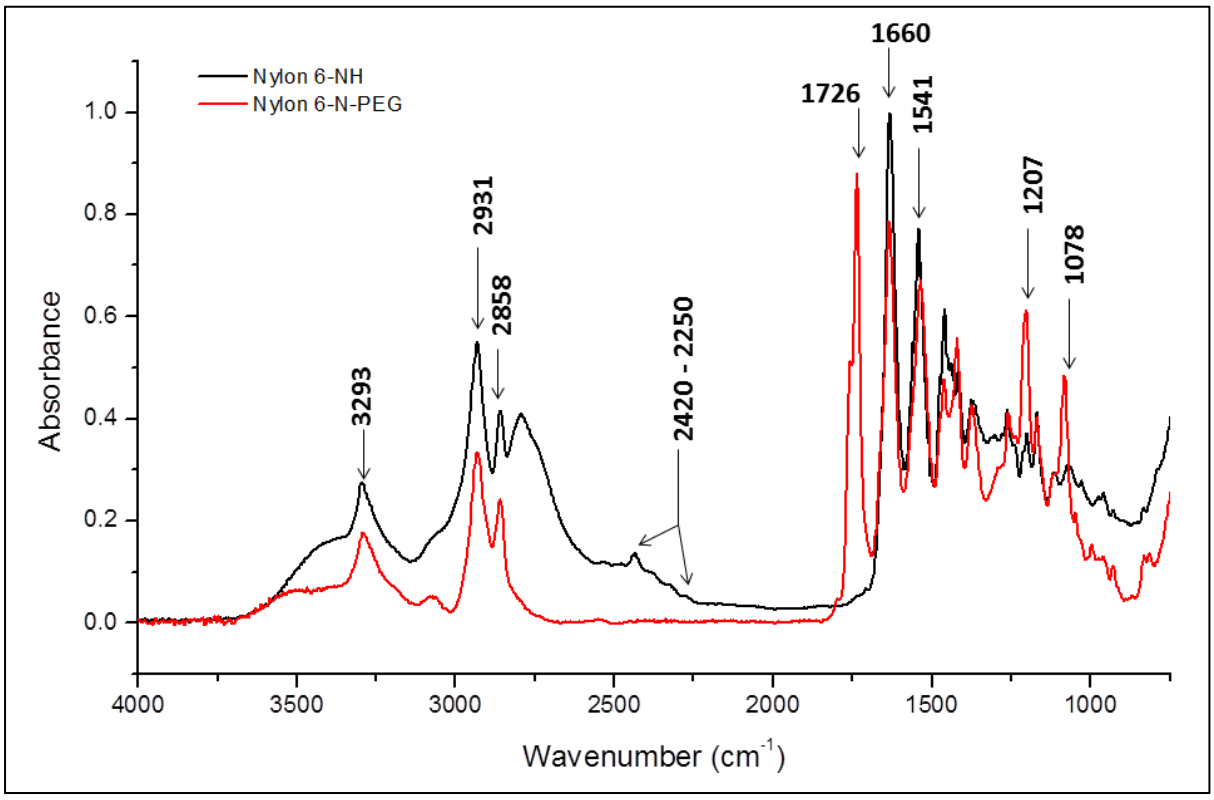

Figure 28: The FTIR spectra comparing Nylon 6-NH and Nylon 6-N-PEG.

Nylon 6-NCH_2Ph films could not be detected by FT-IR due to the sensitivity limitation [161]. Therefore, the surface composition changes were studied by Raman spectroscopy.

The strong Raman shift (**Figure 29**) for C-H stretching vibrations of aromatic ring was visible at 3060 cm^{-1} (i.e. within the range of 2870-3100 cm^{-1}) for Nylon 6-NCH_2Ph films, obtained by both 1 and 3 h reactions. Although the Raman intensity was higher in case of 3 h reaction confirming better modification in longer time. The Nylon 6-NH Raman spectra did not show any stretching band at 3060 cm^{-1}. Moreover new strong stretching vibration bands were seen for Nylon 6-NCH_2Ph films at 1625 cm^{-1} and 1000 cm^{-1} due to the presence of C=C bonds coming from aromatic ring respectively. Raman spectra showed the characteristic stretching bands at 2900 cm^{-1} (aliphatic C-H), 1637 cm^{-1} (amide I groups) and 1439 cm^{-1} (aliphatic CH_2) for Nylon 6-NH as well as Nylon 6-NCH_2Ph films.

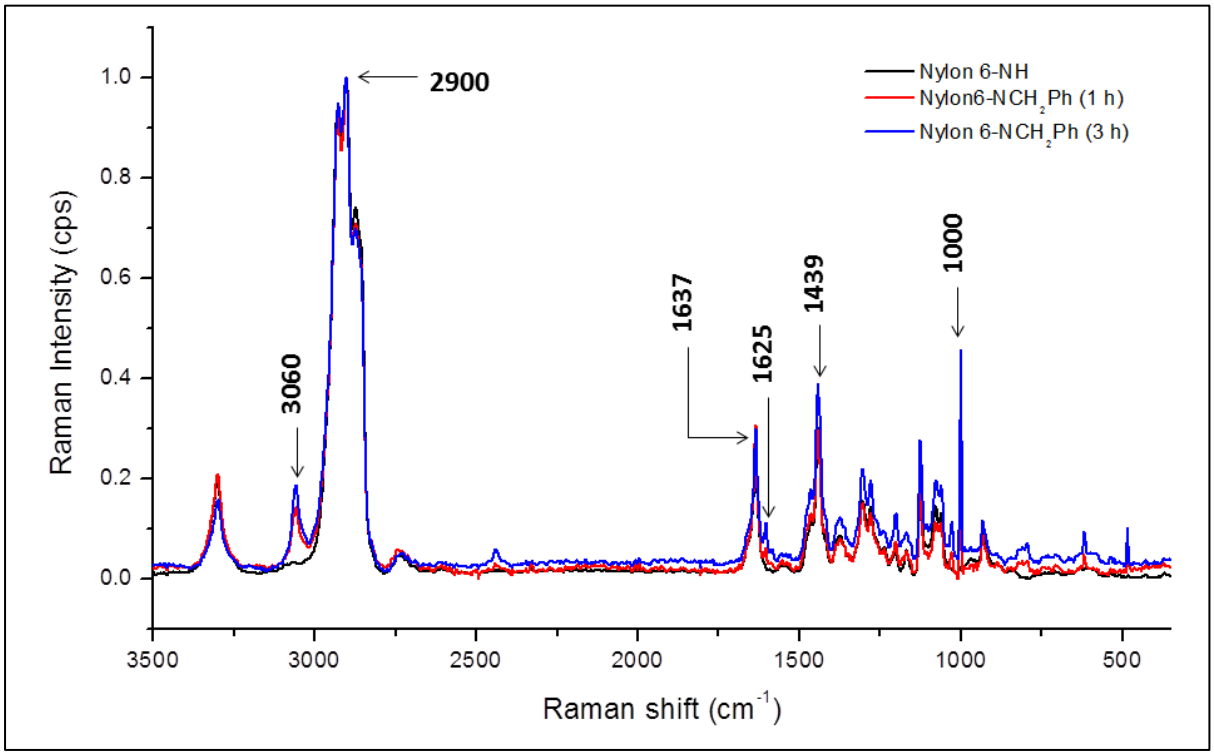

Figure 29: Raman spectra confirming the modification Nylon 6-NH into Nylon 6-NCH_2Ph.

4.2.3. Analyses of antibacterial activity, cytotoxicity and cell adhesion

4.2.3.1. Antibacterial activity of the prepared Nylon 6 samples

Generally accepted principles concerning hydrophobicity in many cases describe how bacterial adhesion directly correlates with the surface [162]. Bacterial adhesion in response to the surface charge is a complex topic involving incubation time and surrounding ionic strength. When we look for the surface topography influence, which is usually described only by the average roughness parameter, it was rarely studied [163]. The exact

correlation between topography and bacterial adhesion is still unclear, although it is generally accepted that bacteriologically similar topographical properties support the adhesion of bacteria, presumably by providing protective effects.

The tested samples were sample 1 – 9, unmodified Nylon 6 and other modified Nylon 6 films mentioned earlier (***Section 3.2.3.2*** and ***3.2.3.3***). All the samples were cut into squares (2 cm x 2 cm size). Obtained results are summarized in **Table 5** for *S. aureus* and in **Table 6** for *P. aeruginosa.*

Results obtained with Gram positive bacteria *S. aureus* showed visible differences among the unmodified sample 1 and modified samples 2 - 9 (**Table 5**), but as it was described previously, pure Nylon 6 films generally exhibit lower adhesion for Gram positive *S. aureus* [164]. All examined grafted samples (3 – 8) seemed to have the significant antibacterial activity compared to the control and pure Nylon 6 (Sample 1). The PEG-CH_3 grafted samples 3, 4 and 6 particularly had high antibacterial activities. Surprisingly, Nylon 6-NH (Sample 2) exhibited significant antibacterial efficacy for both the bacterial strains. Sample 2 showed > 99% inhibition for both *S. aureus* and *P. aeruginosa*. Additionally, Gram negative bacteria *P. aeruginosa* showed more interesting results, where significant differences were seen among the unmodified and modified samples (**Table 6**). Samples 3, 4 and 7 displayed the highest antibacterial activity against *P. aeruginosa* amongst PEG-CH_3 grafted samples that were tested. According to the studies done by Jeon and co-workers, protein resistance to PEG-functionalized surface in water depends on the Van der Waals attractions and steric repulsion between solid substrate and protein [165]. Water molecules of hydrated PEG also play an important role. PEG chains result a low Van der Waals interactions with protein. If protein approaches to surface, the PEG chains are compressed and the steric repulsion becomes greater than attraction. The same mechanism may be applied as the reason for resistance to the bacterial adhesion. The grafting intensity was less in sample 3 compared to other grafted samples. Samples 3 and 4 had more access to the hydrogen bonding with water molecules due to the abundant exposure of $–CH_2-CH_2-O–$ units, making samples 3 and 4 more hydrophilic than others, even though all the samples have hydrophobic terminal $–CH_3$ groups. Samples 5 - 8, as more densely packed with H_3C-PEG chains, may not be able to form hydrogen bonds as efficiently as samples 3 and 4 with water. Moreover, the terminal $–CH_3$ groups of H_3C-PEG chains can make the densely drafted layer less hydrophilic, thus reducing the antibacterial efficacy. Comparing both the bacterial strains, it was clear that *P. aeruginosa* is comparatively less effective for grafted samples as relatively hydrophobic microbes (like *P. aeruginosa*) interact more strongly with PEG grafted materials [44].

In case of Sample 9 (Nylon 6-N-PEG-CH_3-Cu), Metallic Cu NPs of average size ~ 500 nm were deposited by physisorption on Nylon 6-N-PEG-CH_3 sample. Recently, Cu NPs have gained potential as effective and cheaper alternative antibacterial agent, especially after the extensive use of silver (Ag) nanoparticles in biomedical field [127,166]. The antibacterial efficacy of Cu NPs is dependent on the size of the particles and high surface to volume ratio, that allow the microbial membranes to interact effectively [166]. Sample 9 snowed 99% bacterial inhibition against *P. aeruginosa,* whereas, it was not equally effective for *S. aureus* inhibition (**Table 5, 6**). Nylon 6-NH (sample 2) and the grafted samples showed higher inhibition for *S. aureus.* On the contrary, sample 9 exhibited strong antibacterial effect for *P. aeruginosa* compared to the all grafted samples.

Table 5: Antibacterial activity of the unmodified (**S1**) and modified (**S2 – S8**) Nylon 6 samples against *S. aureus*

Sample	**Bacterial inoculum (*S. aureus*) concentration (10^0 = 3 x 10^7 CFU/ ml)**							
	10^0	**10^{-1}**	**10^{-2}**	**10^{-3}**	**10^{-4}**	**10^{-5}**	**10^{-6}**	**10^{-7}**
Control	*	*	*	*	975	107	11	1
S1	*	*	*	603	284	26	5	0
S2	18	2	1	1	0	0	0	0
S3	166	31	10	4	0	1	0	0
S4	562	138	43	7	1	1	0	0
S5	*	*	895	280	33	1	1	0
S6	326	50	3	0	1	0	0	0
S7	*	*	*	763	176	18	2	0
S8	*	*	736	134	7	1	0	0
S9	*	*	*	957	91	22	4	0

(*) implies uncountable number of bacterial colonies.

Table 6: Antibacterial activity of the unmodified (**S1**) and modified (**S2 – S8**) Nylon 6 samples against *P. aeruginosa*

Sample	Bacterial inoculum (*P. aeruginosa*) concentration (10^0 = 3 x 10^7 CFU/ ml)							
	10^0	10^{-1}	10^{-2}	10^{-3}	10^{-4}	10^{-5}	10^{-6}	10^{-7}
Control	*	*	*	*	1102	93	15	3
S1	*	*	*	*	892	131	18	1
S2	923	272	14	4	1	1	0	0
S3	*	456	36	12	2	2	1	0
S4	*	*	452	70	6	2	0	0
S5	*	*	*	879	376	65	6	0
S6	*	*	*	516	104	6	0	0
S7	*	*	464	30	3	0	0	0
S8	*	*	*	604	128	83	3	0
S9	684	88	11	1	0	0	0	0

(*) implies uncountable number of bacterial colonies.

Qualitative antibacterial tests of Nylon 6-N-PEG-CH_3-Cu

The zone of Inhibition Test results are shown in **Figures 30** and **31** that exhibited significant antibacterial effect for both the bacterial strains. The Cu NPs deposited samples (Nylon 6-N-PEG-CH_3-Cu - sample 9) examined by the size of the inhibition zones (**Table 7**) presented stronger sterilization to *P. aeruginosa* compared to *S. aureus.* From both the figures, it can be seen that both the petri dishes were densely populated by both the bacterial colonies, exempting the areas of the samples placed on the agar. Moreover, the experiments showed 1mm zone of inhibition to *P. aeruginosa* around the functional specimen (**Figure 31)**. In case of *S. aureus,* the inhibition zone was seen only below the sample. A few individual tiny bacterial colonies were also spotted on the sample surface (**Figure 30**). According to some literatures, Gram positive bacteria (*S. aureus*) are more sensitive to the Cu NPs than Gram negative ones (*P. aeruginosa*) [59,166,167]. But the degrees of toxic effect of Cu NPs are related to the nanoparticle size, where smaller nanoparticles (less than 100 nm diameter) are much more effective in bacterial sterilization [127]. Less the particle size and the degree of aggregation, the probability of migration

activity, penetration and impact on the cell may be increased [167]. In our experiments, both the qualitative and quantitative antibacterial tests proved to be more effective to *P. aeruginosa* than *S. aureus* for Cu NPs (~500 nm) deposited samples.

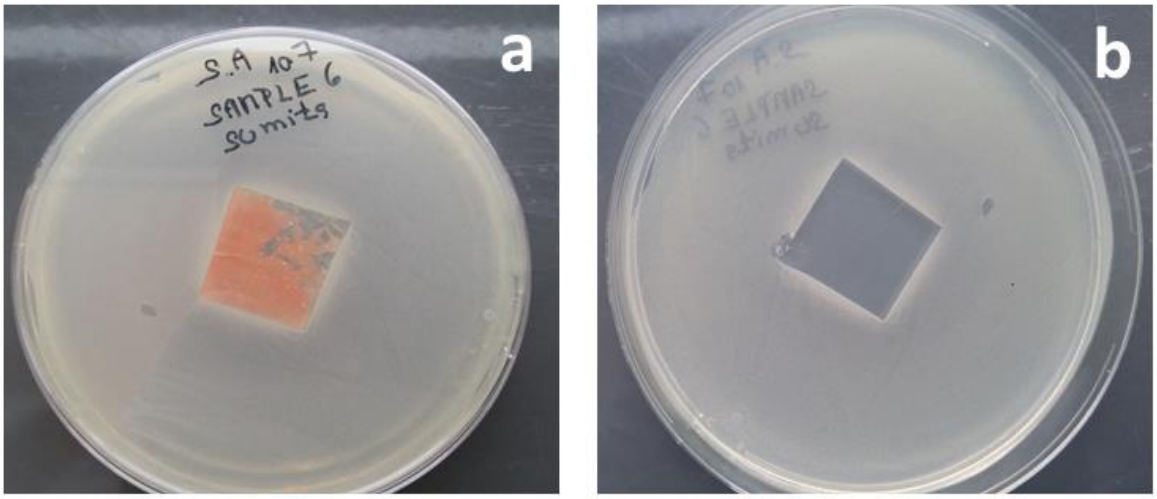

Figure 30: Pictures of the visual control of inhibiting zones of *S. aureus*, exposed to Nylon 6-N-PEG-CH_3-Cu **a**) and after removal of Nylon 6-N-PEG-CH_3-Cu **b**).

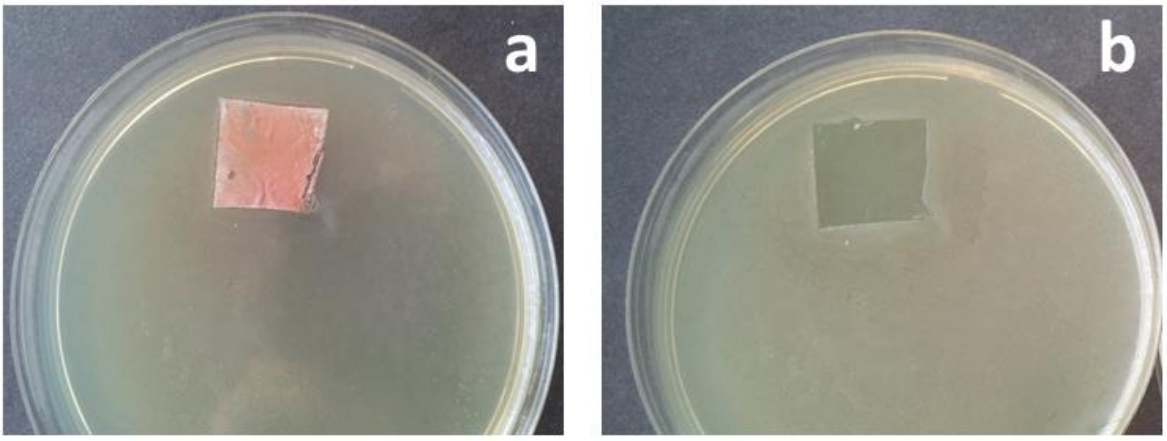

Figure 31: Pictures of the visual control of inhibiting zones of *P. aeruginosa*, exposed to Nylon 6-N-PEG-CH_3-Cu **a**) and after removal of Nylon 6-N-PEG-CH_3-Cu **b**).

Table 7: Zone of inhibition measurement of Nylon 6-N-PEG-CH_3-Cu against two bacterial strains: *S. aureus* and *P. aeruginosa*

	Size of inhibition zone	
Sample size	***S. aureus***	***P. aeruginosa***
20 mm × 20 mm	20 mm × 20 mm (Only below the sample)	22 mm × 22 mm

4.2.3.2. Bacterial adhesion assessment

The bacterial adhesion resistance to the surface of the pure Nylon 6 (sample 1), Nylon 6-NH (sample 2), the previously mentioned grafted Nylon 6-N-mPEG films (samples 3 -8) and Nylon 6-N-PEG-CH_3-Cu (sample 9) against two bacterial strains: *S. aureus* and *P. aeruginosa*, was evaluated by counting the number of bacterial colonies formed in agar media incubated for 48 h/ 37° C. The results are summarized in **Table 8** and **Table 9** respectively. All the grafted Nylon 6-N-PEG-CH_3 samples (samples 3 – 8) exhibited significant resistance towards both *S. aureus* and *P. aeruginosa* adhesion compared to unmodified Nylon 6 (sample 1). Nylon 6-NH (sample 2) demonstrated high efficiency to resist both the bacterial adhesion, which corresponds to the antibacterial tests (**Table 5**, **6**). The performance of samples 3, 4 and 6 were better than the other grafted samples. Pure Nylon 6 was very prone to bacterial adhesion as it showed high number of bacterial colony formation similar to the control. Sample 9 was very effective to *P. aeruginosa* with 99% efficacy, but did not high efficiency to resist *S. aureus* adhesion.

Table 8: Bacterial adhesion analyses on the unmodified (**S1**) and modified (**S2 – S8**) Nylon 6 surfaces against *S. aureus*

Sample	**Bacterial inoculum (*S. aureus*) concentration (10^0 = 3 x 10^7 CFU/ ml in control)**							
	10^0	**10^{-1}**	**10^{-2}**	**10^{-3}**	**10^{-4}**	**10^{-5}**	**10^{-6}**	**10^{-7}**
Control	*	*	*	*	975	107	11	1
S1	*	*	*	904	100	9	1	0
S2	13	11	7	0	0	0	0	0
S3	5	0	0	0	0	0	0	0
S4	61	13	6	0	0	0	0	0
S5	370	59	7	3	0	0	0	0
S6	37	0	0	0	0	0	0	0
S7	*	672	78	8	0	0	0	0
S8	295	36	3	0	0	0	0	0
S9	*	368	73	6	0	0	0	0

(*) implies uncountable number of bacterial colonies.

Table 9: Bacterial adhesion analyses on the unmodified (**S1**) and modified (**S2 – S8**) Nylon 6 surfaces against *P. aeruginosa*

Sample	Bacterial inoculum (*P. aeruginosa*) concentration (10^0 = 3 x 10^7 CFU/ ml in control)							
	10^0	10^{-1}	10^{-2}	10^{-3}	10^{-4}	10^{-5}	10^{-6}	10^{-7}
Control	*	*	*	*	1102	93	15	3
S1	*	*	*	422	37	4	0	0
S2	1	0	0	0	0	0	0	0
S3	12	1	0	0	0	0	0	0
S4	452	69	11	2	0	0	0	0
S5	792	168	30	3	0	0	0	0
S6	45	3	0	0	0	0	0	0
S7	174	63	2	0	0	0	0	0
S8	800	57	6	1	0	0	0	0
S9	8	0	0	0	1	0	0	0

(*) implies uncountable number of bacterial colonies.

4.2.3.3. Cytocompatibility assessment of pure and modified Nylon 6

Cytotoxicity of extracts

Metabolic activities of pure Nylon 6 foil (Sample 1) and all other modified foils (Samples 2 – 9), incubated in complete medium using 10 mg of tested material/ 1 ml of medium for 24 hours, were measured by MTT test. The results are summarized in graph in **Figure 32 a**. Samples 3 and 9 were found to be cytotoxic with cell viabilities 12% and 16% respectively for 10 mg tested material/ ml extract concentration. The rest of the samples (Samples 1, 2, 4 – 8) exhibited no cytotoxicity measure in cells as cell viability exceeded 70% limit of cytotoxicity given by the ISO norm. However, samples 4 – 7 caused the drop of cell viability to 85%, 80%, 79% and 82% respectively, that are close to the determined level of cytotoxic effect given by the norm (70%). Samples 1, 2 and 8 showed high cytocompatibility with cell viabilities of 119%, 95% and 100% respectively. On the other

hand, all the tested materials with lower extract concentration of 5 mg/ ml demonstrated cytocomplatibility. Moreover, samples 3 and 9 led to slight reduction of cell viabilities to 83% and 90% respectively compared to control (**Figure 32 b**) . Lower absorbance of solution reflecting cell metabolic activity suggested potential cytotoxic effect orf the samples 3 and 9 using 10 mg tested material/ ml extract concentration, whereas both the samples were found to be non-cytotoxic for 5 mg tested material/ ml extract concentration.

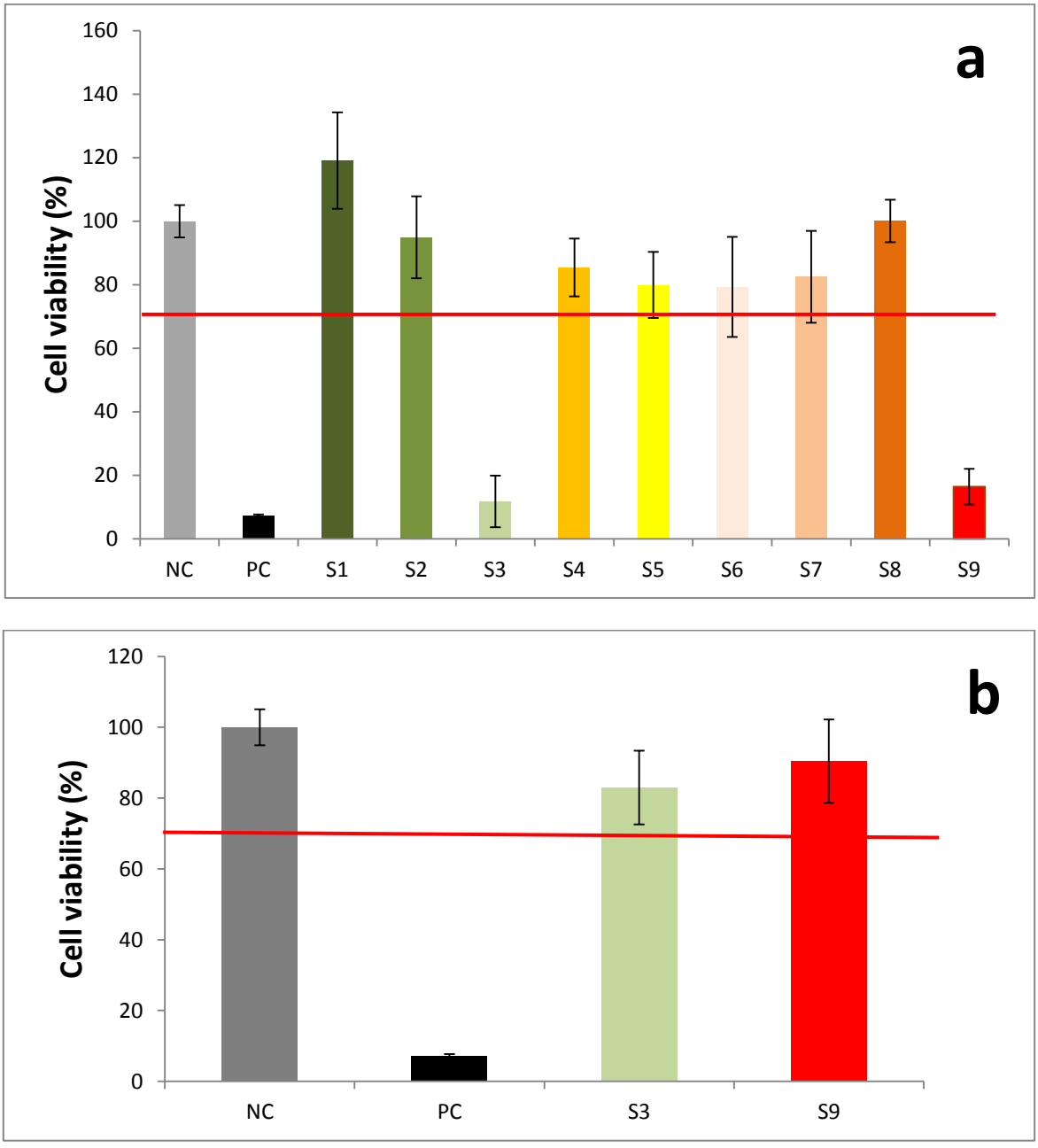

Figure 32: Metabolic activities of fibroblasts (3T3-SA) after 24 hours incubation in complete medium (NC), complete medium containing Triton X-100 (PC) and extracts of the tested samples (Samples 1 - 9) in concentrations of 10 mg/ ml **a**) and in complete medium (NC), complete medium containing Triton X-100 (PC) and extracts of tested samples (3 and 9) in concentrations of 5 mg/ ml **b**).

Before performing metabolic MTT tests for the samples, cells were captured by optical microscopy. Cells cultured in the presence of complete medium (DMEM) had normal spread morphology (**Figure 33 a**). Dead rounded cells were found in wells containing DMEM with addition of cytotoxic Triton X-100 (**Figure 33 b**). Extracts of all the tested samples in lower tested concentration of 5 mg/ ml caused no visible cell damage. On the contrary, extracts of samples 3 and 9 in higher tested concentration (10 mg/ ml) caused visible cell damage (**Figure 33 c – f**). Only for these two samples, extracts in diluted concentration (5 mg/ ml) did not harm the cell morphology. The rest of the samples showed moderate cell growth.

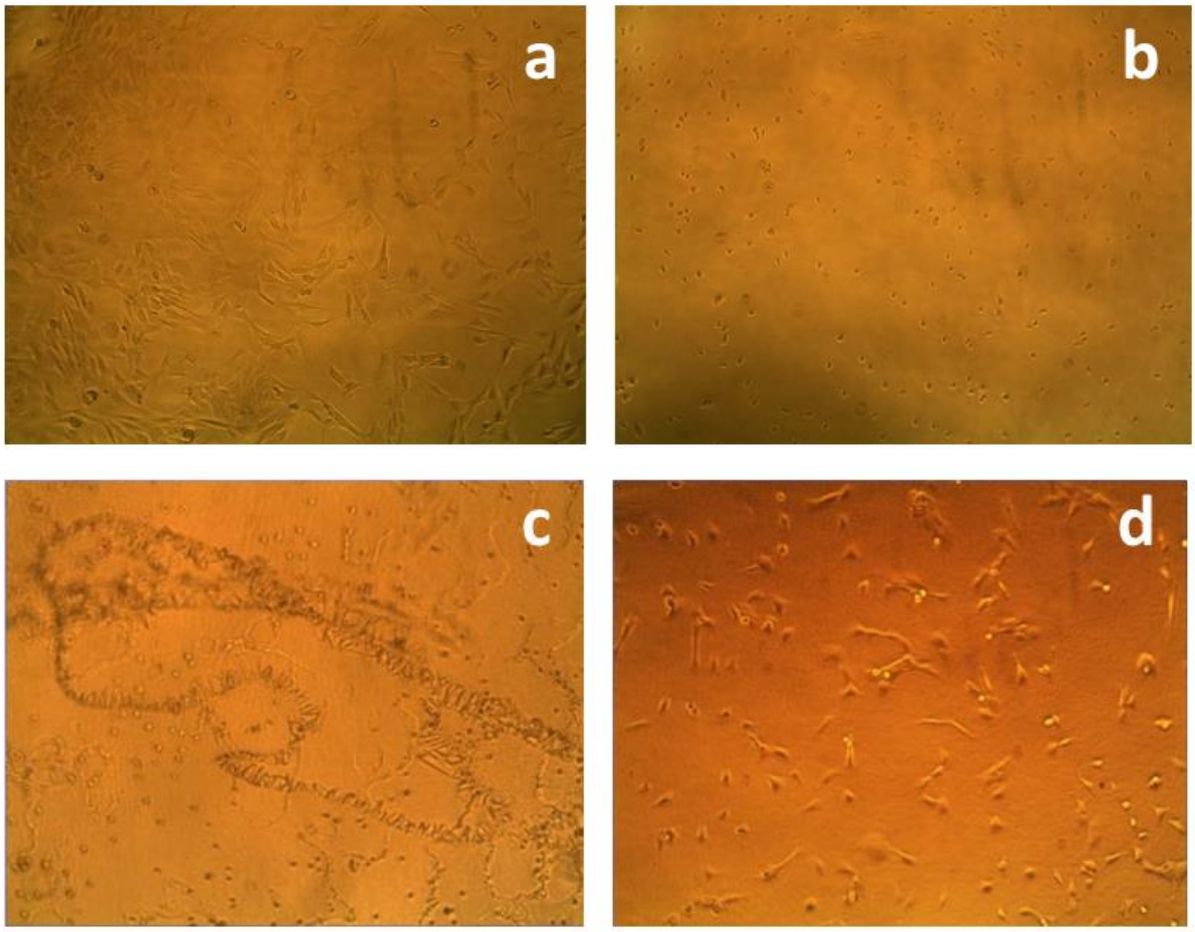

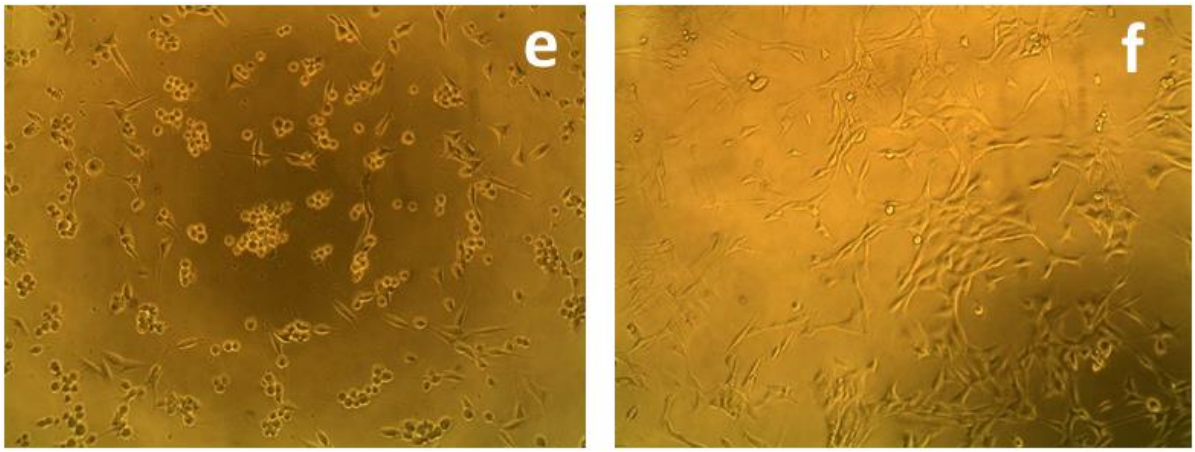

Figure 33: Optical microscopy pictures of 3T3 fibroblasts after 24 hours of incubation in DMEM **a**), DMEM + Triton X-100 **b**), sample 3 in concentrations of 10 mg/ ml **c**), Sample 3 in concentrations of 5 mg/ ml **d**), sample 9 in concentrations of 10 mg/ ml **e**), sample 9 in concentrations of 5 mg/ ml **f**).

Direct contact cytotoxicity

Direct contact cytotoxicity with the tested materials (samples 1 – 9) was evaluated by measurement of cell metabolic activity after 24 hours of incubation and the results are shown in **Figure 34**. The tested foils were floating in the media with subtle contact with the bottom where the cells were grown. Therefore, slightly limited metabolic activity in the wells containing material does not mean the cytotoxic effect of the material. The limited metabolic activity in the wells containing materials also may be observed due to the mechanical damage during foil removal after 24 hour incubation. Measured cell viability for samples 1, 2 and 4 - 8 in contact with foils reached 80-90% of metabolic activity of cells cultured in complete medium. No significant reduction in cell metabolism has been observed for the mentioned samples, therefore materials could be considered as cytocompatible with 3T3 mouse fibroblasts upon direct contact. Samples 3 and 9 were signified to be cytotoxic as the overall metabolic activity decreased up to 25% and 11% respectively of control cells. Moreover, their metabolic activity was also comparable to control cells. Similar results were achieved by Optical microscopy (**Figure 35**).

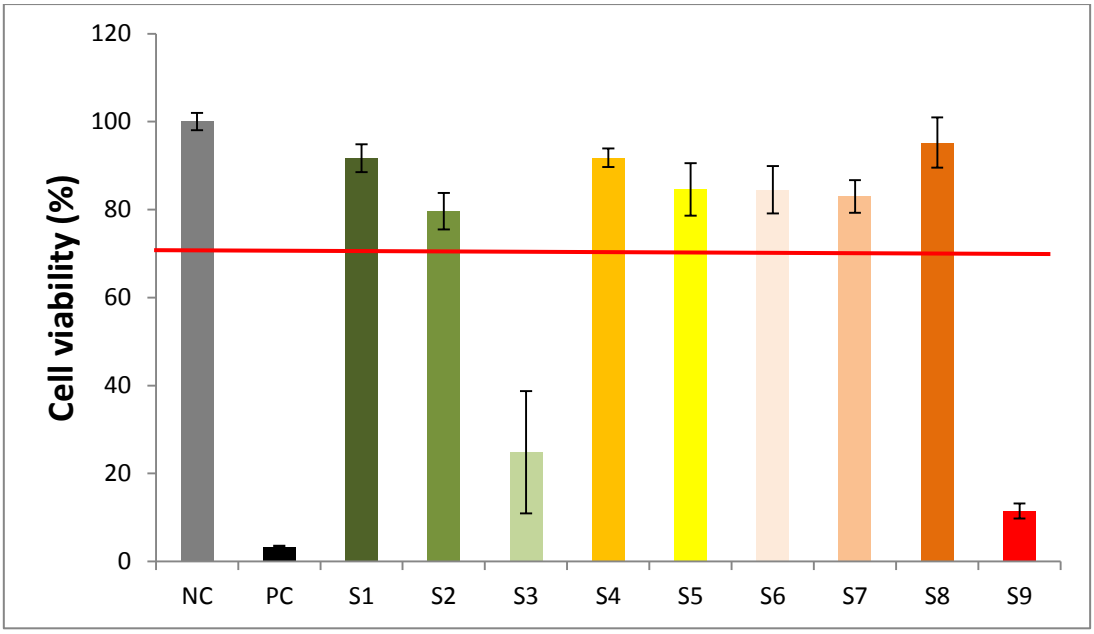

Figure 34: Metabolic activity of fibroblasts after 24 hours incubation in complete medium (NC), in complete medium + Triton X-100 (PC), in complete medium with presence of samples 1 – 9.

Before MTT assay, the incubated cells were assessed microscopically. Control cells cultured in complete media created a confluent layer of spread fibroblasts after 24 h incubation (**Figure 35 a**). When cytotoxic Triton X-100 was present, floating dead cells were seen (**Figure 35 b**). Cells in wells with samples 1, 2 and 4 - 8 were viable with normal morphology. Well plates containing these tested materials were covered with cells. In case of samples 3 and 9, mostly dead cells were found in the wells containing samples. But farther away from these two samples, mixtures of dead and alive cells were observed. The direct contact effect of samples 3 and 9 are exhibited by **Figures 35 c, d**.

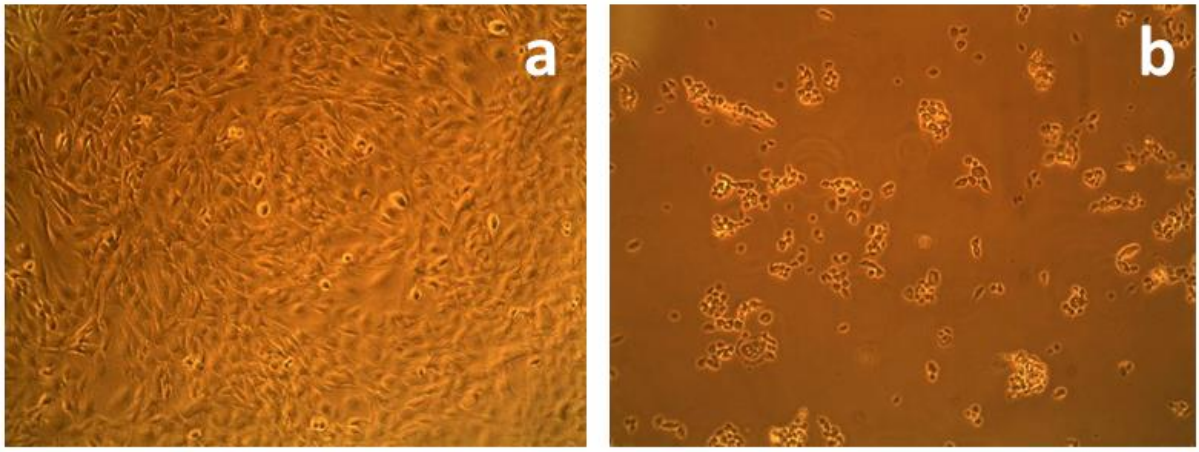

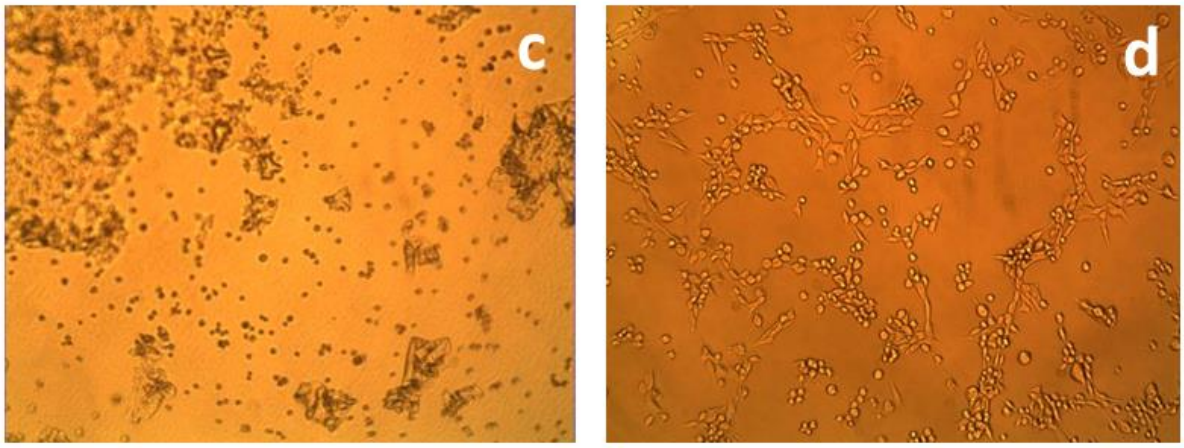

Figure 35: Optical microscopy images of 3T3 fibroblasts grown in presence of DMEM **a**), DMEM + Triton X-100 **b**), cells in the bottom of well plate containing sample 3 **c**) and cells in the bottom of well plate containing sample 9 **d**).

4.2.3.4. Cell adhesion

Staining of adhered cells by phalloidin - FITC in green and DAPI in blue on tested foils (Samples 1 – 8) was used to visualize cell spreading and adhesion after seeding the cells on the top of the materials. Fluorescence microscopy pictures after incubated for 1 day and 7 days are depicted in **Figure 36**. After 1 day, the highest cell adhesion rate was observed within materials 1 and 8. Cells were more spread than on the other samples (samples 2 – 7). Sample 1 (pure Nylon 6) was covered by monolayer of the fibroblast cells. However, the foil was not covered by 100%. There were islets of monolayers and parts without any cells present. It suggested that longer time of incubation would be needed for 100% confluency of the sample 1 surface. After a week of culturing, sample 1 exhibited acceptable adhesion rate followed by high proliferation rate of the cells and cell monolayer with normal cell morphology was observed on the foil surface. On the contrary, after 7 days, the cells on sample 8 had unusual morphology; cell nuclei were bigger than normal cells with a lot of fragments around. After 1 day of incubation, the rest of the samples (samples 2 – 7) did not support cell adhesion as cellular spreading was very limited and only round cells with low amount of cytoplasm was found. After a week of incubation, cell numbers were also decreased further. This observation proposed that most of the samples did not allow further adhesion and proliferation of the cells during a week of culturing. The Nylon 6-NH (sample 2) and other grafter foils did not support fibroblast proliferation although no cytotoxicity of the samples were detected except sample 3. On the samples 5 and 7, occasional monolayer of cells were observed in forms of separated islands. Cell adhesion of fibroblasts to all tested surfaces (samples 1 – 8) after 1 day incubation is depicted in the first column of the **Figure**

36 (**a_1** – **h_1**). The second column in **Figure 36** (**a_2** – **h_2**) represents cell adhesion after 7 days of incubation for the same samples.

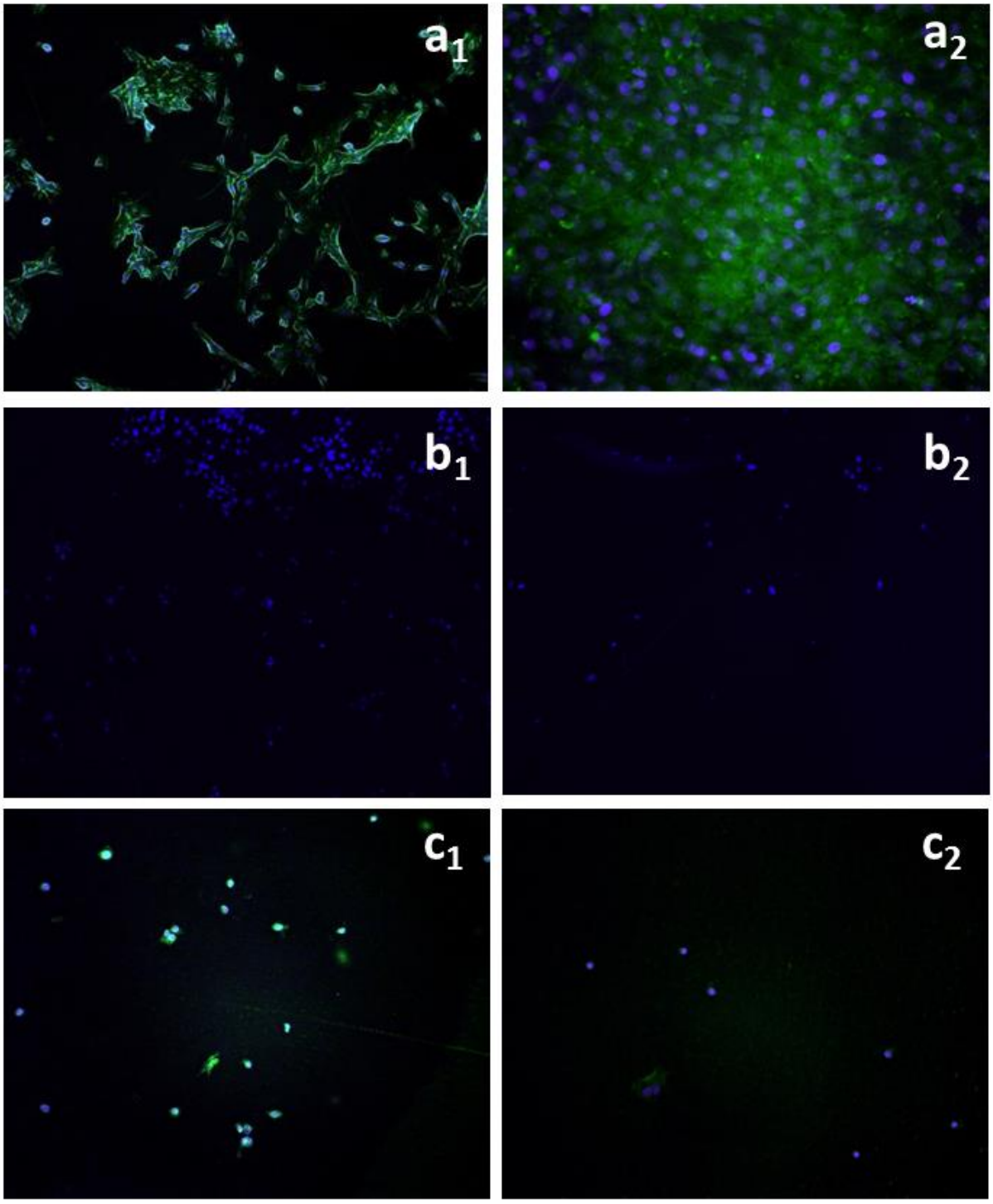

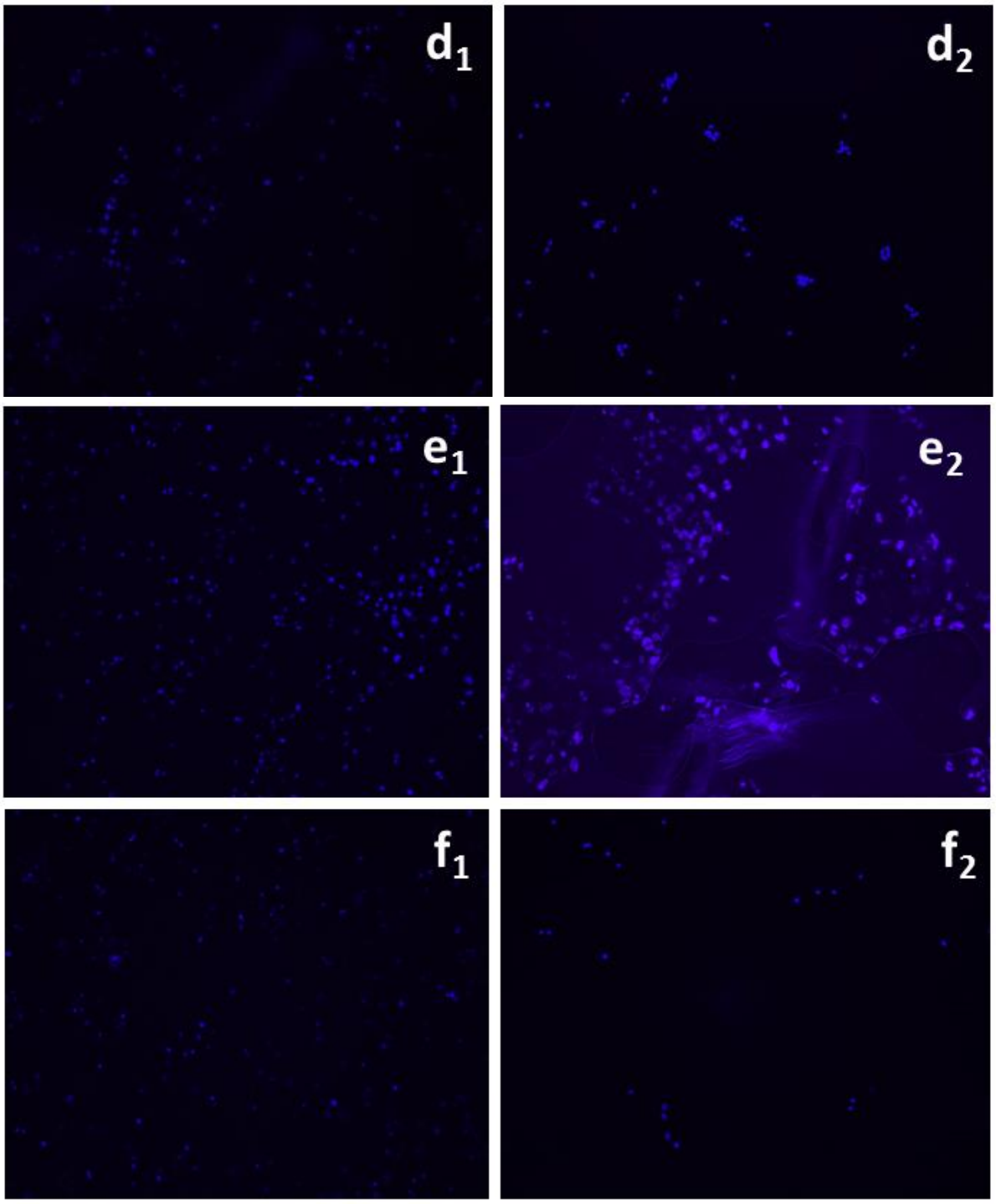
d_1
d_2
e_1
e_2
f_1
f_2

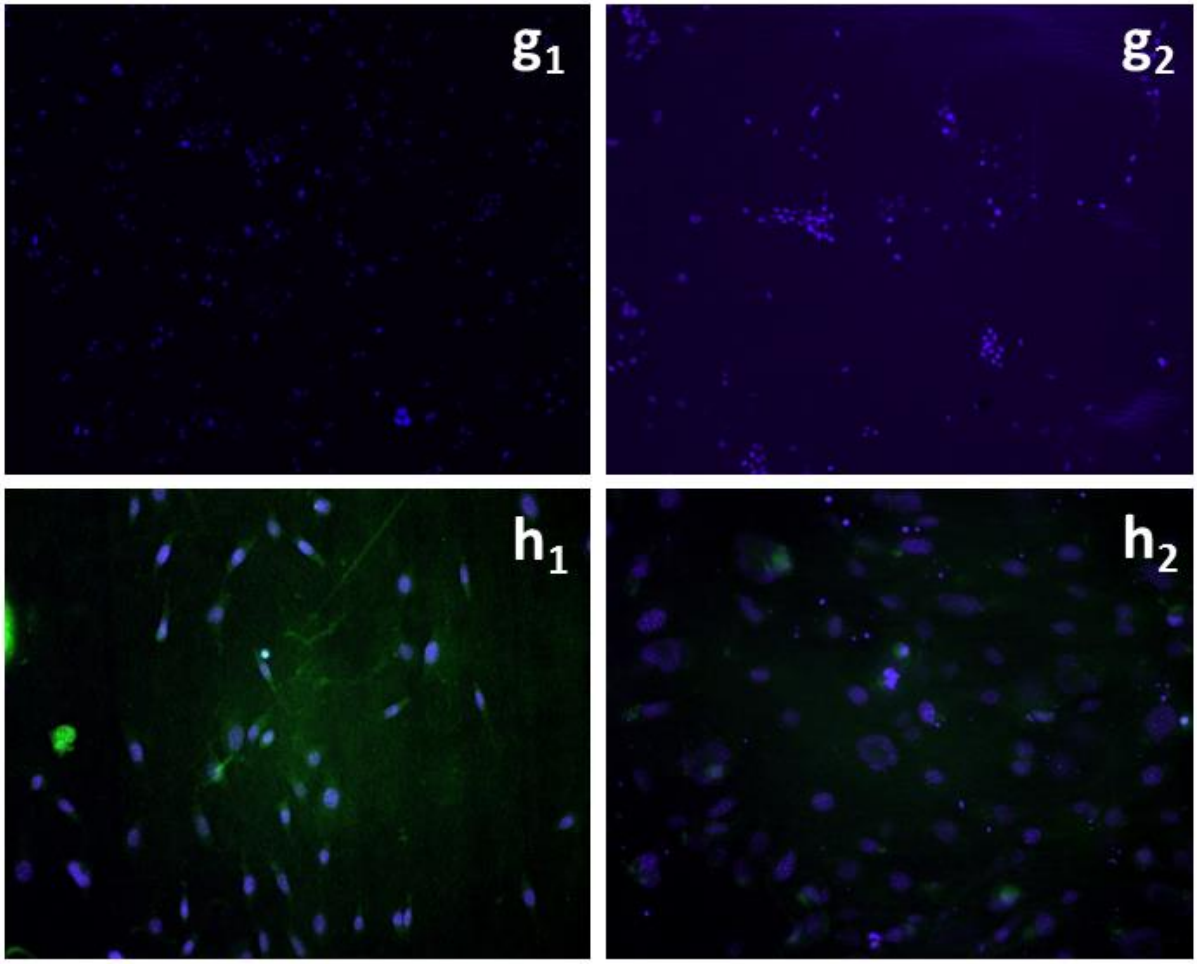

Figure 36: Fluorescence microscopy pictures of foils seeded with fibroblasts after 1 day of culturing for samples 1 – 8 **a_1** – **h_1**) and after 7 days of culturing for samples 1 – 8 **a_2** – **h_2**) [objective 20X].

Cell spreading on pure and functionalized Nylon 6 foil surfaces was assessed by scanning electron microscope (SEM). The results are in agreement with outcomes from fluorescence microscopy described above. 1 day after seeding, cells adhered on the surfaces of foils. Differences in cellular spreading were observed after 7 days. Rounded small cells indicated low adhesion while fully spread cell with creation of fillopodia signifies strong adhesion of cells to the surface. SEM also enabled the visualization on surface of tested materials. Mostly, smooth foils were captured except for sample 5. Increased surface roughness could have influenced cell material interactions. In samples 5, 7 and 8, occasional monolayers were formed (such as observed by fluorescence microscopy). Reduced number of cells after 7 days of incubation was found on samples 2, 3, 4 and 6. Sample 1 showed high proliferation on the sample surface. **Figure 37** (**a** – **h**) represents the SEM pictures depicting fibroblasts captured on tested samples after 7 days of incubation.

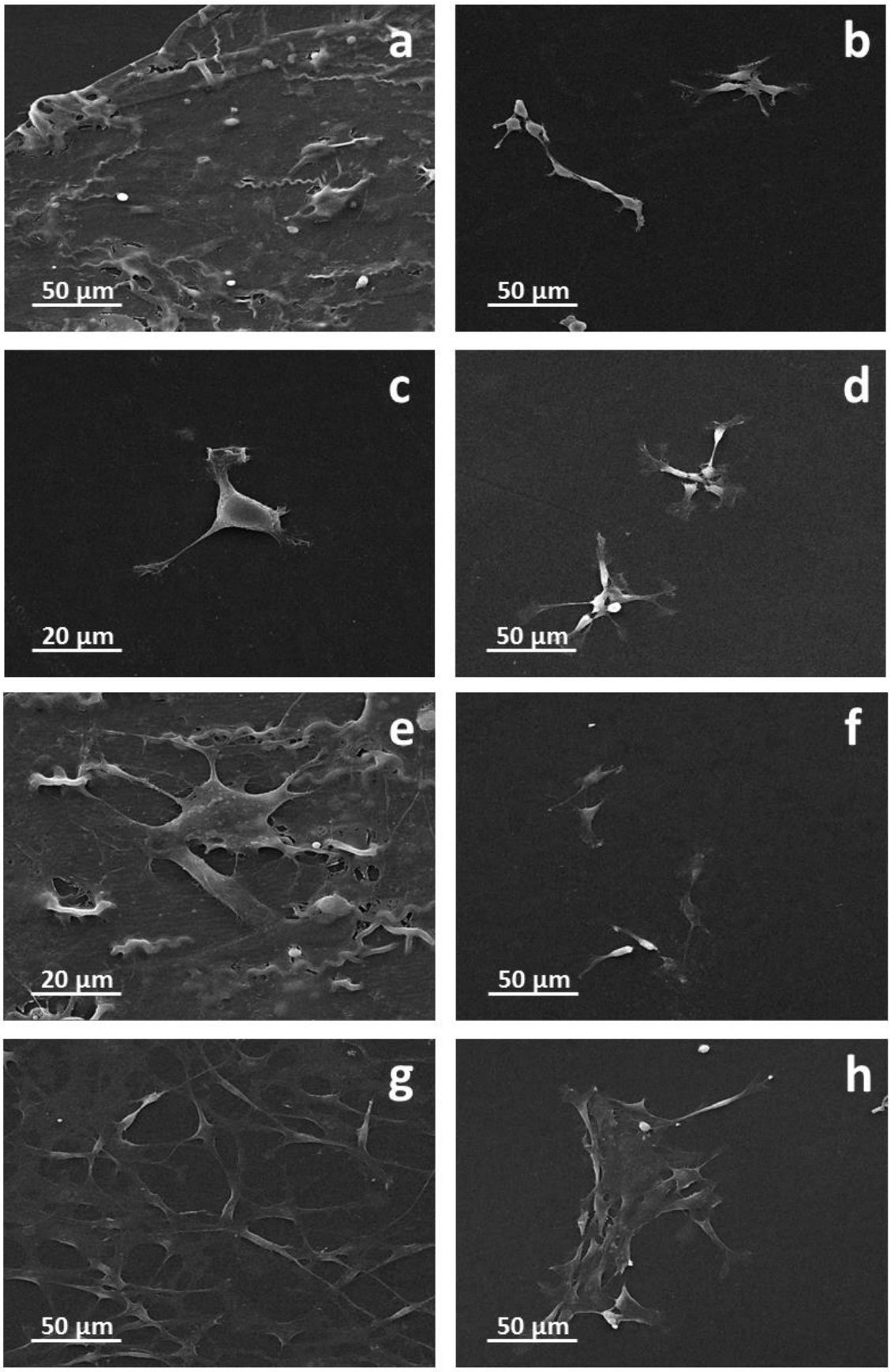

Figure 37: SEM images of fibroblasts captured on tested foils after 7 days of incubation for samples 1 – 8 **a** – **h**).

The PEG based antifouling coatings have been widely reported in various literatures [168–170]. PEG immobilization is the most commonly used approach to impart protein resistance to the surface. Therefore, it was expected that the cell adhesion would be affected on grafted samples of Nylon 6 (samples 3 – 8). Surprisingly, Nylon 6-NH did not allow the fibroblast cell to adhere on the surface although it demonstrated cytocompatibility. Pure Nylon 6 surface provided suitable condition for cell adhesion and proliferation.

Functional metabolic assay (colorimetric MTT assay after 1 and 7 days cell seeding) was used in order to quantify cell viability on tested materials. Results are summarized in **Figure 38** (**a**, **b**). After 1 day, low metabolic activity was measured in all tested samples including the control (tissue culture plastic - TCP). During 7 days of experiments, metabolic activity of cultured cells was increased in TCP and sample 1. On the contrary, cell metabolic activity decreased after 7 days of incubation for the Nylon 6-NH (samples 2) and all the grafted samples (samples 3 – 8). This observation implies that these samples were with a very limited metabolic activity. The outcome confirms assumption of low adhesion of cells to Nylon 6 modified samples. Materials were found to be non-adherent for cells that could be beneficial for certain applications.

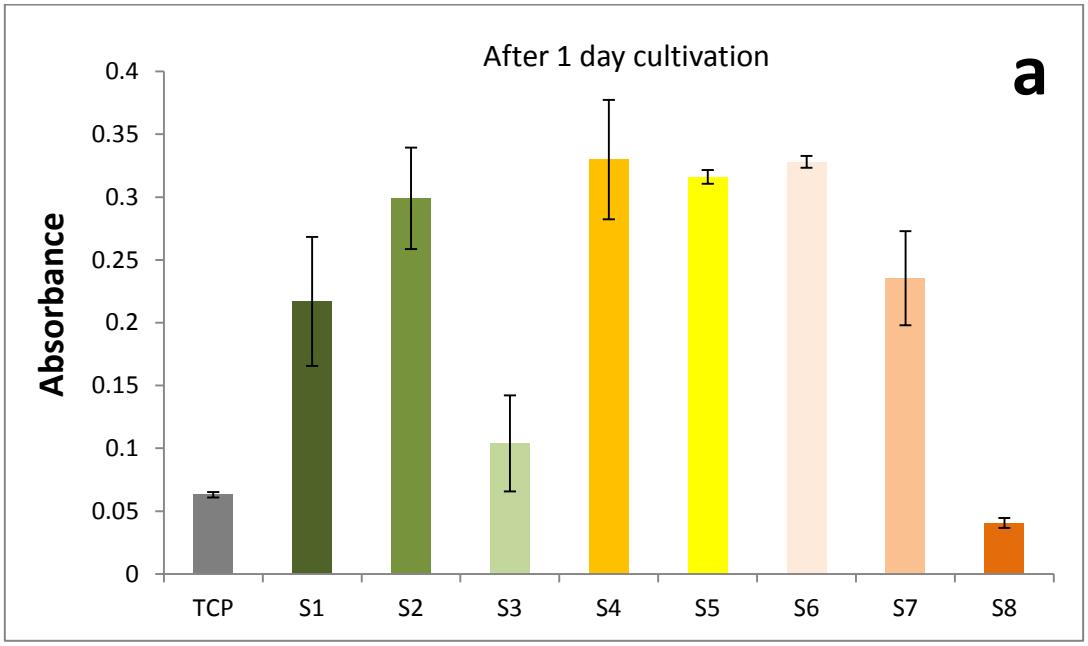

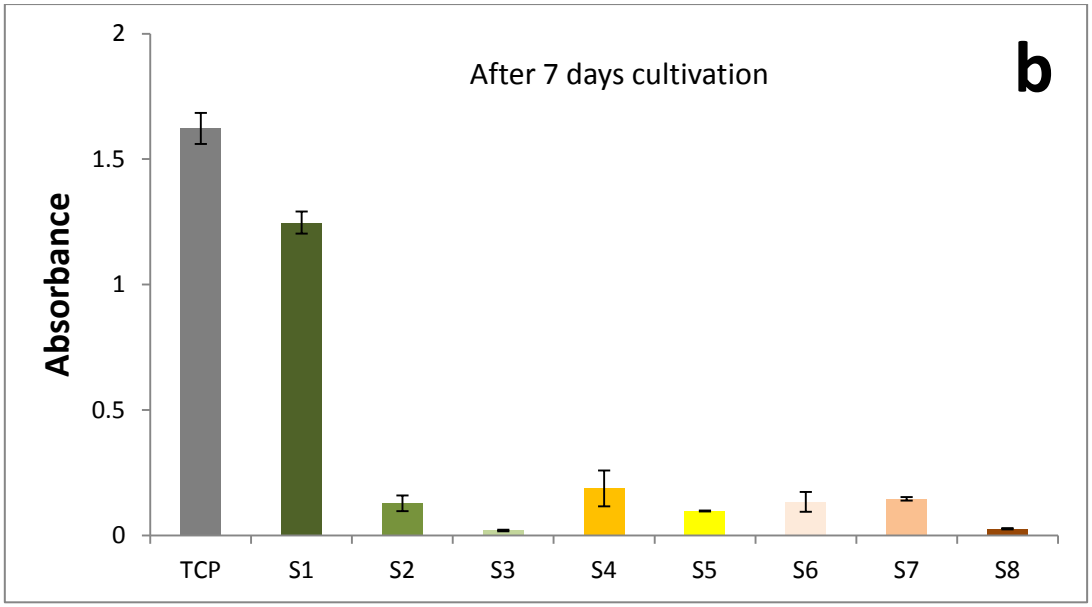

Figure 38: Metabolic MTT test of control (TCP) and tested samples (1 - 8) seeded with fibroblasts after 1 day **a**) and 7 days **b**).

Antibacterial tests for modified Nylon 6-NH and PEG-CH_3 chain grafted Nylon 6 samples against both Gram positive (*S. aureus*) and Gram negative (*P. aeruginosa*) pathogenic bacterial strains exhibited significant effectiveness on the bacterial adhesion compared to pure Nylon 6 sample. Water contact angle values played important role on bacterial adhesion resistance. The increased hydrophilicity imparted positive influence on the bacterial adhesion resistance and antibacterial effect of modified Nylon 6-NH and grafted samples compared to Nylon 6. Pure and most of the modified Nylon 6 samples (except samples 3 and 9), did not exhibit cytotoxicity for the fibroblast cells on direct contact; whereas, all the samples proved to be non-cytotoxic for the fibroblast cells under sample extract with the concentration of 5 mg/ ml. On the other hand, the cell adhesion was adversely influenced by the Nylon 6 surface modification.

4.3. Copper Nanoparticles (Cu NPs)

4.3.1. Synthesis of copper nanoparticles

The synthesis of Cu NPs by reduction is one of the common “bottom up” methods. This wet chemical technique has its own advantages and disadvantages, like other methods. The equation for the reduction of Cu^{+2} to the zero-valent Cu NPs is given below [146]:

$$Cu^{+2} + 2BH_4^- \longrightarrow Cu + H_2 + B_2H_6 \quad (1)$$

Here sodium borohydride ($NaBH_4$) was used as reducing agent along with sodium dodecyl sulphate (SDS) as capping agent to prevent the oxidation of Cu NPs in aqueous medium and the aggregation for ensuring the control on particle growth. The mechanism was seed-mediated growth via external reducing agent ($NaBH_4$) that induced nanoparticle formation in presence of SDS as surface stabilizer (**scheme 6**). The aqueous medium was densely populated with SDS surfactant micelles, as the concentration is above the critical micelle concentration (CMC) [146]. The Cu^{+2} ions in the solution accumulated at the negatively charged micelle head groups due to electrostatic attraction. During the addition of $NaBH_4$ (reducing agent), the electron transfer occurred from borohydride anions (BH_4^-) to copper cations (Cu^{+2}) and that led to the nucleation of copper atoms. The nascent nuclei tended to connect each other to make nanoparticles of definite shape and within a range of size [171].

Metal NPs including Cu NPs have been synthesized in variety of shapes including cube, cuboctahedron, octahedron, tetrahedron, decahedron, thin plate, and rod. NP shape is controlled by the thermodynamics and growth kinetics of the dynamic system composed of the inorganic core, the ligands (surfactant molecules), and the solution that contains chemical precursors and ligand species [172]. Here the shape of Cu NPs synthesised were cubical. Very recent studies have investigated the cube-shaped NP formation [173,174]. The Wulff construction has been used to predict the equilibrium shape of NPs, when Gibbs proposed that the equilibrium shape of a droplet of matter is determined by a surface energy minimization [173]. Intuitively, spherical or roughly spherical polyhedral shapes with the lowest surface-to-volume ratio (i.e. number of surface atoms over number of bulk atoms) are the most likely to form from NP seeds, although NPs with various shapes are obtained. For chemical synthesis, a shape-formation mechanism has been proposed, concerning the ability of surfactant ligands to move selectively on the NP surface, which allows specific

facets to grow instead of others as ligand adhesion decreases the energy. Thus, different growth rates result the specific NP shapes [174]. Temperature and ligand concentration are key parameters in this context. Liao *et al.* showed the sequential images for the growth of the platinum (Pt) nano-cube using high-resolution TEM (transmission electron microscopy) to explain the formation of cubic NPs from spherical seeds [173]. In our case, the same explanation may be applicable.

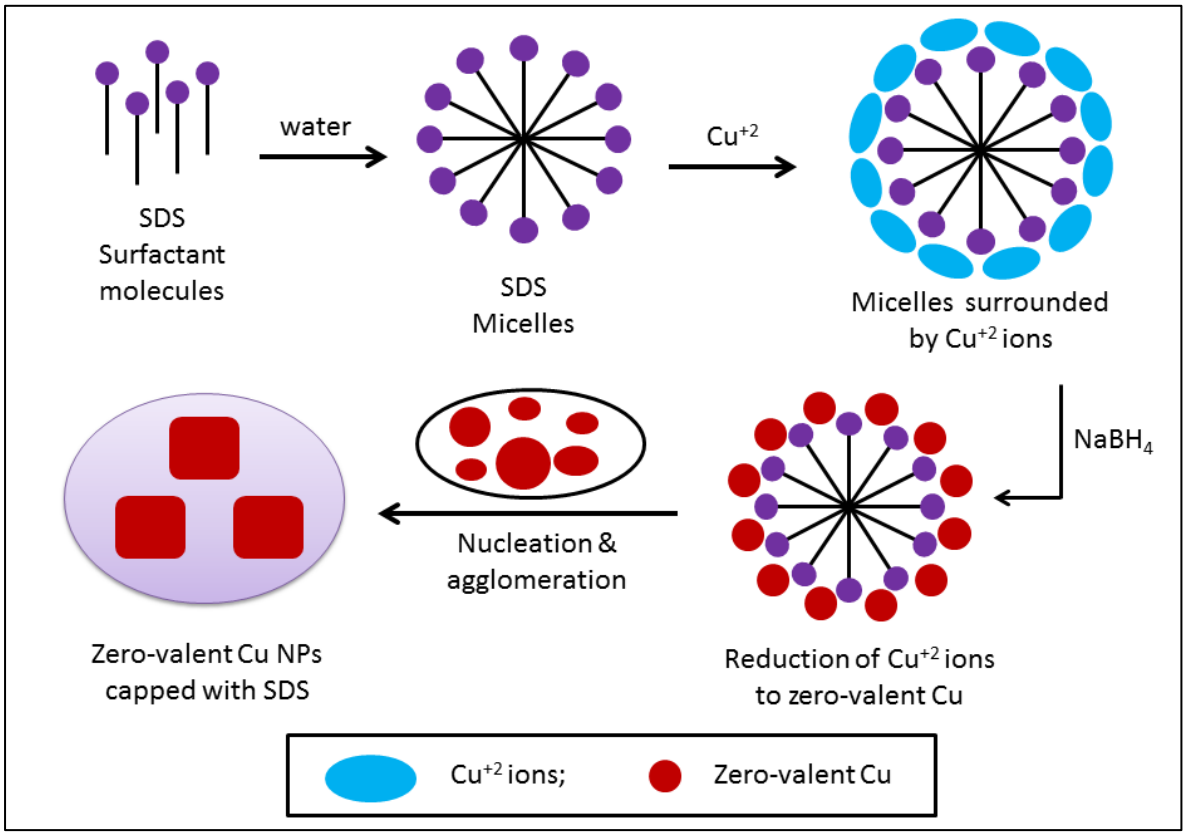

Scheme 6: Mechanism for the formation of Cu NPs in aqueous SDS solution.

4.3.2. Characterization

The DLS measurements were performed to determine the particle size and to evaluate the influence of the reaction time on the particle size. The sizes of the prepared Cu NPs at different time after reaction showed in **Figure 39**. In the graph, the intensity (%) was plotted against the various sizes of Cu NPs (nm). In DLS technique, the particles of different sizes scatter with different intensities in dependence of the scattering angles, therefore there are optimum angles of detection for different particle sizes. After 1 h of reaction the particle size was comparatively less with mean 342 nm, but after 24 h the particle size increased to range of 220 - 825 nm with the mean particle size 459 nm. During 1 h reaction, the colour of the aqueous solution was deep brown, whereas after 24 h the solution turned to

characteristic brick red colour that indicated the stability of Cu NPs in the solution in presence of SDS [175]. Moreover, the Cu NPs aggregated after 15 days forming larger particles with mean particle size 712 nm.

Table 10: The size of Cu NPs at different times after reduction

Time	Particle size range, nm	Average particle size, nm
1 h	51 - 825	342
24 h	220 - 825	459
15 days	460-955	712

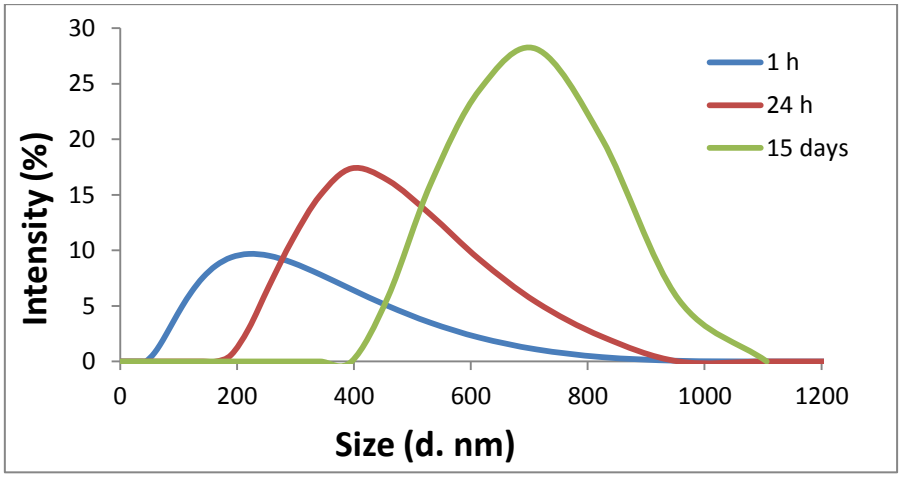

Figure 39: The Copper nanoparticle size distribution by intensity (%) at different time after reaction.

Figure 40 a shows the SEM micrograph of SDS capped Cu nanoparticles prepared by reduction of Cu^{+2} to the zero-valent Cu in aqueous solution. Large Cu NPs were formed after 24 h of reaction by the agglomeration in Cu seed particles, which are nearly spherical in morphology [176]. The seed particles grew exclusively to cubic ones. The particle sizes varied widely although the Cu NPs' morphology was uniformly cube-shaped for all particles. The histogram of particle size distribution (**Figure 40 b**) revealed that the seed particles of Cu agglomerated to form different batches of Cu NPs having different sizes in the wide range of 100 – 1100 nm (Mean = 466 ± 214 nm). This result is nearly corresponding with the particle size values by DLS, where after 24 h the mean particle size was detected as 459 nm. The histogram showed that almost 80% of all the measured particles were falling under 200 – 600 nm sizes. Further agglomeration was prevented by SDS that was used as nanoparticle stabilizer.

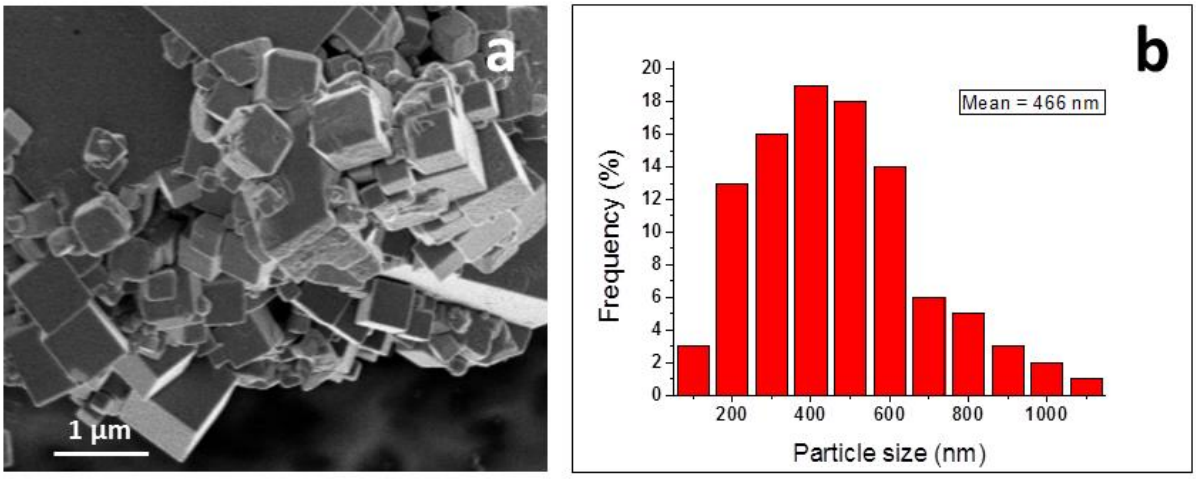

Figure 40: SEM image of SDS stabilized Cu NPs **a**) and a histogram of particle size distribution **b**).

Figure 41 shows the UV-VIS absorption spectra of the Cu NPs. No surface plasmon resonance (SPR) peak was observed after 15 mins reaction. The SPR peak appeared at 570 nm after 1 h of reaction. These results are in good agreement with the reported values of 550 to 590 nm [171]. This confirmed the formation of Cu NPs by the adopted procedure.

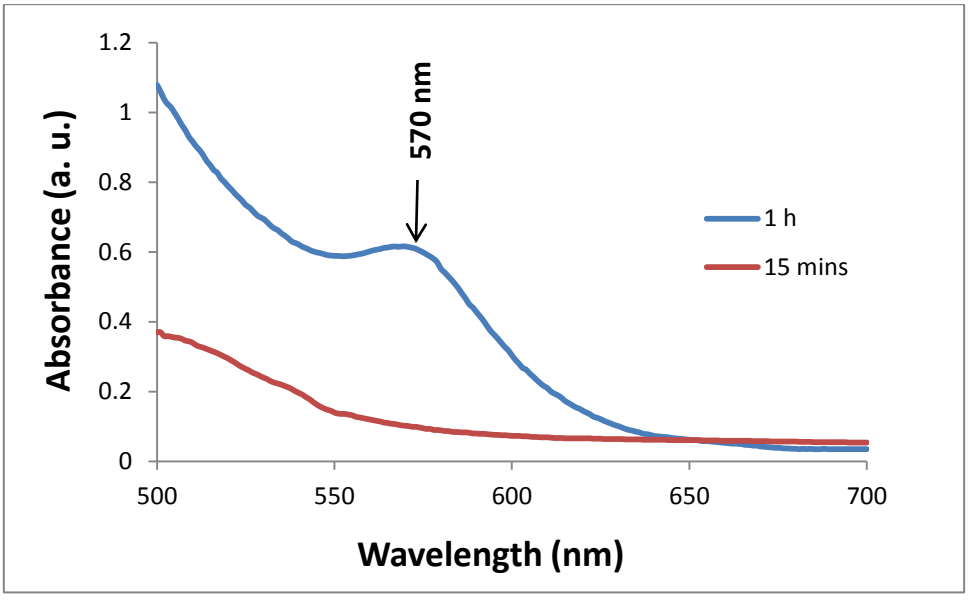

Figure 41: UV-VIS absorption spectra of Cu NPs in aqueous medium, prepared by reduction reaction.

The FT-IR spectra of SDS and SDS stabilized Cu NPs were studied to examine surface binding interactions (**Figure 42**). The characteristic stretching vibrations of SDS were identified at 3460 cm^{-1} (H-bonding due to absorption of moisture), 1471 cm^{-1} and 1383 cm^{-1} (-CH_3 asymmetric and symmetric stretching vibrations). Two absorption bands at 2923 cm^{-1} and 2853 cm^{-1} attributed to the asymmetric and symmetric stretching vibrations of

aliphatic tail group (-CH_2-) in SDS. The spectra bands at 1225 cm^{-1} and 996 cm^{-1} corresponded to sulphate head group (S=O) and C-O-S bond in SDS molecule [160]. Moreover, 1225 cm^{-1} band of pure SDS was blue-shifted to 1252 cm^{-1} due to the presence of Cu NPs. It confirmed the Cu NP stabilization due to the negatively charged head groups SDS [146]. The SDS capped Cu NPs exhibited red shifting of 996 cm^{-1} band to 952 cm^{-1}.

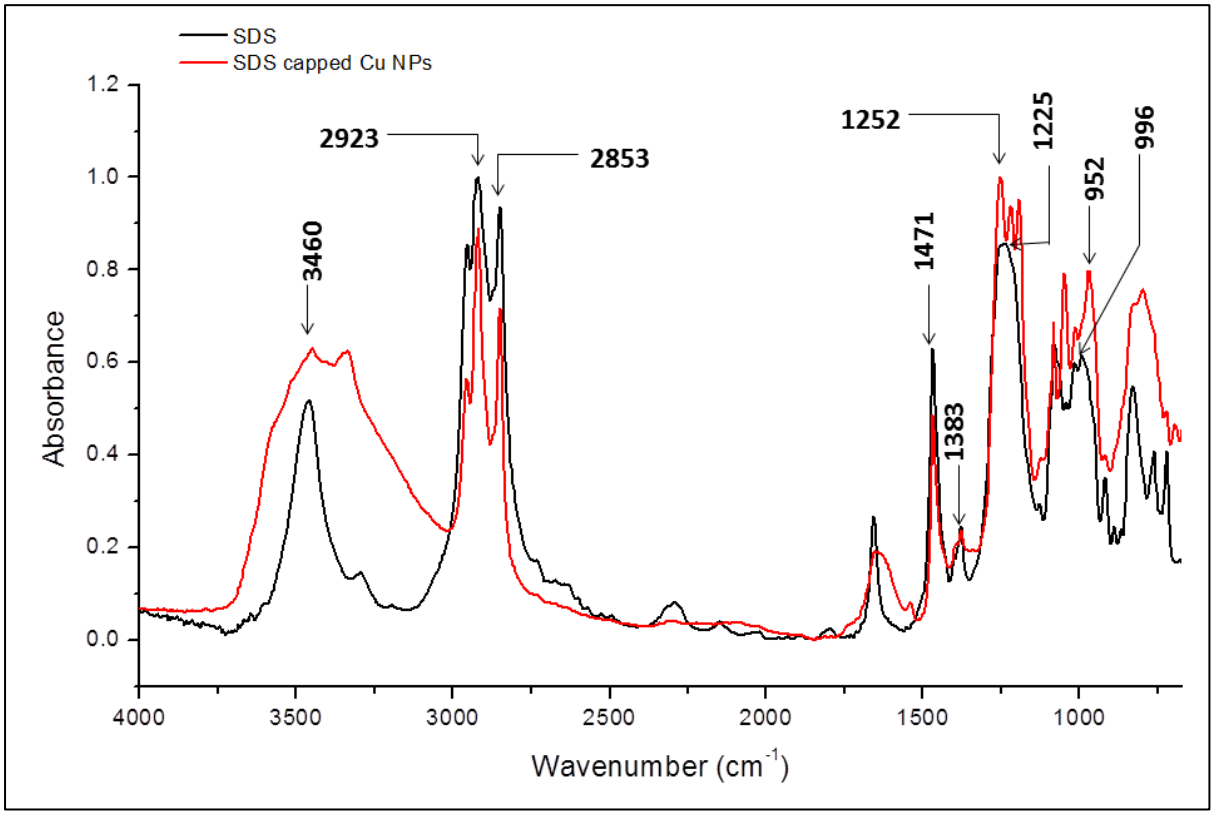

Figure 42: FT-IR spectra of SDS and SDS capped Cu NPs.

4.3.3. Application

The Cu NPs are used in various purposes including as antibacterial agent as we discussed earlier. Here, the prepared Cu NPs were used in the experiment for the deposition of Cu NPs on grafted Nylon 6 (Nylon 6-N-PEG-CH_3) surface (**Section 3.2.1.8.**) after characterization. In this specific work, the Cu NP deposited samples were examined for the efficacy of antibacterial activities for both Gram positive (*S. aureus*) and Gram negative bacteria (*P. aeruginosa*) (**Section 4.2.3**.). The Cu NPs collected after 24 h of reaction were used for the all the antibacterial tests and cytotoxicity assessments.

4.4. Mesoporous Silica Nanoparticles (MSNs)

4.4.1. Synthesis of mesoporous silica (SiO_2) nanoparticles (MSNs)

The schematic overview of the synthetic approach to mesoporous silica materials are shown in **scheme 7**. The synthesis of templated mesoporous silica follows as few steps: dissolution of template molecules (CTAB or P123) in the solvent (usually water), addition of the silica source (TEOS or fumed silica), stirring at required conditions to allow the hydrolysis and pre-condensation, recovery of the product and the final stage of template removal by calcination [135]. Hydrolysis may occur both in acidic or basic medium. The equations for hydrolysis and condensation of silicates are given below [177]:

Hydrolysis: $\mathbf{OH^- + Si(OR)_4 \rightarrow Si(OR)_3OH + RO^-}$ (1)

Condensation: $\mathbf{SiO^- + Si(OH)_4 \rightarrow Si{-}O{-}Si + OH^-}$ (2)

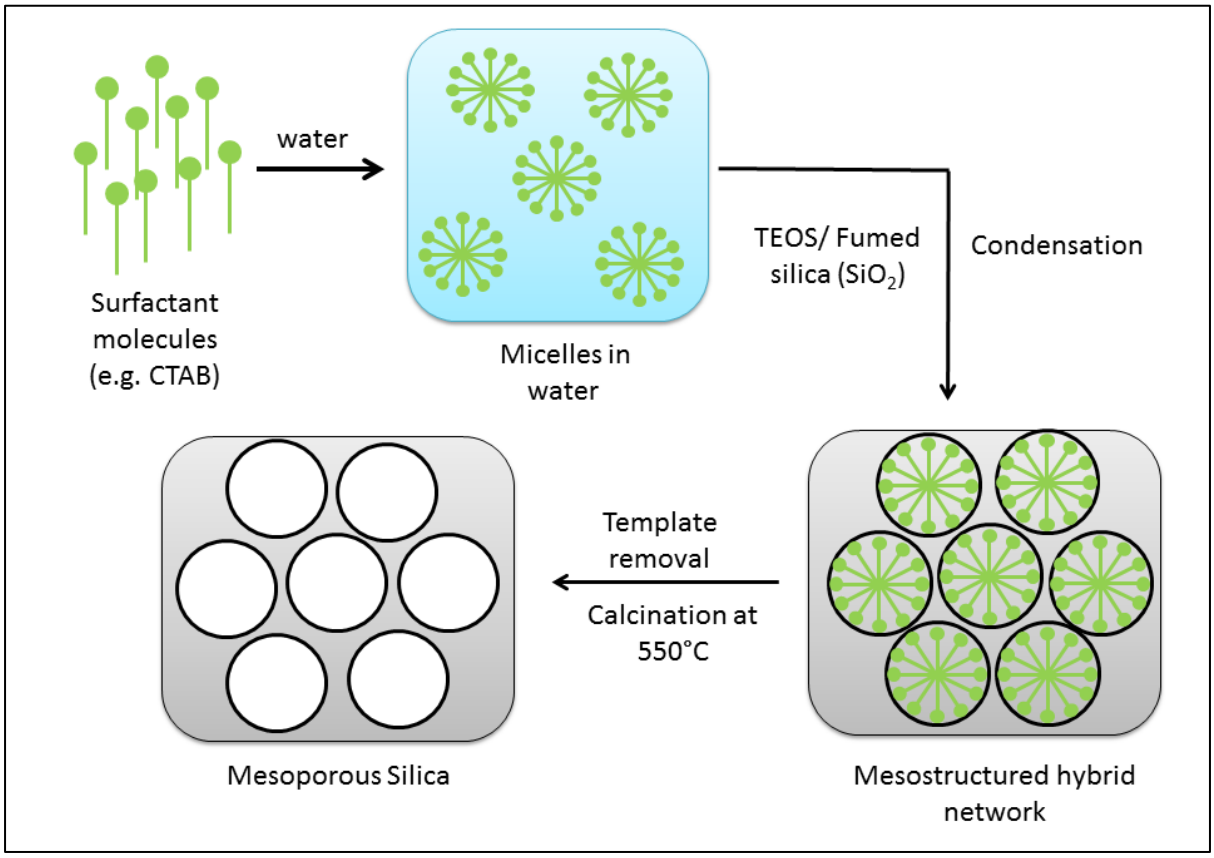

Scheme 7: Overview of synthetic approach to the mesoporous silica formation.

Soft templating, including micelle templating, offers an alternative facile and environmental friendly approach for MSNs preparation. The structure transformation of

amphiphilic surfactant organizations can be understood by the surfactant packing factor/ parameter, **g** = **V/ l.a_0**, where **V** is the volume of the hydrophobic chains in surfactant, **l** is the surfactant chain length, and **a_0** is the effective area of the hydrophilic head group of the surfactant at the interface [136]. Generally, surfactants with lower critical micelle concentration (CMC) are more favoured to obtain ordered structure. According to the classical micelle chemistry, above a critical value, g-packing factor increases and therefore, mesophase transitions occur. When g < 1/ 3, particles tend to form Pm3n cubic structure and mixed 3-D hexagonal structure and cubic structure; when 1/ 3 < g <1/ 2, particles tend to form p6mm hexagonal structure; when 1/ 2 < 2/ 3, particle tend to form Ia3d cubic structure; when g ~ 1, lamellar structures are favoured [135,136]. **Figure 43** depicts the schematic representation of surfactant behaviour in the aqueous medium as a function of g-packing factor.

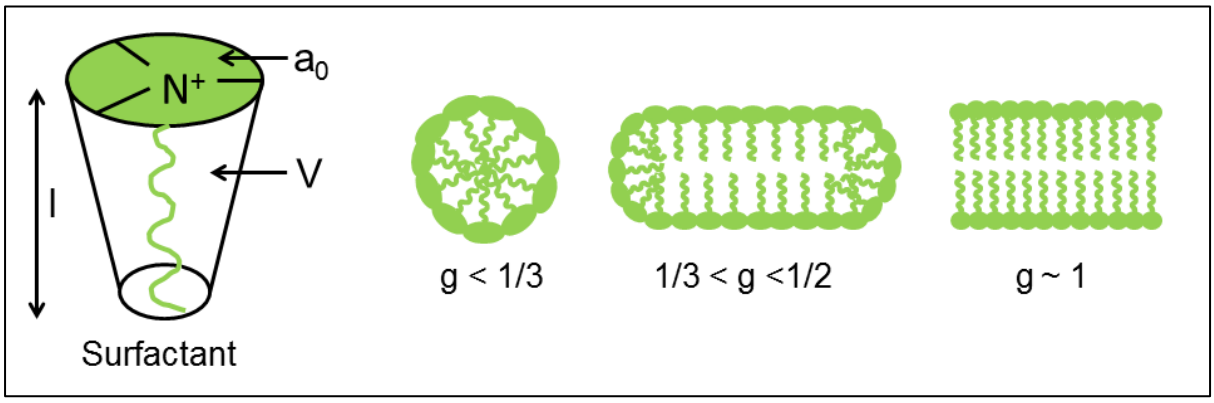

Figure 43: Surfactant behaviour in the aqueous medium as a function of g-packing factor.

The synthesis methods that were applied to produce the specific MSNs in this work are very well verified by various other researches many times [135]. It has been well established that by following these verified procedures the desired MSNs can be formed with distinct properties. Thus, the procedure used for MSNs are extremely reliable in terms of synthesis as well as characterization.

4.4.2. Characterization

The SEM micrographs in **Figure 44** (**a** – **g**) revealed that the obtained samples have different morphologies having various shapes and sizes. The particle sizes and shapes of different MSNs are summarized in **Table 11**. MCM-41 (FS) had agglomerated to form larger particles (> 1 µm), whereas MCM-41 (S) and MCM-41 (HO) showed highly ordered spherical and conical disc shaped nano-sized particles with polydispersity of particle size (**Figures 44 a** – **c**) [135,147,178]. The particle sizes of MCM-41 (S) were seen in the range of 200 – 900

nm. On the other hand, MCM-41 (HO) exhibited more uniform nanoparticles with sizes between 400 – 600 nm. **Figures 44 d, f** and **h** (MCM-48, PHTS and FCF respectively) exhibited the agglomeration of the MSNs into clusters (> 1 µm) where the smaller particles are also clearly visible. SBA-15 (**Figure 44 e**) revealed comparatively uniform particles in terms of shape (bagel-shaped) and size (300 – 500 nm) [179]. The structures of mesopores in the silica particles could not be evaluated by SEM. The nature of the porous structures was examined by BET analysis.

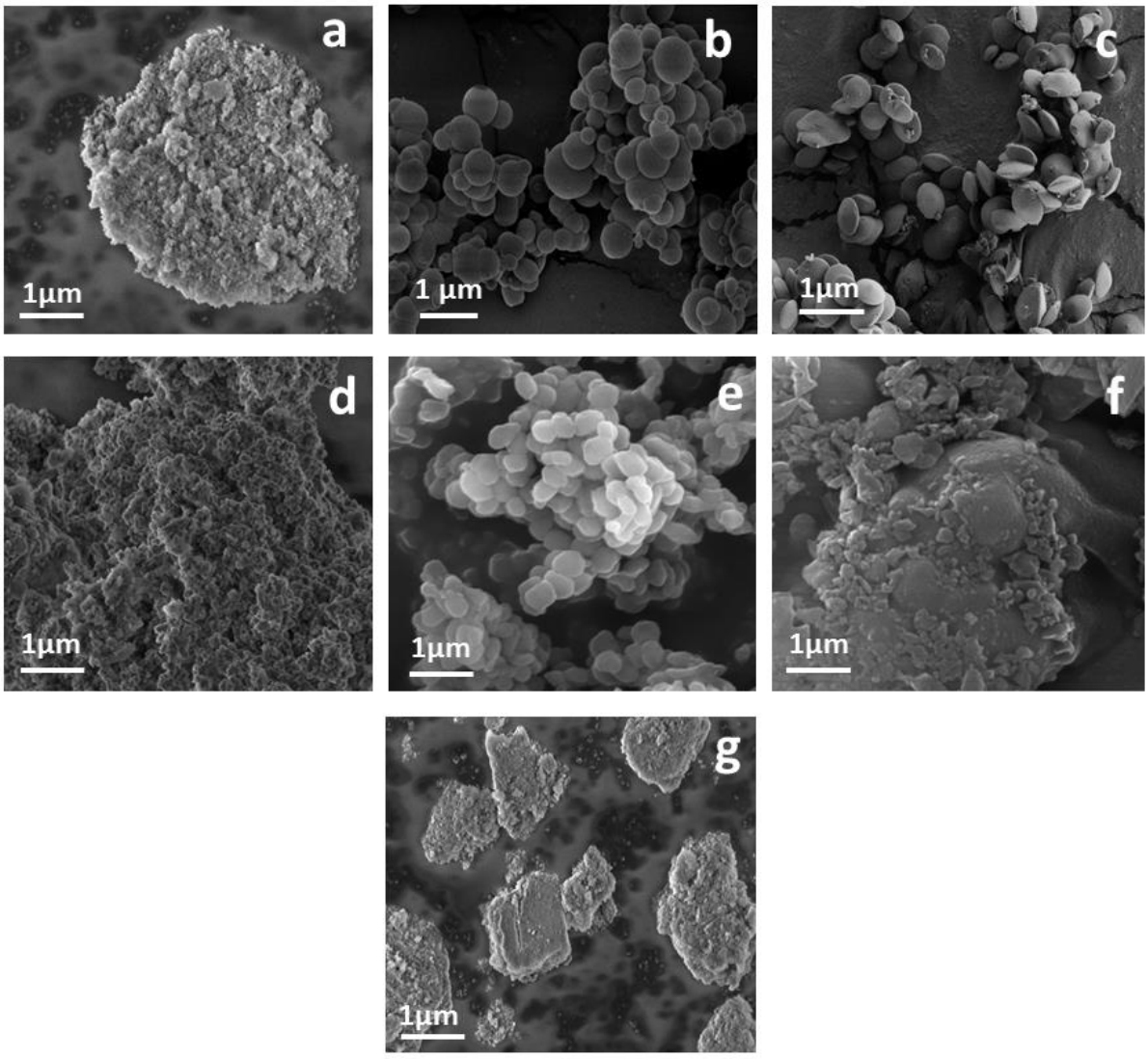

Figure 44: SEM images of MSNs: MCM-41 (FS) **a**); MCM-41 (S) **b**); MCM-41 (HO) **c**); MCM-48 **d**); SBA-15 **e**); PHTS **f**) and MCF **g**).

Table 11: The range of Particle size and geometry of the particles measured by SEM

Sample	Geometry	Particle size (nm)
MCM-41(FS)	agglomerated	>1000
MCM-41(S)	Spheres	200 - 900
MCM-41(HO)	Cone discs	400 - 600
MCM-48	agglomerated	>1000
SBA-15	Bagel-shaped (Short rods)	300 - 500
PHTS	agglomerated	>1000
MCF	agglomerated	>1000

Figure 45 shows N_2 adsorption and desorption isotherms of the three different MCM-41 samples prepared, which can be classified as type IV isotherms according to the IUPAC classification and that is typical to the mesoporous silica materials [180]. MCM-41 (FS) showed hysteresis loop typical of parallel cylindrical pores [181]. MCM-41 (S) and MCM-41 (HO) exhibited similar N_2 sorption isotherms where an increase in adsorption took place above $P/P_0 = 0.2$, suggesting the capillary condensation of N_2 within the pores and confirmed the presence of mesopores [180].

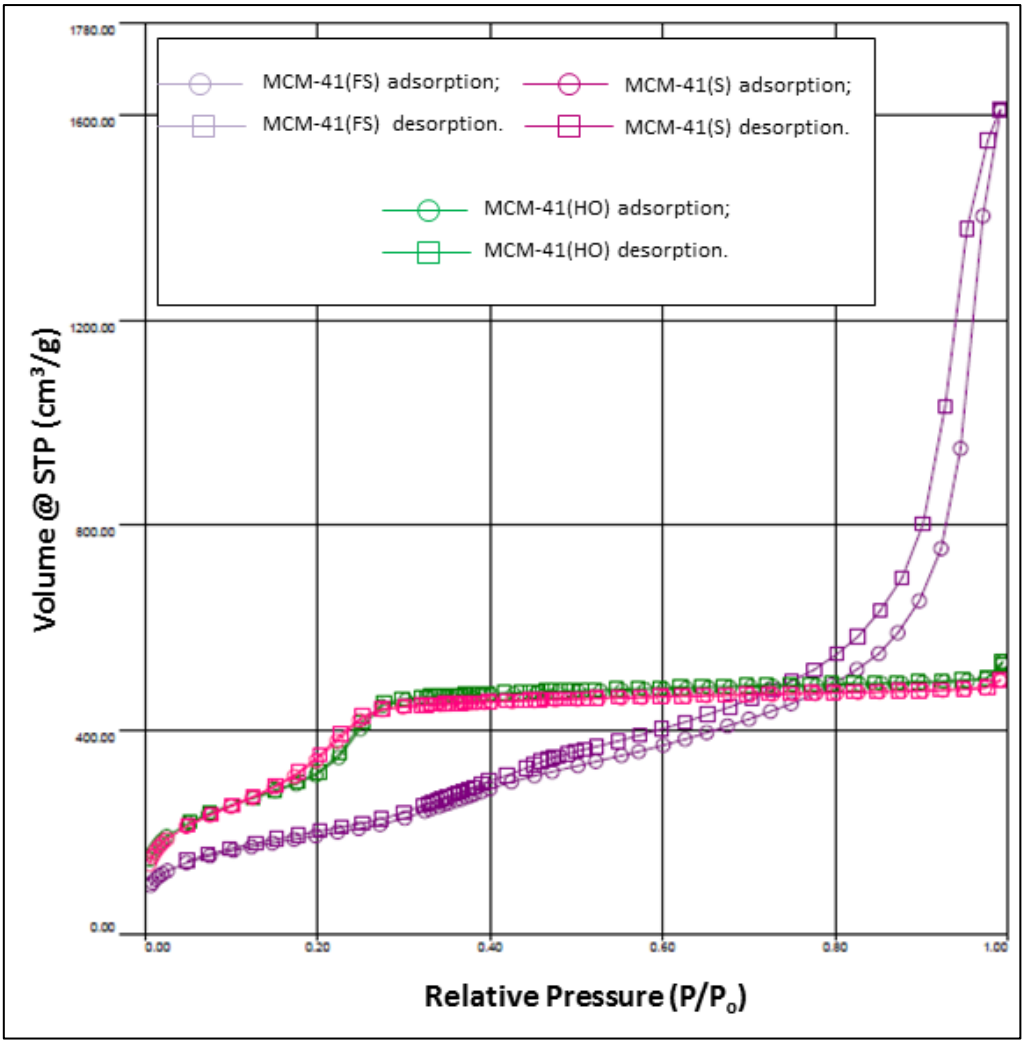

Figure 45: N_2-sorption isotherms at -196° C for MCM-41 (FS), MCM-41 (S) and MCM-41 (HO).

Figure 46 shows the N_2 sorption isotherms of rest of the other four MSNs: MCM-48, SBA-15, PHTS and MCF. All the samples exhibited type IV isotherms as MCM-41. MCM-48 demonstrated adsorption isotherm at higher relative pressure ($P/P_0 > 0.9$) that corresponds to N_2 condensation in the interparticle voids and also reflects the small size of mesoporous [182]. SBA-15 exhibited H1 hysteresis loop starting from $P/P_0 = 0.6$, that is characteristic of SBA-15 with highly ordered pores [179]. The adsorption-desorption behaviour of PHTS was consistent with a structure comprising both open and blocked cylindrical mesopores [183]. PHTS showed two-step desorption where the first desorption step was similar to that of SBA-15, indicating the open mesopores. The second desorption step of PHTS was attributed to the plugs (NPs) within the mesoporous (**Figure 47**). For the plugged pores, desorption was delayed resulting in second desorption [135]. The hysteresis loop was appeared at $P/P_0 = 0.4 – 0.75$. MCF The MCF N_2 sorption isotherm with characteristic long H2 hysteresis loop was good agreement with other articles [184].

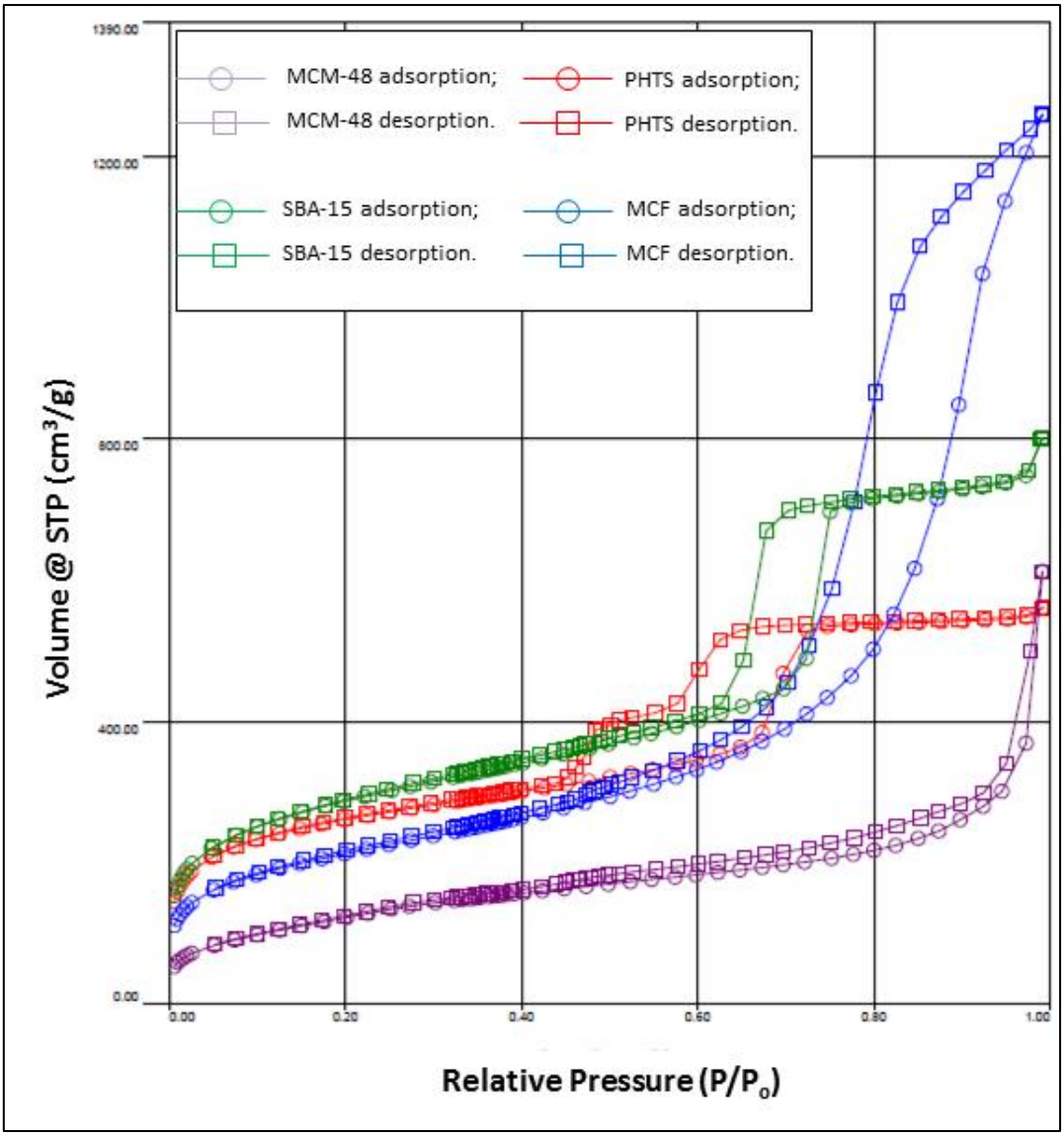

Figure 46: N_2-sorption isotherms at -196° C for MCM-48, SBA-15, PHTS and MCF.

Figure 47 depicts the difference between usual mesoporous material (e.g. SBA-15) and PHTS with plugged pores. PHTS mesopores are narrowed by nanoparticles (plugs) to create inkbottle-like sections. On the contrary, SBA-15 has open mesopores [135]. Usually, small micropores are also exhibited on the walls of MSNs.

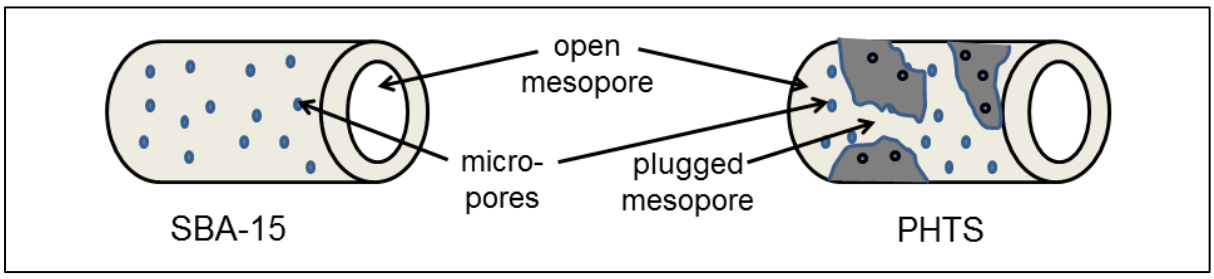

Figure 47: Schematic representation of the pore structure: SBA-15 and PHTS.

The characteristics of calcined mesoporous silica materials were analysed by BET for examining specific surface areas and the pore size distributions were determined by BJH model that were further verified by new DFT model. All the results are summarised in **Table 12**. The previously widely used BJH model is no longer recommended for such applications in micro-mesoporous materials examination as it can significantly underestimate the pore size for narrow mesopores (for pore diameter smaller than 10 nm the pore size may be underestimated even by 30 %) [185]. However, BJH modelling was used to compare the synthesised materials with the specifications found in the literature [135]. The results were good agreements with the previously mentioned published literature. All the MCM-41 samples exhibited high specific surface area lying between 700 – 1120 m^2/ g. The pore diameters are in the range of ~2 – 4 nm, although their morphologies were different. MCM-48 showed relatively low surface area (470 m^2/ g) compared to other MSNs, although the pore diameter is similar to the MCM-41 (S) sample. The specific surface area of SBA-15 was high (1020 m^2/ g) with larger pore diameter (~8 nm) compared to MCM series. PHTS also displayed high surface area with 940 m^2/ g and the pore diameter of open pores were in between 5 – 7.5 nm, whereas the plugged pores were less than 2 nm. In this case, the DFT was considered as more reliable than BJH as there was a significant difference in adsorption/ desorption pore diameter for plugged pores. MCF displayed highest pore size of 15 – 10 nm with 760 m^2/ g surface area. MCM-41 (FS), SBA-15 and MCF exhibited comparatively higher pore volumes (2.34, 1.17 and 1.88 cm^3/ g respectively). On the other hand, MCM-41 (S), MCM-41 (HO), MCM-48 and PHTS possessed the pore volumes ~0.7 – 0.8 88 cm^3/ g.

Table 12: Characteristics of calcined MSN samples

Sample	BET specific surface area (m^2/ g)	Pore volume (cm^3/ g) [DFT model]	Pore diameter (nm)		
			DFT model	BJH model	
				Adsorption branch	Desorption branch
MCM-41(FS)	700	2.34	4.41	2.87	3.07
MCM-41(S)	880	0.72	3.18	2.12	2.14
MCM-41(HO)	1120	0.75	3.3	2.25	2.26
MCM-48	470	0.77	3.18	2.12	2.22
SBA-15	1020	1.17	7.59	8.97	6.33

PHTS	940	0.83	5.06, 1.64	7.12, 0.89	5.23, 3.87
MCF	760	1.88	11.68	15.43	10.19

For all the synthesized MSNs, N_2 sorption isotherms, BET and BJH (verified by DFT) data regarding pore sizes, surface areas and pore volumes were compatible with the verified once given in the literature [135]. Therefore, the pore structures (morphologies) are suggested to be the same as demonstrated in various literature mentioned earlier. **Figure 48** shows the transmission electron microscope (TEM) pictures of various MSNs prepared here. MCM-41(all 3 types) and SBA-15 formed hexagonal mesopores whereas, MCM-48 formed cubic structured mesopores. PHTS exhibited hexagonal large mesopores with micropores On the other hand, very large mesopores were seen in MCF.

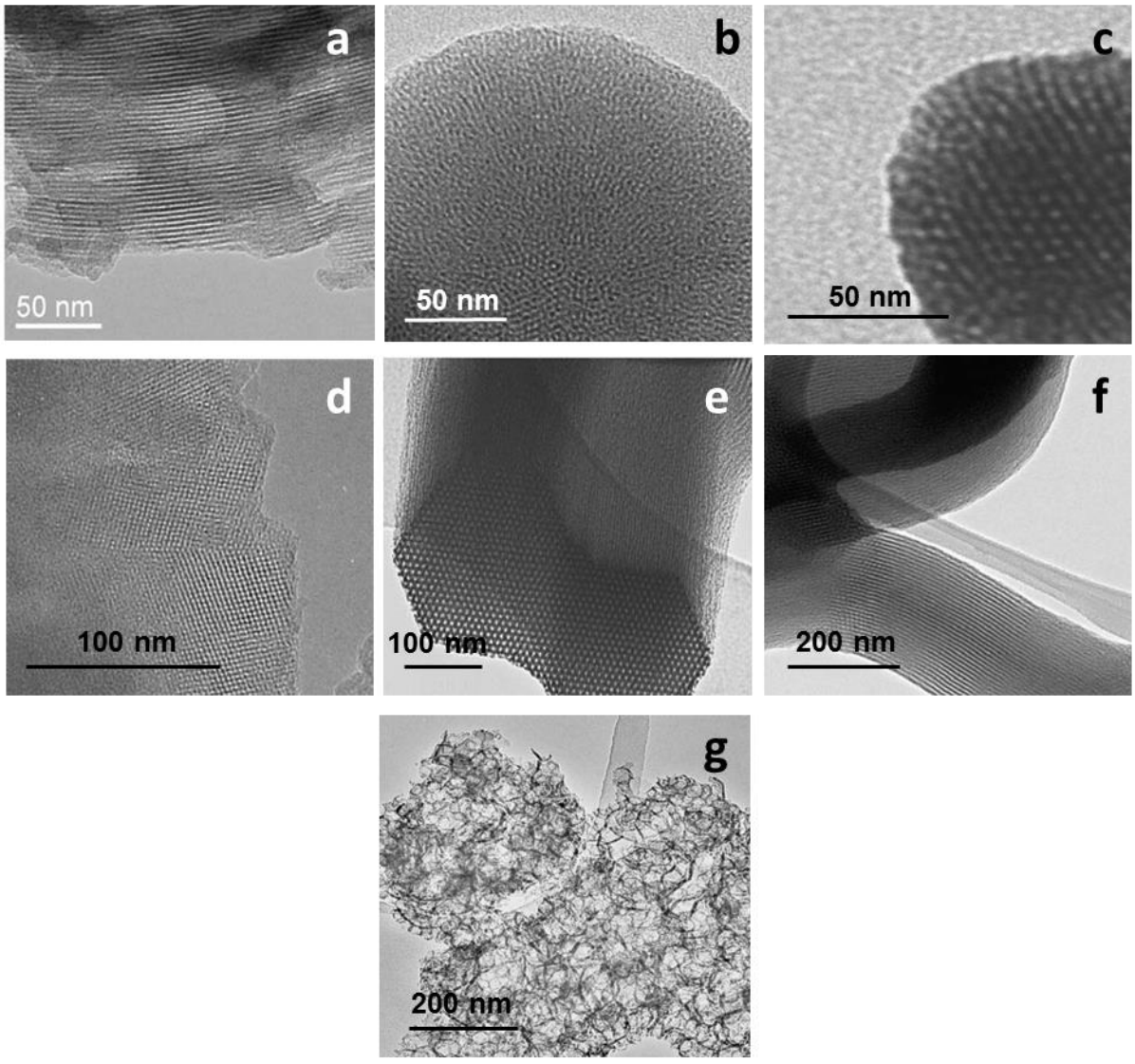

Figure 48: TEM images of MSNs: MCM-41 (FS) **a**); MCM-41 (S) **b**); MCM-41 (HO) **c**); MCM-48 **d**); SBA-15 **e**); PHTS **f**) and MCF **g**) [135].

4.4.3. Application of mesoporous silica (MSNs)

The textural properties such as high surface area, large pore volume and the narrow particle size distribution are well suited for the application of nano-encapsulation for drug delivery. Moreover, different types of prepared mesoporous silica allowed us for precise comparison of their properties (high polydispersity in particle size, different porosity, particle morphology and pore structure) for L-DOPA drug release [186]. For the evaluation of L-DOPA delivery profile, MSNs with same pore sizes but different morphologies (MCM-41, all 3 types) and MSNs with various pore sizes (MCM-48, SBA-15, PHTS and MCF) were chosen to understand the effect of pore size along with particle morphology on drug loading and release profile.

4.4.4. L-dopa loading and release

L-DOPA is an amino acid that is made and used as part of the normal human body as well as some animals and plants. It can cross the protective blood-brain barrier unlike dopamine. Therefore, L-DOPA is used to increase dopamine concentration for the common Parkinson disease treatment. This treatment was proven clinically by G. Cotzias *et. al*. [187]. MSNs were widely explored for drug delivery using various types of drugs, whereas L-DOPA was not given any importance to have MSNs as the potential carriers [148,186]. In our research, the potential of using MSNs for specifically L-DOPA drug loading and release has been studied and evaluated. The illustration of the whole process for drug loading and release is given in **scheme 8**. The calculations for loading and release of drugs using mesoporous have been widely discussed in many research works [188,189].

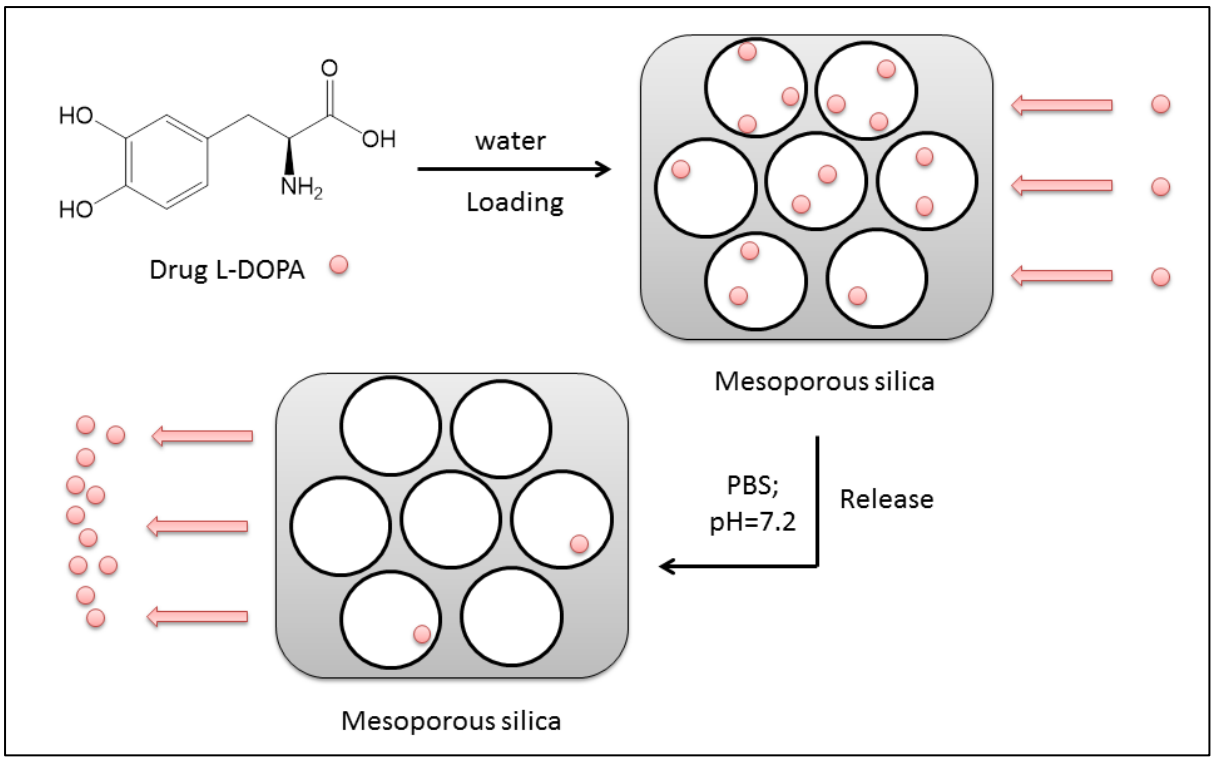

Scheme 8: The illustration for L-DOPA drug loading to and release from mesoporous silica.

4.4.4.1. L-DOPA drug loading

L-DOPA drug loading was monitored by UV-VIS spectrophotometer and the calibration curve (**Figure 49**) was plotted to calculate the concentration change with respect to time using the absorbance spectra for evaluating the L-DOPA loading.

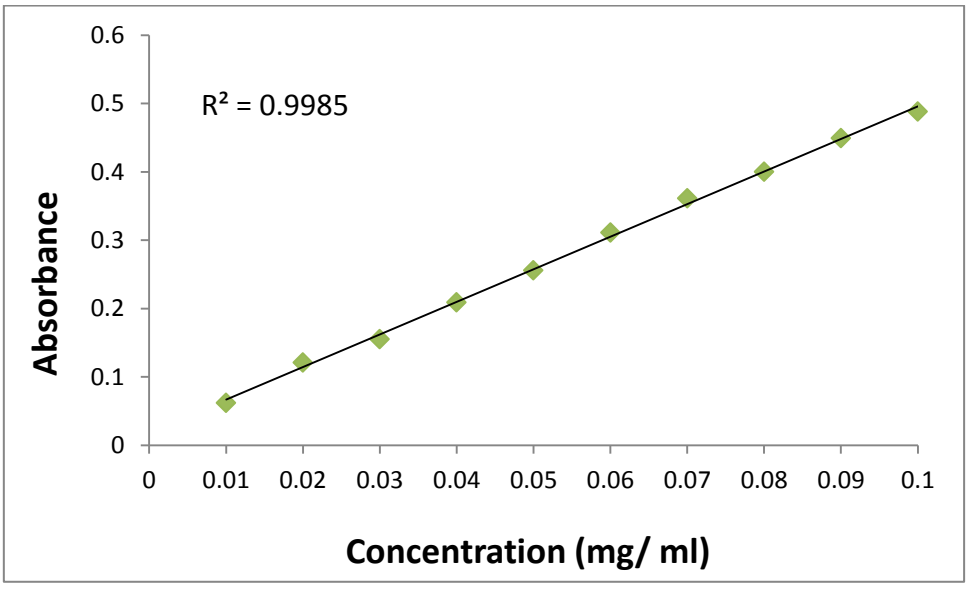

Figure 49: The standard calibration curve of L-DOPA in water.

The loading profiles of L-DOPA for MCM-41 (FS), MCM-41 (S) and MCM-41 (HO) are presented in **Figure 50 a**. It was expected to observe the differences in drug loading amount as the mentioned MSNs had different surface morphologies although the pore sizes were similar. **Figure 50 b** shows the drug loading profiles for rest of the mesoporous silica samples (MCM-48, SBA-15, PHTS and MCF). The curves show the drug loading (in µg) per 10 mg of previously prepared mesoporous silica materials. Maximum loading was allowed by SBA-15 (59 µg) amongst all the mesoporous silica materials. SBA-15 is widely used for drug delivery and the obtained comparative results also support SBA-15 as the best mesoporous silica material. MCM-41 (FS), MCM-41 (S), MCM-41 (HO) and MCM-48 showed narrow difference in loaded drug (49 µg, 51 µg, 53 µg and 49 µg respectively) as the pore diameters of all MCM series materials were found to be similar. Highly ordered MCM-41 (HO) exhibited more loading compared to other MCM series materials due to uniformity of porosity as well as surface morphology. The MCM-41 (S) had spherical morphology, but particle sizes were less uniform than MCM-41 (HO), therefore loading was less than MCM-41 (HO). Due to large pore sizes of MCF, the loading performance of it (56 µg) was very close to SBA-15 and PHTS demonstrated minimum loading (42 µg), probably due to the presence of plugged pores. The L-DOPA loading was observed to be fast (2 h). The loadings were not continued more than 24 h as L-DOPA aqueous solution is very sensitive to light and heat. Moreover, the solution turns black as a result of degradation in solvent [190]. The amounts (wt%) of L-DOPA drug loaded in different samples are summarised in **Table 13**.

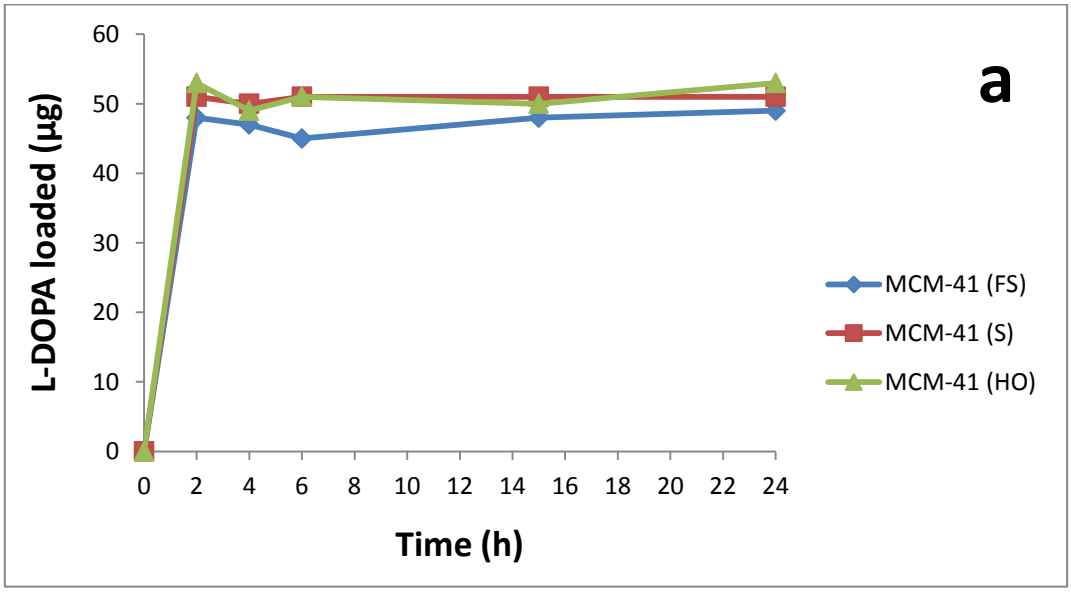

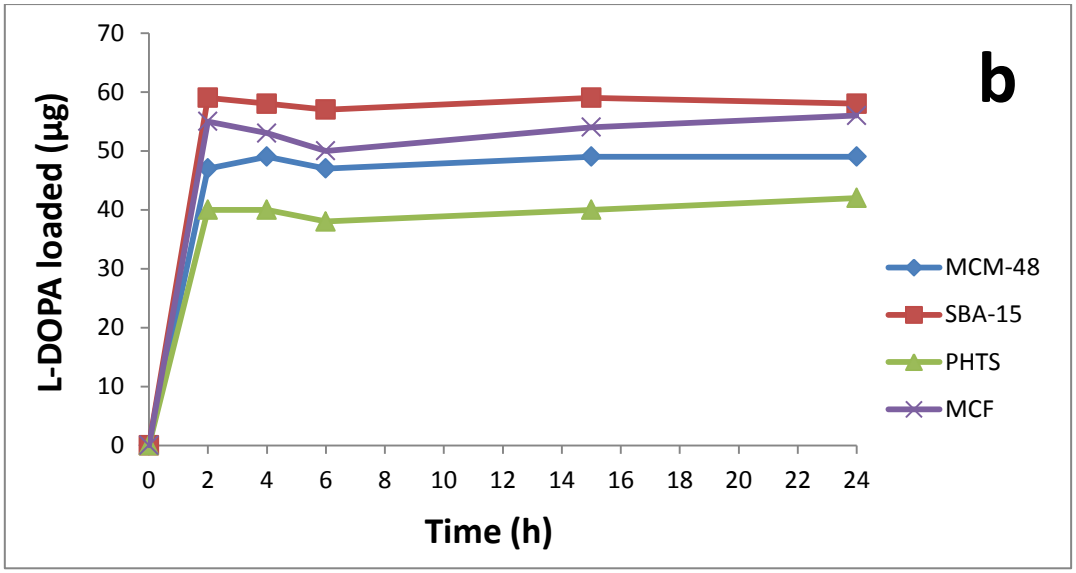

Figure 50: The L-DOPA loading profiles for MCM-41 (FS), MCM-41 (S), MCM-41 (HO) **a**) and MCM-48, SBA-15, PHTS, MCF **b**).

Table 13: L-DOPA loaded within the samples

Sample	MCM-41 (FS)	MCM-41 (S)	MCM-41 (HO)	MCM-48	SBA-15	PHTS	MCF
L-DOPA loaded (wt%)	4.9	5.1	5.3	4.9	5.9	4.2	5.6

4.4.4.2. L-DOPA drug release

Like L-DOPA drug loading, L-DOPA drug release in PBS was also monitored by UV-VIS spectrophotometer. The calibration curve (**Figure 51**) was plotted using the absorbance spectra to measure the released drug concentration directly with respect to time for L-DOPA in PBS at pH 7.2.

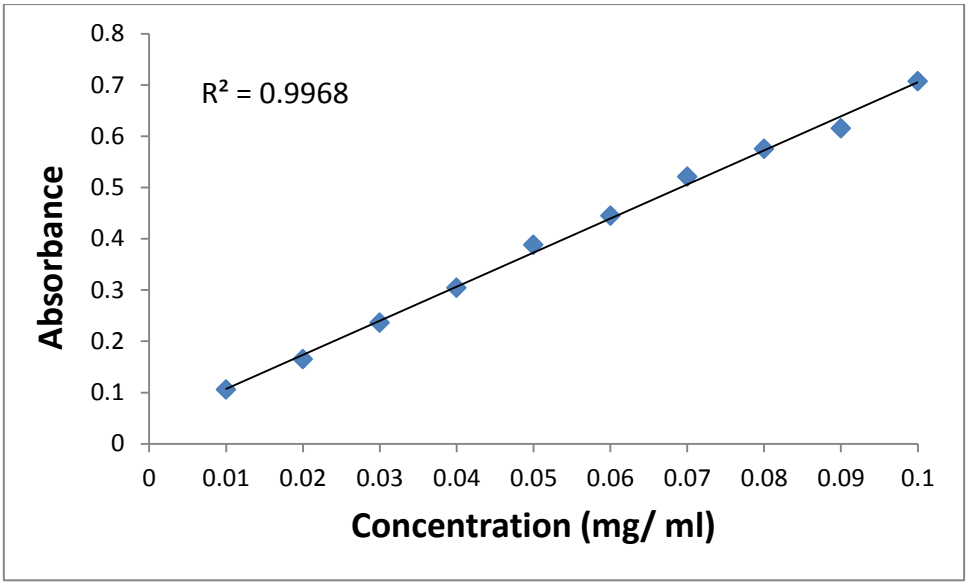

Figure 51: The standard calibration curve of L-DOPA in PBS.

The absorbance spectra recorded during the release of L-DOPA drug in different time intervals were used in order to prepare a plot indicating the release profile. The release profiles are depicted in **Figure 52** (**a**, **b**). The results established that the release is sustained rather than prolonged [148]. The release profiles of all tested materials were quite similar. SBA-15 with high surface area and pore volume (pore diameter ~7.6 nm) achieved highest release amount with ~85% in 1 h whereas, PHTS revealed the lowest release (~74%). In MCM series, MCM-41 (HO) showed more drug release capacity (~81%) than others and all the results were compatible with the drug loading profiles. Both MCM-41 (FS) and MCM-48 released ~78% of loaded L-DOPA, but MCM-41 (S) released ~80%. MCF having comparatively large pores (~12 nm) achieved ~83% drug release.

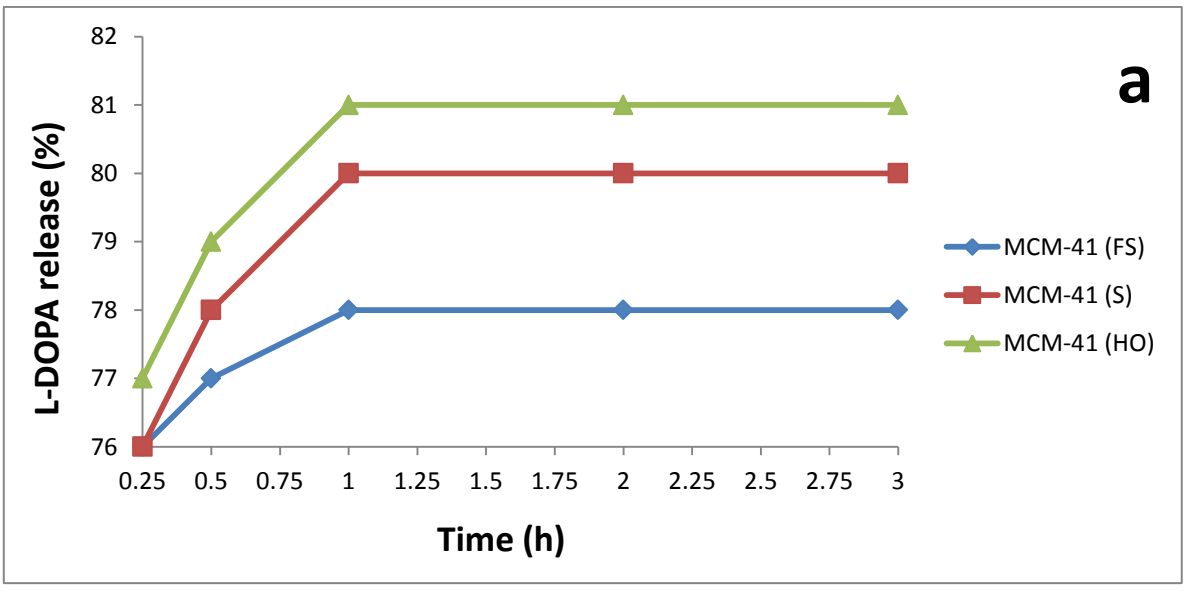

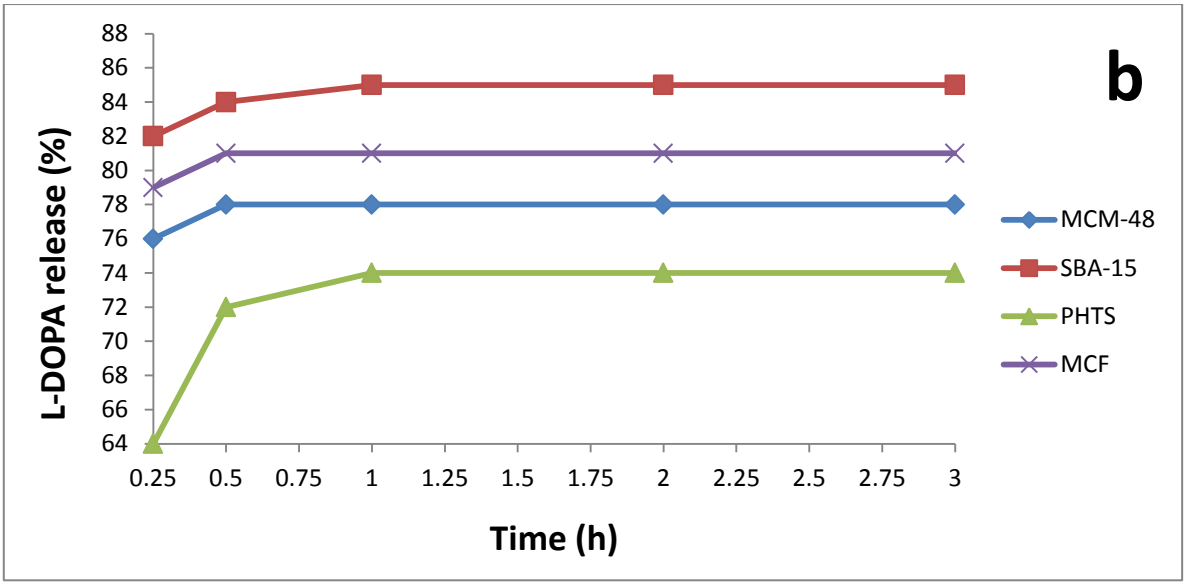

Figure 52: The L-DOPA drug release profiles for MCM-41 (FS), MCM-41 (S), MCM-41 (HO) **a**) and MCM-48, SBA-15, PHTS, MCF **b**).

The comparative studies of drug loading and release revealed that surface morphologies, specific surface area, pore volumes and pore diameters played important role in drug loading and release profiles of different MSNs. Amongst all the tested mesoporous silica materials, SBA-15 was found to be the best for L-DOPA drug loading and release. The analyses of drug loading and release profiles revealed that MSNs can be used for effective L-DOPA drug delivery choosing suitable mesoporous silica.

5. CONCLUSION AND FUTURE WORK

5.1. Conclusion

First, a novel, easily achievable and efficient surface modification of PET via one-step reaction was successfully developed and applied for antibacterial resistance towards both Gram positive (*Staphylococcus aureus and* methicillin-resistant *Staphylococcus aureus* known as MRSA) and Gram negative (*Escherichia coli* and *Pseudomonas aeruginosa)* bacterial strains, without cytotoxic effect according to the ISO norm. The Grignard reagents were capable to react with PET foil and fabric surfaces which were confirmed by different analysis techniques, such as WCAs, and FSEs measurements, FTIR spectroscopy, fluorescence labelling, SEM, AFM microscopies. Ester cleavage of PET by different Grignard reagents resulted to the immobilization of hydroxyl groups (–OH) along with alkyl groups with various length C chains that can tune the hydrophilicity/ hydrophobicity as well as the FSEs which play important role in bacterial adhesion. Both the modified biocompatible PET foils (PET–CH_3 and PET–$C_{12}H_{25}$) were found to be fairly resistant towards tested bacterial adhesion, especially against the pathogenic bacterial strain MRSA whereas the cell viability of all the tested samples was found to be greater than 80%. We would like to emphasize that an efficient fight and easily applicable solutions against increase of antimicrobial resistance generate current key challenges of global importance in biomedical application.

Second, the both non-spectral (WCAs and FSEs) and spectroscopic methods as well as microscopic analyses (SEM, AFM, XPS, FT-IR and Raman) confirmed that the naturally abundant surface amide groups of Nylon 6 were successfully and efficiently reduced to amine groups which were further modified by *N*-alkylation, by tethering PEG via DSC conjugation and by grafting PEG-CH_3 chains via lithiation. The *N*-alkylation model reaction performed on Nylon 6-NH confirmed the scope of tuning the Nylon 6 surface through grafting hydrophilic antifouling PEG-CH_3 chains via lithiation reactions and thus opened up a new efficient way for producing cytocompatible surface which can potentially help to extend the spectrum of applications including biomedical field. Moreover, the BuLi concentration as well as the lithiation time significantly influenced further PEGylation. Antibacterial tests against both Gram positive (*Staphylococcus aureus*) and Gram negative (*Pseudomonas aeruginosa*) pathogenic bacterial strains confirmed significant effect on the bacterial adhesion. Water contact angle values demonstrated the increase in hydrophilicity of modified Nylon 6-NH and grafted samples compared to pure Nylon 6. The hydrophilicity increase employed positive influence on resistance to bacterial adhesion and antibacterial effect on modified samples

compared to Nylon 6. Nylon 6-NH and all other grafted samples except Sample 3, exhibited noncytotoxic effect (on direct contact and under extract) on fibroblast cells. On the contrary, the cell adhesion was adversely influenced by the Nylon 6 surface modification. The modified samples have significant potential to be used in biomedical fields where antibacterial effect as well as bacterial adhesion resistance would be major priority than cell adhesion (e.g. artificial valves, catheters etc.).

Third, Cu NPs were prepared by Cu^{2+} reduction using $NaBH_4$ and characterized by different analysis techniques (DLS, SEM, UV-VIS absorption and FT-IR spectroscopy) for the stable deposition on PEG-CH_3 grafted Nylon 6 samples. The experiments confirmed the possibility of Cu NPs physisorption on PEG-CH_3 grafted samples whereas it failed on pure Nylon 6 and reduced Nylon 6-NH samples. Cu NP deposited samples were found to be significantly efficient in both qualitative and quantitative antibacterial efficacy. Although the Nylon 6-N-PEG-CH_3-Cu demonstrated cytotoxicity for fibroblast cells under direct contact, the extract of the sample was confirmed to be noncytotoxic at 5 mg/ ml concentration. The antibacterial efficacy can be compared and thus improved further by using other different sizes of Cu NPs deposited on grafted Nylon 6 surface.

Fourth, the synthesis of mesoporous silica materials and their application for L-DOPA drug delivery were achieved successfully. The SEM and BET techniques were applied to evaluate the morphology and particle characteristics (surface areas, pore volumes and pore size distributions). The L-DOPA drug loading and release were successfully evaluated by UV-VIS absorption spectra. A comparative study on L-DOPA drug delivery efficiency among all the prepared mesoporous silica samples was performed confirming SBA-15 as the most efficient for both L-DOPA loading and release. The behaviour of drug delivery profile suggested that the pore size of MSNs plays much more important role than the surface morphologies as all the MCM-41 (FS/ HO/ S) samples, with nearly similar pore size, demonstrated almost same drug delivery profiles, although their surface morphologies were very different.

5.2. Future Work

Both bio-stable polyesters and polyamides are used in the field of biomedicine. The further functionalization of PET may be possible for important applications related to new types of antibacterial and biocompatible materials. The Nylon 6 surface modification via lithiation and grafting can further be explored by using different combinations of BuLi concentrations and PEG having various higher molecular weights (Mw > 2000) for the

further study aiming the improvement in antibacterial efficacy. Cu NPs with different other sizes can be deposited to grafted Nylon 6 samples to study the effect for bacterial resistance with the size of Cu NPs. Immobilization od other antibacterial NPs can also be explored for enhancing the efficacy of biomaterial. The mesoporous silica materials are popular in research areas to study the potency of different drug delivery. In our research, we have studied the L-DOPA drug loading on and release by some selected mesoporous silica materials. We have noticed that L-DOPA loading is quite fast and 2 h was reasonable time for complete loading. Therefore, further investigation of the loading profile between 0 – 2 h would be interesting. Besides, there is a scope of continuing the further comparative study on the same topic by functionalizing the mesoporous silica with different functional groups, such as terminal primary amine ($-NH_2$), thiol (-SH) and alkyl groups (-R) etc. to increase the drug loading capacity. There are always more to explore in every segment of research field.

PUBLICATIONS AND CONFERENCE PROCEEDINGS

PUBLICATIONS

1. Swar, S.; Zajícová, V.; Rysová, M.; Lovětinská-Šlamborová, I.; Voleský, L.; Stibor, I. Biocompatible Surface Modification of Poly (ethylene Terephthalate) Focused Against Pathogenic Bacteria: Promising Prospects In Biomedical Applications; *J. APPL. POLYM. SCI.* (2017), 1-11. DOI: 10.1002/APP.44990.

2. Martinek, M.; Swar, S.; Zajícová, V.; Voleský, L.; Blažková, L.; Müllerová, J.; Stuchlík, M.; Řezanka, M.; Stibor, I. Pre-treatment of polyethylene terephthalate by Grignard reagents for high quality polypyrrole coatings and for altering of hydrophobicity**,** *CHEMICAL PAPERS* (2017), 71, 2403-2415. DOI: 10.1007/s11696-017-0235-3.

3. Swar, S.; Zajícová, V.; Müllerová, J.; Voleský, L.; Stibor, I. Importance and Necessity of the Surface Modification of Nylon 6 Films for Future Biomedical Application, In Proceedings of the 8th International Conference Nanocon 2016, BRNO, Oct. 19th - 21st 2016, Czech Republic, EU, pp. 663- 668. ISBN 978-80-87294 -71-0.

4. Sumita, Swar, Veronika Zajícová, Jana Müllerová, Petra Šubrtová and Ivan Stibor. Effective poly(ethylene glycol) methyl ether grafting technique onto Nylon 6 surface to achieve resistance against pathogenic bacteria, *J. MATER. SCI.* (submitted, after major revision).

CONFERENCE PROCEEDINGS

1. Swar, S.; Padil, V.; Černík, M.; Stibor, I. Preparation of Electrospun Nanofibrous Membranes Using Different Blends of Gum Arabic and Polyvinyl Alcohol, In Proceedings of the *15th AUTEX World Textile Conference 2015*, BUCHAREST, June 10-12, 2015, Romania; ISBN: 978-606-685-275-3.

2. Swar, S.; Zajícová, V.; Voleský, L.; *Řezanka, M.;*Stibor, I. AntibacterialSurface Modification of Polymeric Materials Used in Medicine, In Proceedings of the *6th EuCheMS Chemistry Congress 2016*, SEVILLE, Sep. 11-15, 2016, Spain.

3. Swar, S.; Zajícová, V.; Müllerová, J.; Voleský, L.; Stibor, I. Importance and Necessity of the Surface Modification of Nylon 6 Films for Future Biomedical Application, In

Proceedings of the *8th International Conference Nanocon 2016*, BRNO, Oct. 19th - 21st 2016, Czech Republic, EU. ISBN 978-80-87294 -71-0.

4. Swar, S., Zajícová, V., Müllerová, J., Šubrtová, P., Stibor, I. Unique Antibacterial Surface Modification of Nylon 6. ed. Proceedings of the *11th Aachen-Dresden-Denkendorf International Textile Conference 2017*, STUTTGART, 30.11.-1.12., 2017. Denkendorf: DITF, 2017, article_swar on CD-ROM. 6 pg. ISSN 1867-6405.

5. Zajícová,V., Šinkorová,H., Swar, S., Voleský, L., Müllerová, J., Stibor, I. Cytocompatible Modification of Poly(Ethylene Terephthalate) Focused on Biofilm Elimination, In Proceedings of the *11th Aachen-Dresden-Denkendorf International Textile Conference 2017*, STUTTGART, 30.11.-1.12., 2017. Denkendorf: DITF, 2017, article_zajicova on CD-ROM. 6 pg. ISSN1867-6405.

6. S. Swar, V. Zajícová, J. Müllerová, P. Šubrtová and I. Stibor. New Approach Towards m-PEG Grafting Onto Commercially Available Nylon 6 To Resist Bacterial Adhesion On Surface, In Proceedings of the *18th AUTEX World Textile Conference 2018*, ISTANBUL, June 20-22, 2018, Turkey; ISBN: 978-1-53612-855-0.

PARTICIPATION IN THE PROJECTS

1. SGS n. 21207, 2017-2019. Chemical modifications of selected polymers used in medicine. Contractor: Technical University of Liberec, Faculty of Education, Nature Sciences and Humanities, Department of Chemistry. Total budget: 161 000 CZK for 2017 and 224 000 for 2018. Investigator: Dr. Jana Müllerová, Co-investigators: Dr. Veronika Zajícová, MSc. Sumita Swar.

2. SGS n. 21164, 2016. Thin coatings prepared chemically and photochemically related to biofilm inhibition in the health care facilities. Contractor: Technical University of Liberec, Faculty of Education, Nature Sciences and Humanities, Department of Chemistry. Total budget: 144 000 CZK. Investigator: Dr.Veronika Zajícová, co-worker MSc. Sumita Swar.

INTERNSHIP

Completion of 3-month-internship program (05/12/2016 to 04/02/2017) from Jadavpur University, Kolkata, India; that was sponsored jointly by mobility fund of TUL, 2016 and the Faculty of Mechatronics, Informatics and Interdisciplinary studies, TUL, Liberec. The

internship program was focused on the green synthesis of copper oxide nanoparticles under the supervision of Dr. Sudeshna Saha, Assistant Professor, Department of Chemical Engineering, Jadavpur University.

REFERENCES

[1] W.B. Whitman, D.C. Coleman, W.J. Wiebe, Prokaryotes: The unseen majority, Proc. Natl. Acad. Sci. 95 (1998) 6578–6583.

[2] B. Alberts, A. Johnson, J. Lewis, M. Raff, K. Roberts, P. Walter (2002) Molecular biology of the cell, 4th Edn. Garland Science, New York.

[3] M. McFall-Ngai, Care for the community, Nature 445 (2007) 153.

[4] S. Panayidou, E. Ioannidou, Y. Apidianakis, Human pathogenic bacteria, fungi, and viruses in Drosophila, Virulence. 5 (2014) 253–269.

[5] J W Wilson, M J Schurr, C L LeBlanc, R Ramamurthy, K L Buchanan, C A Nickerson, Mechanisms of bacterial pathogenicity, Postgr. Med J. 78 (2002) 216–225.

[6] A. Nazir, S. Kadri, An overview of hospital acquired infections and the role of the microbiology laboratory, Int. J. Res. Med. Sci. 2 (2014) 21-27.

[7] P. Saxena, R.K. Mani, Preventing hospital acquired infections: A challenge we must accept., Indian J. Crit. Care Med. 18 (2014) 125–126.

[8] H.A. Khan, F.K. Baig, R. Mehboob, Nosocomial infections: Epidemiology, prevention, control and surveillance, Asian Pac. J. Trop. Biomed. 7 (2017) 478–482.

[9] A.S. Breathnach, Nosocomial infections and infection control, Med. (United Kingdom). 41 (2013) 649–653.

[10] J.W. Costerton, Z. Lewandowski, D.E. Caldwell, D.R. Korber, H.M. Lappin-Scott, Microbial Biofilms, Annu. Rev. Microbiol. 49 (1995) 711–745.

[11] R.M. Donlan, Biofilms and Device-Associated Infections, Emerg. Infect. Dis. 7 (2001) 277–281.

[12] J.A. Lichter, K.J. Van Vlietpa, M.F. Rubner, Design of antibacterial surfaces and interfaces: Polyelectrolyte multilayers as a multifunctional platform, Macromolecules. 42 (2009) 8573–8586.

[13] M. Scherbaum, K. Kösters, R.E. Mürbeth, U.A. Ngoa, P.G. Kremsner, B. Lell, A. Alabi, Incidence, pathogens and resistance patterns of nosocomial infections at a rural hospital in Gabon, BMC Infect. Dis. 14 (2014) 13–15.

[14] V. Ranganathan, Biofilms : Microbial Cities of Scientific Significance, J. Microbiol. Exp. 1 (2014) 1–16.

[15] M. Jamal, W. Ahmad, S. Andleeb, F. Jalil, M. Imran, M.A. Nawaz, T. Hussain, M. Ali, M. Rafiq, M.A. Kamil, Bacterial biofilm and associated infections, J. Chinese Med. Assoc. 81 (2018) 7–11.

[16] K. Hori, S. Matsumoto, Bacterial adhesion: From mechanism to control, Biochem. Eng. J. 48

(2010) 424–434.

[17] B. Vu, M. Chen, R.J. Crawford, E.P. Ivanova, Bacterial extracellular polysaccharides involved in biofilm formation, Molecules. 14 (2009) 2535–2554.

[18] J.B. Kaplan, Biofilm Dispersal: Mechanisms, Clinical Implications, and Potential Therapeutic Uses, J. Dent. Res. 89 (2010) 205–218.

[19] M.E. Cortés, J.C. Bonilla, R.D. Sinisterra, Biofilm formation, control and novel strategies for eradication, Sci. against Microb. Pathog. Commun. Curr. Res. Technol. Adv. (2011) 896–905.

[20] S. Satpathy, S.K. Sen, S. Pattanaik, S. Raut, Review on bacterial biofilm: An universal cause of contamination, Biocatal. Agric. Biotechnol. 7 (2016) 56–66.

[21] M. Simões, L.C. Simões, M.J. Vieira, A review of current and emergent biofilm control strategies, LWT - Food Sci. Technol. 43 (2010) 573–583.

[22] A.J.T. Teo, A. Mishra, I. Park, Y.-J. Kim, W.-T. Park, Y.-J. Yoon, Polymeric Biomaterials for Medical Implants and Devices, ACS Biomater. Sci. Eng. 2 (2016) 454–472.

[23] A. Taubert, F. Mano, C. Rodriguez-Cabello (2013) Biomaterials Surface Science, Wiley-VCH Verlag GmbH & Co, Germany.

[24] J.W. Costerton, P.S. Stewart, E.P. Greenberg, Bacterial biofilms: A common cause of persistent infections, Science. 284 (1999) 1318–1322.

[25] T. Desmet, R. Morent, N. De Geyter, C. Leys, E. Schacht, P. Dubruel, Nonthermal plasma technology as a versatile strategy for polymeric biomaterials surface modification: A review, Biomacromolecules. 10 (2009) 2351–2378.

[26] X. Zhang, L. Wang, E. Levänen, Superhydrophobic surfaces for the reduction of bacterial adhesion, RSC Adv. 3 (2013) 12003-12020.

[27] J.M. Morais, F. Papadimitrakopoulos, D.J. Burgess, Biomaterials/Tissue Interactions: Possible Solutions to Overcome Foreign Body Response, AAPS J. 12 (2010) 188–196.

[28] J. Gallo, M. Holinka, C.S. Moucha, Antibacterial surface treatment for orthopaedic implants, Int. J. Mol. Sci. 15 (2014) 13849-13880.

[29] M.F. Maitz, Applications of synthetic polymers in clinical medicine, Biosurface and Biotribology. 1 (2015) 161–176.

[30] P. Thevenot, W. Hu, L. Tang, Surface chemistry influences implant biocompatibility., Curr. Top. Med. Chem. 8 (2008) 270–80.

[31] I. Banerjee, R.C. Pangule, R.S. Kane, Antifouling Coatings: Recent Developments in the Design of Surfaces That Prevent Fouling by Proteins, Bacteria, and Marine Organisms, Adv. Mater. 23 (2011) 690–718.

[32] A. Hucknall, S. Rangarajan, A. Chilkoti, In pursuit of zero: Polymer brushes that resist the adsorption of proteins, Adv. Mater. 21 (2009) 2441–2446.

[33] M. Amiji, K. Park, Surface modification of polymeric biomaterials with poly(ethylene oxide), albumin, and heparin for reduced thrombogenicity., J. Biomater. Sci. Polym. Ed. 4 (1993) 217–234.

[34] K. Page, M. Wilson, I.P. Parkin, Antimicrobial surfaces and their potential in reducing the role of the inanimate environment in the incidence of hospital-acquired infections, J. Mater. Chem. 19 (2009) 3819-3831.

[35] Y. Ohko, Y. Utsumi, C. Niwa, T. Tatsuma, K. Kobayakawa, Y. Satoh, Y. Kubota, A. Fujishima, Self-sterilizing and self-cleaning of silicone catheters coated with TiO2 photocatalyst thin films: A preclinical work, J. Biomed. Mater. Res. 58 (2001) 97–101.

[36] I. Perelshtein, G. Applerot, N. Perkas, E. Wehrschuetz-Sigl, A. Hasmann, G. Guebitz, A. Gedanken, CuO-cotton nanocomposite: Formation, morphology, and antibacterial activity, Surf. Coatings Technol. 204 (2009) 54–57.

[37] I. Perelshtein, A. Lipovsky, N. Perkas, T. Tzanov, A. Gedanken, Sonochemical co-deposition of antibacterial nanoparticles and dyes on textiles, Beilstein J. Nanotechnol. 7 (2016) 1–8.

[38] H.F. Chuang, R.C. Smith, P.T. Hammond, Polyelectrolyte multilayers for tunable release of antibiotics, Biomacromolecules. 9 (2008) 1660–1668.

[39] Y.D. Kim, J.S. Dordick, D.S. Clark, Siloxane-based biocatalytic films and paints for use as reactive coatings, Biotechnol. Bioeng. 72 (2001) 475–482.

[40] J. Dai, M.L. Bruening, Catalytic Nanoparticles Formed by Reduction of Metal Ions in Multilayered Polyelectrolyte Films, Nano Lett. 2 (2002) 497–501.

[41] J.P. Bearinger, S. Terrettaz, R. Michel, N. Tirelli, H. Vogel, M. Textor, J. a Hubbell, Chemisorbed poly(propylene sulphide)-based copolymers resist biomolecular interactions., Nat. Mater. 2 (2003) 259–264.

[42] E. Ostuni, R.G. Chapman, R.E. Holmlin, S. Takayama, G.M. Whitesides, A survey of structure-property relationships of surfaces that resist the adsorption of protein, Langmuir. 17 (2001) 5605–5620.

[43] V.A. Liu, W.E. Jastromb, S.N. Bhatia, Engineering protein and cell adhesivity using PEO-terminated triblock polymers, J. Biomed. Mater. Res. 60 (2002) 126–134.

[44] A. Roosjen, H.C. Van Der Mei, H.J. Busscher, W. Norde, Microbial adhesion to poly(ethylene oxide) brushes: Influence of polymer chain length and temperature, Langmuir. 20 (2004) 10949–10955.

[45] K.D. Park, Y.S. Kim, D.K. Han, Y.H. Kim, E.H.B. Lee, H. Suh, K.S. Choi, Bacterial adhesion on PEG modified polyurethan surfaces, Biomaterials. 19 (1998) 851–859.

[46] K. Prime, G. Whitesides, Self-assembled organic monolayers: model systems for studying adsorption of proteins at surfaces, Science. 252 (1991) 1164–1167.

[47] N. Gour, K.X. Ngo, C. Vebert-Nardin, Anti-infectious surfaces achieved by polymer modification, Macromol. Mater. Eng. 299 (2014) 648–668.

[48] G.H. Kingshott, Thissen H, H.J. Griesser, Effects of cloud-point grafting, chain length, and density of PEG layers on competitive adsorption of ocular proteins, Biomaterials 23 (2002) 2043-2056.

[49] B. Dong, S. Manolache, A.C.L. Wong, F.S. Denes, Antifouling ability of polyethylene glycol of different molecular weights grafted onto polyester surfaces by cold plasma, Polym. Bull. 66 (2011) 517–528.

[50] L. Liu, W. Li, Q. Liu, Recent development of antifouling polymers: Structure, evaluation, and biomedical applications in nano/micro-structures, Wiley Interdiscip. Rev. Nanomedicine Nanobiotechnology. 6 (2014) 599–614.

[51] Z. Wang, E. van Andel, S.P. Pujari, H. Feng, J.A. Dijksman, M.M.J. Smulders, H. Zuilhof, Water-repairable zwitterionic polymer coatings for anti-biofouling surfaces, J. Mater. Chem. B. 5 (2017) 6728–6733.

[52] H.J. Kwon, Y. Lee, L.T. Phuong, G.M. Seon, E. Kim, J.C. Park, H. Yoon, K.D. Park, Zwitterionic sulfobetaine polymer-immobilized surface by simple tyrosinase-mediated grafting for enhanced antifouling property, Acta Biomater. 61 (2017) 169–179.

[53] A. Duro-Castano, I. Conejos-Sánchez, M.J. Vicent, Peptide-based polymer therapeutics, Polymers (Basel). 6 (2014) 515–551.

[54] Y. Sekiguchi, Y. Yao, Y. Ohko, K. Tanaka, T. Ishido, A. Fujishima, Y. Kubota, Self-sterilizing catheters with titanium dioxide photocatalyst thin films for clean intermittent catheterization: Basis and study of clinical use, Int. J. Urol. 14 (2007) 426–430.

[55] L. Visai, L. de Nardo, C. Punta, L. Melone, A. Cigada, M. Imbriani, C.R. Arciola, Titanium oxide antibacterial surfaces in biomedical devices, Int. J. Artif. Organs. 34 (2011) 929–946.

[56] D. Shchukin, H. Möhwald, A coat of many functions, Science 341 (2013) 1458–1459.

[57] T.S. Sileika, H. Do Kim, P. Maniak, P.B. Messersmith, Antibacterial performance of polydopamine-modified polymer surfaces containing passive and active components, ACS Appl. Mater. Interfaces. 3 (2011) 4602–4610.

[58] I. V. Korolkov, O. Güven, A.A. Mashentseva, A.B. Atıcı, Y.G. Gorin, M. V. Zdorovets, A.A. Taltenov, Radiation induced deposition of copper nanoparticles inside the nanochannels of poly(acrylic acid)-grafted poly(ethylene terephthalate) track-etched membranes, Radiat. Phys. Chem. 130 (2017) 480–487.

[59] C. Sun, Y. Li, Z. Li, Q. Su, Y. Wang, X. Liu, Durable and Washable Antibacterial Copper Nanoparticles Bridged by Surface Grafting Polymer Brushes on Cotton and Polymeric Materials, J. Nanomater. 2018 (2018) 1-7.

[60] S.N. Davidoff, J.O. Sevy, B.D. Brooks, D.W. Grainger, A.E. Brooks, Evaluating antibiotic

release profiles as a function of polymer coating formulation, Biomed. Sci. Instrum. 47 (2011) 46–51.

[61] J. Yatvin, J. Gao, J. Locklin, Durable defense: robust and varied attachment of non-leaching poly“-onium” bactericidal coatings to reactive and inert surfaces, Chem. Commun. 50 (2014) 9433–9442.

[62] G. Cheng, H. Xue, Z. Zhang, S. Chen, S. Jiang, A switchable biocompatible polymer surface with self-sterilizing and nonfouling capabilities, Angew. Chemie - Int. Ed. 47 (2008) 8831–8834.

[63] E.D. Giol, D. Schaubroeck, K. Kersemans, F. De Vos, S. Van Vlierberghe, P. Dubruel, Bio-inspired surface modification of PET for cardiovascular applications: case study of gelatin, Colloids Surfaces B Biointerfaces. 134 (2015) 113–121.

[64] S. Xiao, W. Xu, H. Ma, Fabrication and characterization of mechano-modulated PET/BPU nanofibrous mats as potential vascular grafts materials, Fibers Polym. 13 (2012) 618–625.

[65] M.T. Lam, J.C. Wu, Biomaterial applications in cardiovascular tissue repair and regeneration, Expert Rev Cardiovasc Ther. 10 (2012) 1039–1049.

[66] K. Singha, M. Singha, Cardio Vascular Grafts: Existing Problems and Proposed Solutions, Int. J. Biol. Eng. 2 (2012) 1–8.

[67] G.S.A. Boersema, N. Grotenhuis, Y. Bayon, J.F. Lange, Y.M. Bastiaansen-Jenniskens, The Effect of Biomaterials Used for Tissue Regeneration Purposes on Polarization of Macrophages, Biores. Open Access. 5 (2016) 6–14.

[68] S. Dimitrievska, M. Maire, G.A. Diaz-Quijada, L. Robitaille, A. Ajji, L. Yahia, M. Moreno, Y. Merhi, M.N. Bureau, Low Thrombogenicity Coating of Nonwoven PET Fiber Structures for Vascular Grafts, Macromol. Biosci. 11 (2011) 493–502.

[69] S. Noel, A. Hachem, Y. Merhi, G. De Crescenzo, Development of a polyester coating combining antithrombogenic and cell adhesive properties: Influence of sequence and surface density of adhesion peptides, Biomacromolecules. 16 (2015) 1682–1694.

[70] R.O. Darouiche, Anti-Infective Efficacy of Silver-Coated Medical Prostheses, Epidemiology. 29 (2011) 1371–1377.

[71] H. Li, S. Chen, Biomedical coatings on polyethylene terephthalate artificial ligaments, J. Biomed. Mater. Res. - Part A. 103 (2015) 839–845.

[72] Paul C.Hiemenz, T. P.Lodge (2007) Polymer Chemistry, Taylor & Francis group, CRC Press: Northwest, Washington, D.C.

[73] A. Bartnik, H. Fiedorowicz, R. Jarocki, J. Kostecki, M. Szczurek, A. Bilinski, O. Chernyayeva, J.W. Sobczak, Physical and chemical modifications of PET surface using a laser-plasma EUV source, Appl. Phys. A Mater. Sci. Process. 99 (2010) 831–836.

[74] J. Zhang, I.W. Boyd, H. Esrom, Surface Modification of Polyethylene Terephthalate with Excimer UV Radiation, Surface Interface Anal. 24 (1996) 718–722.

[75] W. Chen, Chemical surface modification of poly (ethylene terephthalate), Macromolecules. 9297 (1998) 3648–3655.

[76] Y. Liu, T. He, C. Gao, Surface modification of poly(ethylene terephthalate) via hydrolysis and layer-by-layer assembly of chitosan and chondroitin sulfate to construct cytocompatible layer for human endothelial cells, Colloids Surfaces B Biointerfaces. 46 (2005) 117–126.

[77] Y. Zhu, Z. Mao, C. Gao, Aminolysis-based surface modification of polyesters for biomedical applications, RSC Adv. 3 (2013) 2509–2519.

[78] L. Bech, T. Meylheuc, B. Lepoittevin, P. Roger, chemical surface modification pf PET fibers by aminolysis, J. Polym. Sci. Part A Polym. Chem. 45 (2007) 2172– 2183.

[79] X. Ping, M. Wang, G. Xuewu, Surface modification of poly(ethylene terephthalate) (PET) film by gamma-ray induced grafting of poly(acrylic acid) and its application in antibacterial hybrid film, Radiat. Phys. Chem. 80 (2011) 567–572.

[80] M. Abdolahifard, S.H. Bahrami, R.M. a. Malek, Surface Modification of PET Fabric by Graft Copolymerization with Acrylic Acid and Its Antibacterial Properties, ISRN Org. Chem. 2011 (2011) 1–8.

[81] I. Donelli, P. Taddei, P.F. Smet, D. Poelman, V.A. Nierstrasz, G. Freddi, Enzymatic surface modification and functionalization of PET: A water contact angle, FTIR, and fluorescence spectroscopy study, Biotechnol. Bioeng. 103 (2009) 845–856.

[82] B. Dong, H. Jiang, S. Manolache, A.C.L. Wong, F.S. Denes, Plasma-mediated grafting of poly(ethylene glycol) on polyamide and polyester surfaces and evaluation of antifouling ability of modified substrates, Langmuir. 23 (2007) 7306–7313.

[83] S. Shahidi, J. Wiener, M. Ghoranneviss, Surface Modification Methods for Improving the Dyeability of Textile Fabrics, Intech. (2013) 34–54.

[84] R. Balamurugan, S. Sundarrajan, S. Ramakrishna, Recent trends in nanofibrous membranes and their suitability for air and water filtrations, Membranes. 1 (2011) 232–248.

[85] H. Seyednejad, A.H. Ghassemi, C.F. Van Nostrum, T. Vermonden, W.E. Hennink, Functional aliphatic polyesters for biomedical and pharmaceutical applications, J. Control. Release. 152 (2011) 168–176.

[86] X. Cai, J. Yuan, S. Chen, P. Li, L. Li, J. Shen, Hemocompatibility improvement of poly(ethylene terephthalate) via self-polymerization of dopamine and covalent graft of zwitterions, Mater. Sci. Eng. C. 36 (2014) 42–48.

[87] C. Rode, M. Zieger, R. Wyrwa, S. Thein, C. Wiegand, M. Weiser, A. Ludwig, D. Wehner, U. Hipler, Antibacterial Zinc Oxide Nanoparticle Coating of Polyester Fabrics, J. Text. Sci. Technol. 1 (2015) 65–74.

[88] S.L. Fávaro, A.F. Rubira, E.C. Muniz, E. Radovanovic, Surface modification of HDPE, PP, and PET films with KMnO4/HCl solutions, Polym. Degrad. Stab. 92 (2007) 1219–1226.

[89] A. Bhattacharya, B.N. Misra, Grafting: A versatile means to modify polymers: Techniques, factors and applications, Prog. Polym. Sci. 29 (2004) 767–814.

[90] N. Inagaki, S. Tasaka, K. Narushima, H. Kobayashi, Surface modification of PET films by pulsed argon plasma, J. Appl. Polym. Sci. 85 (2002) 2845–2852.

[91] P. Esena, S. Zanini, C. Riccardi, Plasma processing for surface optical modifications of PET films, Vacuum. 82 (2007) 232–235.

[92] F. Espinoza Beltran, I.C. Sanchez, B.L. España Sánchez, J.D. Mota Morales, S. Carrillo, C.I. Enríquez Flores, F. Poncin Epaillard, G. Luna Barcenas, Scanning-probe-microscopy of polyethylene terephthalate surface treatment by argon ion beam, Elsevier - Nucl. Instruments Methods Phys. Res. Sect. B Beam Interact. with Mater. Atoms. 362 (2015) 49–56.

[93] X. Jia, M. Herrera-Alonso, T.J. McCarthy, Nylon surface modification. Part 1. Targeting the amide groups for selective introduction of reactive functionalities, Polymer (Guildf). 47 (2006) 4916–4924.

[94] C.C. Chu, In vitro qualitative and in vivo preliminary, Biomed. Mater. 21 (1987) 1281–1300.

[95] M. Jassal, Textiles for Hygiene and Infection Control, Text. Hyg. Infect. Control. (2011) 3–13.

[96] H. Wang, Y. Li, Y. Zuo, J. Li, S. Ma, L. Cheng, Biocompatibility and osteogenesis of biomimetic nano-hydroxyapatite/polyamide composite scaffolds for bone tissue engineering, Biomaterials. 28 (2007) 3338–3348.

[97] F. Abedini, A. Ahmadi, A. Yavari, V. Hosseini, S. Mousavi, Comparison of silver nylon wound dressing and silver sulfadiazine in partial burn wound therapy, Int. Wound J. 10 (2013) 573–578.

[98] R.H. Wilkinson, C.E. Bayliss, The Utilization of Long Nylon Catheters for Prolonged Intravenous Infusions, Can. Med. Assoc. J. 96 (1967) 94–97.

[99] M.R. Fazeli, V. Hosseini, F. Shamsa, H. Jamalifar, Preparation and in-vitro antibacterial evaluation of electroless silver coated polymers, Iran. J. Pharm. Res. 9 (2010) 259–264.

[100] C. Mao, W. Zhao, C. Zhu, A. Zhu, J. Shen, S. Lin, In vitro studies of platelet adhesion on UV radiation-treated nylon surface, Carbohydr. Polym. 59 (2005) 19–25.

[101] T. Beeskow, K.H. Kroner, F.B. Anspach, Nylon-Based Affinity Membranes: Impacts of Surface Modification on Protein Adsorption, J. Colloid Interface Sci. 196 (1997) 278–291.

[102] M. Ulbricht, Photograft-polymer-modified microporous membranes with environment-sensitive permeabilities, React. Funct. Polym. 31 (1996) 165–177.

[103] R. Foerch, D.H. Hunter, Remote nitrogen plasma treatment of polymers: Polyethylene, nylon 6,6, poly(ethylene vinyl alcohol), and poly(ethylene terephthalate), J. Polym. Sci. Part A Polym.

Chem. 30 (1992) 279–286.

[104] C. Weikart, M. Miyama, H. Yasuda, Surface Modification of Conventional Polymers by Depositing Plasma Polymers of Trimethylsilane and of Trimethylsilane + O2., J. Colloid Interface Sci. 211 (1999) 28–38.

[105] B.D.J. Inman, W.E. Hornby, The Immobilization of Enzymes on Nylon Structures and their Use in Automated Analysis, Biochem. J. 129 (1972) 255–262.

[106] C. Enzymes, J. Campbell, W.E. Hornby, A Chemistry for the Immobilization of Enzymes on Nylon, Biochem. J. 147 (1975) 593–603.

[107] F.N. Onyezili, Nylon Tube O-Alkylation for Immobilisation of Covalent Enzymes, Analyst. 114 (1989) 789–791.

[108] T.L. Cairns, H.D. Foster, A.W. Larchar, A.K. Schneider, R.S. Schreiber, Preparation and Properties of N-Methylol, N-Alkoxymethyl and N-Alkylthiomethyl Polyamides, J. Am. Chem. Soc. 71 (1949) 651–655.

[109] E. Perry, J. Savory, Modification of nylon 66 with diisocyanates and diacid chlorides. II. Physical properties, J. Appl. Polym. Sci. 11 (1967) 2485–2497.

[110] T.J. Dennes, G.C. Hunt, J.E. Schwarzbauer, J. Schwartz, High-yield activation of scaffold polymer surfaces to attach cell adhesion molecules, J. Am. Chem. Soc. 129 (2007) 93–97.

[111] J. Shen, Y. Li, Y. Zuo, Q. Zou, L. Zhang, H. Liu, Surface Modification of Polyamide 6 Immobilized with Collagen: Characterization and Cytocompatibility, Int. J. Polym. Mater. 60 (2011) 907–921.

[112] M. Herrera-Alonso, T.J. McCarthy, X. Jia, Nylon surface modification: 2. Nylon-supported composite films, Langmuir. 22 (2006) 1646–1651.

[113] D.G. Waugh, J. Lawrence, D.J. Morgan, C.L. Thomas, Interaction of CO2laser-modified nylon with osteoblast cells in relation to wettability, Mater. Sci. Eng. C. 29 (2009) 2514–2524.

[114] D.G. Waugh, J. Lawrence, C.D. Walton, R.B. Zakaria, On the effects of using CO2 and F2 lasers to modify the wettability of a polymeric biomaterial, Opt. Laser Technol. 42 (2010) 347–356.

[115] A. Abdal-Hay, A. Salam Hamdy, Y. Morsi, K. Abdelrazek Khalil, J. Hyun Lim, Novel bone regeneration matrix for next-generation biomaterial using a vertical array of carbonated hydroxyapatite nanoplates coated onto electrospun nylon 6 nanofibers, Mater. Lett. 137 (2014) 378–381.

[116] A. Abdal-hay, L.D. Tijing, J.K. Lim, Characterization of the surface biocompatibility of an electrospun nylon 6/CaP nanofiber scaffold using osteoblasts, Chem. Eng. J. 215–216 (2013) 57–64.

[117] J.M. García Páez, A. Carrera, E. Jorge Herrero, I. Millán, A. Rocha, A. Cordón, G. Téllez, M.

Maestro, P. Calero, J.L. Castillo-Olivares, Mechanical behavior of chemically treated ostrich pericardium subjected to uniaxial tensile testing: Influence of the suture, J. Biomed. Mater. Res. 62 (2002) 73–81.

[118] R.D.K. Misra, P.M. Chaudhari, Osteoblasts response to nylon 6,6 blended with single-walled carbon nanohorn, J. Biomed. Mater. Res. - Part A. 101 A (2013) 1059–1068.

[119] I. Khan, K. Saeed, I. Khan, Nanoparticles: Properties, applications and toxicities, Arab. J. Chem. 2017 (2017) 1-24.

[120] K. Ganesh, D. Archana, Review Article on Targeted Polymeric Nanoparticles : An Overview, Am. J. Adv. Drug Deliv. 3 (2013) 196–215.

[121] S. Hasan, A Review on Nanoparticles : Their Synthesis and Types, Res. J. Recent. Sci. 4 (2015) 9–11.

[122] H.L. Nguyen, H.N. Nguyen, H.H. Nguyen, M.Q. Luu, M.H. Nguyen, Nanoparticles: Synthesis and applications in life science and environmental technology, Adv. Nat. Sci. Nanosci. Nanotechnol. 6 (2015) 1-10.

[123] B.L. Banik, P. Fattahi, J.L. Brown, Polymeric nanoparticles: The future of nanomedicine, Wiley Interdiscip. Rev. Nanomedicine Nanobiotechnology. 8 (2016) 271–299.

[124] C.I.C. Crucho, M.T. Barros, Polymeric nanoparticles: A study on the preparation variables and characterization methods, Mater. Sci. Eng. C. 80 (2017) 771–784.

[125] Y. He, L. Luo, S. Liang, M. Long, H. Xu, Amino-functionalized mesoporous silica nanoparticles as efficient carriers for anticancer drug delivery, J. Biomater. Appl. 32 (2017) 524–532.

[126] A.J.B. V. Ravishankar Rai, Nanoparticles and their potential application as antimicrobials, Sci. Against Microb. Pathog. Commun. Curr. Res. Technol. Adv. (2011) 197-20.

[127] M.D.L. Balela, K.L.S. Amores, Formation of Highly Antimicrobial Copper Nanoparticles by Electroless Deposition in Water, Science Diliman 27 (2015) 10–20.

[128] A. Panáček, L. Kvítek, M. Smékalová, R. Večeřová, M. Kolář, M. Röderová, F. Dyčka, M. Šebela, R. Prucek, O. Tomanec, R. Zbořil, Bacterial resistance to silver nanoparticles and how to overcome it, Nat. Nanotechnol. 13 (2018) 65–71.

[129] M. Kumar, A. Curtis, C. Hoskins, Application of nanoparticle technologies in the combat against anti-microbial resistance, Pharmaceutics. 10 (2018) 1–17.

[130] A. Munoz-Bonilla, M.L. Cerrada, M. Fernandez-Garcia (2014) Polymeric Materials with Antimicrobial Activity.The Royal Society of Chemistry, Cambridge (UK).

[131] M.B. Gawande, A. Goswami, F.X. Felpin, T. Asefa, X. Huang, R. Silva, X. Zou, R. Zboril, R.S. Varma, Cu and Cu-Based Nanoparticles: Synthesis and Applications in Catalysis, Chem. Rev. 116 (2016) 3722–3811.

[132] A.K. Chatterjee, R. Chakraborty, T. Basu, Mechanism of antibacterial activity of copper

nanoparticles, Nanotechnology. 25 (2014) 1-12.

[133] L. Sheng, S. Huang, M. Sui, L. Zhang, L. She, Y. Chen, Deposition of copper nanoparticles on multiwalled carbon nanotubes modified with poly (acrylic acid) and their antimicrobial application in water treatment, Front. Environ. Sci. Eng. 9 (2015) 625–633.

[134] N.M. Barkoula, B. Alcock, N.O. Cabrera, T. Peijs, Fatigue properties of highly oriented polypropylene tapes and all-polypropylene composites, Polym. Polym. Compos. 16 (2008) 101–113.

[135] V. Meynen, P. Cool, E.F. Vansant, Verified syntheses of mesoporous materials, Microporous Mesoporous Mater. 125 (2009) 170–223.

[136] S.-H. Wu, C.-Y. Mou, H.-P. Lin, Synthesis of mesoporous silica nanoparticles, Chem. Soc. Rev. 42 (2013) 3862-3875.

[137] D. Douroumis, I. Onyesom, M. Maniruzzaman, J. Mitchell, Mesoporous silica nanoparticles in nanotechnology, Crit. Rev. Biotechnol. 33 (2013) 229–245.

[138] P. Yang, S. Gai, J. Lin, Functionalized mesoporous silica materials for controlled drug delivery, Chem. Soc. Rev. 41 (2012) 3679-3698.

[139] X. Xu, C. Wu, A. Bai, X. Liu, H. Lv, Y. Liu, Folate-Functionalized Mesoporous Silica Nanoparticles as a Liver Tumor-Targeted Drug Delivery System to Improve the Antitumor Effect of Paclitaxel, J. Nanomater. 2017 (2017) 1-13.

[140] L. Maggini, I. Cabrera, A. Ruiz-Carretero, E.A. Prasetyanto, E. Robinet, L. De Cola, Breakable mesoporous silica nanoparticles for targeted drug delivery, Nanoscale. 8 (2016) 7240–7247.

[141] V.B. Ivanov, J. Behnisch, A. Holländer, F. Mehdorn, H. Zimmermann, Determination of functional groups on polymer surfaces using fluorescence labelling, Surf. Interface Anal. 24 (1996) 257–262.

[142] G.T. Hermanson (2013) Bioconjugate Techniques 3rd Edn. Elsevier Inc., San Diego (USA).

[143] J.M. Goddard, J.H. Hotchkiss, Polymer surface modification for the attachment of bioactive compounds, Prog. Polym. Sci. 32 (2007) 698–725.

[144] J.M. Schuster, C.E. Schvezov, M.R. Rosenberger, Analysis of the Results of Surface Free Energy Measurement of Ti6Al4V by Different Methods, Procedia Mater. Sci. 8 (2015) 732–741.

[145] D. Djordjevic, Microtiter plate assay for assessment of Listeria monocytogenes biofilm formation, Appl. Environ. Microbiol. 68 (2002) 2950–2958.

[146] R.A. Soomro, S.T. Hussain Sherazi, Sirajuddin, N. Memon, M.R. Shah, N.H. Kalwar, K.R. Hallam, A. Shah, Synthesis of air stable copper nanoparticles and their use in catalysis, Adv. Mater. Lett. 5 (2014) 191–198.

[147] X. Deng, K. Chen, H. Tüysüz, Protocol for the Nanocasting Method: Preparation of Ordered

Mesoporous Metal Oxides, Chem. Mater. 29 (2017) 40–52.

[148] F. Sevimli, A. Yilmaz, Surface functionalization of SBA-15 particles for amoxicillin delivery, Microporous Mesoporous Mater. 158 (2012) 281–291.

[149] F.A. Carey (2000) Organic Chemistry 4th Edn. The McGraw-Hill Companies, Inc., USA.

[150] S. Swar, V. Zajícová, M. Rysová, I. Lovětinská-Šlamborová, L. Voleský, I. Stibor, Biocompatible surface modification of poly(ethylene terephthalate) focused on pathogenic bacteria: Promising prospects in biomedical applications, J. Appl. Polym. Sci. 134 (2017) 1-11.

[151] R. Bartzatt, Dansylation of hydroxyl and carboxylic acid functional groups, J. Biochem. Biophys. Methods. 47 (2001) 189–195.

[152] Q. Zhao, S. Wang, H. Müller-Steinhagen, Tailored surface free energy of membrane diffusers to minimize microbial adhesion, Appl. Surf. Sci. 230 (2004) 371–378.

[153] Y. Arima, H. Iwata, Effect of wettability and surface functional groups on protein adsorption and cell adhesion using well-defined mixed self-assembled monolayers, Biomaterials. 28 (2007) 3074–3082.

[154] R. Pignatello (2013) Advances in Biomaterials Science and Biomedicl Applications. InTech, Croatia.

[155] G.A. Abraham, A.A.A. De Queiroz, J.S. Román, Hydrophilic hybrid IPNs of segmented polyurethanes and copolymers of vinylpyrrolidone for applications in medicine, Biomaterials. 22 (2001) 1971–1985.

[156] J. Clayden, N. Greevs, S. Warren, Peter Wothers (2012) Organic chemistry 2nd Edn. Oxford Universiry Press, UK.

[157] J.P. Hitchcock, A.L. Tasker, K. Stark, A. Leeson, E.A. Baxter, S. Biggs, O.J. Cayre, Adsorption of Catalytic Nanoparticles onto Polymer Substrates for Controlled Deposition of Microcapsule Metal Shells, Langmuir. 34 (2018) 1473–1480.

[158] S. Romero-Vargas Castrillón, X. Lu, D.L. Shaffer, M. Elimelech, Amine enrichment and poly(ethylene glycol) (PEG) surface modification of thin-film composite forward osmosis membranes for organic fouling control, J. Memb. Sci. 450 (2014) 331–339.

[159] K.L. Prime, G.M. Whitesides, Adsorption of proteins onto surfaces containing end-attached oligo(ethylene oxide): a model system using self-assembled monolayers, J. Am. Chem. Soc. 115 (1993) 10714–10721.

[160] S. Chatterjee, F. Salaun, C. Campagne, The influence of 1-butanol and trisodium citrate ion on morphology and chemical properties of chitosan-based microcapsules during rigidification by alkali treatment, Mar. Drugs. 12 (2014) 5801–5816.

[161] E.M. Van Wagner, A.C. Sagle, M.M. Sharma, Y.H. La, B.D. Freeman, Surface modification of commercial polyamide desalination membranes using poly(ethylene glycol) diglycidyl ether to

enhance membrane fouling resistance, J. Memb. Sci. 367 (2011) 273–287.

[162] G.M. Bruinsma, H.C. van der Mei, H.J. Busscher, Bactetial Adhesion to Surface Hydrophlic and Hydrophobic Contact Lenses, Biomaterials. 22 (2001) 3217–3224.

[163] K. Anselme, P. Davidson, A.M. Popa, M. Giazzon, M. Liley, L. Ploux, The interaction of cells and bacteria with surfaces structured at the nanometre scale, Acta Biomater. 6 (2010) 3824–3846.

[164] Y. Lo Hsieh, D.A. Timm, Relationship of substratum wettability measurements and initial Staphylococcus aureau adhesion to films and fabrics, J. Colloid Interface Sci. 123 (1988) 275–286.

[165] S.I. Jeon, J.H. Lee, J.D. Andrade, P.G. De Gennes, Protein Surface Interactions in the Presence of Polyethylene Oxide, J. Colloid Interface Sci. 142 (1991) 149–158.

[166] J. Ramyadevi, K. Jeyasubramanian, A. Marikani, G. Rajakumar, A.A. Rahuman, Synthesis and antimicrobial activity of copper nanoparticles, Mater. Lett. 71 (2012) 114–116.

[167] A. Godymchuk, G. Frolov, A. Gusev, O. Zakharova, E. Yunda, D. Kuznetsov, E. Kolesnikov, Antibacterial Properties of Copper Nanoparticle Dispersions: Influence of Synthesis Conditions and Physicochemical Characteristics, IOP Conf. Ser. Mater. Sci. Eng. 98 (2015) 1-8.

[168] A. De Los Santos Pereira, T. Riedel, E. Brynda, C. Rodriguez-Emmenegger, Hierarchical antifouling brushes for biosensing applications, Sensors Actuators, B Chem. 202 (2014) 1313–1321.

[169] U. Bog, A. De los Santos Pereira, S.L. Mueller, S. Havenridge, V. Parrillo, M. Bruns, A.E. Holmes, C. Rodriguez-Emmenegger, H. Fuchs, M. Hirtz, Clickable Antifouling Polymer Brushes for Polymer Pen Lithography, ACS Appl. Mater. Interfaces. 9 (2017) 12109–12117.

[170] T. Riedel, Z. Riedelová-Reicheltová, P. Májek, C. Rodriguez-Emmenegger, M. Houska, J.E. Dyr, E. Brynda, Complete identification of proteins responsible for human blood plasma fouling on poly(ethylene glycol)-based surfaces, Langmuir. 29 (2013) 3388–3397.

[171] C.M. Liu, L. Guo, H.B. Xu, Z.Y. Wu, J. Weber, Seed-mediated growth and properties of copper nanoparticles, nanoparticle 1D arrays and nanorods, Microelectron. Eng. 66 (2003) 107–114.

[172] C.R. Bealing, W.J. Baumgardner, J.J. Choi, T. Hanrath, R.G. Hennig, Predicting nanocrystal shape through consideration of surface-ligand interactions, ACS Nano. 6 (2012) 2118–2127.

[173] H.G. Liao, D. Zherebetskyy, H. Xin, C. Czarnik, P. Ercius, H. Elmlund, M. Pan, L.W. Wang, H. Zheng, Facet development during platinum nanocube growth, Science. 345 (2014) 916–919.

[174] J. Zhao, E. Baibuz, J. Vernieres, P. Grammatikopoulos, V. Jansson, M. Nagel, S. Steinhauer, M. Sowwan, A. Kuronen, K. Nordlund, F. Djurabekova, Formation Mechanism of Fe Nanocubes by Magnetron Sputtering Inert Gas Condensation, ACS Nano. 10 (2016) 4684–4694.

[175] M.J. Guajardo-Pacheco, J.E. Morales-Sánchez, J. González-Hernández, F. Ruiz, Synthesis of copper nanoparticles using soybeans as a chelant agent, Mater. Lett. 64 (2010) 1361–1364.

[176] N.R. Jana, Z.L. Wang, T.K. Sau, T. Pal, Seed-mediated growth method to prepare cubic copper nanoparticles, Curr. Sci. 79 (2000) 1367–1370.

[177] C.J. Brinker, Hydrolysis And Condensation Of Silicates: Effects On Structure, J. Non. Cryst. Solids. 100 (1988) 31–50.

[178] A. Zukal, M. Thommes, J. Čejka, Synthesis of highly ordered MCM-41 silica with spherical particles, Microporous Mesoporous Mater. 104 (2007) 52–58.

[179] J. Yu, A. Shen, Y. Cao, G. Lu, Preparation of Pd-Diimine @ SBA-15 and Its Catalytic Performance for the Suzuki Coupling Reaction, Catalysts. 6 (2016) 181-197.

[180] N.I. Vazquez, Z. Gonzalez, B. Ferrari, Y. Castro, Synthesis of mesoporous silica nanoparticles by sol-gel as nanocontainer for future drug delivery applications, Bol. La Soc. Esp. Ceram. Y Vidr. 56 (2017) 139–145.

[181] S.M.L. Dos Santos, K.A.B. Nogueira, M. De Souza Gama, J.D.F. Lima, I.J. Da Silva Júnior, D.C.S. De Azevedo, Synthesis and characterization of ordered mesoporous silica (SBA-15 and SBA-16) for adsorption of biomolecules, Microporous Mesoporous Mater. 180 (2013) 284–292.

[182] P.K. Chen, N.C. Lai, C.H. Ho, Y.W. Hu, J.F. Lee, C.M. Yang, New synthesis of MCM-48 nanospheres and facile replication to mesoporous platinum nanospheres as highly active electrocatalysts for the oxygen reduction reaction, Chem. Mater. 25 (2013) 4269–4277.

[183] E. Van Bavel, P. Cool, K. Aerts, E.F. Vansant, Plugged Hexagonal Templated Silica (PHTS): An In-Depth Study of the Structural Characteristics, J. Phys. Chem. B. 108 (2004) 5263–5268.

[184] L. Hermida, A.Z. Abdullah, A.R. Mohamed, Synthesis and Characterization of Mesostructured Cellular Foam (MCF) Silica Loaded with Nickel Nanoparticles as a Novel Catalyst, Mater. Sci. Appl. 4 (2013) 52–62.

[185] M. Thommes, K. Kaneko, A. V. Neimark, J.P. Olivier, F. Rodriguez-Reinoso, J. Rouquerol, K.S.W. Sing, Physisorption of gases, with special reference to the evaluation of surface area and pore size distribution (IUPAC Technical Report), Pure Appl. Chem. 87 (2015) 1051–1069.

[186] S. Rahmani, J.O. Durand, C. Charnay, L. Lichon, M. Férid, M. Garcia, M. Gary-Bobo, Synthesis of mesoporous silica nanoparticles and nanorods: Application to doxorubicin delivery, Solid State Sci. 68 (2017) 25–31.

[187] G. Nicholson, A.C. Pereira, G.M. Hall, Parkinson's disease and anaesthesia, Br. J. Anaesth. 89 (2002) 904–916.

[188] S. Jangra, S. Duhan, M.S. Goyat, V. Chhokar, S. Singh, A. Manuja, Influence of functionalized mesoporous silica in controlling azathioprine drug release and cytotoxicity properties, Mater.

Res. Innov. 21 (2017) 413–425.

[189] S. Jangra, P. Girotra, V. Chhokar, V.K. Tomer, A.K. Sharma, S. Duhan, In-vitro drug release kinetics studies of mesoporous SBA-15-azathioprine composite, J. Porous Mater. 23 (2016) 679–688.

[190] H. Pulikkalpura, R. Kurup, P.J. Mathew, S. Baby, Levodopa in Mucuna pruriens and its degradation, Sci. Rep. 5 (2015) 2–10.